Motion Estimation for Inverse Synthetic Aperture Radar Imaging

Stephen Edward Simmons

B.Sc. (1992)
B.E. (Elec) (1992)
University of Melbourne

January 1995

*Submitted in total fulfilment
of the requirements of the
degree of Doctor of Philosophy*

**Department of Electrical and Electronic Engineering,
University of Melbourne,
Parkville 3052, Australia.**

Motion Estimation for Inverse Synthetic Aperture Radar Imaging

Stephen Edward Simmons
B.Sc. (1992)
B.E. (Elec) (1992)
University of Melbourne

January 1995

Submitted in total fulfilment
of the requirements of the
degree of Doctor of Philosophy

Department of Electrical and Electronic Engineering,
University of Melbourne,
Parkville 3052, Australia.

Produced on acid-free paper

Abstract

Inverse synthetic aperture radar (ISAR) forms high resolution radar images of a moving target by using the target's changing aspect angle to create a synthetic aperture. Estimates of changes in the target's position accurate to a tenth of a wavelength are essential for sharply focussed ISAR images.

This thesis investigates the use of estimation theory to find optimal estimators of a target's radial motion during stepped-frequency ISAR imaging and to analyse their performance. The aim of this is two-fold: to apply a rigorously mathematical approach to a problem that has traditionally been solved using more intuitive methods, and to develop a unifying framework in whose terms the intuitive methods can be reinterpreted and reappraised.

The maximum likelihood estimator of the radial distance moved by the target is derived as the location of the global minimum of a cost function. The cost function has a slowly varying envelope modulated by a high frequency carrier. The envelope shows the approximate distance the target has moved and the high frequency modulation allows the distance to be determined within a small fraction of a wavelength.

Four efficient algorithms for minimizing the cost function are derived. Two are approximate global algorithms based on the fast Fourier transform and the chirp-Z transform. The other two are more precise local minimization algorithms. The second of these is an iterative contraction mapping with the rate of convergence equal to the stepped-frequency waveform's relative bandwidth.

The statistical properties of the maximum likelihood motion estimator are examined and the estimator is shown to be unbiased.

To illustrate connections between conventional methods of range profile alignment and phase compensation, the maximum likelihood motion estimator is shown to be equivalent to the location of the maximum of the cross-correlation of the target's complex range profiles. Cross-correlating the magnitudes of the range profiles, as in conventional motion estimation, is shown to be less accurate but less susceptible to phase errors caused by the target rotating.

Phase alignment techniques of adaptive beamforming and the phase gradient autofocus are also compared to the maximum likelihood estimator. It

is found that the phase gradient part of phase gradient autofocus can be implemented using slightly sub-optimal versions of the algorithm developed for the local minimization of the estimator's cost function.

Finally, some common assumptions of ISAR imaging are analysed, including the conditions under which polar reformatting may be neglected, the assumption that the target's rotation may be neglected during motion estimation, and the assumption that range profile alignment need only be accurate to one range bin. These assumptions are found to impose some new sets of constraints on the target's motion and the ISAR image's resolution.

This work illustrates how a mathematical approach using estimation theory can be used to obtain useful ISAR motion estimators and provide valuable insights into related motion estimators whose derivations otherwise could not be justified so easily.

Declaration

This thesis contains fewer than 100,000 words.

Acknowledgements

Contents

List of Figures

Chapter 1

Introduction

Radar has been used for over fifty years to locate and track distant aircraft and ships, but it is only comparatively recently that it has been used for forming high resolution two-dimensional images. Since the size of a radar system's antenna determines its angular resolution, radar imaging systems would ordinarily require a prohibitively large antenna to obtain a high enough angular resolution. However, by combining measurements made by an antenna as it moves to different locations over a large synthetic aperture, digital signal processing creates a synthetic aperture much larger than physical size of the radar's antenna. This synthetic aperture has a very high angular resolution and is used to form the radar image.

The two forms of radar imaging are synthetic aperture radar (SAR) and inverse synthetic aperture radar (ISAR). In SAR imaging, the radar is carried aboard a moving platform such as an aircraft or satellite. The platform's motion creates the synthetic aperture which is used to form high resolution maps of the terrain below. ISAR imaging recognises that the synthetic aperture may be created just as effectively if the target being imaged is moving and the radar is stationary.

The success of radar imaging relies on the relative position and orientation of the radar antenna and the target being known precisely at all times. Radar signal processing is coherent, so it is important that any errors in forming the synthetic aperture are less than a small fraction of a radar wavelength. For microwave radar systems operating at X-band, the wavelength is about 3 cm, so this places very strict requirements on the stability of the synthetic aperture.

The movement of the radar antenna and the target cannot be expected to produce a synthetic aperture that is this accurate. To prevent the radar image becoming degraded, the relative motion between radar and target must be continuously measured and appropriate corrections made to the synthetic

aperture. Measuring the relative motion is called motion estimation and correcting the radar measurements for distortions in the synthetic aperture is called motion compensation.

With SAR imaging, the radar moves and the target is stationary. Therefore an inertial nagivation unit carried with the radar can be used to measure the position of the radar antenna at all times. This is not accurate to a small fraction of a wavelength, but it is good enough to correct for most of the radar's motion. Some further autofocusing may be required for very high resolution SAR images to remove blurring caused by small residual motion errors.

In ISAR imaging, the target moves and the radar is stationary. Because the target's motion is not known *a priori*, it must be obtained solely from the radar measurements that are processed to form the radar image. This makes ISAR imaging, particularly the motion estimation and motion compensation parts, a much more difficult problem than SAR. As a result, SAR systems have been operating for more than thirty years while robust ISAR systems are still at the research and development stage.

A number of methods of ISAR motion estimation and motion compensation have been developed. These methods can generally be classed as either range profile alignment, where range profiles of the target over time are roughly aligned to correct for the target's large scale radial movement, or as phase compensation, where residual motion errors less than the size of a radar wavelength are corrected. Range profile alignment is usually performed by cross-correlating range profiles of the target measured at different times. Phase compensation algorithms, such as adaptive beamforming and the phase gradient autofocus, compare the phases of radar measurements made at different times to correct for slight motion errors.

Many variations on these basic methods of motion estimation have been developed. All are based on intuitive notions of what constitutes the best approach to estimating the target's motion. The result is many *ad hoc* methods of motion estimation. Few make any concrete claims about the accuracy of their estimates or analyse the conditions under which they perform well or badly.

In this thesis, statistical estimation theory is used to obtain the maximum likelihood solution of the ISAR motion estimation problem. From this, the estimator's statistical performance is characterised and connections are made with methods of range profile alignment and phase compensation.

1.1 Outline of Thesis

This thesis considers the problem of estimating the radial motion of a moving target during ISAR imaging. Statistical estimation theory is used to derive a

new motion estimator that is the maximum likelihood solution of the motion estimation problem. Efficient algorithms are developed for evaluating the estimator and its statistical performance is analysed in detail. Similarities between the maximum likelihood solution and other *ad hoc* methods of motion estimation are considered. The thesis concludes with a detailed analysis of some of the assumptions implicitly or explicitly made during ISAR imaging. This places several new constraints on the motion of the target and the resolution of the ISAR image.

Chapter 2 is an introduction to the principles of statistical estimation theory, and in particular, to maximum likelihood estimation. The various forms of the maximum likelihood estimator for scalar and vector parameters are derived, along with the Cramér-Rao bounds on any estimator's variance. The chapter concludes with a discussion of applying estimation theory when the parameters being estimated are complex numbers.

Chapters 3 to 5 serve as an introduction to high resolution radar and radar imaging and as a detailed description of some motion estimation algorithms that are curently used in ISAR imaging.

Chapter 3 begins with an overview of radar imaging using SAR and ISAR and a qualitative description of the requirements for achieving a high resolution two-dimensional radar image of a moving target. Once the general model for radar reflections from a distributed target has been derived, the requirements for a high range resolution and a high cross-range resolution are analysed to obtain some conditions on the radar's waveforms and the the target's motion. This demonstrates the need for a wideband waveform such as a chirp or a stepped-frequency waveform; both chirp and stepped-frequency waveforms are considered, but the remainder of the thesis assumes that a stepped-frequency radar is being used.

Chapter 4 defines the basic model used for ISAR imaging and obtains ISAR imaging algorithms using range-Doppler processing and wavenumber $(\omega - k)$ processing. The traditional view of ISAR as a Doppler phenomenon is criticised, and this old-fashioned description of ISAR has been included for completeness in appendix 4B at the end of the chapter.

Chapter 5 emphasises the importance of motion estimation and motion compensation in ISAR imaging. Methods of correcting deviations in the target's radial position and orientation are derived, and these motion compensation algorithms are used to suggest how the target's radial position and orientation may be estimated. A number of radial motion estimation algorithms are discussed. These methods include range profile alignment using cross-correlation and image feedback control, and phase compensation using adaptive beamforming and the phase gradient autofocus.

The next three chapters, chapters 6 to 8, are a detailed examination of a new method of radial motion estimation for ISAR based on the principles of maximum likelihood estimation. Expressions for the maximum likelihood

estimator are derived, algorithms for evaluating the estimator efficiently are developed and the estimator's statistical performance is carefully analysed.

Chapter 6 sets up a model for estimating the radial distance Δr moved by a target in the time between two frequency responses being measured. The maximum likelihood estimator of Δr is derived in two different ways based on this model. The first assumes that the radial distance moved by the target is the only unknown parameter, treating the problem as one of estimating a scalar parameter. The second form of the maximum likelihood estimator recognises that the measurement noise variance and the target's frequency response are also unknown, and should be included with Δr to give a vector of unknown parameters. These two estimators of Δr have the same mathematical form, namely a cost function $J(r)$ whose global minimum gives the maximum likelihood estimate of Δr. The chapter also obtains expressions for the maximum likelihood estimators of the noise variance and of the target's frequency response.

Chapter 7 considers possible methods of finding the global minimum of the cost function $J(r)$. This is not a simple task because $J(r)$ has a slowly varying envelope, giving a coarse estimate of Δr, and a high frequency modulation, which allows a very accurate estimate of the fractional part of the number of half-wavelengths the target has moved. Reflecting these characteristics of $J(r)$ at the two different scales, algorithms are developed which first find the approximate location of the minimum of $J(r)$, and then refine this estimate until Δr has been estimated to within a fraction of a radar wavelength. The algorithms for finding the approximate location of the global minimum of $J(r)$ are based on the fast Fourier transform and the chirp-Z transform. Two algorithms for finding the fraction of half a wavelength the target has moved have been developed. The first is an approximation that estimates the parameters of a sinusoid fitted to the high frequency modulation. The second is an iterative scheme that uses a contraction mapping converging to the local minima of $J(r)$. The accuracies of each of these algorithms in finding the location of the maximum likelihood estimator have been specified and guaranteed by rigorous proofs of convergence.

Chapter 8 is a detailed examination of the maximum likelihood estimators' statistical properties. These include showing that the maximum likelihood estimator of Δr is unbiased and obtaining bounds on the estimator's variance for both the scalar and vector forms of the maximum likelihood estimator. Some suggestions are made towards obtaining non-asymptotic expressions for the estimator's probability density function, but complete non-asymptotic results could not be obtained.

Chapter 9 is a comparison between some of the conventional methods of ISAR radial motion estimation from chapter 5 and the maximum likelihood solution from chapters 6 to 8. The maximum likelihood estimator is rewritten as the cross-correlation of the target's complex range profiles. Phase gradient

autofocus, adaptive beamforming and conventional range profile alignment using cross-correlation are shown to be closely related to modified forms of the maximum likelihood solution, a result which gives a sound theoretical basis to these largely *ad hoc* methods of radial motion estimation. The differences between these methods and the maximum likelihood estimator suggest that they sacrifice accuracy for a decreased sensitivity to phase noise caused by the target's rotation.

Chapter 10, the penultimate chapter in the thesis, is a detailed examination of four of the approximations and assumptions that are frequently made in ISAR imaging. These four are the plane-wave approximation in range-Doppler ISAR processing, the conditions under which polar reformatting may be omitted, the assumption of negligible rotation during radial motion estimation, and the assumption that motion compensation need only correct the target's radial motion to the nearest multiple of a range bin and then within half a wavelength. All four approximations are analysed in the same way, using a technique that can be used to analyse any approximation in ISAR imaging. This leads to four sets of constraints on the ISAR image's resolution and the target's motion. The set of constraints arising from neglecting polar reformatting is shown to be indentical to the constraints obtained by restricting the motion of scatterers on the target through range and cross-range resolution cells, a situation which appears to have nothing in common with polar reformatting. The analysis of a target's rotation during radial motion estimation shows that the target should rotate sufficiently slowly that it fills no more than one-quarter of the ISAR image in the cross-range direction. The analysis of the final assumption shows that provided phase compensation is perfect, the range profile alignment can misestimate the target's radial position by one-quarter of a range bin before the quality of the resulting ISAR image is adversely affected.

The last chapter of the thesis, chapter 11, contains the conclusions of this research into ISAR motion estimation and suggests some avenues for future research.

1.2 Original Contributions

This thesis contains the following major contributions to the field of ISAR imaging:

- The whole of chapter 6, including the maximum likelihood formulation of the ISAR motion estimation problem, the two forms of the maximum likelihood estimator of the target's radial movement and the maximum likelihood estimator of the noise variance.

- The whole of chapter 7, including all algorithms for the global and local

minimization of the cost function $J(r)$. Algorithm 7.1 is superficially similar to motion estimation by cross-correlating range profiles, but it is actually quite different because it does not take the magnitude before correlating. Algorithm 7.3 is the first time the chirp-Z transform has been used in ISAR motion estimation. The two algorithms for the local minimization of the cost function are also new. These algorithms are all proved to behave as claimed. Such rigorous proofs are rare in the ISAR literature.

- The whole of chapter 8, especially the results concerning the unbiased nature of the maximum likelihood estimator of Δr, and the Cramér-Rao bounds. The work on non-asymptotic results has prompted several general questions in the field of extreme value theory. These are stated in section 11.2.2, and concern the probability density function of the location of the maximum of a known bandlimited function in bandlimited noise.

- The whole of chapter 9, especially the formulation of the maximum likelihood estimator in terms of the cross-correlation of the complex range profiles and the connections between the maximum likelihood estimator and conventional methods of range profile alignment and phase compensation.

- Chapter 10 is the first time that a single approach to analysing approximations in ISAR has been used to test so many assumptions. The constraints for neglecting polar reformatting are derived completely differently from the usual analysis of motion through resolution cells, leading to identical constraints. Section 10.4 is the first time the effect of the target's rotation on radial motion estimation has been considered. The constraint that the target should occupy no more than one-quarter of the cross-range window is new, as is the definition and measurement of rotation-induced noise. Section 10.5 is the first analysis of the accuracy required for motion compensation, and it justifies the use of range profile alignment followed by phase compensation.

- The critical review of ISAR imaging in chapters 3 to 5 is also an important but less major contribution.

A number of papers resulting from this research are in preparation:

- S. E. Simmons and R. J. Evans, "Maximum Likelihood Motion Estimation for ISAR Imaging." (to be submitted to *IEEE Transactions on Information Theory*)

- S. E. Simmons and R. J. Evans, "Resolution and Motion Constraints in ISAR." (to be submitted to *IEEE Transactions on Signal Processing*)

- S. E. Simmons and R. J. Evans, "ISAR Motion Estimators and the Maximum Likelihood Solution." (to be submitted to *IEEE Transactions on Aerospace and Electronic Systems*)

Three conference papers on this and earlier research have been presented:

- S. E. Simmons and R. J. Evans, "Maximum Likelihood Autofocusing of Radar Images", to appear in *Proc. Radar '95*, Washington D.C., 8–11 May 1995.

- S. E. Simmons and R. J. Evans, "A New Approach to Motion Estimation for ISAR Imaging", *Proc. ICASSP '94*, Adelaide, 19–22 April 1994, pp. V-201–V-204.

- S. E. Simmons, D. J. Heilbronn and D. Nandagopal, "Kalman Range Tracking for ISAR Motion Compensation", *Proc. Radarcon '90*, Adelaide, 18–20 April 1990, pp. 689–694.

The ICASSP paper uses the same motion estimator as the maximum likelihood estimator derived here, except that at the time it was not recognised as such. The methods of evaluating the motion estimator in that paper are far less efficient than the methods presented in chapter 7 of this thesis. The Radarcon paper was an early attempt to derive a frequency domain motion estimator that is not affected by 2π ambiguities.

The material in chapter 2 is very similar to the following course notes on maximum likelihood estimation:

- S. E. Simmons, *Maximum Likelihood Estimation* in "Course Notes on Estimation Theory" prepared for the CSSIP Estimation Theory Course, Department of Electrical Engineering, University of Melbourne, 14–16 February 1994.

Chapter 2

Mathematical Preliminaries

Statistical estimation theory is used throughout this thesis to derive and analyse estimators of a radar target's motion. This chapter summarizes the main results of maximum likelihood estimation for real parameters, and extends it for use with complex parameters.

Full derivations of the results mentioned here may be found in the papers by Fisher [28, 30, 31], and the books by Cramér [22], Kay [51], Kendall, Stuart and Ord [92, 93], Rao [69], and Van Trees [95].

2.1 Statistical Estimation Theory

As expressed by Fisher in *Theory of Statistical Estimation* [28],

> "Problems of estimation arise when we know, or are willing to assume, the form of the frequency distribution of the population, as a mathematical function involving one or more unknown parameters, and wish to estimate the values of these parameters by means of the observational record available. A statistic may be defined as a function of the observations designed as an estimate of any such parameter." *R. A. Fisher, 1925.*

The population's known frequency distribution takes the form of a probability density function $p(\boldsymbol{x}; \boldsymbol{\theta})$.[1] This is one member of the family of probability distributions $p(\boldsymbol{x}; \cdot)$ selected by the vector of unknown parameters

$$\boldsymbol{\theta} = [\theta_1, \theta_2, \cdots, \theta_M]^T \tag{2.1}$$

---

[1]To distinguish scalars, vectors and matrices, scalars usually appear in a normal-weight typeface x, vectors as bold lower-case letters $\boldsymbol{x}$ and matrices as bold upper-case letters $\boldsymbol{X}$.

The estimator $\widehat{\boldsymbol{\theta}}$ is a function of the measured data $\boldsymbol{x}$ used to estimate $\boldsymbol{\theta}$, and the estimate is the value of the estimator for one particular realization of $\boldsymbol{x}$.[2]

In general, there are infinitely many ways in which $\boldsymbol{x}$ can be processed to give $\widehat{\boldsymbol{\theta}}$. Estimation theory is used to select one particular way of processing the measurements to give the "best" estimate of $\boldsymbol{\theta}$, where "best" is defined in terms of some optimality criteria. Three useful optimality criteria are consistency, bias and efficiency.

An estimator is consistent if the estimates tend to the parameter as the number of measurements tends to infinity. Formally, this convergence in probability is written that for any $\epsilon > 0$ and any $\nu > 0$, there exists some N such that

$$\Pr\left\{\left|\widehat{\boldsymbol{\theta}}_n - \boldsymbol{\theta}\right| < \epsilon\right\} > 1 - \nu \qquad \forall n > N \qquad (2.2)$$

where n is the number of measurements in $\boldsymbol{x}$ combined to form the estimate $\widehat{\boldsymbol{\theta}}_n$.

An estimator is unbiased if its expectation is equal to the unknown parameter

$$\mathrm{E}\left\{\widehat{\boldsymbol{\theta}}\right\} = \boldsymbol{\theta} \qquad (2.3)$$

This is a stronger condition than consistency, because a consistent estimator with a finite expectation is asymptotically unbiased as the number of measurements tends to infinity. A consistent estimator is not, in general, unbiased for a finite number of measurements.

If an estimator is not unbiased, it is biased. The expectation of a biased estimator is

$$\mathrm{E}\left\{\widehat{\boldsymbol{\theta}}\right\} = \boldsymbol{\theta} + \boldsymbol{b}(\boldsymbol{\theta}) \qquad (2.4)$$

where $\boldsymbol{b}(\boldsymbol{\theta})$ is the bias. Depending on the form of $\boldsymbol{b}(\boldsymbol{\theta})$, it may be possible to modify the estimator so that it becomes unbiased.

Bias and consistency are important criteria, but they are not the only criteria by which estimators should be judged. When $\boldsymbol{\theta}$ has a number of unbiased estimators, the optimal estimator is the one which makes best use of the information contained in the set of measurements.[3]

Fisher measured an estimator's efficiency as the ratio of the estimator's variance to the most efficient estimator's variance, expressed as a percentage. Then an efficient estimator, with an efficiency of $100\,\%$, has the lowest variance of all consistent estimators. Another estimator, with an efficiency of

---

[2]Some authors use an upper-case letter for an estimator and a lower-case letter for an estimate. Here both are indicated by the same symbol $\widehat{\theta}$ and the context indicates whether the estimator or an estimate is meant.

[3]Fisher was critical of the method of moments for ignoring efficiency and using consistency as the only criterion, saying "estimates of the parameters may be obtained ... but they are often estimates of little value" [28].

$\eta\,\%$, requires approximately $100N/\eta$ measurements to have the same variance as the efficient estimator has with N measurements.

Terminology has evolved since Fisher's papers on statistical estimation theory. Optimal estimators are now minimum variance unbiased estimators (MVUE) and efficient now means a MVUE which also attains the Cramér-Rao bound. Rao [69, p. 283] complains that "logically, this does not appear to be a good definition" because the Cramér-Rao bound is only one among many lower bounds. The word "efficient" has such strong non-mathematical connotations that it seems wrong not calling a minimum-variance estimator efficient if the Cramér-Rao bound is unobtainable by any estimator.

The difficulty with using the MVUE criterion to select an estimator is that there is no general method for minimizing $\mathrm{Var}\left\{\widehat{\boldsymbol{\theta}}\right\}$ over all unbiased estimators. All that can be done is analyse different estimators to compare their biases and variances.

2.2　The Cramér-Rao Bound

The Cramér-Rao bound provides a simple lower bound on the variance of any unbiased estimator $\widehat{\boldsymbol{\theta}}$. It is stated first for a scalar parameter θ, then for a vector parameter $\boldsymbol{\theta}$, and finally, it is restated as a lower bound on the mean square error of any biased estimator. The Cramér-Rao bound is sometimes called the minimum variance bound, or MVB [93].

2.2.1　The Scalar Cramér-Rao Bound

Let $\boldsymbol{x}$ be a set of measurements used to estimate an unknown parameter θ where the probability density function $p(\boldsymbol{x};\theta)$ is known and the partial derivatives

$$\frac{\partial p(\boldsymbol{x};\theta)}{\partial \theta}$$

and

$$\frac{\partial^2 p(\boldsymbol{x};\theta)}{\partial \theta^2}$$

exist and are absolutely integrable. If $\widehat{\theta}$ is an unbiased estimator of θ, the variance of $\widehat{\theta}$ is always bounded below by the Cramér-Rao bound

$$\mathrm{Var}\left\{\widehat{\theta}\right\} \geq \left[\mathrm{E}\left\{\left(\frac{\partial \ln p(\boldsymbol{x};\theta)}{\partial \theta}\right)^2\right\}\right]^{-1} = \left[-\mathrm{E}\left\{\frac{\partial^2 \ln p(\boldsymbol{x};\theta)}{\partial \theta^2}\right\}\right]^{-1} \qquad (2.5)$$

The Cramér-Rao bound is satisfied with equality exactly when

$$\frac{\partial \ln p(\boldsymbol{x};\theta)}{\partial \theta} = k(\theta)\left(\widehat{\theta} - \theta\right) \qquad (2.6)$$

for some function $k(\theta)$ not dependent on $\boldsymbol{x}$. If this is the case, the estimator has the lowest variance of all unbiased estimators and is called efficient.

2.2.2   The Vector Cramér-Rao Bound

When the unknown parameter $\boldsymbol{\theta}$ is a vector, the Cramér-Rao bound is expressed in terms of the Fisher information matrix $\boldsymbol{I}(\boldsymbol{\theta})$. The elements of $\boldsymbol{I}(\boldsymbol{\theta})$ are

$$
\begin{aligned}
I_{ij} &= \mathrm{E}\left\{\frac{\partial \ln p(\boldsymbol{x};\boldsymbol{\theta})}{\partial \theta_i}\frac{\partial \ln p(\boldsymbol{x};\boldsymbol{\theta})}{\partial \theta_j}\right\} \\
&= -\mathrm{E}\left\{\frac{\partial^2 \ln p(\boldsymbol{x};\boldsymbol{\theta})}{\partial \theta_i \partial \theta_j}\right\}
\end{aligned}
\tag{2.7}
$$

Then, following the notation used by Bhattacharyya in [8], if I^{ii} is the ith element on the diagonal of $\boldsymbol{I}^{-1}(\boldsymbol{\theta})$, the vector Cramér-Rao bound is

$$
\mathrm{Var}\left\{\widehat{\theta}_i\right\} \geq I^{ii}
\tag{2.8}
$$

provided $\widehat{\theta}_i$ is an unbiased estimator of θ_i. This follows from the more general result that the covariance of $\widehat{\boldsymbol{\theta}}$, defined by

$$
\mathrm{Cov}\left\{\widehat{\boldsymbol{\theta}}\right\} = \mathrm{E}\left\{(\widehat{\boldsymbol{\theta}} - \boldsymbol{\theta})(\widehat{\boldsymbol{\theta}} - \boldsymbol{\theta})^T\right\}
\tag{2.9}
$$

satisfies

$$
\mathrm{Cov}\left\{\widehat{\boldsymbol{\theta}}\right\} - \boldsymbol{I}^{-1}(\boldsymbol{\theta}) \geq 0
\tag{2.10}
$$

which is read as "the matrix $\mathrm{Cov}\left\{\widehat{\boldsymbol{\theta}}\right\} - \boldsymbol{I}^{-1}(\boldsymbol{\theta})$ is positive semidefinite."

The vector Cramér-Rao bound is satisfied with equality if and only if

$$
\widehat{\theta}_i - \theta_i = \sum_{j=1}^{M} k_{ij}(\boldsymbol{\theta})\frac{\partial \ln p(\boldsymbol{x};\boldsymbol{\theta})}{\partial \theta_j}
\tag{2.11}
$$

for all $\boldsymbol{x}$ and all i from 1 to M and for some set of functions $k_{ij}(\boldsymbol{\theta})$ not dependent on $\boldsymbol{x}$.

2.2.3   The Scalar Cramér-Rao Bound for a Biased Estimator

When the estimator $\widehat{\theta}$ is biased, the Cramér-Rao bound becomes a lower bound on the mean square error

$$
\mathrm{E}\left\{\left(\widehat{\theta} - \theta\right)^2\right\} \geq \frac{\left(1 + \frac{db(\theta)}{d\theta}\right)^2}{\mathrm{E}\left\{\left(\frac{\partial \ln p(\boldsymbol{x};\theta)}{\partial \theta}\right)^2\right\}}
\tag{2.12}
$$

Note that if $-2 < db(\theta)/d\theta < 0$, the mean square error of the biased estimator may be lower than the variance of an unbiased estimator.

2.2.4 Some Other Bounds

If an efficient estimator does not exist, the Cramér-Rao bound sets a lower limit on an estimator's variance that cannot be attained. This makes it difficult to find how close a particular estimator is to the MVUE.

A number of other bounds may be used instead of the Cramér-Rao bound to give greater lower bounds on the variance of any unbiased estimator. The Bhattacharyya bound [8, 9, 10] gives a tighter bound than the Cramér-Rao bound by considering higher-order partial derivatives of $p(\boldsymbol{x}; \theta)$. The Barankin bound [6] is a more general bound on the estimator's s^{th} central moments that includes both the Cramér-Rao and the Bhattacharyya bounds as special cases.

One of the problems with these bounds is that improving the variance's lower bound comes at the price of increased complexity. Therefore the Cramér-Rao bound is often the only bound considered, even when no efficient estimator exists.

2.3 Maximum Likelihood Estimation

In maximum likelihood estimation, the population's probability density function $p(\boldsymbol{x}; \boldsymbol{\theta})$ dependent on the unknown parameters is called the likelihood function[4]

Since there is no *a priori* knowledge about $\boldsymbol{\theta}$, the most likely value of $\boldsymbol{\theta}$ is that which maximizes $p(\boldsymbol{x}; \boldsymbol{\theta})$. If $p(\boldsymbol{x}; \boldsymbol{\theta})$ has a unique maximum over the domain of $\boldsymbol{\theta}$, the maximum likelihood estimate of $\boldsymbol{\theta}$ is

$$\widehat{\boldsymbol{\theta}}_{ml} = \arg \max_{\boldsymbol{\theta}} \; p(\boldsymbol{x}; \boldsymbol{\theta}) \tag{2.13}$$

The maximum likelihood estimator $\widehat{\boldsymbol{\theta}}_{ml}$ is also a solution to the likelihood equation

$$\left. \frac{\partial p(\boldsymbol{x}; \boldsymbol{\theta})}{\partial \theta_i} \right|_{\boldsymbol{\theta} = \widehat{\boldsymbol{\theta}}_{ml}} = 0 \qquad \forall \, i = 1, 2, \ldots, M \tag{2.14}$$

---

[4]Fisher would not approve of this! In [29], he complained "In spite of the emphasis I have always laid upon the difference between probability and likelihood there is still a tendency to treat likelihood as though it were a sort of probability." Probability relates a population with known parameters to an unknown sample. Likelihood relates a known sample to a population with unknown parameters. The conceptual difference is important, but mathematically it is just a scaling factor which usually may be ignored.

Since $\ln x$ is strictly monotonically increasing with x, the global maximum of $p(\boldsymbol{x}; \boldsymbol{\theta})$ occurs at the same value of $\boldsymbol{\theta}$ as the global maximum of $\ln p(\boldsymbol{x}; \boldsymbol{\theta})$. The maximum likelihood estimator may be found by maximizing $\ln p(\boldsymbol{x}; \boldsymbol{\theta})$

$$\widehat{\boldsymbol{\theta}}_{ml} = \arg \max_{\boldsymbol{\theta}} \; \ln p(\boldsymbol{x}; \boldsymbol{\theta}) \tag{2.15}$$

or equivalently by solving the log-likelihood equation

$$\left. \frac{\partial \ln p(\boldsymbol{x}; \boldsymbol{\theta})}{\partial \theta_i} \right|_{\boldsymbol{\theta} = \widehat{\boldsymbol{\theta}}_{ml}} = 0 \qquad \forall\, i = 1, 2, \ldots, M \tag{2.16}$$

Note that the global maximum of $p(\boldsymbol{x}; \boldsymbol{\theta})$ must be unique for the maximum likelihood estimator to exist.

If the maximum likelihood estimator is unbiased and $\partial \ln p(\boldsymbol{x}; \boldsymbol{\theta}) / \partial \theta_i$ can be written in the form of equation (2.6), the maximum likelihood estimator satisfies the Cramér-Rao bound with equality.

If $\partial \ln p(\boldsymbol{x}; \boldsymbol{\theta}) / \partial \theta_i$ cannot be written in this form, all that can be said is that the maximum likelihood estimator's variance is greater than the Cramér-Rao lower bound. Other estimators may have lower variances than $\widehat{\boldsymbol{\theta}}_{ml}$, but there is no simple way of finding them.

Conversely, if an efficient estimator exists, then it is necessarily the maximum likelihood solution $\widehat{\boldsymbol{\theta}}_{ml}$ which is the unique solution of the likelihood equation.

In general, $\widehat{\boldsymbol{\theta}}_{ml}$ is neither unbiased nor efficient. But as the number of data samples tends to infinity,

$$\widehat{\boldsymbol{\theta}}_{ml} \to \boldsymbol{\theta} \tag{2.17}$$

and

$$\mathrm{Cov}\left\{ \widehat{\boldsymbol{\theta}}_{ml} \right\} \to \boldsymbol{I}^{-1}(\boldsymbol{\theta}) \tag{2.18}$$

so $\widehat{\boldsymbol{\theta}}_{ml}$ is asymptotically unbiased and asymptotically efficient, and tends to a normal distribution with mean $\boldsymbol{\theta}$ and variance equal to the Cramér-Rao lower bound

$$\widehat{\boldsymbol{\theta}}_{ml} \overset{d}{\sim} \mathcal{N}\left(\boldsymbol{\theta}, \boldsymbol{I}^{-1}(\boldsymbol{\theta}) \right) \tag{2.19}$$

as $N \to \infty$. The $\overset{d}{\sim}$ indicates that probability distribution of $\widehat{\boldsymbol{\theta}}_{ml}$ is asymptotically equal to the normal distribution on the right-hand side.

In order for the maximum likelihood estimator to be asymptotically normal, the likelihood function must satisfy a number of regularity conditions.

One approach [62, p. 175] combines the likelihood function $p(\boldsymbol{x}; \boldsymbol{\theta})$ and the regions of support of $\boldsymbol{x}$ and $\boldsymbol{\theta}$ to form a model. If the model satisfies seven regularity conditions, then it is called a regular model. Finally, a necessary and sufficient condition for the asymptotic normality of the maximum likelihood estimator is that it is formed from a regular model.

A simpler set of regularity conditions can be used if they are to be sufficient but not necessarily necessary. Examples of sufficient sets of regularity conditions are given by [69, section 5f.1] and [51, appendix 7B]. The following theorem from [51] is for a scalar parameter.

Theorem 2.1 (Asymptotic Properties of the MLE) *Given a likelihood function $p(\boldsymbol{x}; \theta)$, the maximum likelihood estimator $\widehat{\theta}_{ml}$ of the unknown parameter θ has a probability density function for large data records that is asymptotically normal*

$$\widehat{\theta}_{ml} \overset{d}{\sim} \mathcal{N}\left(\theta, \boldsymbol{I}^{-1}(\theta)\right) \tag{2.20}$$

if the first and second-order partial derivatives of the log-likelihood function are well-defined and

$$\mathrm{E}\left\{\frac{\partial \ln p(\boldsymbol{x}; \theta)}{\partial \theta}\right\} = 0 \tag{2.21}$$

Proof: See appendix 7B of [51]. ∎

Similar regularity conditions apply for maximum likelihood estimators $\widehat{\boldsymbol{\theta}}_{ml}$ of vector parameters $\boldsymbol{\theta}$ provided that the estimators of each of the parameters average the measurements so that the central limit theorem applies.

2.4   Bayesian Estimation

Maximum likelihood estimation assumes that nothing is known about the unknown parameters $\boldsymbol{\theta}$ before the measurements $\boldsymbol{x}$ are made. This means that in order to use maximum likelihood estimation, any *a priori* information must be discarded.

Bayesian estimation, a completely different estimation philosophy from maximum likelihood estimation, assumes that the unknown parameters are random. The prior information takes the form of an *a priori* probability density function $p(\boldsymbol{\theta})$ on the unknown parameters.

This prior knowledge can be combined with the model's conditional probability density $p(\boldsymbol{x}|\boldsymbol{\theta})$ to give the joint probability density function

$$p(\boldsymbol{x}, \boldsymbol{\theta}) = p(\boldsymbol{x}|\boldsymbol{\theta})\, p(\boldsymbol{\theta}) \tag{2.22}$$

The performance of a Bayesian estimator is measured a little differently from a maximum likelihood estimator. The minimum variance criterion is not appropriate because the $\boldsymbol{\theta}$ in

$$\mathrm{Var}\left\{\widehat{\boldsymbol{\theta}}\right\} = \mathrm{E}\left\{(\widehat{\boldsymbol{\theta}} - \boldsymbol{\theta})^2\right\} \tag{2.23}$$

is a random parameter, not a constant. However, this concept can be generalized to random parameters using the Bayes risk $\mathcal{R}$.

Define the error $\boldsymbol{\epsilon}$ as the difference between the random parameters and their estimates

$$\boldsymbol{\epsilon} = \boldsymbol{\theta} - \widehat{\boldsymbol{\theta}} \tag{2.24}$$

for one particular set of measurements $\boldsymbol{x}$ and realization of $\boldsymbol{\theta}$. Then the seriousness of making a particular error is measured using a cost function $\mathcal{C}(\boldsymbol{\epsilon})$. The Bayes risk associated with a particular estimator $\widehat{\boldsymbol{\theta}}$ and cost function $\mathcal{C}(\boldsymbol{\epsilon})$ is the expected cost averaged over all values of $\boldsymbol{x}$ and $\boldsymbol{\theta}$

$$\mathcal{R} = \iint \mathcal{C}(\boldsymbol{\theta} - \widehat{\boldsymbol{\theta}}) \, p(\boldsymbol{x}, \boldsymbol{\theta}) \, d\boldsymbol{x} \, d\boldsymbol{\theta} \tag{2.25}$$

Minimizing $\mathcal{R}$ over all estimators gives the Bayesian estimator for that particular cost function.

When the cost function is 1 unless the error is less than a threshold δ,

$$\mathcal{C}(\boldsymbol{\epsilon}) = \begin{cases} 0 & |\boldsymbol{\epsilon}| < \delta \\ 1 & |\boldsymbol{\epsilon}| \geq \delta \end{cases} \tag{2.26}$$

the Bayesian estimator in the limit $\delta \to 0$ is the value of $\boldsymbol{\theta}$ that maximizes the posterior density function

$$\widehat{\boldsymbol{\theta}} = \arg\max_{\boldsymbol{\theta}} p(\boldsymbol{\theta}|\boldsymbol{x}) \tag{2.27}$$

which is called the maximum *a posteriori* (MAP) estimator.

Using Bayes' rule,

$$p(\boldsymbol{\theta}|\boldsymbol{x}) = \frac{p(\boldsymbol{x}|\boldsymbol{\theta}) \, p(\boldsymbol{\theta})}{p(\boldsymbol{x})} \tag{2.28}$$

Since the denominator is independent of $\boldsymbol{\theta}$, the MAP estimator can be written

$$\widehat{\boldsymbol{\theta}} = \arg\max_{\boldsymbol{\theta}} p(\boldsymbol{x}|\boldsymbol{\theta}) \, p(\boldsymbol{\theta}) \tag{2.29}$$

2.4.1 Diffuse Priors

If the *a priori* probability density is uniform

$$p(\boldsymbol{\theta}) = \frac{1}{\epsilon} \tag{2.30}$$

over a sufficiently large region of volume $1/\epsilon$, and zero elsewhere, the MAP estimator coincides with the maximum likelihood estimator in the limit that $\epsilon \to 0$. A $p(\boldsymbol{\theta})$ like this is called a diffuse prior [5].

In the special case that $p(\boldsymbol{\theta})$ is constant on some closed subset $\boldsymbol{\Theta}$, the MAP estimator becomes

$$\widehat{\boldsymbol{\theta}} = \arg\max_{\boldsymbol{\theta} \in \boldsymbol{\Theta}} p(\boldsymbol{x}|\boldsymbol{\theta}) \tag{2.31}$$

Provided that $\widehat{\boldsymbol{\theta}}_{ml} \in \boldsymbol{\Theta}$, this has the same form as the maximum likelihood estimator

$$\widehat{\boldsymbol{\theta}}_{ml} = \arg\max_{\boldsymbol{\theta}} p(\boldsymbol{x}; \boldsymbol{\theta}) \tag{2.32}$$

because the *a posteriori* probability density function $p(\boldsymbol{x}|\boldsymbol{\theta})$ has the same form as the likelihood function $p(\boldsymbol{x}; \boldsymbol{\theta})$. This provides the justification for using maximum likelihood estimation over a restricted domain $\boldsymbol{\Theta}$ which is known *a priori* to contain $\boldsymbol{\theta}$.

2.5 Estimation with Complex Parameters

When the unknown parameter in an estimation problem is a complex vector $\boldsymbol{\theta}$, the maximum likelihood estimator $\widehat{\boldsymbol{\theta}}_{ml}$ and the Fisher information matrix $\boldsymbol{I}(\boldsymbol{\theta})$ may be found by forming a new vector $\tilde{\boldsymbol{\theta}}$ of real parameters

$$\tilde{\boldsymbol{\theta}} = \left[\begin{array}{c} \Re\{\boldsymbol{\theta}\} \\ \Im\{\boldsymbol{\theta}\} \end{array} \right] \tag{2.33}$$

and proceed as for the real case to find the maximum likelihood estimator and Fisher information matrix of $\tilde{\boldsymbol{\theta}}$.

A more satisfying approach is to reformulate real parameter estimation for complex parameters. This is a brief summary of the results obtained by Kay in section 15.7 of [51].

The derivative of a function $f(z)$ with respect to the complex argument z is defined as

$$\frac{\partial f(z)}{\partial z} = \frac{1}{2} \left(\frac{\partial f(x + jy)}{\partial x} - j\frac{\partial f(x + jy)}{\partial y} \right) \tag{2.34}$$

where $z = x + jy$ with x and y real. Then it is easy to show that

$$\frac{\partial z}{\partial z} = 1 \qquad \text{and} \qquad \frac{\partial \overline{z}}{\partial z} = 0 \tag{2.35}$$

One surprising consequence of this is that

$$\frac{\partial |z|^2}{\partial z} = \overline{z} \tag{2.36}$$

with no factor of 2 as in the real case.

The maximum likelihood estimator $\widehat{\boldsymbol{\theta}}_{ml}$ is, as for real $\boldsymbol{\theta}$,

$$\widehat{\boldsymbol{\theta}}_{ml} = \arg\max_{\boldsymbol{\theta}} p(\boldsymbol{x}; \boldsymbol{\theta}) \tag{2.37}$$

If $\widehat{\boldsymbol{\theta}}$ is any unbiased estimator of $\boldsymbol{\theta}$, the Cramér-Rao bound is

$$\text{Cov}\left\{\widehat{\boldsymbol{\theta}}\right\} \geq \boldsymbol{I}^{-1}(\boldsymbol{\theta}) \tag{2.38}$$

which is interpreted to mean that $\mathrm{Cov}\left\{\widehat{\boldsymbol{\theta}}\right\} - \boldsymbol{I}^{-1}(\boldsymbol{\theta})$ is positive semidefinite. The elements of the covariance matrix are

$$\left(\mathrm{Cov}\left\{\widehat{\boldsymbol{\theta}}\right\}\right)_{ij} = \mathrm{E}\left\{\left(\widehat{\theta}_i - \theta_i\right)\overline{\left(\widehat{\theta}_j - \theta_j\right)}\right\} \tag{2.39}$$

and the elements of the Fisher information matrix $\boldsymbol{I}(\boldsymbol{\theta})$ are

$$I_{ij} = \mathrm{E}\left\{\frac{\partial \ln p(\boldsymbol{x}; \boldsymbol{\theta})}{\partial \overline{\theta}_i}\frac{\partial \ln p(\boldsymbol{x}; \boldsymbol{\theta})}{\partial \theta_j}\right\} = -\mathrm{E}\left\{\frac{\partial^2 \ln p(\boldsymbol{x}; \boldsymbol{\theta})}{\partial \overline{\theta}_i \partial \theta_j}\right\} \tag{2.40}$$

Chapter 3

High Resolution Radar

This chapter is an introduction to high resolution radar in general and radar imaging using inverse synthetic aperture radar in particular. The constraints on radar imaging using synthetic apertures are examined by considering the implications of scaling up an optical imaging system operating in the visible spectrum to operate at radar wavelengths while maintaining the same angular resolution. This suggests that a stationary radar may be used to obtain a high resolution radar image of a moving target if the target's motion forms a suitable synthetic aperture.

After discussing the validity of representing distributed targets as noninteracting point scatterers, the radar waveforms and target motions necessary for high resolution images are derived. This justifies the simple model that will be used for radar imaging for the remainder of the thesis.

3.1 An Overview of SAR and ISAR

When a radar transmitter points its antenna in the direction of a target[1], the transmitter's power is distributed according to the antenna's radiation pattern. Most power is directed in the approximate direction the antenna is pointing (this direction is called the antenna's boresight axis, or its line-of-sight), and the angular width of this main beam determines the radar's angular resolution.

The radiation pattern of an antenna is wavelength-dependent and is given by the Fourier transform of its aperture [15]. For a one-dimensional aperture of length D, the relative power radiated at an angle θ to the aperture's normal

---

[1]Because most radar engineers have a military background, the word "target" means any object of interest.

is

$$P(\theta) = \left| \text{sinc}\left(\frac{D}{\lambda}\sin\theta\right) \right|^2 \qquad (3.1)$$

For a circular antenna with diameter D, the relative power radiated at an angle θ to the boresight axis is

$$P(\theta) = \left| \text{jinc}\left(\frac{D}{\lambda}\sin\theta\right) \right|^2 \qquad (3.2)$$

where $\text{jinc}(x) = J_1(\pi x)/\pi x$ is the Bessel function-equivalent of $\text{sinc}(x) = \sin(\pi x)/x$.

Radiation patterns like these are characterized by a strong central lobe and weaker sidelobes. The angular width $\Delta\theta$ of the mainlobe is determined by the angular separation of the points at which the transmitted power density is half the power density on the boresight axis. This can be written as [79, eq. (6.11)]

$$\Delta\theta = K\frac{\lambda}{D} \qquad (3.3)$$

where the beamwidth factor K is a constant, usually close to unity, which depends on the antenna's shape and the uniformity of its illumination.

Taking $K = 1$, the illumination from an antenna with a diameter D spreads to a width of $R\lambda/D$ a distance R from the radar. A 60 cm antenna operated at X-band, where the wavelength is $\lambda = 3$ cm, has a main lobe that is 500 m across at a distance of 10 km. This suggests that such a radar would have a cross-range resolution of about 500 m.

However, with more sophisticated processing, it is possible to resolve radar scatterers on targets with a resolution better than 1 m. Scatterers at different distances from the radar are resolved by measuring differences in the times at which echoes from them are received. Scatterers with identical ranges but separated in the cross-range direction may be resolved if there is some relative motion between the radar and the target which changes these scatterers' ranges at different rates.

This necessity for some relative motion between the radar and the target to change the target's aspect angle leads to synthetic aperture radar (SAR) and inverse synthetic aperture radar (ISAR), the two basic forms of high resolution radar imaging.

In SAR imaging, the radar is carried aboard a moving platform, usually an aircraft or a satellite and the target is the surface of the Earth beneath or to the side of the platform. SAR is widely used for remote sensing because it is able to produce ground maps with a width of 100 km and a resolution of 10 m from hundreds of kilometres away.

ISAR imaging uses a stationary radar to form an image of a moving target, usually an aircraft or a ship. The target's changing aspect angle may be a

result of it moving in a straight line or turning during manoeuvres. If ocean waves cause a ship to pitch or roll, this can also form a synthetic aperture for radar imaging. ISAR is used for target identification, so a resolution of 1 m or better is often needed.

The principles behind SAR and ISAR are identical, but their implementations are slightly different because of differences in the target's and the radar's motions, the target's range and the desired resolution. Since the relative motion between radar and target is crucial to the imaging process, their relative positions must be known to within a fraction of a radar wavelength. Motion estimation is used to estimate any unwanted components of the relative motion. The effects of any unwanted movement are corrected using motion compensation before the radar image is formed.

Motion estimation is more difficult for ISAR imaging than for SAR because the target's motion is not known *a priori*. With SAR imaging, the radar is the one that moves so an inertial navigation unit or global positioning system (GPS) can provide estimates of its position at all times.

3.2 Deriving ISAR from Optical Imaging

Tutorials about ISAR tend to begin "Consider a target that is slowly rotating at a distance R from the radar ...". This does little to answer the question of why ISAR imaging is done like that, except for the circular reply "because it works".[2] It is instructive to look at the requirements of radar imaging a little more directly, and see how these affect the design of a radar imaging system. This qualitative derivation of ISAR begins with the human eye, an optical imaging system with which we all have direct experience. By considering the implications of scaling up such an optical system to operate at radar wavelengths, ISAR is placed in its proper context among imaging systems.

Consider a typical ISAR scenario where an X-band radar operating at 10 GHz (a wavelength of 3 cm) forms an image of an aircraft that is 10 km away. To be useful for target identification, the image needs a spatial resolution of about 1 m. Consequently, the radar imaging system must be capable of resolving individual radar scatterers on the target with an angular separation of $\Delta\theta = \frac{1 \text{ m}}{10 \text{ km}} = 10^{-4}$ radians.

An angular resolution of 10^{-4} radians is comparable to the diffraction-limited resolving power of the human eye. The eye's aperture, determined by the size of the pupil, has a diameter which varies between 2 mm and 8 mm. The diffraction-limited angular resolution of any optical system is

---

[2]Polya emphasizes the need to appreciate the *why* as well as the *how*. As a student, he asked "Yes, the solution seems to work, it appears to be correct; but how is it possible to invent such a solution?"[65, p. vi]. This section aims to illustrate how ISAR is part of a natural progression from ordinary optical imaging.

given by Rayleigh's criterion [38]

$$\Delta\theta = \frac{\lambda}{D} \tag{3.4}$$

where λ is the wavelength of the light and D the diameter of the aperture. This is the same form as the beamwidth of an antenna in equation (3.3). Taking the pupil's diameter as 5 mm and the wavelength as 500 nm, that of blue-green light, the eye's angular resolution is $\Delta\theta = \frac{500 \text{ nm}}{5 \text{ mm}} = 10^{-4}$ radians.

From a signal processing perspective, imaging occurs in two fundamental steps, sampling and processing. Light is reflected from the target and strikes the imaging system, where it is sampled over the aperture. These samples are processed to form the image. In an optical imaging system, such as the eye, the lens is both the sampler and the signal processor. Under the Fraunhofer approximation, the light striking the lens is the spatial frequency domain representation of the target's reflectivity. The lens acts as a Fourier transformer, which focuses an image of the target onto the image plane (onto the retina in the case of the eye).

In principle, a radar imaging system could operate in the same way as this signal processing view of an optical system. A radar transmitter could illuminate the target with X-band radiation, some of which would be scattered back towards a receiver which samples the reflected wavefront. The eye's 5 mm aperture at 500 nm is equivalent to an aperture some 300 m in diameter at the X-band wavelength of 3 cm. To achieve the diffraction-limited resolution of $\Delta\theta = 10^{-4}$ radians, the backscattered signal must be sampled over the whole aperture with sensor elements spaced no more than $\lambda/2$ apart [88]. Approximately $4(\Delta\theta)^{-2} = 4 \times 10^8$ sensors are needed, which is clearly impractical.

If the spacing between sensors is increased above the $\lambda/2$ minimum, the total number of sensors may be greatly reduced. The disadvantage of such a thinned array is that it cannot distinguish signals whose angles of incidence differ by

$$\Delta\phi = \arcsin\left(n\frac{\lambda}{d}\right) \tag{3.5}$$

for some integer n where d is the distance between elements in the array. This is the same effect that causes grating lobes on a diffraction grating.

An example of a thinned array is Raytheon's Cobra Dane radar. This is an L-band phased array radar with a 28.5 m diameter steerable antenna. The antenna's diameter is 120λ at a wavelength of 24 cm, giving a theoretical angular resolution of 0.5^o. An unthinned array this size would require more than 45,000 elements. The Cobra Dane array is thinned, and has only 15,360 elements [79].

Experiments on highly-thinned arrays have been performed by Steinberg. His radio camera is a radar imaging system that achieves a high angular

resolution with a very small number of receiving elements [87, 89]. The closely spaced sidelobes that normally accompany a thinned array are reduced in amplitude by selecting the positions of the receiving elements at random. Extensive discussions of the properties of random arrays may be found in Steinberg's books, [86] and [88], and the papers [2], [87] and [94].

An alternative to using many receivers in a large array is to have a smaller number of receivers that move over the whole of the array's aperture. Over a period of time, the received signal is sampled over the entire aperture. By correcting for any change in the target's position or orientation during the sampling period, the data is equivalent to that collected at one instant by a much larger number of receivers. Now the reduction in the number of receivers comes at the expense of a much longer data acquisition time.

The distance between samples can be made larger than $\lambda/2$ provided each receiver has an antenna whose beamwidth given by (3.3) is smaller than the spacing between the thinned array's lobes. This requires the distance between samples over the aperture to be smaller than the receiving antennas' diameters.[3]

Radio astronomy using very-long-baseline interferometry (VLBI) is a very good example of this time-sharing approach to imaging [21]. A small number, usually between two and thirty, of widely separated radio telescopes are linked electronically to simulate an aperture whose size is equal to their separation. Over a period lasting up to twelve hours, the Earth's rotation moves the radio telescopes so that samples can be acquired over most of the aperture, thus reducing the level of the sidelobes in the synthesized antenna's radiation pattern. An impressive application of VLBI is the baseline of 8,000 km obtained by arraying radars in California, Massachusetts and the Crimea. Earth-rotation aperture synthesis [34] gives an angular resolution better than 10^{-8} radians at a wavelength of 10 cm.

Because the angle of arrival of a plane wave is established from differences in the wave's phase at different receivers, it takes at least two receivers for VLBI. A single receiver can be used only when the incoming radar signals maintain coherence over the whole time interval required to sample the aperture. Then the single receiver's measurement at the first position in the aperture can be used as a phase reference for measurements made at different positions within the aperture. Astronomical radar sources, however, do not maintain coherence over the length of time that Earth-rotation synthesis requires, so a single receiver cannot be used in interferometric radio astronomy.

A fundamental difference between the imaging of interstellar objects and

---

[3]This is similar to the problem of a tracking radar deciding whether a detection is due to a weak target in the mainlobe or a strong target in a sidelobe. A secondary receiver, called a guard horn, with a very wide mainlobe, is used. The ambiguity is resolved by comparing the strengths of the detected target given by the main antenna and the guard horn [90].

targets such as aircraft and ships is that the interstellar objects are radar sources, while aircraft and ships are radar reflectors. Targets that are passive reflectors need a radar transmitter to illuminate them. If the radar transmitter is coherent, radar imaging can be achieved with only a single receiver sampling within a larger aperture. In fact, if the transmitter's oscillator is connected directly to the receiver, this may serve as the phase reference for each measurement. Then the transmitter need be coherent over the time taken for a measurement at a single position within the aperture, not for the whole of the imaging period.

So far, this overview of the design principles behind radar imaging has indicated how a high resolution may be obtained in the two spatial dimensions perpendicular to the radar's line-of-sight. The initial design requiring a very large number of receiving elements spread over a large two-dimensional aperture has been simplified to a single transmitter and receiver moving over the large two-dimensional aperture. Decreasing the number of receiving elements has been offset by an increase in the time taken to acquire the measurements for the radar image.

However the design at this stage is still not practical for imaging moving targets such as ships and aircraft. It takes too long to move the radar and make the measurement at each position within the two-dimensional aperture. Moving the radar is the most time consuming part of this, so to make the imaging feasible much of the radar's movement within the aperture has to be eliminated.

Two dimensions of measurements are needed to form a two-dimensional image, but there is no reason why both have to be spatial dimensions. Close coupling between the radar transmitter and receiver—they often share the antenna—means that time delay can be used as one of the measurement dimensions. If the transmitter sends out a short pulse, the signal measured at the receiver is the superposition of the pulse's reflections from the target's scatterers. Each reflection is delayed by $2r_i/c$, the time it takes the pulse, propagating at the speed of light c, to travel the distance r_i from the transmitter to the ith scatterer, and return to the receiver.

Therefore, the time delay from scatterers at different ranges can be used as one of the measurement dimensions. The aperture now need be large only in one spatial dimension, and the number of positions within the aperture's one spatial dimension where measurements are made is the square-root of the number needed with the two-dimensional aperture. The image of the target lies in the plane containing the time-delay measurements and the one-dimensional aperture. This plane is parallel to the radar's line-of-sight whereas before the image plane was normal to the radar's line-of-sight. This gives one important difference in the images from a time-delay/linear synthetic aperture and a two-dimensional aperture such as an optical system or Steinberg's radio camera: the time-delay/linear synthetic aperture's image

is a plan view of the target, even though the target is viewed from a shallow angle.

A very important example of radar imaging using a time-delay/linear synthetic aperture is synthetic aperture radar, or SAR, used for mapping large areas of the Earth's surface. The radar is carried on a moving platform, such as an aircraft or a satellite, and the platform's motion creates the synthetic aperture. The Seasat-A synthetic aperture radar orbited at an altitude of 780 km and produced ground maps with a width of 100 km and a resolution of 25 m [79, ch. 22].

An important point to note about SAR imaging is that the synthetic aperture is needed so that measurements can be made with the radar and the target at different relative positions and orientations. This requirement can be met just as well if the radar is stationary and the target moves along the synthetic aperture. These are just the conditions for ISAR.

So, starting at a familiar optical imaging system, the trade-offs necessary for high resolution radar imaging have been discussed and the conditions for ISAR imaging have been derived qualitatively. Next, the process of radar scattering will be analysed to obtain a mathematical model for radar reflections. This allows the constraints ISAR places on the radar system and the target's motion to be calculated in a more quantitative way.

3.3   Radar Scattering Mechanisms

When a target such as an aircraft is illuminated by a radar transmitter, the reflected electromagnetic wave is a combination of reradiated fields due to a number of complex electromagnetic phenomena. If the target's conductivity and permittivity are known perfectly, Maxwell's equations may be evaluated to give an exact description of the reflected wave. For real targets—all but a few simple geometric shapes—Maxwell's equations are too complex for an exact solution. Simplified methods such as the method of moments, geometrical optics, physical optics or the geometrical theory of diffraction may be used to estimate the target's reflections.

However in radar imaging, only a portion of the reflected wave is known and the target's structure must be estimated. This is too complicated, and the measurements too incomplete, to solve even for the simplified methods mentioned above.

Radar imaging is made tractable by assuming an even simpler electromagnetic model: a target composed of point scatterers. After analysing reflections from an isolated point scatterer, this model is generalized to a description of a target in terms of its two-dimensional reflectivity function $g(x, y)$.

3.3.1 Isolated Point Scatterers

The strength of the radar reflection from a point scatterer is determined by σ, its radar cross-section or RCS. This is a measure of the scatterer's effective cross-sectional area, with units of m^2. Suppose this point scatterer is located a distance r from a radar that is transmitting a sinusoidal signal $p_t(t)$ with a frequency $\omega/2\pi$

$$p_t(t) = A \cos \omega t \tag{3.6}$$

The incident wave striking the scatterer, $p_i(t)$, is $p_t(t)$ delayed by r/c, where c is the speed of light

$$p_i(t) = \frac{A}{\sqrt{4\pi r^2}} \cos \left(\omega \left[t - \frac{r}{c} \right] \right) \tag{3.7}$$

The amplitude is attenuated by $4\pi r^2$ because the transmitter's fixed power is being distributed over a spherical wavefront with surface area $4\pi r^2$.

When $p_i(t)$ is reflected from the scatterer, the backscattered waveform has a power density of σ times the incident power density. There may also be a phase shift ϕ due to a discontinuity between the conductivity and permittivity of the scatterer and free space. Therefore the backscattered wave is

$$p_b(t) = \frac{A\sqrt{\sigma}}{\sqrt{4\pi r^2}} \cos \left(\omega \left[t - \frac{r}{c} \right] + \phi \right) \tag{3.8}$$

By the time this reflection reaches the radar antenna, there has been an additional time delay of r/c and another attenuation of $\sqrt{4\pi r^2}$ because the point scatterer radiates in all directions. The received waveform is

$$p_r(t) = \frac{A\sqrt{\sigma}}{4\pi r^2} \cos \left(\omega \left[t - \frac{2r}{c} \right] + \phi \right) \tag{3.9}$$

which can be written as

$$p_r(t) = \Re \left\{ \frac{g}{r^2} e^{j\omega \left[t - \frac{2r}{c} \right]} \right\} \tag{3.10}$$

where the scatterer's radar reflectivity

$$g = \frac{A}{4\pi} \sqrt{\sigma} \, e^{j\phi} \tag{3.11}$$

incorporates the scatterer's RCS and phase shift, and for notational simplicity, the transmitter's amplitude and the factor of 4π.

3.3.2 Reflections From a Distributed Target

This model of an isolated point scatterer will now be extended to the radar reflectivity of a distributed target. Define $g(x, y)\, dx\, dy$ to be the overall reflectivity of the differential region located at (x, y) on the target with extent (dx, dy). All coordinates are measured in a Cartesian coordinate system that has its origin at the target's centre and is fixed to the target. The received signal due to this differential area is

$$dp_r(t) = \Re \left\{ \frac{g(x, y)}{r_{xy}^2}\, e^{j\omega \left[t - \frac{2r_{xy}}{c} \right]}\, dx\, dy \right\} \qquad (3.12)$$

where r_{xy} is the distance from the radar to (x, y). By combining the received contributions from all parts of the target, the total received signal becomes

$$p_r(t) = \Re \left\{ \iint \frac{g(x, y)}{r_{xy}^2}\, e^{j\omega \left[t - \frac{2r_{xy}}{c} \right]}\, dx\, dy \right\} \qquad (3.13)$$

where the integration is taken over the region occupied by the target.

A number of assumptions are implicit in this model and its application to radar imaging [74, ch. 9]:

1. The target is uniformly illuminated by the radar transmitter.

2. $g(x, y)$ is independent of the target's orientation.

3. $g(x, y)$ is independent of the radar's frequency ω.

4. The only scatterering mechanism is direct reflection; there are no multiple reflections, creeping waves or diffraction phenomena.

In general, all of these assumptions are invalid. Since radar targets are three-dimensional, part of the target may be obscured by other parts between it and the radar. Shadowing like this is orientation-dependent, which immediately invalidates the second assumption. Furthermore, even direct reflections are orientation-dependent. Reflections from flat surfaces are specular so a strong reflection is only apparent when the surface is normal to the radar's line-of-sight.[4]

The third assumption is invalid because the reflections are only frequency-independent when the features on the target responsible for the scattering are large compared to the wavelength. This can be seen in figure 3-1 of [12], where the RCS of a conducting sphere is very oscillatory when the sphere's radius is smaller than about five wavelengths.

---

[4]This was the rationale behind the faceted design of the F-117A Stealth Fighter. The aircraft's skin is formed from flat surfaces oriented in small number of different directions. Therefore an F-117A is nearly invisible unless viewed from one of these directions [37].

The final assumption is also invalid because radar wavelengths are long enough to diffract around features on typical man-made targets. Waves may diffract around one side of the target, emerge on the other side and travel back to the radar. They may also interfere constructively or destructively behind the target with waves diffracting around the other side. The incident radar wave also induces currents on the target's surface which cause creeping waves and other effects. The result of some of these indirect propagation modes on an ISAR image is clearly shown in figure 4.39 of [55].

Even though these four assumptions are generally not valid, they can be quite accurate under restricted circumstances. If the target is viewed over a narrow range of viewing angles, $g(x, y)$ may be considered independent of orientation. This also justifies the first assumption because scatterers that start in shadow are likely to remain shadowed if the target's orientation changes only slightly. The frequency independence of $g(x, y)$ is appropriate if the target is illuminated with waves whose wavelength varies little. In other words, a narrow relative bandwidth—the ratio of bandwidth to centre frequency—should be used.

The final assumption is harder to justify, because multiple reflections and diffraction phenomena do occur. It is difficult to distinguish reflections due to these phenomena from ordinary reflections so they get treated like direct reflections and appear as artifacts such as phantom scatterers at locations where there is no structural justification for them. In figure 6 of [106], multiple reflections inside the engine intakes of a Mirage aircraft are manifested in an ISAR image as extra scatterers located at regularly increasing intervals in range from their true location. Therefore the final assumption is replaced with an assumption that the target's estimated reflectivity combines the effects of direct reflections located at their correct positions and the effects of indirect reflections offset from their correct positions by amount attributable to the propagation phenomenon interacting with a particular part of the target's structure.

In conclusion, it is assumed for the purposes of radar imaging that the target's reflection can be modelled as

$$
p_r(t) = \Re \left\{ \int\!\!\int \frac{g(x, y)}{r_{xy}^2} \, e^{j\omega \left[t - \frac{2r_{xy}}{c} \right]} \, dx \, dy \right\} \tag{3.14}
$$

where the spatial radar reflectivity function $g(x, y)$ is independent of the target's orientation and the radar frequency, at least over small changes in aspect angle and for frequencies within a small relative bandwidth.

3.3.3 The Dynamic Range of Radar and Optical Images

People viewing ISAR images for the first time often are disappointed by the poor image quality compared to a photograph. Partly this is because radar images of targets are usually taken from further away than photographs. But partly it is because they do not appreciate the different information content caused by a five order-of-magnitude change in wavelength.

Reflections in the visible spectrum from most objects are diffuse because the surface roughness is larger than the wavelength of visible light. Because even dark surfaces are diffuse scatterers, optical images have a relatively low dynamic range. Radar wavelengths are large in comparison to the surface roughness, especially for man-made targets. Therefore most radar reflections are specular, and radar images have such a high dynamic range that only the strongest specular scatterers are detectable above noise and background clutter.

Taking this reasoning to the extreme suggests an even simpler model. This model, used in the superresolution approaches to ISAR imaging discussed in section 4.4.3, leads to a model of a radar target as a small collection of ideal point scatterers. The target's reflection using this model is

$$p_r(t) = \Re\left\{ \sum_{k=1}^{K} \frac{g_k}{r_k^2}\, e^{j\omega\left[t - \frac{2r_k}{c}\right]} \right\} \tag{3.15}$$

where there are K discrete scatterers and the kth scatterer has reflectivity g_k and is located r_k from the radar.

3.4 Achieving a High Range Resolution

Section 3.2 established, at a qualitative level, that by sampling the time-delay response of a moving target over a period of time, a high resolution estimate of the target's radar reflectivity could be obtained. In this section and the next, quantitative aspects of achieving a high resolution image in range and cross-range are examined. This indicates the constraints that ISAR imaging imposes on the radar waveform and the target's motion.

Consider the situation illustrated in figure 3.1, where the distance between two radar scatterers, A and B, and the radar are $r_A = r_0 - d/2$ and $r_B = r_0 + d/2$ respectively.

If the radar transmits a short pulse $p_t(t)$, the received signal $p_r(t)$ is the superposition of the reflections from the two scatterers

$$p_r(t) = g_A\, p(t - \tau_A) + g_B\, p(t - \tau_B) \tag{3.16}$$

Figure 3.1: Geometry of a radar and two scatterers, A and B, used to calculate the range resolution of a radar with bandwidth β.
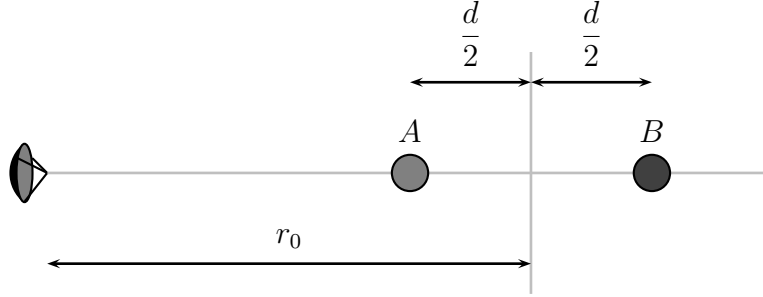
where $\tau_A = 2r_A/c$ and $\tau_B = 2r_B/c$ are the times it takes the pulse to reach each of the scatterers and return to the radar. g_A and g_B are the scatterers' reflectivities scaled to account for the $1/r^2$ amplitude attenuation with range.

The two pulses may be separated, hence the two scatterers distinguished, if the trailing edge of the pulse reflected from A arrives before the leading edge of the pulse reflected from B. For a pulse $p_t(t)$ with duration $\Delta\tau$, this implies that

$$\tau_A + \Delta\tau < \tau_B \tag{3.17}$$

which is equivalent to saying that

$$\Delta\tau < \frac{2d}{c} \tag{3.18}$$

or that scatterers separated by d in range may only be resolved if

$$d > \frac{c\Delta\tau}{2} \tag{3.19}$$

Since the bandwidth β of a rectangular pulse is approximately equal to the reciprocal of its duration $\Delta\tau$, the range resolution Δr_r of such a pulsed radar is

$$\Delta r_r = \frac{c\Delta\tau}{2} = \frac{c}{2\beta} \tag{3.20}$$

ISAR's high range resolution requires very, very short pulses; a range resolution of $\Delta r_r = 1$ m means a pulse width of $\Delta\tau = 6$ ns. As the pulse width decreases, the peak transmitted power must increase so that the signal-to-noise ratio is not adversely affected. At pulse widths small enough for ISAR imaging, the peak powers are very high. In addition, magnetrons that are specially designed for very short pulses still have $\Delta\tau > 50$ ns, so the best range resolution is $\Delta r_r = 6$ m, which is not sufficient for most ISAR applications [98, p. 104].

The solution is to transmit a waveform with a slowly changing instantaneous frequency that covers the required bandwidth over a long period of time. If the waveform's centre frequency is large compared with β, the relative bandwidth is small, which justifies assuming that the target's reflectivity is independent of frequency. As an example, a total bandwidth of 150 MHz corresponds to a range resolution of 1 m. With a centre frequency of 10 GHz, the relative bandwidth is $\frac{150\text{ MHz}}{10\text{ GHz}} = 1.5\%$. This is small enough for the target's reflectivity to be considered uniform, and it is also small enough for an X-band antenna to radiate efficiently over the whole frequency range.

Two such wideband waveforms, chirps and stepped-frequency waveforms, will now be examined.

3.4.1 Chirp Waveforms

A waveform such as $e^{j2\pi(f_c t + \frac{1}{2}Kt^2)}$ for $t \in [-T/2, T/2]$ is called a chirp [53] because the instantaneous frequency

$$\frac{d}{dt}\left[f_c t + \tfrac{1}{2}Kt^2\right] = f_c + Kt \tag{3.21}$$

increases linearly from $f_c - KT/2$ to $f_c + KT/2$. This is illustrated in figure 3.2(a).

Consider what happens when a one-dimensional target is illuminated with the chirp

$$p_t(t) = \Re\left\{e^{j\left(\omega t + \alpha t^2\right)}\right\} \tag{3.22}$$

Here, following [60], $\omega = 2\pi f_c$ and $\alpha = \pi K$ to reduce the number of symbols.

Repeating the derivation of (3.13), but with a one-dimensional target $g(r)$ instead of $g(x, y)$ and (3.22) as $p_t(t)$ rather than (3.6), shows that

$$p_r(t) = \Re\left\{\int \frac{g(r)}{r^2}\, e^{j\left(\omega(t-2r/c)+\alpha(t-2r/c)^2\right)}\, dr\right\} \tag{3.23}$$

As shown in [61], the target's reflectivity $g(r)$ may be recovered by mixing $p_r(t)$ either with $2e^{j\omega t}$ or with the chirp itself. The second method, known as deramp-FFT, is illustrated here.

The received signal $p_r(t)$ is mixed with $e^{j\left(\omega(t-t_0)+\alpha(t-t_0)^2\right)}$, which is the complex form of the original chirp, in a quadrature modulator. The delay t_0 is equal to $2r_0/c$ where r_0 is the target's range. The output of the quadrature modulator is passed through a low-pass filter (LPF) to give in-phase and quadrature components $s_I(t)$ and $s_Q(t)$

$$s_I(t) = \text{LPF}\left\{p_r(t) \cdot 2\cos\left(\omega(t - t_0) + \alpha(t - t_0)^2\right)\right\}$$

Figure 3.2: This shows two wideband waveforms commonly used to obtain a high range resolution. (a) is a chirp waveform and (b) is a stepped-frequency waveform. In both cases, the range resolution is $c/2\beta$ where β is the waveform's bandwidth.
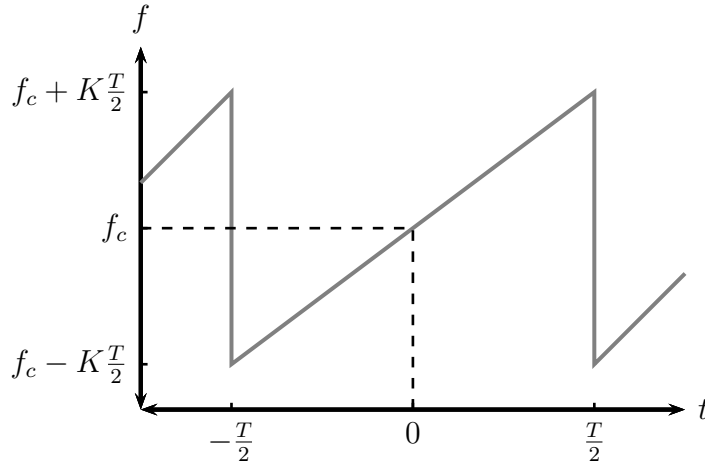
(a) A chirp waveform with duration T and total bandwidth $\beta = KT$.
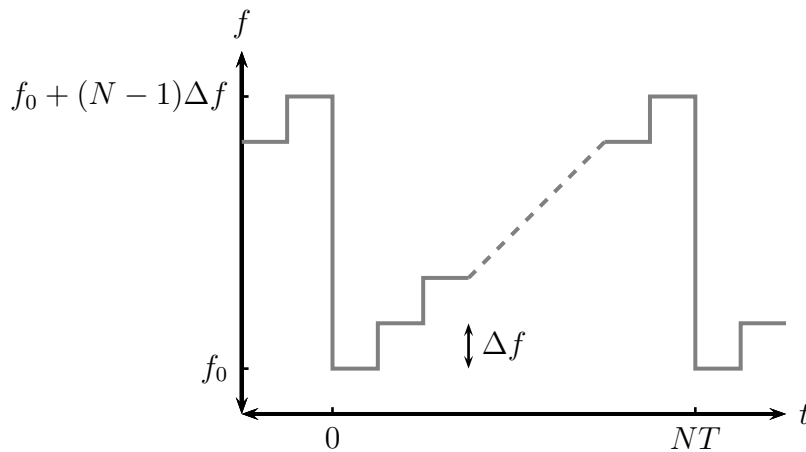
(b) A stepped-frequency waveform with total bandwidth $\beta = N\Delta f$.

$$= \Re \left\{ \int \frac{g(r)}{r^2} e^{j\left[\omega\left(t_0 - 2\frac{r}{c}\right) - \alpha t_0^2 + \alpha\left(2\frac{r}{c}\right)^2\right]} e^{j2\alpha\left(t_0 - \frac{2r}{c}\right)} dr \right\} \tag{3.24}$$

$$s_Q(t) = \text{LPF} \left\{ p_r(t) \cdot 2 \sin\left(\omega(t - t_0) + \alpha(t - t_0)^2\right) \right\}$$

$$= \Im \left\{ \int \frac{g(r)}{r^2} e^{j\left[\omega\left(t_0 - 2\frac{r}{c}\right) - \alpha t_0^2 + \alpha\left(2\frac{r}{c}\right)^2\right]} e^{j2\alpha\left(t_0 - \frac{2r}{c}\right)t} dr \right\} \tag{3.25}$$

This shows that the in-phase and quadrature components form the real and imaginary parts of $s(t)$ where

$$s(t) = s_I(t) + js_Q(t)$$

$$= \int \frac{g(r)}{r^2} e^{j\left[\omega\left(t_0 - 2\frac{r}{c}\right) - \alpha t_0^2 + \alpha\left(\frac{2r}{c}\right)^2\right]} e^{j2\alpha\left(t_0 - \frac{2r}{c}\right)t} dr \tag{3.26}$$

which has the form of an inverse Fourier transform

$$s(t) = \int \left[\frac{g(r(f))}{r^2(f)} e^{j\phi(r(f))} \frac{dr}{df} \right] e^{j2\pi ft} df \tag{3.27}$$

where

$$f = \frac{\alpha}{\pi}\left(t_0 - \frac{2r}{c}\right) \tag{3.28}$$

and

$$\phi(r) = \omega\left(t_0 - 2\frac{r}{c}\right) - \alpha t_0^2 + \alpha\left(\frac{2r}{c}\right)^2 \tag{3.29}$$

The duration of the chirp is T, so $s(t)$ is sampled over an interval of length T. The Fourier transform's frequency resolution is $\Delta f = 1/T$. Using (3.28) and writing $\alpha = \pi K$, the range resolution Δr_r satisfies

$$\frac{1}{T} = \Delta f = K\frac{2\Delta r_r}{c} \tag{3.30}$$

which is

$$\Delta r_r = \frac{c}{2KT} \tag{3.31}$$

Now KT is the spread of instantaneous frequencies swept out by the chirp during $[-T/2, T/2]$. Associating this with the bandwidth β of the chirp waveform, the range resolution can be expressed as

$$\Delta r_r = \frac{c}{2\beta} \tag{3.32}$$

which is the same as the expression obtained in (3.20).

Note that the chirp's duration is T, which is KT^2 longer than the equivalent single pulse. Therefore, for identical signal-to-noise ratios, the chirp's average power is KT^2 times lower than a single pulse's peak power.

3.4.2   Stepped-Frequency Waveforms

Another type of wideband waveform is a stepped-frequency waveform [98]. As shown in figure 3.2(b), this consists of N discrete frequencies f_n, where

$$f_n = f_0 + n\Delta f \qquad \text{for } n = 0, 1, \ldots, N-1 \tag{3.33}$$

and each frequency is transmitted for the same duration.

When frequency f_n is transmitted, the transmitted waveform is

$$p_{n,t}(t) = \cos(2\pi f_n t) = \Re\left\{e^{j2\pi f_n t}\right\} \tag{3.34}$$

Following the same reasoning as equations (3.6) to (3.13), the received waveform is

$$p_{n,r}(t) = \Re\left\{\int \frac{g(r)}{r^2}\, e^{j2\pi f_n(t-2r/c)}\, dr\right\} \tag{3.35}$$

This is passed through a quadrature modulator and low-pass filtered to give in-phase and quadrature components that are independent of time once reflections from the whole target have been received

$$s_I(f_n) = \text{LPF}\left\{p_{n,r}(t) \cdot 2\cos\left(2\pi f_n t\right)\right\}$$
$$= \Re\left\{\int \frac{g(r)}{r^2}\, e^{-j2\pi f_n \cdot 2\frac{r}{c}}\, dr\right\} \tag{3.36}$$

and

$$s_Q(f_n) = \text{LPF}\left\{p_{n,r}(t) \cdot 2\sin\left(2\pi f_n t\right)\right\}$$
$$= \Im\left\{\int \frac{g(r)}{r^2}\, e^{-j2\pi f_n \cdot 2\frac{r}{c}}\, dr\right\} \tag{3.37}$$

When these are added together in quadrature,

$$s(f_n) = s_I(f_n) + j s_Q(f_n)$$
$$= \int \frac{g(r)}{r^2}\, e^{-j2\pi f_n \cdot \frac{2r}{c}}\, dr \tag{3.38}$$

which is the Fourier transform of the target's reflectivity, sampled at frequency f_n.

Therefore, if the target's frequency responses $\{s(f_n)\}$ are measured for the N evenly spaced frequencies in the stepped-frequency waveform, an inverse discrete Fourier transform (DFT) may be used to estimate the target's one-dimensional reflectivity $g(r)$.

The temporal resolution Δt of an inverse DFT where the N frequency samples are spaced by Δf is $1/N\Delta f$. The range resolution corresponding to this time resolution is $\Delta r_r = c\Delta t/2$, which is

$$\Delta r_r = \frac{c}{2N\Delta f} \tag{3.39}$$

Figure 3.3: Geometry of a radar and two scatterers, A and B, used to calculate the cross-range resolution of a radar.
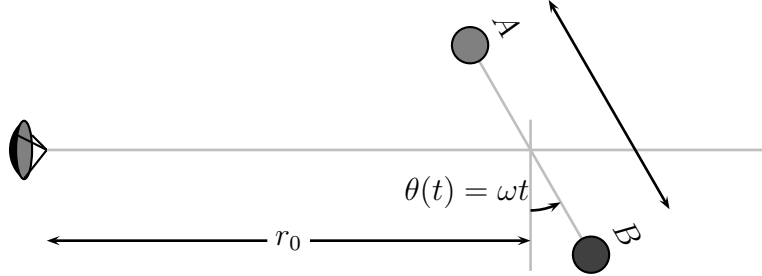
Since $N\Delta f$ is the total frequency covered by the stepped-frequency waveform, its bandwidth may be written $\beta = N\Delta f$ and the range resolution for a stepped-frequency waveform becomes

$$\Delta r_r = \frac{c}{2\beta} \tag{3.40}$$

This is the same as the equivalent expressions for a single pulse and a chirp given in (3.20) and (3.32).

3.5 Achieving a High Cross-Range Resolution

The second dimension for radar imaging is the cross-range dimension. Since the radar is only capable of distinguishing scatterers by differences in range, the target must move during the imaging interval in such a way that the range of each of the scatterers changes by a different amount. This happens when the target's aspect angle changes over time, which is the situation illustrated in figure 3.3. Here a target composed of two radar scatterers, A and B, separated by d in cross-range, are rotating at angular speed ω at a distance r_0 from the radar. With $\theta(t) = \omega t$ being the angle that A and B make with the cross-range, and assuming that $r_0 \gg d$, the ranges of the scatterers are

$$r_A(t) = \sqrt{(r_0 - \tfrac{d}{2}\sin\omega t)^2 + (\tfrac{d}{2}\cos\omega t)^2}$$
$$\approx r_0 - \tfrac{d}{2}\sin\omega t \tag{3.41}$$
$$r_B(t) = \sqrt{(r_0 + \tfrac{d}{2}\sin\omega t)^2 + (\tfrac{d}{2}\cos\omega t)^2}$$
$$\approx r_0 + \tfrac{d}{2}\sin\omega t \tag{3.42}$$

If the target is rotating sufficiently slowly, $\sin\omega t \approx \omega t$ during the period $t \in [-T/2, T/2]$. When illuminated by a radar at a frequency f, the difference

in phase between the two scatterers' reflections is

$$\Delta\theta(t) = 2\pi f \frac{2d\sin\omega t}{c} \approx \frac{4\pi}{c} f d\omega t \tag{3.43}$$

which has an instantaneous frequency of

$$\frac{1}{2\pi}\frac{d}{dt}\left[\frac{4\pi}{c}fd\omega t\right] = \frac{2fd\omega}{c} \tag{3.44}$$

Since the rotating target's phase is observing for a total time T, a Fourier transform can determine the rate at which the phase changes with an accuracy of $\Delta f = 1/T$. Setting this to the phase's instantaneous frequency shows that

$$\frac{1}{T} = \frac{2fd\omega}{c} \tag{3.45}$$

Rearranging to make d the subject then replacing it with the cross-range resolution Δr_c gives

$$\Delta r_c = \frac{c}{2f\omega T} = \frac{c}{2f\Delta\theta} \tag{3.46}$$

where $\Delta\theta$ is the target's total rotation during $[-T/2, T/2]$. Therefore, the cross-range resolution for the radar image is inversely proportional to the total change in the target's aspect angle during the imaging period.

3.5.1   Doppler Shifts

When a target rotates, the scatterers on one side of the target move towards the radar and those on the other side move away. With the target illuminated by a radar transmitting a single frequency, the phase of the radar reflection from each scatterer is shifted linearly in time due to that scatterer's changing range. This appears as a shift in the frequency of the reflected wave.

It is a common misconception in the ISAR literature[5] that cross-range processing separates targets in cross-range because their reflections have Doppler shifts due to each scatterer's velocity towards or away from the radar. However, the apparent frequency shifts are due to each scatterers' changing position, not their velocities. Soumekh [84] calls this a spatial Doppler phenomenon, to emphasize that it is not velocity-related. He also calls the Doppler effect a temporal Doppler phenomenon to make the distinction absolutely clear.

---

[5]See, for example, the criticisms of Harris [40] and Munson [61]. Many papers, for example [3] and [97], and even Wehner's book [98], use the Doppler shift as an intuitive explanation of cross-range processing. Even if they later analyse ISAR properly, this perpetuates the myth that ISAR is a result of the Doppler effect. While some intuition is useful, false intuition hampers a proper understanding of ISAR. Even when range-Doppler processing is properly described without the Doppler effect, the appearance of the word "Doppler" when there is no Doppler effect causes more confusion.

Nevertheless, the scatterers are moving with radial components, so their temporal Doppler shifts should be considered. This is studied by Wehner in [98] for ISAR and by Munson in [60] for SAR. In the case of ISAR, each scatterer's radial velocity has two components, a radial velocity due to the translational movement of the target as a whole, and a radial velocity due to its rotation. The former causes a slight shift of the whole target in the range direction, hence it can be ignored. The latter component causes phase shifts which degrade the ISAR image. From equation (30) of [60], the Doppler effect can be neglected as long as v_R, the radial component of any scatterer's velocity due solely to the target's rotation, satisfies

$$v_R < \frac{\lambda c}{8 r_0} \tag{3.47}$$

For a target 10 km from the radar imaged at X-band, this is a radial velocity of over 100 ms^{-1} just from the target's rotation. Therefore, the temporal Doppler effect may be neglected for many ISAR targets.

3.6   Imaging Two-Dimensional Moving Targets

The quantitative and qualitative analyses of ISAR in this chapter indicate that ISAR imaging requires a target whose motion causes a small change in its aspect angle over a period during which its radar reflection is repeatedly sampled by a wideband signal with a narrow relative bandwidth.

Either a stepped-frequency or a chirp waveform could be used. For simplicity, the remainder of this thesis will assume that a stepped-frequency waveform is used to sample the target's reflectivity at N discrete frequencies

$$f_n = f_0 + n\Delta f \qquad \text{for } n = 0, 1, \ldots, N-1 \tag{3.48}$$

Since the target is moving, its reflectivity $g(x, y)$ must be measured in a coordinate system that moves with the target. The distance between the point (x, y) on the target and the radar is now a function of time $r_{xy}(t)$. Equation (3.14) for the signal received from a stationary two-dimensional target illuminated by a radar at frequency f_n becomes

$$p_r(f_n, t) = \Re\left\{ \iint \frac{g(x, y)}{r_{xy}^2(t)} e^{j2\pi f_n \left[t - \frac{2r_{xy}(t)}{c}\right]} dx\, dy \right\} \tag{3.49}$$

for a moving target.

Because quadrature demodulation and low-pass filtering assume a carrier of frequency f_n, phase shifts caused by changes in $r_{xy}(t)$ are too low a frequency to be affected and the $e^{-j2\pi f_n \frac{2r_{xy}(t)}{c}}$ term passes through the demodulator unchanged. Using the same steps as (3.38) with $r_{xy}(t)$ considered

a constant, the frequency response of a moving target at time t and at frequency f is

$$s(f,t) = \iint \frac{g(x,y)}{r_{xy}^2(t)}\, e^{-j\frac{4\pi}{c}fr_{xy}(t)}\, dx\, dy \qquad (3.50)$$

where the region of integration includes the whole of the target. Actually, the region is determined by the location of the target within the target's mainlobe, the width of the mainlobe and the times at which the receiver's output is sampled, but these should be set to cover the entire target.

One final assumption about the target's frequency response will be made for convenience, although the effects of it can easily be compensated for. The notation $s(f,t)$ for the target's frequency response at frequency f and at time t should really be written $s(f(t),t)$ to emphasize that $f(t)$ is actually a single-valued function determining which frequency in the stepped-frequency waveform is transmitted at which time. By suppressing the "(t)" in $f(t)$, it is implicitly stated that frequency response may be measured at any number of frequencies in one single instant of time. This is not too unrealistic if the duration of each step in the stepped-frequency waveform is very short so that the stepped-frequency waveform repeats with a frequency that is high enough to capture the changes in the target's reflections with time. This requires a fast digital frequency synthesiser to generate the stepped-frequency waveform.

Now, all that ISAR requires is suitable algorithms to estimate $g(x,y)$ from measurements of $s(f,t)$ taken over a set of discrete frequencies $\{f_n\}$ at each of a set of discrete times $\{t_m\}$. A number of ISAR inversion algorithms suitable for different target motions are the subject of the next chapter.

Chapter 4

ISAR Imaging

The analysis in chapter 3 of radar reflections from a moving target concluded with the simple model in equation (3.50). This expressed the target's frequency response at any time as a function of its motion and its spatial radar reflectivity. In ISAR, the frequency responses are known but the target's motion and reflectivity are not. An inversion algorithm is needed to specify how to estimate a target's reflectivity from measurements of its frequency responses over a period of time. Because the target's motion creates the synthetic aperture that ISAR needs, the complexity of an ISAR algorithm is directly related to the complexity of the target's motion.

In this chapter, some efficient ISAR inversion algorithms are derived for certain assumptions about the form of the target's motion. Constraining the target's motion allows approximations based on Fourier transforms, which can be evaluated efficiently using the fast Fourier transform. Range-Doppler ISAR processing is derived for uniformly rotating targets, and for targets moving in a straight line at constant speed. A more recent method of ISAR inversion, called wavenumber processing, is derived for targets moving in a straight line. Some other approaches to ISAR, and imaging using superresolution spectral estimators, are briefly discussed.

As the motion of a target may not exactly match the assumptions built into the ISAR inversion algorithm, motion estimation is needed to measure how the target moves and compensate for it. A number of methods for motion estimation are discussed in chapter 5 and a new method of motion estimation, the subject of this thesis, is derived in chapters 6 to 8.

Traditionally, ISAR has been described in terms of the Doppler effect. This gives a misleading view of the ISAR imaging mechanism, and should be rejected in favour of the modern signal processing approach which allows a more complete model of the ISAR imaging process and explicitly states the approximations that have been made. The Doppler description is so

common in the ISAR literature, however, that it has been included for the sake of completeness. Its proper place in the modern view of ISAR is reflected in its location, appendix 4B at the end of the chapter.

4.1   The ISAR Imaging Model

The model for a moving target's frequency response, developed in chapter 3, is

$$s(f,t) = \iint \frac{g(x,y)}{r_{xy}^2(t)} \, e^{-j\frac{4\pi}{c}fr_{xy}(t)} \, dx \, dy \tag{4.1}$$

where $g(x,y)$ is the target's unknown radar reflectivity, measured in a Cartesian coordinate system which moves with the target. $r_{xy}(t)$ is the distance from the radar to the point (x,y) on the target at time t. For convenience, the coordinate system's origin is usually taken to be the centre of the target.

4.1.1   Simplifying the Model

Writing the frequency response in terms of f leads to a factor of $4\pi/c$ in the argument of the complex exponential. The notation may be simplified slightly by using the wavenumber k instead of the frequency f. This still leaves a factor of 2 because ranges are measured as round-trip distances. When this factor of 2 is also included in the wavenumber,

$$k = \frac{4\pi}{c}f \tag{4.2}$$

and the frequency response becomes

$$s(k,t) = \iint \frac{g(x,y)}{r_{xy}^2(t)} \, e^{-jkr_{xy}(t)} \, dx \, dy \tag{4.3}$$

To emphasize this point, the wavenumber is $2\pi/\lambda = 2\pi f/c$, but throughout this thesis, the symbol k is used to represent twice the wavenumber, so $k = 4\pi f/c$. This is equivalent to pretending that the scatterers on the target are radar sources and that the frequency has doubled or the speed of light has halved.[1] For convenience, both f and $k = 4\pi f/c$ will be called frequencies; the context will determine which is intended.

ISAR is designed for high-resolution imaging of small targets that are a long way from the radar, so the $r_{xy}^2(t)$ term in the denominator of the integrand of (4.3) varies little over the whole of the target. Therefore, $r_{xy}(t)$

---

[1] Cafforio *et al.* describe this as the "radiating reflector" model [17]. Its counterpart in seismic imaging is the "exploding reflector" model which sounds much more exciting (see the footnote on page 49).

may be regarded as a constant, r_0, which is the distance between the radar and the centre of the target at time $t = 0$. Being a constant, the $1/r_0^2$ can be included with $g(x, y)$ to give an alternative model

$$s(k, t) = \iint g(x, y) \, e^{-jkr_{xy}(t)} \, dx \, dy \qquad (4.4)$$

In extreme cases where the target's range changes appreciably during the imaging period, this approximation may not be appropriate. But if the target's size is still small compared with its minimum range, the $r_{xy}(t)$ in the denominator may be replaced by $r_0(t)$, the range of the target's centre at time t. This gives a third form of the target's frequency response

$$s(k, t) = \frac{1}{r_0^2(t)} \iint g(x, y) \, e^{-jkr_{xy}(t)} \, dx \, dy \qquad (4.5)$$

Note that similar approximations cannot be made for the $r_{xy}(t)$ in the argument of the complex exponential because the complex exponential is sensitive to $kr_{xy}(t)$ modulo 2π.

4.1.2 Measurements for the ISAR Inversion

When a stepped-frequency waveform containing N evenly spaced frequencies

$$f_n = f_0 + n\Delta f \qquad \text{for } n = 0, 1, \dots, N - 1 \qquad (4.6)$$

is transmitted at a time t and the backscattererd signal sampled, the target's frequency response $s(k, t)$ is measured for the N uniformly spaced values of k in the stepped-frequency waveform

$$k_n = k_0 + n \, \Delta k \qquad n = 0, 1, \dots, N - 1 \qquad (4.7)$$

This is repeated at each of M uniformly spaced times t_m over the time interval $[-T/2, T/2]$

$$t_m = \left(\frac{m}{M - 1} - \frac{1}{2} \right) T \qquad \text{for } m = 0, 1, \dots, M - 1 \qquad (4.8)$$

to give the full set of measurements used for ISAR imaging

$$s(k_n, t_m) \qquad \text{for } n = 0, 1, \dots, N - 1 \text{ and } m = 0, 1, \dots, M - 1 \qquad (4.9)$$

Some ISAR inversion algorithms that use this set of measurements will now be derived. The two methods examined are range-Doppler processing, where $r_{xy}(t)$ is approximated using a linear function of x and y, and wavenumber processing, where the circular nature of the radar's wavefront is exploited to give a more exact inversion.

Figure 4.1: Imaging geometry for range-Doppler ISAR with a target rotating at an angular speed ω situated a fixed distance r_0 from the radar.
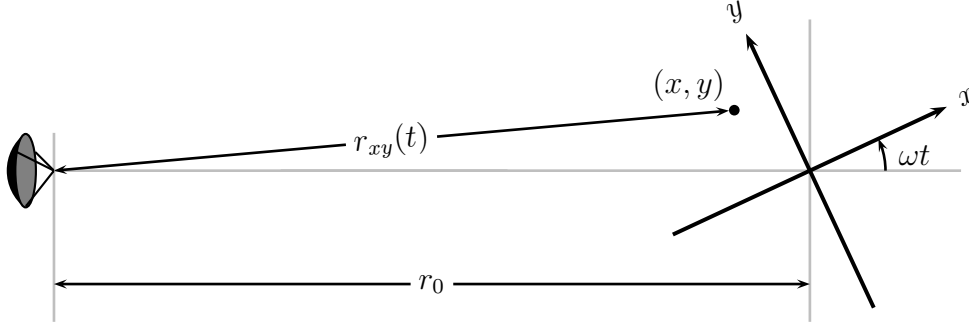
4.2 Range-Doppler Processing

The simplest formulation of ISAR is range-Doppler processing. This uses the first-order Taylor series for $r_{xy}(t)$ expanded about the centre of the target to show that the measured $s(k, t)$ are samples of the Fourier transform of the target's reflectivity $g(x, y)$.

The points in the spatial frequency domain at which the Fourier transform of $g(x, y)$ is sampled depend on the target's motion. Consequently, any range-Doppler ISAR inversion depends on the way the target moves. This is analysed for two types of target motion; first for a uniformly rotating target, then for a target moving in a straight line with constant speed.

4.2.1 Uniformly Rotating Target

Consider a target, such as an object mounted on a turntable in a radar test range [18] or a ship pitching and rolling at anchor, which rotates with a uniform angular velocity a fixed distance from the radar.

The imaging geometry is shown in figure 4.1, where the target is located on the radar's boresight axis a distance r_0 from the radar antenna. The target rotates at constant angular velocity ω. The target's coordinate system has its origin at the centre of rotation and it rotates with the target. At time $t = 0$, the target's x axis is aligned with the boresight axis.

The angle at time t between the target's x axis and the boresight axis is ωt. Using Pythagoras' theorem, the distance at time t from the radar to a scatterer at (x, y) is

$$r_{xy}(t) = \sqrt{(r_0 + x\cos\omega t - y\sin\omega t)^2 + (x\sin\omega t + y\cos\omega t)^2} \qquad (4.10)$$

If the size of the target is very small in comparison to its distance from the

radar, so that

$$\sqrt{x^2 + y^2} \ll r_0 \tag{4.11}$$

for all points (x, y) on the target, $r_{xy}(t)$ may be approximated by a first order Taylor series in x and y, expanded about the centre of the target at $(0, 0)$

$$r_{xy}(t) \approx r_0 + x \cos \omega t - y \sin \omega t \tag{4.12}$$

Substituting this Taylor series into the measurement model in (4.4) shows that

$$s(k, t) = e^{-jkr_0} \int\!\!\int g(x, y) \, e^{-jk(x \cos \omega t - y \sin \omega t)} \, dx \, dy \tag{4.13}$$

is approximately $G(k_x, k_y)$, the two-dimensional Fourier transform of $g(x, y)$ given by

$$G(k_x, k_y) = \int\!\!\int g(x, y) \, e^{-j(xk_x + yk_y)} \, dx \, dy \tag{4.14}$$

Make a transformation in (4.13) from the (k, t) measurement space to the spatial frequency (k_x, k_y)-space where

$$k_x = k \cos \omega t \tag{4.15}$$
$$k_y = -k \sin \omega t \tag{4.16}$$

to show that $s(k, t)$ is $G(k_x, k_y)$ sampled at points on a polar grid in (k_x, k_y)-space according to

$$s(k, t) = e^{-jkr_0} G(k \cos \omega t, -k \sin \omega t) \tag{4.17}$$

This is illustrated in figure 4.2.

The inverse Fourier transform required to obtain $g(x, y)$ from $G(k_x, k_y)$ can be implemented efficiently using a fast Fourier transform (FFT) only if the points at which $G(k_x, k_y)$ is known lie on a rectangular grid. The grid in figure 4.2 is approximately rectangular because the radar has a narrow relative bandwidth. However, for an accurate ISAR image of the target, the samples of $G(k_x, k_y)$ have to be resampled so that the grid on which the resampled points lie is rectangular.

The e^{-jkr_0} phase term centres the target's image in the range direction and may be neglected. This gives the following algorithm for range-Doppler processing applied to a uniformly rotating target:

Algorithm 4.1 (Range-Doppler ISAR—uniformly rotating target)

To obtain a uniformly rotating target's spatial radar reflectivity $g(x, y)$ from uniformly spaced measurements of the target's frequency response $s(k, t)$ over a period of time:

Figure 4.2: The points at which $G(k_x, k_y)$ is known for range-Doppler ISAR with a uniformly rotating target lie on a small segment of a polar grid. They lie at the intersection of concentric circles (whose radii are the k_n of the stepped-frequency waveform) and straight lines (whose orientations are those of the target at each time t_m).
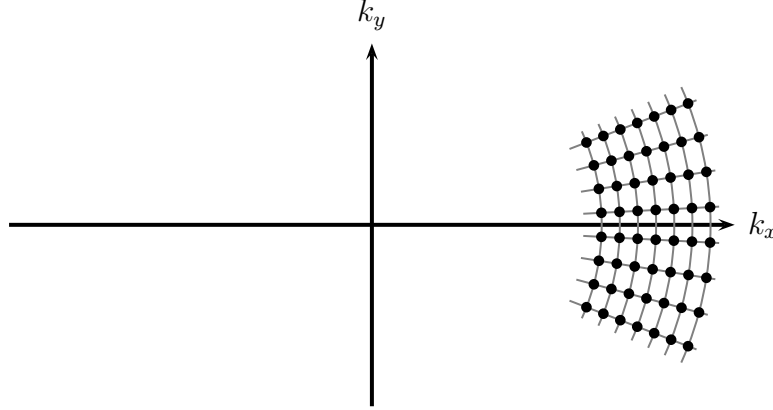
1. *Use the radar data or* a priori *information to estimate the target's angular speed ω.*

2. *Associate the measurements $s(k, t)$ with samples of the target's reflectivity $G(k_x, k_y)$ using*

$$G(k \cos \omega t, -k \sin \omega t) = s(k, t) \qquad (4.18)$$

3. *Resample the $G(k \cos \omega t, -k \sin \omega t)$ from the polar grid of figure 4.2 to give $G(k_x, k_y)$ uniformly sampled on a rectangular grid.*

4. *Take the two-dimensional inverse Fourier transform of the rectangularly-sampled $G(k_x, k_y)$ to give an estimate $\widehat{g}(x, y)$ of the target's spatial reflectivity $g(x, y)$*

$$\widehat{g}(x, y) = \mathcal{F}^{-1} \left\{ G(k_x, k_y) \right\} \qquad (4.19)$$

5. *Display $\log |\widehat{g}(x, y)|$ as the target's ISAR image.*

4.2.2   Target Moving in a Straight Line

The second basic motion that has an efficient inversion using range-Doppler processing is that of a target moving at uniform speed along a straight line at an angle to the boresight axis.

The geometry of the radar and target is shown in figure 4.3. The target moves at constant speed v along a straight line at an angle θ to the boresight axis. θ must not be close to 0° or 180° because the cross-range component of

Figure 4.3: Imaging geometry for range-Doppler ISAR with a target moving in a straight line at constant speed v. The target crosses the boresight axis at $t = 0$ at an angle θ and a distance r_0 from the radar.
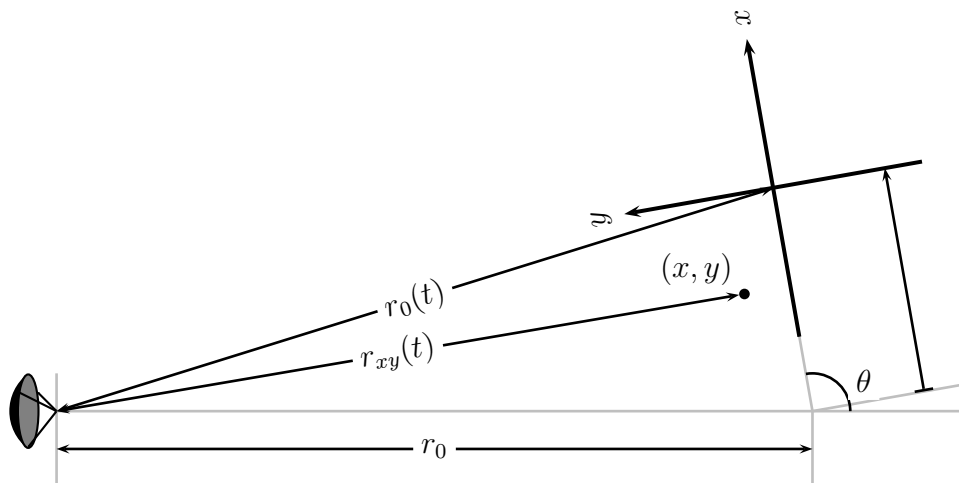
the target's motion is needed to change its aspect angle and so generate the synthetic aperture. The target is observed for the time interval $[-T/2, T/2]$, and at $t = 0$ the target lies a distance r_0 from the radar on the boresight axis. The coordinate system for $g(x, y)$ has its origin at the target's geometric centre and the x axis points in the direction the target is moving.

The distance between the radar and the point at (x, y) on the target at time t is

$$r_{xy}(t) = \sqrt{(x + vt + r_0 \cos\theta)^2 + (y - r_0 \sin\theta)^2} \tag{4.20}$$

Let $r_0(t)$ be the distance of the target's centre from the radar at time t

$$r_0(t) = \sqrt{(vt + r_0 \cos\theta)^2 + r_0^2 \sin^2\theta} \tag{4.21}$$

so that $r_0 = r_0(0)$.

Assume as before that the size of the target is very small in comparison to $r_0(t)$ for $t \in [-T/2, T/2]$. This justifies expanding $r_{xy}(t)$ in a first order Taylor series about the centre of the target, giving

$$r_{xy}(t) \approx r_0(t) + \frac{x(r_0 \cos\theta + vt) - yr_0 \sin\theta}{r_0(t)} \tag{4.22}$$

Writing

$$\cos\phi(t) = \frac{r_0 \cos\theta + vt}{r_0(t)} \tag{4.23}$$

and

$$\sin\phi(t) = -\frac{r_0 \sin\theta}{r_0(t)} \tag{4.24}$$

Figure 4.4: The points at which $G(k_x, k_y)$ is known for range-Doppler ISAR with a target moving in a straight line at constant speed lie on a small segment of a polar grid. They lie at the intersection of concentric circles (whose radii are the k_n of the stepped-frequency waveform) and straight lines (whose orientations are those of the target at each time t_m).
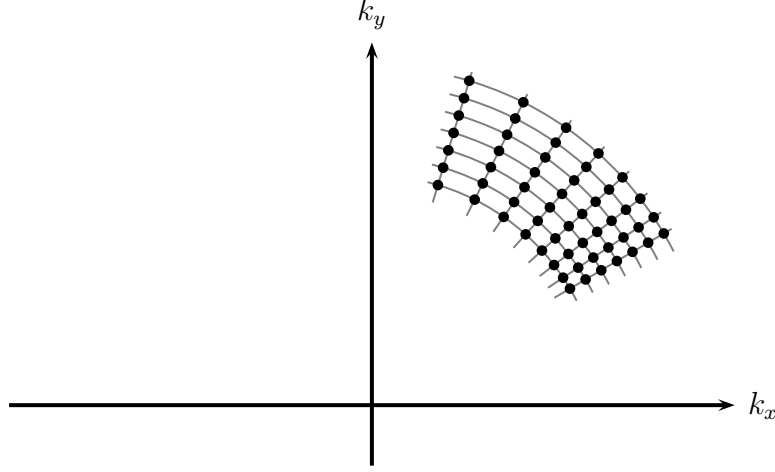
allows $r_{xy}(t)$ to be written as

$$r_{xy}(t) = r_0(t) + x \cos \phi(t) + y \sin \phi(t) \tag{4.25}$$

Substituting this into the measurement model (4.4) shows that

$$s(k, t) = e^{-jkr_0(t)} \iint g(x, y) \, e^{-jk(x \cos \phi(t) + y \sin \phi(t))} \, dx \, dy \tag{4.26}$$

is approximately $G(k_x, k_y)$, the two-dimensional Fourier transform of $g(x, y)$ from (4.14). To see this more clearly, make a slightly different transformation from the (k, t) measurement space to the spatial frequencies (k_x, k_y)

$$k_x = k \cos \phi(t)$$
$$= k \frac{r_0 \cos \theta + vt}{r_0(t)} \tag{4.27}$$
$$k_y = k \sin \phi(t)$$
$$= -k \frac{r_0 \sin \theta}{r_0(t)} \tag{4.28}$$

This shows that $s(k, t)$ and $G(k_x, k_y)$ are related by

$$s(k, t) = e^{-jkr_0(t)} G\left(k \frac{r_0 \cos \theta + vt}{r_0(t)}, -k \frac{r_0 \sin \theta}{r_0(t)} \right) \tag{4.29}$$

Therefore the set of measurements of $s(k, t)$ gives $G(k_x, k_y)$ on a polar grid in (k_x, k_y)-space that is the intersection of concentric circles of radius k_n for

$n = 0, 1, \ldots, N - 1$ with radial lines at angles of $\phi(t_m)$, which is the target's aspect angle at time t_m. This is illustrated in figure 4.4, where the cotangents of the angles of the radial lines are evenly spaced.

So except for differences in the polar reformatting and a phase function $e^{-jkr_0(t)}$ which cannot be neglected because it is not a linear function of time, the inversion algorithm for targets moving in a straight line is identical to the inversion in algorithm 4.1.

Algorithm 4.2 (Range-Doppler ISAR—straight line motion)
To obtain the spatial radar reflectivity $g(x, y)$ of a target with constant velocity from uniformly spaced measurements of the target's frequency response $s(k, t)$ over a period of time:

1. *Use the radar data or* a priori *information to estimate the target's speed v and heading θ.*

2. *Associate the measurements $s(k, t)$ with samples of the target's reflectivity $G(k_x, k_y)$ using*

$$G\left(k\frac{r_0 \cos \theta + vt}{r_0(t)}, -k\frac{r_0 \sin \theta}{r_0(t)}\right) = e^{jkr_0(t)} s(k, t) \qquad (4.30)$$

   where

$$r_0(t) = \sqrt{(vt + r_0 \cos \theta)^2 + r_0^2 \sin^2 \theta} \qquad (4.31)$$

3. *Resample the $G\left(k\frac{r_0 \cos \theta + vt}{r_0(t)}, -k\frac{r_0 \sin \theta}{r_0(t)}\right)$ from the grid of figure 4.4 to give $G(k_x, k_y)$ uniformly sampled on a rectangular grid.*

4. *Take the two-dimensional inverse Fourier transform of the rectangularly-sampled $G(k_x, k_y)$ to give an estimate $\widehat{g}(x, y)$ of the target's spatial reflectivity $g(x, y)$*

$$\widehat{g}(x, y) = \mathcal{F}^{-1}\left\{G(k_x, k_y)\right\} \qquad (4.32)$$

5. *Display $\log|\widehat{g}(x, y)|$ as the target's ISAR image.*

4.2.3 Resolution of Range-Doppler Processing

The resolution of the resulting ISAR image using range-Doppler processing depends on the spacing of the known values of $G(k_x, k_y)$ after polar reformatting so exact expressions for the range and cross-range resolution can only be calculated once the resampling scheme has been specified.

Nevertheless, since the stepped-frequency waveform has a narrow relative bandwidth and the change in the target's aspect angle is slight, the grids in (k_x, k_y)-space are nearly rectangular and simple approximate range and cross-range resolutions can be derived.

The resolution in range and cross-range, Δr_r and Δr_c respectively, are related to the radial and transverse extents, Δk_r and Δk_t respectively, of the polar grid in (k_x, k_y) space according to the formula for the resolution of a Fourier transform

$$\Delta r_r = \frac{2\pi}{\Delta k_r} \tag{4.33}$$

$$\Delta r_c = \frac{2\pi}{\Delta k_t} \tag{4.34}$$

For both types of target motions considered, the radial extent of the (k, t) polar grid is from k_0 to k_{N-1}, which suggests $\Delta k_r = (N-1)\Delta k$. However, the Fourier transform is discrete (implemented as an FFT for efficiency) so values of k should be taken as extending from $k_0 - \Delta k/2$ to $k_{N-1} + \Delta k/2$, a total spread of $N\Delta k$. This gives a range resolution of

$$\Delta r_r = \frac{2\pi}{N\Delta k} = \frac{c}{2N\Delta f} \tag{4.35}$$

The transverse extent of the grid is at its narrowest when $k = k_0$. For the uniformly rotating target imaged over the period $[-T/2, T/2]$, the grid covers angles from $-\omega T/2$ to $\omega T/2$. At a radial distance k_0, this is a transverse extent of

$$\Delta k_t = 2k_0 \sin(\omega T/2) \approx k_0 \omega T \tag{4.36}$$

giving an approximate cross-range resolution for a uniformly rotating target of

$$\Delta r_c = \frac{2\pi}{\Delta k_t} \approx \frac{c}{2f_0 \omega T} \tag{4.37}$$

For the target moving in a straight line at speed v during the imaging period $[-T/2, T/2]$, the grid covered angles whose tangents varied from

$$\tan\phi(-T/2) = -\frac{r_0 \sin\theta}{r_0 \cos\theta - \frac{1}{2}vT} \tag{4.38}$$

to

$$\tan\phi(T/2) = \frac{r_0 \sin\theta}{r_0 \cos\theta + \frac{1}{2}vT} \tag{4.39}$$

so the total angular spread is

$$\begin{aligned}
\Delta\phi &= \phi(T/2) - \phi(-T/2) \\
&= \arctan\left(\frac{r_0 \sin\theta}{r_0 \cos\theta + \frac{1}{2}vT}\right) + \arctan\left(\frac{r_0 \sin\theta}{r_0 \cos\theta - \frac{1}{2}vT}\right)
\end{aligned} \tag{4.40}$$

Using the identity

$$\tan(x+y) = \frac{\tan x + \tan y}{1 - \tan x \tan y} \tag{4.41}$$

and some algebra shows that

$$\Delta\phi = \arctan\left(\frac{r_0 vT\sin\theta}{r_0^2 - \frac{1}{4}v^2T^2}\right) \qquad (4.42)$$

If $r_0 \gg vT$, this is approximately

$$\Delta\phi \approx \arctan\left(\frac{vT\sin\theta}{r_0}\right) \approx \frac{vT\sin\theta}{r_0} \qquad (4.43)$$

from which the approximate cross-range resolution for a target moving at an angle θ to the boresight axis is

$$\Delta r_c = \frac{2\pi}{\Delta k_t} \approx \frac{c}{2f_0\frac{vT}{r_0}\sin\theta} \qquad (4.44)$$

4.3 Wavenumber Processing

A relatively recent inversion for SAR and ISAR imaging writes the spherical wave $e^{-jkr_{xy}}/r_{xy}$ as the superposition of plane waves

$$\frac{e^{-jkr_{xy}}}{r_{xy}} \approx -j\sqrt{\frac{k}{2\pi r_{xy}}}\int_{-k}^{k}\frac{1}{\sqrt{k^2 - k_x^2}}e^{-j(xk_x + y\sqrt{k^2 - k_x^2})}\,dk_x \qquad (4.45)$$

where $r_{xy} = \sqrt{x^2 + y^2}$ is the distance from the source to the radar. This expression, derived in appendix 4A, assumes that the target is more than ten wavelengths from the radar in the y direction. Radar targets are usually tens of thousands of wavelengths away from the antenna so this condition is easily met if the y axis is not perpendicular to the radar's boresight axis.

For many years, theoretical physicists have used an eigendecomposition of a spherical wave into plane wave eigenfunctions to solve scattering and diffraction problems [59, sec. 9.3]. In 1978, Stolt analysed seismic imaging using range migration[2] and found an equivalent expression to (4.45) [91]. From his work, changing coordinates from (k_x, k_y) to $(k_x, \sqrt{k^2 - k_x^2})$ has come to be called the Stolt transformation. Similar inversions have been developed

---

[2]Range migration in seismic imaging causes reflections from a subsurface layer at an angle to the horizontal to appear in an incorrect position. Seismic imaging may be considered equivalent to firing sources located at the subsurface layer and measuring the arrival times of the wavefronts at the surface. Propagating the wavefield measured at the surface back in time using the wave equation gives the location of the subsurface layer.

This model of imaginary sources at a subsurface layer is called the "exploding reflector" model [41, ch. 2]. Notice how similar this is to radar imaging, where the target is modelled as radiating reflectors, as mentioned in the footnote on page 40.

for tomography with diffracting sources, such as medical imaging using ultrasound [41, ch. 6].

In the last few years, radar imaging has been reformulated using this decomposition [17] instead of range-Doppler processing. A comparison of SAR using range-Doppler processing and this new method, called wavenumber processing or $\omega - k$ processing, is given in [4]. The description of $\omega - k$ processing for ISAR presented here closely follows that of Soumekh for SAR and ISAR imaging [84].

4.3.1 Imaging Geometry

Soumekh's work is primarily concerned with SAR imaging, so his description of ISAR is in the context of imaging a slowly moving target against the stationary background of a SAR image. The development of his imaging model and inversion in [104] and [84] is presented here in a form suitable for ISAR-only imaging. Consequently, the radar is assumed to be stationary.

The geometry of the radar and target is the same as that in figure 4.3 on page 45 used for range-Doppler imaging of a target moving in a straight line at constant speed. From equation (4.20), the distance at time t from the point (x, y) on the target to the radar is

$$r_{xy}(t) = \sqrt{(x + vt + r_0 \cos \theta)^2 + (y - r_0 \sin \theta)^2} \qquad (4.46)$$

Make the substitutions

$$x_0 = -r_0 \cos \theta \qquad (4.47)$$
$$y_0 = r_0 \sin \theta \qquad (4.48)$$

so that

$$r_{xy}(t) = \sqrt{(x + vt - x_0)^2 + (y - y_0)^2} \qquad (4.49)$$

Then the measurement of the target's reflectivity made at time t and at frequency f is given by equation (4.3)

$$
\begin{aligned}
s(k, t) &= \iint g(x, y) \frac{e^{-jkr_{xy}(t)}}{r_{xy}^2(t)} \, dx \, dy \\
&\approx \frac{1}{r_0} \iint g(x, y) \frac{e^{-jkr_{xy}(t)}}{r_{xy}(t)} \, dx \, dy
\end{aligned}
\qquad (4.50)
$$

where the limits of integration include the whole of the target.

4.3.2 $\omega - k$ ISAR Inversion

The spherical wave in the integrand of (4.50) may be written using the decomposition in (4.45). This gives

$$s(k,t) \approx -j\sqrt{\frac{k}{2\pi r_0^3}} \iint g(x,y) \int_{-k}^{k} \frac{1}{\sqrt{k^2 - k_x^2}}$$

$$\times\, e^{-j((x_0 - x - vt)k_x + (y_0 - y)\sqrt{k^2 - k_x^2})}\, dk_x\, dx\, dy \qquad (4.51)$$

This approximation is only valid if $y_0 - y \gg 0$ for all scatterers on the target. This implies that r_0 must be significantly larger than the size of the target and that θ, the angle the target's path makes with the boresight axis, must not be close to $0°$ or $180°$. Equivalently, the target must be far from the radar and have a velocity vector with a non-zero cross-range component. Note that these conditions are less restrictive than in range-Doppler ISAR which assume that the spherical wavefront at the target is flat.

Absorb the constants into $g(x,y)$ and write the "$\approx$" as equality.[3] This shows that

$$s(k,t) = \int_{-k}^{k} \frac{1}{\sqrt{k^2 - k_x^2}}\, e^{-j(x_0 k_x + y_0\sqrt{k^2 - k_x^2})}$$

$$\times\, G(-k_x, -\sqrt{k^2 - k_x^2})\, e^{jvtk_x}\, dk_x \qquad (4.52)$$

where $G(k_x, k_y)$ is the two-dimensional Fourier transform of $g(x,y)$

$$G(k_x, k_y) = \iint g(x,y)\, e^{-j(k_x x + k_y y)}\, dx\, dy \qquad (4.53)$$

The e^{jvtk_x} term in the integrand indicates that (4.52) is an inverse Fourier transform. Taking the Fourier transform of (4.52) with respect to t gives

$$s(k,\omega) = \int s(k,t) e^{-j\omega t}\, dt$$

$$= \frac{e^{-j(x_0\omega/v + y_0\sqrt{k^2 - \omega^2/v^2})}}{\sqrt{k^2 - \omega^2/v^2}}\, G(-\omega/v, -\sqrt{k^2 - \omega^2/v^2}) \qquad (4.54)$$

The $e^{-j(x_0\omega/v + y_0\sqrt{k^2 - \omega^2/v^2})}$ term just shifts the target to the centre of the ISAR image. Neglecting that,

$$G(-\omega/v, -\sqrt{k^2 - \omega^2/v^2}) = \sqrt{k^2 - \omega^2/v^2}\, s(k,\omega) \qquad (4.55)$$

This gives the following algorithm for ISAR imaging using $\omega - k$ processing:

---

[3]In the preface to [84], Soumekh states that his method is "an approximation-free inversion". Yang and Soumekh, in [104] describe it as a "SAR inversion without any need for approximations." While these are slight exaggerations, it is true that ISAR inversions based on $\omega - k$ processing are substantially better than range-Doppler processing.

Figure 4.5: The points at which $G(k_x, k_y)$ is known for $\omega - k$ ISAR with a target moving in a straight line at constant speed lie at the intersection of concentric circles (whose radii are the k_n of the stepped-frequency waveform) and parallel straight lines. Compare this with the range-Doppler grids in figures 4.2 and 4.4 where the straight lines are radial.
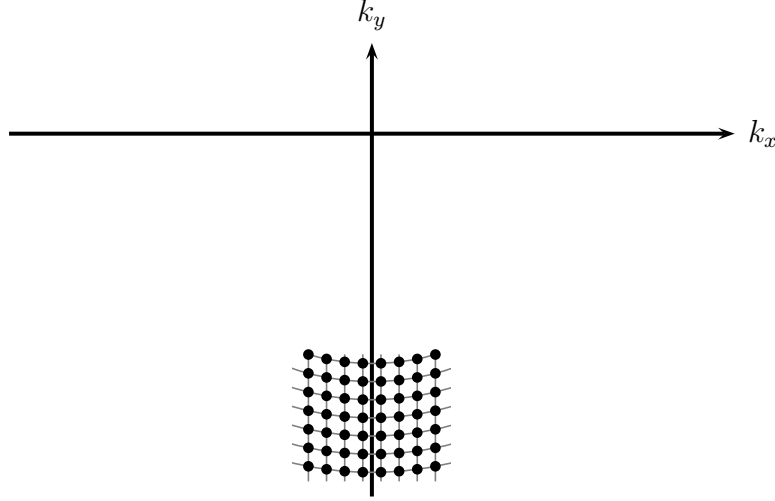
Algorithm 4.3 ($\omega - k$ ISAR Inversion)

  To obtain the spatial radar reflectivity $g(x, y)$ of a target with constant velocity from uniformly spaced measurements of the target's frequency response $s(k, t)$ over a period of time:

  1. *Use the radar data or* a priori *information to estimate the target's speed v.*

  2. *Take the Fourier transform (in the form of an FFT) of the $s(k, t)$ with respect to t to give $s(k, \omega)$.*

  3. *Multiply $s(k, \omega)$ by $\sqrt{k^2 - \omega^2/v^2}$ to give $G(k_x, k_y)$ sampled as shown in figure 4.5.*

$$G(-\omega/v, -\sqrt{k^2 - \omega^2/v^2}) = \sqrt{k^2 - \omega^2/v^2}\, s(k, \omega) \qquad (4.56)$$

  4. *Resample $G(-\omega/v, -\sqrt{k^2 - \omega^2/v^2})$ in the k_y direction to give $G(k_x, k_y)$ uniformly sampled on a rectangular grid.*

  5. *Take the two-dimensional inverse Fourier transform of the rectangularly-sampled $G(k_x, k_y)$ to give an estimate $\widehat{g}(x, y)$ of the target's spatial reflectivity $g(x, y)$*

$$\widehat{g}(x, y) = \mathcal{F}^{-1}\left\{G(k_x, k_y)\right\} \qquad (4.57)$$

6. Display $\log |\hat{g}(x, y)|$ as the target's ISAR image.

Actually the image produced by this algorithm is $g(x - x_0, y - y_0)$ because the linearly increasing phase term in (4.55) has been neglected. Shifting the image by (x_0, y_0) will centre it.

Modifications to the $\omega - k$ inversion have been proposed for cases when the target's frequency response is sampled unevenly or for SAR imaging where the target terrain is three-dimensional [33]. Soumekh and Choi describe estimating and correcting noisy SAR data with multiplicative noise affecting phase only, or both phase and magnitude [85]. Soumekh also presents inversions using his method that are suitable for tomographic imaging and geophysical imaging [84].

4.4 Other Approaches to ISAR Imaging

This section is a very brief discussion of some other approaches to ISAR imaging and ISAR inversion algorithms. These include comments that have appeared in the literature about eliminating polar reformatting, ISAR inversion using tomography, and achieving a higher resolution from less data with superresolution spectral estimation methods.

4.4.1 Polar Reformatting During Sampling

ISAR inversion algorithms use Fourier transforms to convert the target's frequency response $G(k_x, k_y)$ to an estimate of its spatial radar reflectivity $g(x, y)$. Polar reformatting is needed because sampling $s(k, t)$ on a rectangular grid in (k, t)-space gives $G(k_x, k_y)$ at points that lie on a polar grid in (k_x, k_y)-space while FFTs need samples on a rectangular grid, not a polar grid.

One way to avoid polar reformatting altogether has been suggested by Harris [40]. If the target's motion is known *a priori*, it is in principle possible to sample $s(k, t)$ non-uniformly in such a way that the equivalent samples of $G(k_x, k_y)$ lie on uniformly spaced rectangular grid so that an FFT can be applied directly to the measurements without the need for polar reformatting.

A slightly different sampling scheme for SAR has been suggested by Lawton in [54]. This gives $G(k_x, k_y)$ on a grid in (k_x, k_y)-space that is evenly spaced in the k_x direction and has a linearly increasing spacing in the k_y direction, a bit like a chirp. The inversion can be done without reformatting using the Bluestein chirp form of the FFT [13].

The success of methods such as these depends on how accurately the position and orientation of the target can be predicted at each time and frequency that $s(k, t)$ is sampled. Any residual errors in the target's predicted

location and orientation will still require polar resampling to correct. No
ISAR images of real targets using these methods have been published, so it
is difficult to judge whether they are feasible or just theoretical curiosities.

4.4.2   Tomographic ISAR

Similarities in the geometry of ISAR imaging, where a target uniformly ro-
tates, and X-ray tomography, where a detector rotates around a patient,
suggest that tomographic inversions may be applicable to radar imaging.
This has been examined by Bernfeld [7], Snyder *et al.* [81], Munson *et al.*
[60] and Mensa *et al.* [56, 55] among others.

   One important difference between tomography and ISAR is that tomog-
raphy requires projections of a full 180° view of the target. This is difficult
for ISAR because the orientation-independence of a radar target's reflectiv-
ity function $g(x, y)$ is based on the assumption that the target's aspect angle
changes by at most only a few degrees.

   Experiments on ISAR imaging have been conducted by Gerlach using
tomographic methods for targets viewed over very wide aspect angles [35].
Using filtered backprojection to image a model target on a turntable, he
found that individual scatterers on the target generally only persisted for
aspect angle changes considerably less than 60°. This degraded the point
spread function of each scatterer, causing streaks in the ISAR image. The
orientation of each scatterer's streak depended on the range of aspect angles
for which that scatterer was a strong reflector.

4.4.3   Superresolution Techniques

ISAR imaging requires a two-dimensional fast Fourier transform to convert
the measurements $G(k_x, k_y)$ of the target taken in the spatial frequency do-
main to the radar's reflectivity $g(x, y)$ in the spatial domain. This is essen-
tially a spectral estimation problem, and the resolution of the final ISAR
image is limited to the inherent resolution of the Fourier transform.

   Since modern spectral estimation methods can achieve a higher resolu-
tion than classical Fourier-based spectral estimation, they have been applied
to ISAR imaging, where collectively they are known as superresolution algo-
rithms. Some examples of superresolution imaging are papers by Gupta [39]
and Nuthalapati [63] using two-dimensional linear prediction, Odendaal *et al.*
using the MUSIC algorithm [64], Farina *et al.* using autoregressive and min-
imum variance methods [27], Hua *et al.* using the matrix-pencil algorithm
[47, 46], and Haywood and Evans using system identification [45, 44].

   The supposed advantage of superresolution estimators is that they can
achieve a much higher resolution than conventional Fourier processing, or
achieve the same resolution with much less data.

While the superresolution estimators mentioned above may achieve a higher resolution than Fourier processing with less data, they only work if the data fits their model, which is the superposition of a small number of two-dimensional sinusoids. This assumes that the target is composed of a small number of ideal point scatterers (as in equation (3.15)), and that polar reformatting has been done exactly.

The superresolution approach was criticized by Rihaczek in 1981, who pointed out the problems caused by radar targets having many scattering centres which are subject to shadowing and masking, and which interfere with one another [76]. In his reply to a comment by Jackson [49], Rihaczek said [75]

> "If the practical radar task were to generate an image of an array of ideal point scatterers, I might have a different opinion. ...The fact is that the superresolution methods did not fail because of any lack of signal processing techniques; they failed because they were based on models of the target which were simply inadequate for real targets. ...What we really need is improved target models."

This criticism was made in 1981, and the superresolution papers cited above date from 1992 to 1994. They are still using the same simple point scatterer model that Rihaczek called "inadequate", and the results of an extra eleven to thirteen years' research are perhaps best summed up by one sentence from the conclusion of [64]: "At this stage, it is not possible to claim a certain degree of improvement in resolution using the MUSIC algorithm, as opposed to the Fourier transform." This also applies to other modern spectral estimators, so the current verdict on superresolution ISAR must be that it is not yet demonstrably superior to ordinary Fourier processing for real targets under uncontrolled conditions.

4A   Decomposition of a Spherical Wave into Plane Waves

This appendix contains a derivation of the eigendecomposition of a spherical wave into plane waves. This result is well-known in theoretical physics, but it has only recently been used among the signal processing community.

This forms the basis for SAR and ISAR inversions using wavenumber processing. Soumekh's book [84] contains a derivation of this result, but it mixes up the physics and engineering conventions for diverging waves[4] and

---

[4]Physicists use e^{ikx} to represent a wave moving in the $+x$ direction whereas engineers use the conjugate, e^{-jkx}. In equation (4.63), the solution corresponding to the diverging wave

neglects many constants and slowly-varying magnitude functions, making it hard to rederive. To complicate matters, some of his earlier papers on which the book is based, such as [82] and [83], use slightly different derivations which are not easy to follow because of typographical errors and because contour integrals giving integral representations of functions do not have their contours specified.

The decomposition presented here is a rederivation of that in [84] with the approximations clearly stated and all constants and slowly-varying magnitude functions included.

Consider a source at the origin emitting an electromagnetic wave, $\psi(t, \boldsymbol{r})$. This wave diverges from the origin according to the wave equation

$$\nabla^2 \psi(t, \boldsymbol{r}) - \frac{1}{c^2} \psi(t, \boldsymbol{r}) = 0 \tag{4.58}$$

where c is the speed of light. If the wave is harmonic with frequency ω, $\psi(t, \boldsymbol{r})$ may be written

$$\psi(t, \boldsymbol{r}) = e^{j\omega t} h(\boldsymbol{r}) \tag{4.59}$$

where $h(\boldsymbol{r})$ is the phasor representation of the wave's spatial dependence. Substituting this separable expression for the wave into the wave equation gives $h(\boldsymbol{r})$ as a solution of the homogeneous Hemholtz equation

$$\nabla^2 h(\boldsymbol{r}) + k^2 h(\boldsymbol{r}) = 0 \tag{4.60}$$

where $k = \omega/c$ is the wavenumber. This may be solved for the case of a source at the origin using the Green's function $G(\boldsymbol{r})$ [58, Ch. 7], which is a solution of the inhomogeneous Hemholtz equation

$$\nabla^2 G(\boldsymbol{r}) + k^2 G(\boldsymbol{r}) = -4\pi \delta(\boldsymbol{r}) \tag{4.61}$$

The solutions of this corresponding to outward-moving waves are, in three dimensions, a spherical wave

$$G_3(\boldsymbol{r}) = \frac{e^{-jk|\boldsymbol{r}|}}{|\boldsymbol{r}|} \tag{4.62}$$

and in two dimensions, a Hankel function with circular symmetry

$$G_2(\boldsymbol{r}) = -j\pi H_0^{(2)}(k\,|\boldsymbol{r}|) \tag{4.63}$$

where the Hankel function $H_\nu^{(2)}(z)$ is a solution to

$$z^2 \frac{d^2 w}{dz^2} + z \frac{dw}{dz} + (z^2 - \nu^2)w = 0 \tag{4.64}$$

---

would be $i\pi H_0^{(1)}(kr)$ to a physicist, but its conjugate $-j\pi H_0^{(2)}(kr)$ to an engineer. As well using i rather than j for $\sqrt{-1}$, physicists define Fourier transforms and inverse transforms the oppposite way from engineers.

The two real linearly independent solutions of this are the Bessel functions of the first and second kind, $J_\nu(z)$ and $Y_\nu(z)$. A different set of linearly independent solutions is given by the Hankel functions, $H_\nu(z) = H_\nu^{(1)}(z)$ and $H_\nu^{(2)}(z)$, which are related to $J_\nu(z)$ and $Y_\nu(z)$ by[5] [1]

$$H_\nu^{(1)}(z) = J_\nu(z) + jY_\nu(z) \tag{4.65}$$
$$H_\nu^{(2)}(z) = J_\nu(z) - jY_\nu(z) \tag{4.66}$$

The two-dimensional and three-dimensional Green's functions have asymptotically equal phases but different magnitudes. From equation (9.2.4) of [1]

$$H_0^{(2)}(z) \sim j\sqrt{\frac{2}{\pi z}}\, e^{-jz} \qquad \text{as } |z| \to \infty \tag{4.67}$$

Using this, the two- and three-dimensional Green's functions are asymptotically related by

$$G_3(|\boldsymbol{r}|) \sim \sqrt{\frac{k}{2\pi\,|\boldsymbol{r}|}}\, G_2(|\boldsymbol{r}|) \tag{4.68}$$

as $k\,|\boldsymbol{r}| \to \infty$.

The rationale behind writing the spherical wave as an asymptotic Hankel function is that it is relatively straightforward to derive an integral representation for the Hankel function that is valid in a two-dimensional plane. This integral representation can be used to describe the spherical waves reflected from a radar target because ISAR imaging considers targets to be two-dimensional, lying in a plane parallel to the radar's line-of-sight.

The Fourier transform of the two-dimensional inhomogeneous Hemholtz equation is

$$-(k_x^2 + k_y^2)G_2(\boldsymbol{k}) + k^2 G_2(\boldsymbol{k}) = -4\pi \tag{4.69}$$

where $\boldsymbol{k} = (k_x, k_y)$ are the spatial frequencies that are the Fourier-domain counterparts of $\boldsymbol{r} = (x, y)$, and $G_2(\boldsymbol{r})$ is the inverse Fourier transform of $G(\boldsymbol{k})$

$$G_2(\boldsymbol{r}) = \frac{1}{4\pi^2}\int_{-\infty}^{\infty}\int_{-\infty}^{\infty} G_2(\boldsymbol{k})\, e^{j(xk_x + yk_y)}\, dk_x\, dk_y \tag{4.70}$$

Since (4.69) shows that

$$G_2(\boldsymbol{k}) = \frac{4\pi}{k_x^2 + k_y^2 - k^2} \tag{4.71}$$

the two-dimensional Green's function has the following integral representation (this is similar to (7.2.42) of [58])

$$G_2(|\boldsymbol{r}|) = \frac{1}{\pi}\int_{-\infty}^{\infty}\int_{-\infty}^{\infty} \frac{1}{k_x^2 + k_y^2 - k^2}\, e^{j(xk_x + yk_y)}\, dk_x\, dk_y \tag{4.72}$$

---

[5]This is analogous to the way e^{jx} and e^{-jx} are related to $\sin x$ and $\cos x$.

where $\boldsymbol{r} = (x, y)$.

The double integral may be simplified by evaluating one of the integrals explicitly using contour integration. Then the remaining single integral gives the desired decomposition of a spherical wave into plane waves.

The choice of which integral to evaluate depends on where in the (x, y) plane the spherical decomposition is to be used. If the spherical wave is measured at a point where $|x| \gg 0$, the contour integration may be performed with respect to k_x. If the spherical wave is measured at a point where $|y| \gg 0$, the contour integration may be performed with respect to k_y. Since the ISAR imaging geometry in figure 4.3 assumes that the radar is far from the target in the positive y direction, the contour integral will be performed here with respect to k_y.

The inner integral has poles at $k_y = \pm\sqrt{k^2 - k_x^2}$. Integrating over a contour including only the singularity at $k_y = +\sqrt{k^2 - k_x^2}$ gives a wave that is converging when $y > 0$ and diverging when $y < 0$. Integrating over a contour including only the other singularity at $k_y = -\sqrt{k^2 - k_x^2}$ gives a wave that is converging when $y < 0$ and diverging when $y > 0$. Since the desired solution is wave that diverges when measured in the upper half-plane, only the pole at $k_y = -\sqrt{k^2 - k_x^2}$ should be included in the contour integration. This contour is illustrated in figure 4.6. Using the residue theorem,

$$\int_{-\infty}^{\infty} \frac{1}{k_y^2 - (k^2 - k_x^2)} e^{jyk_y} \, dk_y = 2\pi j \left. \frac{e^{jyk_y}}{k_y - \sqrt{k^2 - k_x^2}} \right|_{k_y = -\sqrt{k^2 - k_x^2}}$$

$$= -j \frac{\pi e^{-jy\sqrt{k^2 - k_x^2}}}{\sqrt{k^2 - k_x^2}} \tag{4.73}$$

Substituting this for the inner integral of the Green's function's integral representation shows that

$$G_2(|\boldsymbol{r}|) = -j \int_{-\infty}^{\infty} \frac{1}{\sqrt{k^2 - k_x^2}} e^{j(xk_x - y\sqrt{k^2 - k_x^2})} \, dk_x \tag{4.74}$$

From the relationship in (4.68), this is also an asymptotic integral representation for $G_3(|r|)$

$$G_3(|\boldsymbol{r}|) \sim -j \sqrt{\frac{k}{2\pi |\boldsymbol{r}|}} \int_{-\infty}^{\infty} \frac{1}{\sqrt{k^2 - k_x^2}} e^{j(xk_x - y\sqrt{k^2 - k_x^2})} \, dk_x \tag{4.75}$$

Since $\sqrt{k^2 - k_x^2}$ is imaginary for $|k_x| > k$, it makes sense to split the integral representation for $G_3(|r|)$ into an integral for $|k_x| < k$ and an integral for $|k_x| > k$.

Let $I_1(|\boldsymbol{r}|)$ be the integral for $|k_x| < k$ and $I_2(|\boldsymbol{r}|)$ be the integral for $|k_x| > k$. Make the substitution $u = \sqrt{k_x^2 - k^2}$ to show that

$$|I_2(|\boldsymbol{r}|)| = \sqrt{\frac{2k}{\pi \, |\boldsymbol{r}|}} \left| \int_k^\infty \frac{1}{\sqrt{k_x^2 - k^2}} \cos(xk_x) \, e^{-y\sqrt{k_x^2 - k^2}} \, dk_x \right|$$

$$\leq \sqrt{\frac{2}{\pi k \, |\boldsymbol{r}|}} \int_0^\infty e^{-yu} \, du$$

$$= \frac{1}{y} \sqrt{\frac{2}{\pi k \, |\boldsymbol{r}|}} \tag{4.76}$$

This suggests that $|I_2(|\boldsymbol{r}|)|$ falls off faster than $1/y^{3/2}$ whereas $|G_3(|r|)|$ falls off as $1/y$. So for measurements made far from the origin in the y direction, $I_2(|\boldsymbol{r}|)$ is negligible in comparison to $I_1(|\boldsymbol{r}|)$. Kak says that $I_2(|\boldsymbol{r}|)$ is an evanescent component which is usually of no signficance more than ten wavelengths from the source [41, p. 367]. Since radar targets are often thousands of times further from the antenna than this, this justifies tightening the limits of integration from $(-\infty, \infty)$ to $(-k, k)$.

Therefore the decomposition of a spherical wave into plane waves useful for ISAR imaging is

$$\frac{e^{-jk|\boldsymbol{r}|}}{|\boldsymbol{r}|} = G_3(|\boldsymbol{r}|) \sim -j\sqrt{\frac{k}{2\pi \, |\boldsymbol{r}|}} \int_{-k}^k \frac{1}{\sqrt{k^2 - k_x^2}} \, e^{j(xk_x - y\sqrt{k^2 - k_x^2})} \, dk_x \tag{4.77}$$

which is valid if the radar's y coordinate is much greater than the target's greatest y coordinate. This can be made slightly neater by changing the sign of k_x giving the final form of the plane wave decomposition

$$\frac{e^{-jk|\boldsymbol{r}|}}{|\boldsymbol{r}|} \sim -j\sqrt{\frac{k}{2\pi \, |\boldsymbol{r}|}} \int_{-k}^k \frac{1}{\sqrt{k^2 - k_x^2}} \, e^{-j(xk_x + y\sqrt{k^2 - k_x^2})} \, dk_x \tag{4.78}$$

A slightly different derivation[6]is presented in appendix A of Soumekh's 1991 paper [82] using an integral representation of the Hankel function of

---

[6]The decomposition in [82] is hard to follow because the slowly changing amplitude functions and constants are omitted throughout, factors of $\frac{1}{2}$ are written as .5 to give terms like $j.5\phi$, and all paths in the contour integrals have been left out. Furthermore, in his 1992 paper [83], this derivation is repeated with a typographical error which renders $jkr\cos\phi + j\frac{1}{2}\phi$ as $jkr \cdot \cos\phi + j \cdot 5\phi$, where the first "·" is a multiplication sign and the second "·" is the decimal point in 0.5 with the zero omitted.

To make matters worse, the source for equation (2) of [83] is quoted as equation (5.3.89) of the 1968 edition of Morse and Feshbach [58, 59]. However, there is no 1968 edition of Morse and Feshbach, only the original 1953 edition. Equation (5.3.89) in the 1953 edition is an integral equation of the Mathieu function $Se_{2m}(z, q)$, and has no relevance for Hankel functions. Perhaps the (5.3.89) should read (5.3.69), an equation which is relevant. If so, the 1968 is a mistake and should be corrected in [82] and [85] as well as [83]. Alternatively, if the 1968 is correct, the references may mean Morse and Ingard's *Theoretical Acoustics*, instead of Morse and Feshbach, in which case, equation (5.3.89) may actually be relevant.

Figure 4.6: This indicates the contour in complex k_y-space the integral in equation (4.73) must take to give the solution in the half-plane $y > 0$ corresponding to an outwardly propagating wave.
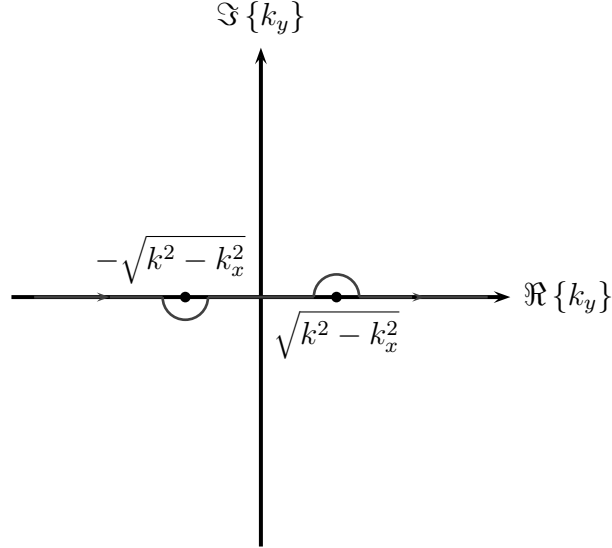
order $\frac{1}{2}$ because of the exact relationship

$$\frac{e^{jk|\boldsymbol{r}|}}{|\boldsymbol{r}|} = jkh_0(k\,|\boldsymbol{r}|) = j\sqrt{\frac{\pi k}{2\,|\boldsymbol{r}|}}H_{\frac{1}{2}}(k\,|\boldsymbol{r}|) \tag{4.79}$$

4B The Doppler-Shift Formulation of ISAR

Many early papers about ISAR describe scatterers being resolved in cross-range due to differences in the Doppler shifts of their reflections. This description is intuitively appealing, but completely incorrect because it is the change in the scatterer's position that alters the round-trip distance and is manifested as a phase shift. The radial velocity of each scatterer does cause a Doppler shift, but as discussed in section 3.5.1, the Doppler shift is usually negligible.

This appendix has been included for completeness, not because it correctly describes ISAR. With this disclaimer in mind, here is an historically accurate but technically incorrect description of ISAR cross-range processing using the Doppler shift. The treatment follows Wehner [98], and is very similar to the 1969 paper by Brown [16] and the 1980 work of Chen and Andrews [19].

4B.1   Cross-Range Processing

Consider a target a fixed distance r_0 from the radar rotating at constant angular speed ω at time $t = 0$, as shown in figure 4.1 on page 42. The scatterer at a distance x in cross-range from the target's centre of rotation is moving directly towards the radar with instantaneous speed

$$v(x) = \omega x \tag{4.80}$$

For a radar transmitting at a frequency f_0, the reflection has a Doppler frequency shift f_D directly proportional to the scatterer's cross-range position

$$f_D(x) = \frac{2 f_0}{c} v(x) = x \frac{2 \omega f_0}{c} \tag{4.81}$$

If two scatterers the same range from the radar are separated by d in cross-range, their Doppler frequencies differ by

$$\Delta f_D = d \frac{2 \omega f_0}{c} \tag{4.82}$$

The target's reflections are sampled for a total time T, called the coherent Doppler integration time, and the different Doppler frequencies are detected using a Fourier transform. Close scatterers are resolvable if the difference in their Doppler shifts is greater than the resolution of the Fourier transform

$$\Delta f_D \geq \frac{1}{T} \tag{4.83}$$

Combining this with (4.82) and writing the cross-range resolution Δr_c for d shows that

$$\Delta r_c = \frac{c}{2 f_0 \omega T} \tag{4.84}$$

which is the same as the approximate expression in equation (4.37).

4B.2   Resolution Restrictions

The Doppler-shift analysis assumes that each scatterer can be found in the same range cell for the whole of the Doppler integration time. For large targets or rapidly rotating targets, this may not be so. If a scatterer spends only a fraction of the Doppler integration time in a range cell, the cross-range resolution of that scatterer in that range cell will be decreased accordingly.

Blurring in the final ISAR image depends on the number of range and cross-range cells that each scatterer moves through. Suppose the target's size is D_r in the range direction and D_c in the cross-range direction. If no

scatterer is allowed to move through more than one range cell, the total angle through which the target rotates, $\Delta\theta$, must satisfy

$$\frac{D_c}{2}\Delta\theta < \Delta r_r \qquad (4.85)$$

Using $\Delta\theta = \omega T$ and $\lambda = c/f_0$ shows that this is equivalent to the condition

$$\Delta r_r \Delta r_c > \frac{\lambda D_c}{4} \qquad (4.86)$$

If no scatterer is allowed to move through more than one cross-range cell, $\Delta\theta$ must satisfy

$$\frac{D_r}{2}\Delta\theta < \Delta r_c \qquad (4.87)$$

which is equivalent to the condition

$$\Delta r_c^2 > \frac{\lambda D_r}{4} \qquad (4.88)$$

Chapter 5

Motion Estimation and Motion Compensation

Since the target's motion creates the synthetic aperture in ISAR imaging, a high cross-range resolution can only be obtained if the position and orientation of the target matches that assumed by the ISAR inversion algorithm. Furthermore, the ISAR inversion can be implemented efficiently only if the target moves in one of two basic ways; either rotating with uniform angular velocity a fixed distance from the radar, or moving along a straight line at constant speed. If the target deviates by even a small fraction of a wavelength from its presumed position, the ISAR image becomes badly blurred in the cross-range direction.

Consequently, the first and most delicate part of ISAR imaging is motion estimation, the process of measuring the target's position and orientation at all times from its radar reflections. Once the inversion algorithm has been chosen, motion compensation is performed. This adjusts the radar measurements to compensate for deviations from the target's presumed location and aspect angle. Finally, the compensated radar measurements match those expected by the ISAR inversion algorithm and the ISAR image can be formed.

In this chapter, these ideas about motion estimation and motion compensation are explored in detail. After describing how to apply motion compensation to correct for deviations in the target's range and aspect angle, various methods of motion estimation suitable for ISAR are discussed.

In chapter 6, a general model for radial motion estimation is developed and this is used to find the maximum likelihood solution of the ISAR motion estimation problem. After chapter 7 constructs efficient algorithms for evaluating the maximum likelihood motion estimator, and chapter 8 analyses the estimator's statistical properties, chapter 9 shows how some of the radial motion estimators in this chapter are related to the maximum likelihood radial

motion estimator.

5.1 Motion Errors

When an ISAR inversion algorithm estimates a target's spatial radar reflectivity, $g(x, y)$, from a set of radar measurements

$$s(k_n, t_m) \quad \text{for } n = 0, 1, \ldots, N - 1 \text{ and } m = 0, 1, \ldots, M - 1 \tag{5.1}$$

the measurements are related to the target's unknown reflectivity $g(x, y)$ according to the model in equation (4.4)

$$s(k, t) = \iint g(x, y) \, e^{-jkr_{xy}(t)} \, dx \, dy \tag{5.2}$$

where $r_{xy}(t)$ is the distance between a scatterer at (x, y) on the target and the radar at time t. The inversion algorithm assumes a certain form for $r_{xy}(t)$, and if the target's motion deviates from this, the resulting ISAR image will be blurred.

If at time t, the target's centre is located a radial distance $r(t)$ from the radar and is oriented so that its x axis is at an angle $\theta(t)$ to the line between the target and the radar antenna, $r_{xy}(t)$ is

$$r_{xy}(t) = \sqrt{(r(t) + x \cos \theta(t) - y \sin \theta(t))^2 + (x \sin \theta(t) + y \cos \theta(t))^2} \tag{5.3}$$

This shows that $r(t)$ and $\theta(t)$ are the important factors in ensuring that the target's motion corresponds to the model.

Suppose an ISAR inversion algorithm requires a target moving in such a way that its radial position and orientation are $r_0(t)$ and $\theta_0(t)$ respectively. But as the target may be moving slightly differently, its actual radial position and orientation are given by the functions $r(t)$ and $\theta(t)$.

The problem now is to estimate $r(t)$ and $\theta(t)$ sufficiently accurately that $r_{xy}(t)$, the range of any point on the target at any time, can be calculated with an accuracy of a fraction of a wavelength, and then to adjust the radar measurements to account for any differences between $r(t)$ and $r_0(t)$ and between $\theta(t)$ and $\theta_0(t)$.

The second part of this problem, that of motion compensation, is discussed first because it is considerably simpler than motion estimation.

5.2 Motion Compensation

Motion compensation has to adjust the radar measurements $s(k, t)$ to compensate for the target being a distance $r(t)$ from the radar when it should be

a distance $r_0(t)$ away, and having an orientation $\theta(t)$ rather than the $\theta_0(t)$ expected by the inversion algorithm.

The corrections are made in two stages; first radial motion compensation is used to correct for deviations in the target's range, then angular motion compensation is used to correct for deviations in the target's aspect angle.[1]

For radar imaging at X-band, radial motion compensation is mandatory because a moving target's range is almost guaranteed to deviate from the ideal by more than $\lambda/10 = 3$ mm. Angular motion compensation will probably not be necessary if the target is small and the ISAR image has a low enough cross-range resolution that polar reformatting can be left out of the inversion algorithm. This is fortunate because radial motion affects the whole target in the same way and is comparatively easy to estimate. On the other hand, the target's angular motion affects different parts of the target in different ways and is much harder to estimate.

5.2.1 Radial Compensation

At first glance, $r_{xy}(t)$ in (5.3) is a complicated function of $r(t)$ and $\theta(t)$, so correcting deviations from both $r_0(t)$ and $\theta_0(t)$ appears very difficult. However, using the simple assumptions that the size of the target is small in comparison to its range

$$\sqrt{x^2 + y^2} \ll r(t) \tag{5.4}$$

and that deviations from the assumed radial position are also relatively small

$$|r_0(t) - r(t)| \ll r_0(t) \tag{5.5}$$

the range to a scatterer at (x, y) can be written in terms of $r_0(t)$

$$
\begin{aligned}
r_{xy}(t) &= \sqrt{(r(t) + x\cos\theta(t) - y\sin\theta(t))^2 + (x\sin\theta(t) + y\cos\theta(t))^2} \\
&\approx [r(t) - r_0(t)] \\
&\quad + \sqrt{(r_0(t) + x\cos\theta(t) - y\sin\theta(t))^2 + (x\sin\theta(t) + y\cos\theta(t))^2}
\end{aligned}
\tag{5.6}
$$

This means that when the target moves a small radial distance, the ranges of all points on the target change by the same amount.

---

[1]Sometimes these stages are called translational motion compensation (TMC) and rotational motion compensation (RMC) [14]. These names are slightly misleading when the target is moving in a straight line at constant speed because a deviation in the target's translational motion changes both its range and aspect angle. TMC corrects errors in the target's range and RMC corrects errors in the target's aspect angle. However TMC's name suggests that it can correct errors in the target's translational motion, which involves corrections both in range and in aspect angle.

Since the reflection from a scatterer at (x, y) undergoes a phase change of $-kr_{xy}(t)$, a radial deviation of

$$\Delta r(t) = r(t) - r_0(t) \tag{5.7}$$

causes an extra phase shift of $-k\Delta r(t)$. This phase error is common to the reflections from all scatterers on the target, so the measurement $s(k, t)$ at frequency k has suffered an additional phase shift of $-k\Delta r(t)$. This can be corrected by multiplying $s(k, t)$ by $e^{jk\Delta r(t)}$ to give

$$s'(k, t) = e^{jk\Delta r(t)} s(k, t) \tag{5.8}$$

where $s'(k, t)$ is $s(k, t)$ with radial motion compensation applied.

5.2.2   Angular Compensation

Once radial motion compensation has been applied to the radar measurements, they have to be corrected for deviations in the target's aspect angle. The measurement $s(k, t)$ with radial motion compensation applied, $s'(k, t)$, is given by

$$s'(k, t) = \iint g(x, y) e^{-jkr'_{xy}(t)} dx \, dy \tag{5.9}$$

where $r'_{xy}(t)$ is r_{xy} with radial motion compensation

$$
\begin{aligned}
r'_{xy}(t) &= r_{xy}(t) - \Delta r(t) \\
&= \sqrt{(r_0(t) + x\cos\theta(t) - y\sin\theta(t))^2 + (x\sin\theta(t) + y\sin\theta(t))^2}
\end{aligned} \tag{5.10}
$$

Correcting the measurements so that the target's actual aspect angle $\theta(t)$ in (5.10) becomes the presumed aspect angle $\theta_0(t)$ is more complicated because the dependence of $r'_{xy}(t)$ on $\theta(t)$ varies with x and y.

The only way of rotating the target so that its aspect angle changes from $\theta(t)$ to $\theta_0(t)$ is to warp the time axis. Then when the inversion algorithm requires the target's frequency response at time t, the actual frequency response used is $s'(k, t')$ where the target's aspect angle at t' is equal to the desired aspect angle at time t

$$\theta(t') = \theta_0(t) \tag{5.11}$$

So t' is related to t by a function $t' = \tau(t)$ which accomplishes the time-warping

$$\tau(t) = \theta^{-1}(\theta_0(t)) \tag{5.12}$$

Therefore the radar measurements with both radial and angular motion compensation are

$$s_0(k, t) = s'(k, \tau(t)) \tag{5.13}$$

Since the radar measurements $s(k,t)$ are only made at discrete times t_m, the radially-compensated measurements $s'(k,t_m)$ generally have to be resampled in the time domain to give the fully motion-compensated $s_0(k,t)$.

For range-Doppler ISAR inversions, the angular coordinate of $s'(k,t)$ in (k_x, k_y)-space is given by the orientation of the target at time t. Therefore angular motion compensation is the same as moving the angular coordinates of each measurement $s'(k,t)$ by $\theta_0(t) - \theta(t)$. This shows that angular motion compensation and polar reformatting are very similar operations, so they can be performed together during the polar reformatting stage of range-Doppler ISAR inversions.[2]

One slight complication arises from angular motion compensation because radial motion compensation moves $s(k,t)$ to a range of $r_0(t)$. However, angular motion compensation pretends that $s(k,t)$ was actually sampled at time $\tau^{-1}(t)$ so the measurement should have had its range adjusted to $r_0(\tau^{-1}(t))$. When the radial motion compensation's phase correction is combined with angular motion compensation's time-warping, the desired measurements at time t, $s_0(k,t)$, are found from the actual measurements, $s(k,t)$, according to

$$s_0(k,t) = e^{jk\Delta r(t)} s(k, \tau(t)) \tag{5.14}$$

where $\Delta r(t)$ has been modified to take into account the time-warping

$$\Delta r(t) = r(\tau(t)) - r_0(t) \tag{5.15}$$

This complication does not arise when the inversion algorithm presumes that the target is rotating uniformly a fixed distance from the radar, but it is important for the alternative model of a target moving in a straight line at constant speed.

5.3 Motion Estimation in the Range and Frequency Domains

Motion estimation methods are classified as frequency domain or range domain methods depending on whether the target's frequency responses $s(k,t)$ or its range profiles $s(r,t)$ are used. As shown later in this section, range profiles are the inverse Fourier transforms of the frequency responses with respect to k

$$s(r,t) = \mathcal{F}_k^{-1}\{s(k,t)\} \tag{5.16}$$

---

[2]Angular motion compensation must be performed before ISAR inversions using wavenumber processing because step 2 of the wavenumber inversion (algorithm 4.3 on page 52) is a Fourier transform of $s(k,t)$ with respect to time. This requires that the target have the correct orientation $\theta_0(t)$ at each time.

This section introduces the terminology of radial motion estimation and shows how a target's frequency responses and range profiles change as its range from the radar changes. The relationships developed in equations (5.17) and (5.26) are the basis for the radial motion estimation algorithms which are described in detail in section 5.4.

5.3.1   Frequency Domain Motion Estimation

At each one of the M discrete times t_m during the ISAR imaging period $[-T/2, T/2]$, the target's radar reflectivity $s(k_n, t_m)$ is measured at the N frequencies $k_n = 4\pi f_n/c$ in the stepped-frequency waveform. These N measurements, sometimes collectively called a sweep, constitute one sample of the target's frequency response over the frequency range $[k_0, k_{N-1}]$.

The goal of motion estimation is to measure the target's range $r(t)$ during $[-T/2, T/2]$. The target's average range during this period only needs to be known approximately but changes in its range must be known within a small fraction of a wavelength. So any motion estimation method must be capable of estimating changes in range this accurately.

From the discussion of radial motion compensation in section 5.2.1, a measurement $s(k, t)$ has a phase shift $e^{-jk\Delta r}$ if the target moves a radial distance Δr. This phase shift can be used for estimating the radial distance an ISAR target moves over a period of time providing the target rotates a negligible amount during this period.[3] If the moving target is rotating slowly enough,

$$s(k, t_1) \approx e^{-jk[r(t_2)-r(t_1)]} \, s(k, t_2) \tag{5.17}$$

and the target's radial motion can be detected via the phase shift in its frequency responses measured at different times.

Motion estimation methods using the frequency responses like this to measure $r(t_2) - r(t_1)$ are said to be operating in the frequency domain.

5.3.2   Range Domain Motion Estimation

Motion estimation can also be performed using Fourier transforms of the frequency responses and such methods of motion estimation are called range domain methods. This is because the inverse Fourier transform of $s(k, t)$ with respect to k gives $s(r, t)$, a one-dimensional image of the target called a range profile.

Each measurement $s(k, t)$ in the frequency response is related to the target's spatial reflectivity $g(x, y)$ according to equation (4.4), which is an integral representation of $s(k, t)$ in terms of the (x, y) coordinates of scatterers

---

[3]From here until section 10.4, where this assumption is properly tested, the target's rotation will be assumed negligible.

on the target. Radial motion estimation is concerned with the radial position of the target, so $s(k, t)$ is more usefully expressed as an integral over r, the radial distance from the radar

$$s(k, t) = \int g(r, t) e^{-jkr} dr \qquad (5.18)$$

Here $g(r, t)$ is the target's reflectivity at time t as a function of radial position

$$g(r, t) = \iint g(x, y) \, \delta(r_{xy}(t) - r) \, dx \, dy \qquad (5.19)$$

where the delta function $\delta(r_{xy}(t) - r)$ selects those points on the target that are a radial distance r from the radar.

From equation (5.18), $s(k, t)$ is the Fourier transform with respect to r of $g(r, t)$ so $g(r, t)$ can be recovered by taking the inverse Fourier transform with respect to k of the $s(k, t)$. However, $s(k, t)$ is only known for the N discrete frequencies in the stepped-frequency waveform so $s(r, t)$, the inverse Fourier transform of $s(k, t)$, is different from $g(r, t)$.

$$
\begin{aligned}
s(r, t) &= \frac{1}{N} \sum_{n=0}^{N-1} s(k_n, t) \, e^{jk_n r} \\
&= \int g(r', t) \left[\frac{1}{N} \sum_{n=0}^{N-1} e^{jk_n(r - r')} \right] dr' \\
&= \int g(r', t) \, h(r - r') \, dr' \\
&= g(r', t) \star h(r')
\end{aligned}
\qquad (5.20)
$$

which is a convolution with kernel $h(r)$

$$
\begin{aligned}
h(r) &= \frac{1}{N} \sum_{n=0}^{N-1} e^{jk_n r} \\
&= e^{j\bar{k}r} \frac{\sin\left(\dfrac{N\Delta k r}{2}\right)}{N \sin\left(\dfrac{\Delta k r}{2}\right)}
\end{aligned}
\qquad (5.21)
$$

where $\bar{k} = (k_0 + k_{N-1})/2$ is the average frequency of the stepped-frequency waveform. This shows that $s(r, t)$ is $g(r, t)$ smoothed with a resolution equal to the stepped-frequency waveform's range resolution

$$\Delta r_r = \frac{2\pi}{N\Delta k} = \frac{c}{2N\Delta f} \qquad (5.22)$$

For efficiency, range profiles are usually calculated from their corresponding frequency responses using an inverse fast Fourier transform (FFT). This gives $s(r, t)$ sampled at N discrete ranges r_n

$$r_n = r_0 + n\Delta r_r \qquad (5.23)$$

where each discrete range is called a range cell or a range bin. The range profiles $s(r_n, t)$ are cyclic because the FFT on which they are based have a period of $N\Delta r_r = c/2\Delta f$. The length of each range profile is W_r, the length of what is called the range ambiguity window

$$W_r = N\Delta r_r = \frac{c}{2\Delta f} \tag{5.24}$$

because scatterers separated in range by multiples of W_r appear at the same position in the range profile. Because of this, the origin of the range profile r_0 is arbitrary. This usually does not matter because motion estimation and motion compensation are concerned with estimating changes in radial position, not absolute ranges.

This detailed examination of range profiles will now be used to show how range profiles can be used for radial motion estimation. If a target's range changes from $r(t_1)$ to $r(t_2)$ between times t_1 and t_2 respectively, its radial reflectivities at t_1 and t_2 are

$$g(r + r(t_2), t_2) \approx g(r + r(t_1), t_1) \tag{5.25}$$

provided its aspect angle changes by a negligible amount between t_1 and t_2. Therefore, from equation (5.20), the two range profiles $s(r, t_1)$ and $s(r, t_2)$ are related by

$$s(r, t_2) \approx e^{-j\overline{k}[r(t_2)-r(t_1)]} \, s(r - [r(t_2) - r(t_1)], t_1) \tag{5.26}$$

Motion estimation methods based on differences between $s(r, t_1)$ and $s(r, t_2)$ like this are called range domain motion estimators.

5.4   Radial Motion Estimation

This section is a detailed examination of some radial motion estimation algorithms that have been used for ISAR imaging. They are described from the perspective of a stepped-frequency radar, so the measurements for one ISAR image takes the form of M sets of frequency responses, one measured at each of M uniformly spaced times t_m during $[-T/2, T/2]$. Each frequency response contains $s(k_n, t_m)$ sampled at the N frequencies k_n in the stepped-frequency waveform.[4]

None of the methods presented here is designed to estimate changes in a target's radial position with an accuracy better than $\lambda/10$. Generally, radial motion estimators can be divided into coarse estimators, which tend to have an accuracy of one range bin Δr_r, and fine estimators, that are capable of

---

[4]If the radar uses a chirp instead of a stepped-frequency waveform, the measurements consist of M sets of range profiles $s(r_n, t_m)$, where each profile consists of N discrete range bins separated by Δr_r.

measuring the fractional part of the number of wavelengths that the target moves. For reasons that will shortly become apparent, motion compensation using the coarse estimators is often described as range profile alignment and motion compensation using the fine estimators is called phase compensation.

5.4.1 Range Profile Alignment and Phase Compensation

From equation (5.8), the measurement $s(k, t)$ with a radial motion of $\Delta r(t)$ corrected is

$$s'(k, t) = e^{jk\Delta r(t)} s(k, t) \qquad (5.27)$$

When k_n is written as $k_0 + n\Delta k$, this equation becomes

$$s'(k_n, t) = e^{jk_0\Delta r(t)} e^{jn\Delta k\Delta r(t)} s(k_n, t) \qquad (5.28)$$

Since the radar has a small relative bandwidth, $k_0 \gg n\Delta k$ for all frequencies in the stepped-frequency waveform and $e^{jn\Delta k\Delta r(t)}$ varies only a very small amount for $\Delta r(t)$ less than Δr_r, the size of one range bin. On the other hand, $e^{jk_0\Delta r(t)}$ varies rapidly for changes in $\Delta r(t)$ that are less than a wavelength and is only sensitive to $\Delta r(t)$ modulo $\lambda/2$.

This suggests that radial motion estimation needs to be able to estimate changes in the target's position at the scale of a range bin and at the scale of a fraction of a wavelength. If motion compensation leaves a residual motion error that is smaller than a range bin and an exact half-integral multiple of a wavelength, this is probably sufficient for ISAR imaging.[5]

On this basis, most radial motion estimators can be classified as either a method of range profile alignment or a method of phase compensation depending on whether they are accurate to the nearest multiple of a range bin or accurate within a fraction of a wavelength.

Most methods of range profile alignment are unable to use the target's frequency responses directly but convert the frequency responses to range profiles (or if the ISAR uses a chirp instead of a stepped-frequency waveform, the range profiles are obtained directly) and measure the radial motion using

$$|s(r, t_2)| \approx |s(r - \Delta r, t_1)| \qquad (5.29)$$

which is the magnitude of equation (5.26). Therefore the offset between the magnitudes of two range profiles at different times is equal to the radial distance moved by the target. Range profile alignment in the frequency domain is more difficult because $s(k_n, t_1)$ and $s(k_n, t_2)$ differ by $e^{jk_n\Delta r}$. If

---

[5]This assumption, one of the many "self-evident" truths of ISAR imaging, is tested properly in section 10.5.

$\Delta r > \lambda/2$, the phase changes are greater than 2π and cannot be measured without potential ambiguities.

Phase compensation methods can operate equally well in the frequency domain

$$s(k_n, t_2) \approx e^{-jk_n \Delta r} s(k_n, t_1) \tag{5.30}$$

or in the range domain

$$s(r, t_2) \approx e^{-j\bar{k}\Delta r} s(r - \Delta r, t_1) \tag{5.31}$$

because $|s(r - \Delta r, t_1)|$ is approximately equal to $|s(r, t_1)|$ when $\Delta r < \lambda/2 \ll \Delta r_r$.

The following sections analyse two methods of range profile alignment, cross-correlation and image feedback control, and two methods of phase compensation, adaptive beamforming and the phase gradient autofocus.[6]

5.4.2 Cross-Correlation

Cross-correlation is a simple method of estimating the radial offset between range profiles at different times, hence estimating the radial distance that the target moves. This was first used by Chen and Andrews [19] and later by Wehner [98]. They noted that because

$$|s(r, t_2)| \approx |s(r - \Delta r, t_1)| \tag{5.32}$$

Δr could be estimated by cross-correlating the magnitudes of the two range profiles

$$R_{12}(r) = \int |s(r', t_1)| \, |s(r' + r, t_2)| \, dr' \tag{5.33}$$

Then by the Cauchy-Schwartz inequality,

$$R_{12}(r) \leq R_{12}(\Delta r) \tag{5.34}$$

if there is no noise, so the location of the peak of the cross-correlation gives an estimate of Δr.

Since the range profiles are discrete, the cross-correlation is also discrete with a resolution of Δr_r, or one ISAR range bin. The discrete correlation

---

[6]Of course there is also the possibility of ISAR imaging without having to do any motion estimation or motion compensation. Zhao [105] tried ISAR imaging using only the magnitude of the target's frequency response. Certainly this removes the phase shift due to the target's radial motion but it also removes most of the information used to resolve scatterers in the cross-range direction. Zhao's examples were only 8×8 and 16×16 pixels so it is hard to tell anything meaningful from them. However, common sense suggests that it would be more sensible to develop effective motion estimation methods and then use the target's phase information.

is usually implemented as a fast correlation via a fast Fourier transform. The correlations implemented in this way are cyclic, but this is appropriate because the discrete range profiles themselves are cyclic as they have been formed by transforming the target's frequency responses.

The inherent resolution of the correlation is Δr_r because this is the spacing between samples of the discrete range profiles, but interpolation can be used to give estimates of Δr that lie between the discrete points at which the correlation is available. Two methods have been suggested by Xu *et al.* [101, 102, 103]. One is interpolation by padding the range profiles with zeros before applying the fast correlation. Another is to measure the cross-correlation at the discrete range bin where it is maximum, and at the range bins either side of the maximum. By fitting a quadratic curve between the value of the cross-correlation at these three points, the location of the maximum of the quadratic curve can be used as a better estimate of Δr.[7]

Like any method of motion estimation, cross-correlating range profiles has advantages and drawbacks. It is quick and simple and usually works well. However, the amplitude of the response from strong scatterers can vary considerably with time if they are affected by scintillation or their response varies as they move between resolution cells. This may cause the cross-correlation to match a prominant scatterer in one profile with a different prominant scatterer in another profile, giving estimates of Δr with very large errors.

5.4.3 Image Feedback Control

In [89], Steinberg proposed using image feedback control, a combination of motion estimation and motion compensation which uses the sharpness of the resulting radar image as a measure of how well the target's motion has been estimated. Steinberg mentioned a number of techniques that might potentially be useful for ISAR imaging, but concluded that "none has yet been satisfactorily developed for radarlike waveforms."

Bocker *et al.* have proposed a similar method of ISAR motion estimation that uses the quality of the resulting ISAR image to gauge the target's motion [14]. The target is assumed to be moving in such a way that its range can be described by a low-degree polynomial such as

$$r_0(t) = r_0 + v_0 t + \frac{1}{2} a_0 t^2 + \frac{1}{6} j_0 t^3 \tag{5.35}$$

where r_0, v_0 and a_0 are the target's radial position, velocity and acceleration at time $t = 0$. The third derivative of the target's position is given by j_0,

---

[7]It is surprising that the chirp-Z transform (CZT) has not been used to zoom into any portion of the cross-correlation between range profiles. This approach is taken in algorithm 7.3 in chapter 7 to accomplish essentially the same task.

which is sometimes called the jerk component.

Bocker's method tries to find the set of parameters (v_0, a_0, j_0) describing the target's motion by choosing some (v, a, j) and reconstructing the ISAR image using those (v, a, j) as the parameters of the target's motion for motion compensation. The best estimate of the target's motion is found by searching over the three-dimensional (v, a, j) parameter space for the values which give the highest quality ISAR image.

The quality measure used by Bocker was

$$H(v, a, j) = - \iint |\widehat{g}(x, y)|^2 \log |\widehat{g}(x, y)|^2 \, dx \, dy \qquad (5.36)$$

where $\widehat{g}(x, y)$ is the ISAR image of the target reconstructed with the specified velocity, acceleration and jerk. The target's position r_0 cannot be estimated in this way because the quality of the image is independent of its position. The same measure was also used by Flores [32] in an investigation of some of the ideas in Bocker's paper.[8]

While this method of motion estimation seems attractive, it has three serious difficulties:

- The conditions under which the search converges to the correct value of (v, a, j) have not been established. The few examples of motion estimation using entropy methods in the ISAR literature use simple targets composed of a few point scatterers where the target's radial motion is precisely a cubic polynomial.

- Because the multidimensional search through (v, a, j) parameter space requires that an ISAR image be formed and its entropy measured for each estimate, this is a very slow method of motion estimation and motion compensation.

- The algorithm makes no use of the information about the target's radial motion that can be obtained much more efficiently by more direct methods of motion estimation.

In view of these problems, such entropy-based methods are not yet suitable for motion estimation and motion compensation in ISAR imaging.

----

[8]Bocker and Flores call this an entropy-based method, but this is a bit of a misnomer. It is true that (5.36) has the mathematical form for differential entropy

$$H(X, Y) = - \iint f(x, y) \log f(x, y) \, dx \, dy$$

but in this context, $f(x, y)$ is the joint probability density function of the random variables X and Y.

The "entropy" in (5.36) is just one of many non-linear functions that could have been used to measure the ISAR image's quality, where the notion of quality is determined by the particular non-linear function used.

5.4.4 Adaptive Beamforming

Adaptive beamforming is a range-domain method of phase compensation. Using a number of range profiles that have been motion-compensated using some method of range profile alignment, adaptive beamforming can correct for residual radial motions of fractions of a wavelength.

Once the range profiles have been aligned so that the target is at essentially the same radial position in each range profile, the main difference between range profiles is a phase shift due to small residual errors in the target's corrected radial position or due to atmospheric turbulence. From equation (5.26), range profiles at times t_m and $t_{M/2}$ (the range profile at $t_{M/2}$ is used as a reference range profile) differ by a phase shift, ϕ_m, that is common to all pairs of range bins at time t_m

$$s(r_n, t_m) = e^{-j\phi_m} s(r_n, t_{M/2}) \qquad \forall m, n \tag{5.37}$$

Adaptive beamforming measures each ϕ_m by finding a range resolution cell containing a single strong scatterer that can be used as a phase reference. With this reference range bin at r_d, for some $0 \leq d \leq N - 1$, the phase shift of each range profile is estimated using

$$\widehat{\phi}_m = \arg\left(\frac{s(r_d, t_{M/2})}{s(r_d, t_m)}\right) \tag{5.38}$$

Finally, each range profile's phase shift is corrected by multiplying $s(r_n, t_m)$ in each range bin by $e^{-j\widehat{\phi}_m}$ to give

$$s'(r_n, t_m) = e^{-j\widehat{\phi}_m} s(r_n, t_m) \tag{5.39}$$

The particular algorithm described here is that developed by Steinberg [87, 88] for focusing his radio camera [89]. Sometimes the algorithm is called the dominant scatterer algorithm (DSA) because the strongest scatterer is used to establish the phase reference. Sometimes the algorithm is called the minium variance algorithm (MVA) because the range bin containing the dominant scatterer is determined by finding the range bin whose amplitude has the least variance over all range profiles. A similar form of phase compensation using the first strong scatterer, such as an aircraft's leading wingtip, as the phase reference, was described by Chen and Andrews in [19].

A slightly modified dominant scatterer algorithm has been used by Haywood for phase compensation in ISAR imaging [43, 42]. Haywood changed the criterion for finding the range bin containing the dominant scatterer so that it is the range bin with the smallest variance of all range bins whose average amplitudes are above a threshold. The addition of the threshold helps prevent the algorithm from selecting a reference range bin that is not part of the target.

Adaptive beamforming methods of phase compensation are widely used in ISAR imaging, but they do have some drawbacks. One disadvantage is that there is no guarantee that the reference range bin is suitable for use as a phase reference.

A more serious disadvantage of adaptive beamforming is that it assumes that the measured responses in the reference range bin have identical phases in all range profiles. Since the reference range bin is selected because its magnitude has a low variance, the responses in this range bin after beamforming are approximately constant across all range profiles.

Information for the target's cross-range profile is contained in both the phases and the magnitudes of the evolution of each range bin over time. By finding the range bin whose magnitude has the smallest variance, adaptive beamforming selects as its reference the range bin whose magnitude contains the least information. Then by removing all of the phase information in the reference range bin, the result is no variation in phase and minimal variation in magnitude.

When the cross-range profile of the target is formed by taking the Fourier transform of each range bin across all range profiles, the cross-range profile in the reference range bin is nearly a delta function. While adaptive beamforming focusses the rest of the target, it artificially increases the power of the dominant scatterer by suppressing other scatterers in that range bin.[9]

5.4.5   Phase Gradient Autofocus

The phase gradient autofocus (PGA) is an effective method of phase compensation that has been developed for SAR imaging by Eichel, Ghiglia and Jakowatz [25, 26, 50]. It estimates the modulo-2π variation with time of phase errors due to slight residual errors in the corrected position of the SAR antenna.

The basis of the phase gradient autofocus is the observation that if $s_n(t) = s(r_n, t)$ is the time-history of the response in the nth range bin,

$$s_n(t) = e^{j\phi(t)} g_n(t) \tag{5.40}$$

where $\phi(t)$ is the time-varying phase error which affects all range bins in a range profile in the same way. $g_n(t)$ is the range bin's time-history whose Fourier transform gives the cross-range profile $g_n(\omega)$ in the nth range bin

$$g_n(\omega) = \mathcal{F}\{g_n(t)\} \tag{5.41}$$

---

[9]Distortions such as this may unwittingly make adaptive beamforming appear to perform better than it actually does. ISAR images are often displayed with a fixed dynamic range relative to the brightest scatterer in the image. Because adaptive beamforming increases the power of the dominant scatterer, the powers of other scatterers and of the background noise decrease relative to that of the dominant scatterer. This makes the image appear sharper when really it is just being displayed with an offset intensity scale.

If each range bin contains a single point scatterer, then

$$s_n(t) = A_n e^{j\omega_n t} e^{j\phi(t)} \tag{5.42}$$

where A_n is the scatterer's amplitude and ω_n determines its cross-range position. Therefore, the time-derivative of the phase of $s_n(t)$ is

$$\frac{d}{dt} \arg(s_n(t)) = \omega_n + \dot{\phi}(t) \tag{5.43}$$

where $\dot{\phi}(t)$ is the derivative of the phase error. This derivative can be implemented using the identity

$$\frac{d}{dt} \arg(s_n(t)) = \frac{\Im\left\{\dot{s}_n(t)\overline{s_n(t)}\right\}}{|s_n(t)|^2} \tag{5.44}$$

Using this, the non-constant part of (5.44) can be used to estimate $\dot{\phi}(t)$ within a constant. Integrating this gives an estimate of $\phi(t)$ within a linear term

$$\widehat{\phi}(t) = \int \widehat{\dot{\phi}}(t)\, dt \approx \phi(t) + at + b \tag{5.45}$$

The linear term $at+b$ does not affect the SAR image's focus, only its position.

This only uses the information contained in one range bin to estimate $\phi(t)$, so a more accurate estimate can be obtained by using all range bins. From (5.43), the time-derivative of $s_n(t)$ has a constant term of ω_n, which is different for each range bin. These can be removed by preprocessing each $s_n(t)$. First, the scatterer's location is found by forming the cross-range profile (which is slightly blurred due to $\phi(t)$), and the cross-range profile is shifted so that the scatterer is at the origin. When the shifted cross-range profile is transformed back to the time-domain, $s'_n(t)$, the preprocessed $s_n(t)$, is just $s_n(t)$ with the linear shift due to the scatterer at ω_n removed. Thus

$$s'_n(t) = A_n e^{j\phi(t)} \tag{5.46}$$

and $\dot{\phi}(t)$ may be estimated using

$$\frac{d}{dt} \arg(s'_n(t)) = \frac{\sum_n \Im\left\{\dot{s}'_n(t)\overline{s'_n(t)}\right\}}{\sum_n |s'_n(t)|^2} \tag{5.47}$$

The full phase gradient autofocus algorithm is more complicated than this because SAR images contain more than a single scatterer in each range bin. The actual time-history of each range bin is

$$s_n(t) = \sum_p A_{pn} e^{j\omega_{pn} t} e^{j\phi(t)} \tag{5.48}$$

where the scatterers in the range bin at r_n have amplitudes A_{pn} and cross-range positions determined by ω_{pn}. Now the derivative of the argument of $s_n(t)$ is

$$\frac{d}{dt} \arg\left(s_n(t)\right) = \dot{\phi}(t) + \frac{d}{dt} \arg\left(\sum_p A_{pn}e^{j\omega_{pn}t}\right) \qquad (5.49)$$

The second term of this is no longer constant, so it cannot be removed so simply from $\dot{\phi}(t)$. This problem is resolved by preprocessing $s_n(t)$ slightly differently. The cross-range profile is formed and the scatterer with the greatest amplitude is moved to the origin (once again this can only be done approximately because the phase error blurs the cross-range profile). The shifted cross-range profile is windowed so that only the portion of the cross-range profile close to the origin is retained. Finally the windowed and shifted cross-range profile is transformed back to the time domain to give $s'_n(t)$.

The combination of shifting and windowing is the crucial part of this process because this changes the second term of (5.49) to

$$\frac{d}{dt} \arg\left(\sum_{p:|\omega_{pn}-\omega_n|<W} A_{pn}e^{j(\omega_{pn}-\omega_n)t}\right) \qquad (5.50)$$

where ω_n is the cross-range position ω_{pn} of the dominant scatterer in the nth range bin and W is half the width of the window.

The width of the window has to be chosen carefully. If the window is too wide, the estimate of $\dot{\phi}(t)$ will be badly affected by the second term of (5.49). If the window is too narrow, the second term of (5.49) will be small but the high frequency content of $\phi(t)$ will also be lost.

A compromise between using a large and a small window is reached by running the phase gradient autofocus as an iterative algorithm. The window is initially large. At each successive iteration, the size of the window is decreased and the estimate of $\phi(t)$ at that iteration used to correct the phase of the range profiles before the next iteration. Typically five to ten iterations are required to focus the SAR image.

Therefore, the full phase gradient autofocus algorithm is:

Algorithm 5.1 (Phase Gradient Autofocus)
To correct for a phase error $e^{j\phi(t)}$ affecting range profiles $s(r_n,t)$:

1. *Set i, the iteration counter, to 1 and set the initial width of the window W to W_1.*

2. *For each range bin at r_n, take the Fourier transform of $s(r_n,t)$ with respect to t to give the cross-range profile $s(r_n,\omega)$.*

3. *In each range bin, r_n, locate the strongest scatterer at $\omega = \omega_n$ and shift the cross-range profile so that the strongest scatterer is at the origin, giving*

$$s'(r_n, \omega) = s(r_n, \omega - \omega_n) \tag{5.51}$$

4. *Window each $s'(r_n, \omega)$, keeping only the portion of the shifted profile with $|\omega| < W_i$, and transform back to the time domain to give $s'(r_n, t)$.*

5. *Estimate the derivative of the remaining phase error using*

$$\widehat{\dot{\phi}_i}(t) = \frac{\sum_n \Im\left\{\dot{s}'(r_n, t)\overline{s'(r_n, t)}\right\}}{\sum_n |s'(r_n, t)|^2} \tag{5.52}$$

6. *Integrate $\widehat{\dot{\phi}_i}(t)$ and remove any bias or linear trend to give this iteration's estimate of the remaining phase error, $\widehat{\phi_i}(t)$.*

7. *Correct for $\widehat{\phi_i}(t)$ in the range profiles, replacing $s(r_n, t)$ by $e^{-j\widehat{\phi_i}(t)}s(r_n, t)$.*

8. *Decrease the size of the window from W_i to W_{i+1} and, after incrementing i for the next iteration, return to step 2.*

Examples of phase gradient autofocus's performance on SAR data are given in the papers cited earlier and in [96]. These seem to indicate that the phase gradient autofocus works very well for autofocussing SAR images.

The phase gradient autofocus has also been applied to ISAR imaging by Robertson and Munson [78]. Their simulations were of a target composed of a few point scatterers, so the results are not necessarily representative of what would happen with real ISAR data.

The success that phase gradient autofocus has had with SAR suggests that it should be considered for ISAR phase compensation, especially as it does not suffer from some of the distortions that adaptive beamforming introduces.[10]

5.5 Angular Motion Estimation

Angular motion estimation is a much more difficult problem than radial motion estimation because each scatterer's phase history depends on its location within the target as well as the target's overall rotation.

---

[10]It may be that the phase gradient autofocus's shifting and windowing can be left out when applied to ISAR targets because they have a much narrower cross-range extent than the cross-range extent of a SAR image. This and many other questions about the statistical performance and robustness of the phase gradient autofocus can only be answered by a rigorous mathematical analysis, something that is currently lacking.

In [100], Werness *et al.* propose an algorithm for imaging moving targets in SAR data. This involves tracking three point scatterers on the target. The first point scatterer is used to compensate for the target's radial motion, the second point scatterer is used to detect deviations from uniform rotation and the third point scatterer is used to estimate the angular velocity to set the cross-range scaling for the whole image.

While this is a nice idea, the examples in [100] were of very simple simulated point scatterers which indicate little about how the algorithm would perform with real radar data. In [24], Delisle and Wu comment that "selection of multiple reference points and evaluation of the quadratic phase component are difficult in practice because of the target's scintillation, clutter and trajectory perturbations."

A simpler problem than complete angular motion estimation is the fitting of a low-degree polynomial

$$\theta(t) = \omega t + \frac{\alpha t^2}{2} \tag{5.53}$$

to the target's aspect angle over time. Bocker *et al.* [14] proposed a multidimensional search over the two-dimensional (ω, α) parameter space that is essentially the same as their entropy method of image feedback control for radial motion estimation. By measuring the sharpness of the reconstructed ISAR image for each value of (ω, α), the best estimate of the target's rotational motion is given by the image with the least blurring. A simplification of Bocker's idea has been experimentally tested by Flores, who tried to estimate ω for a target composed of three aluminimum cylinders rotating at a known angular velocity [32]. Flores' results indicate that for this simple target under very controlled conditions, the rotation rate could be measured accurately.

Chuang and Huang [20] used a similar scheme to estimate ω by comparing tomographic inversions with different assumed rotation rates. They reasoned that the image reconstructed with the correct value of ω should have minimum variance. Since their experimental results consisted of simulations involving a single point scatterer in no noise, few conclusions can be drawn from it.

The difficulty of angular motion estimation is indicated by the fact that no results have been published for angular motion estimation for real targets under uncontrolled conditions.

Since the subject of this thesis is radial motion estimation rather than angular motion estimation, because angular motion estimation is of secondary importance to radial motion estimation in ISAR, and because no demonstrably successful angular motion estimators have been published in the unclassified literature, none of the angular motion estimators mentioned above will be discussed in detail.

Chapter 6

Maximum Likelihood Motion Estimation

Chapter 5 introduced a number of methods for estimating the radial motion of a target during ISAR imaging. Each measured changes in the target's frequency responses or range profiles in different ways, and each justified their derivation on different intuitive grounds.

This chapter does not present another *ad hoc* method of radial motion estimation. Rather it uses the full machinery of statistical estimation theory to derive the maximum likelihood estimator $\widehat{r}_{ml}$ of the radial distance Δr the target moves between two times at which its frequency response is sampled.

The maximum likelihood estimator is obtained in two different ways. The first approach assumes that Δr is the only unknown parameter, so the scalar form of the maximum likelihood estimator is used to obtain $\widehat{r}_{ml}$. The second approach uses the vector form of the maximum likelihood estimator to estimate the value of a vector $\boldsymbol{\theta}$ of unknown parameters which includes Δr along with the measurement noise's variance σ_w^2 and the target's frequency response.

Both approaches give the maximum likelihood estimate of Δr in the form of a cost function $J(r)$ which is minimized when $r = \widehat{r}_{ml}$. The cost function is analysed and the properties that make it suitable for motion estimation for ISAR imaging are discussed.

Efficient methods of finding the minimum of $J(r)$ are the subject of chapter 7 and the statistical properties of $\widehat{r}_{ml}$ are discussed in chapter 8. Finally, in chapter 9, some of the *ad hoc* motion estimators from chapter 5 are reappraised in the light of the maximum likelihood solution.

6.1   The Motion Estimation Model

The first step towards deriving any estimator involves writing down a mathematical model expressing the relationship between the measurements and the unknown parameters on which the measurements depend.

For ISAR motion estimation, the unknown parameter of most interest is the radial change in the target's position at each discrete time step during the ISAR imaging period. If the solution has to allow for a target moving in a totally arbitrary way, the fundamental problem is one of estimating a target's radial movement between any two times at which its frequency response has been measured. After briefly discussing the set of measurements for a whole ISAR image, a model for this more fundamental problem will be constructed.

6.1.1   A Model for a Whole ISAR Image

For stepped-frequency ISAR imaging, the measurements x consist of the target's frequency responses sampled at M evenly spaced times t_m during the imaging period of $[-T/2, T/2]$

$$t_m = t_0 + m\Delta t \qquad \text{for } m = 0, 1, \ldots, M-1 \tag{6.1}$$

where $t_0 = -T/2$ and $t_{M-1} = T/2$. Each frequency response at time t_m is composed of samples of the target's radar reflectivity $s(k_n, t_m)$ at the N discrete frequencies k_n in the stepped-frequency waveform

$$k_n = k_0 + n\Delta k \qquad \text{for } n = 0, 1, \ldots, N-1 \tag{6.2}$$

As in chapters 3 to 5, the k_n are really twice the wavenumber, so that $k_n = 4\pi f_n/c$ where

$$f_n = f_0 + n\Delta f \tag{6.3}$$

For convenience, the single word "frequency" is often used to refer to both f and to $k = 4\pi f/c$; the difference, if it is important, is indicated by the context.

Using the notation and the results of chapter 5, the full ISAR motion estimation problem is to estimate the change in radial position

$$\Delta r(t_m) = r(t_m) - r(t_0) \tag{6.4}$$

of a moving target for all M time steps using only the radar measurements

$$s_{mn} = s(k_n, t_m) + w_{mn} \tag{6.5}$$

where $s(k_n, t_m)$ is the target's frequency response at time t_m and frequency k_n, and w_{mn} is the measurement noise affecting s_{mn}. The target is assumed

to be rotating sufficiently slowly[1] during the ISAR imaging period that any two samples at the same frequency of $s(k_n, t_m)$ from different times, t_m and $t_{m'}$, are related by a phase shift depending on the radial distance moved by the target between these times

$$s(k_n, t_m) = e^{-jk_n(r(t_m) - r(t_{m'}))} s(k_n, t_{m'}) \tag{6.6}$$

6.1.2 The Fundamental Motion Estimation Problem

As mentioned at the start of this chapter, the fundamental problem of ISAR radial motion estimation is finding the radial distance Δr moved by a target between two times at which the target's frequency response is measured.

Suppose the target rotates a negligible amount between two times $t = 0$ and $t = T$.[2] Then any change in its frequency response is directly attributable to the radial distance Δr moved by the target. Using this model, the measurements of the target's frequency responses at times $t = 0$ and $t = T$ are

$$\begin{aligned} a_n &= s_n + w_{1,n} \\ b_n &= s_n e^{-jk_n \Delta r} + w_{2,n} \end{aligned} \tag{6.7}$$

respectively where s_n is the target's complex frequency response at frequency k_n, the nth frequency in the stepped-frequency waveform. The phase shifts in the measurements of b_n at time $t = T$ are proportional to Δr, the unknown distance the target moved during this interval. $w_{1,n}$ and $w_{2,n}$ are measurement noise terms that are assumed to be independent and identically distributed zero-mean complex Gaussian random processes with variance σ_w^2

$$\mathrm{E}\left\{w_{1,n}\overline{w_{1,n}}\right\} = \mathrm{E}\left\{w_{2,n}\overline{w_{2,n}}\right\} = \sigma_w^2 \tag{6.8}$$

Therefore the complete data set available for estimating Δr is the set of N pairs of frequency responses

$$\boldsymbol{x} = \{a_n, b_n \mid n = 0, 1, \ldots, N - 1\} \tag{6.9}$$

where a_n and b_n are the target's noisy frequency responses at times $t = 0$ and $t = T$ respectively, as given in equation (6.7). In practice, the frequencies at which the a_n and b_n are measured are uniformly spaced so that $k_n = k_0 + n\Delta k$, but this is not a necessary condition for deriving the maximum likelihood estimator of Δr.

---

[1]This assumption is questioned in section 10.4.

[2]From here to the end of chapter 8, T will be generally be used to represent the time between the two frequency responses, not the ISAR imaging period. This saves introducing yet another symbol.

Now that the measurement model in (6.7) and the measurement vector $\boldsymbol{x}$ in (6.9) have been defined, maximum likelihood estimation can be used to find the maximum likelihood estimate $\hat{r}_{ml}$ of the unknown radial distance Δr that the target has moved between $t = 0$ and $t = T$.

6.2   Estimating Δr Only

The model in (6.7) has $N + 1$ unknown parameters, the target's radial displacement Δr and the target's reflectivities s_n at each of the N frequencies in the stepped-frequency waveform. By combining the two measurement equations at each frequency to eliminate s_n,

$$w_{2,n} = b_n - (a_n - w_{1,n})e^{-jk_n\Delta r} \tag{6.10}$$

which now only contains one unknown parameter, namely Δr.

Following the description of maximum likelihood estimation in chapter 2, the maximum likelihood estimate $\hat{r}_{ml}$ of Δr is the value of Δr which maximizes the likelihood function $p(\boldsymbol{x}; \Delta r)$, the probability density function of observing the measurements $\boldsymbol{x}$ conditional on the value of the unknown parameter Δr.

Since noise in the measurements at each of the N frequencies is independent, the N pairs of measurements are themselves independent and

$$p(\boldsymbol{x}; \Delta r) = \prod_{n=0}^{N-1} p(a_n, b_n; \Delta r) \tag{6.11}$$

The individual likelihood functions $p(a_n, b_n; \Delta r)$ can be calculated from the probability density function of the two complex noise processes $w_{1,n}$ and $w_{2,n}$

$$p_{w_{1,n}}(z) = p_{w_{2,n}}(z) = \frac{1}{\pi\sigma_w^2}\, e^{-|z|^2/\sigma_w^2} \tag{6.12}$$

by noting that $p(a_n, b_n; \Delta r)$ is the convolution

$$p(a_n, b_n; \Delta r) = \int_{\mathcal{C}} p_{w_{1,n}}(z) \cdot p_{w_{2,n}}\left(b_n - (a_n - z)e^{-jk_n\Delta r}\right)\, dz \tag{6.13}$$

where the subscript $\mathcal{C}$ on the integral sign indicates that the integral is evaluated over the whole complex plane. Then substituting in the probability density functions of $w_{1,n}$ and $w_{2,n}$ and using the identity

$$|u|^2 + |v|^2 = \frac{1}{2}\left(|u - v|^2 + |u + v|^2\right) \tag{6.14}$$

the likelihood function $p(a_n, b_n; \Delta r)$ is

$$
\begin{aligned}
p(a_n, b_n; \Delta r) &= \frac{1}{(\pi \sigma_w^2)^2} \int_{\mathcal{C}} e^{-|z|^2/\sigma_w^2} e^{-\left|b_n - (a_n - z)e^{-jk_n \Delta r}\right|^2/\sigma_w^2} \, dz \\
&= \frac{1}{\pi \sigma_w^2} e^{-\left|a_n - b_n e^{jk_n \Delta r}\right|^2/2\sigma_w^2} \cdot \frac{1}{\pi \sigma_w^2} \int_{\mathcal{C}} e^{-\left|2z - (a_n - b_n e^{jk_n \Delta r})\right|^2/2\sigma_w^2} \, dz \\
&= \frac{2}{\pi \sigma_w^2} e^{-\left|a_n - b_n e^{jk_n \Delta r}\right|^2/2\sigma_w^2}
\end{aligned}
\tag{6.15}
$$

Applying this result to (6.11) gives the likelihood function for all N pairs of measurements

$$
\begin{aligned}
p(\boldsymbol{x}; \Delta r) &= \prod_{n=0}^{N-1} p(a_n, b_n; \Delta r) \\
&= \prod_{n=0}^{N-1} \frac{2}{\pi \sigma_w^2} e^{-\left|a_n - b_n e^{jk_n \Delta r}\right|^2/2\sigma_w^2} \\
&= \frac{2^N}{(\pi \sigma_w^2)^N} \exp\left(-\frac{1}{2\sigma_w^2} \sum_{n=0}^{N-1} \left|a_n - b_n e^{jk_n \Delta r}\right|^2\right) \\
&= \frac{2^N}{(\pi \sigma_w^2)^N} \exp\left(-\frac{1}{2\sigma_w^2} J(\Delta r)\right)
\end{aligned}
\tag{6.16}
$$

where the cost function $J(r)$ is

$$
J(r) = \sum_{n=0}^{N-1} \left|a_n - b_n e^{jk_n r}\right|^2
\tag{6.17}
$$

Since (6.16) shows that $p(\boldsymbol{x}; \Delta r)$ is a monotonically decreasing function of $J(r)$, the local maxima of $p(\boldsymbol{x}; \Delta r)$ are the local minima of $J(r)$ and the global maximum of $p(\boldsymbol{x}; \Delta r)$ is the global minimum of $J(r)$. Therefore a necessary and sufficient condition for the existence of a maximum likelihood estimator of Δr is a unique global minimum of $J(r)$. A proof of the uniqueness of the global maximum of $J(r)$ is given in section 6.4.2, so the maximum likelihood estimator $\widehat{r}_{ml}$ exists and is given by

$$
\widehat{r}_{ml} = \arg \min_r J(r)
\tag{6.18}
$$

6.3 Estimating All Parameters

The maximum likelihood derivation of the previous section assumed that Δr was the only unknown parameter. However this is an oversimplification of the model because the target's frequency responses s_n are always unknown and the noise variance σ_w^2 is normally unknown or has been estimated from

the radar data. It is not apparent that it is legitimate to eliminate the s_n as in equation (6.10) and assume that σ_w^2 is known when deriving $\widehat{r}_{ml}$. It is even less apparent that this is valid when analysing the statistical performance of $\widehat{r}_{ml}$, such as while calculating the Cramér-Rao bound.

The correct technique is to treat all unknown parameters as components of a vector of parameters to be estimated, and apply the vector form of maximum likelihood estimation. In this case, the column vector of unknown parameters is

$$\boldsymbol{\theta} = \left[\sigma_w^2, \Delta r, s_0, s_1, \ldots, s_{N-1}\right]^T \tag{6.19}$$

where σ_w^2 and Δr are real and the s_n are complex.

Solving the vector likelihood equations shows that the maximum likelihood estimator of Δr is the same as the expression obtained in equation (6.18) when Δr was considered the only unknown. An obvious question to ask is "why should the vector maximum likelihood estimator be used when the two methods of estimating Δr produce the same answer?" Three reasons why the vector estimator should be used are:

- Maximum likelihood estimation demands that the likelihood equations maximizing $p(\boldsymbol{x}; \boldsymbol{\theta})$ with respect to each θ_i in $\boldsymbol{\theta}$ be solved simultaneously. Solving just one of the likelihood equations (which is what the scalar unknown case does) does not guaranteed that the others are also solved.

- Finding the maximum likelihood estimates of σ_w^2 and s_n gives expressions that are useful in their own right.

- The vector and the scalar maximum likelihood estimators may have different statistical properties even though the estimator of Δr is the same in both cases. In particular the Cramér-Rao bound is higher for the vector estimator than for the scalar estimator.

A little thought shows that the first of these reasons is not entirely valid. This is because if the scalar maximum likelihood estimator can be evaluated, the neglected unknown parameters must have been eliminated. This lack of dependence of the unknown parameter on the other neglected unknown parameters is reflected in the vector case by the likelihood equation for the one unknown parameter from the scalar case becoming decoupled from the likelihood equations for the unknown parameters that were ignored in the scalar case.

The second and third reasons, however, are strong enough to justify the additional complexity of the full multiple-parameter maximum likelihood solution.

6.3.1 The Vector Maximum Likelihood Estimator

The likelihood function for estimating the vector $\boldsymbol{\theta}$ of unknown parameters from the data set $\boldsymbol{x}$ can be broken into the product of N likelihood functions of the form $p(a_n, b_n; \Delta r, s_n, \sigma_w^2)$ because each of the noise terms in (6.7) is independent. Then

$$p(\boldsymbol{x}; \boldsymbol{\theta}) = \prod_{n=0}^{N-1} p(a_n, b_n; \Delta r, s_n, \sigma_w^2) \tag{6.20}$$

Furthermore, because $w_{1,n}$ and $w_{2,n}$ are independent, $p(a_n, b_n; \Delta r, s_n, \sigma_w^2)$ is the product

$$p(a_n, b_n; \Delta r, s_n, \sigma_w^2) = p(a_n; \Delta r, s_n, \sigma_w^2) \cdot p(b_n; \Delta r, s_n, \sigma_w^2) \tag{6.21}$$

Each of these can be written down in terms of the complex Gaussian probability density function

$$p(a_n; \Delta r, s_n, \sigma_w^2) = \frac{1}{\pi \sigma_w^2} \exp\left(-\frac{1}{\sigma_w^2} |a_n - s_n|^2\right) \tag{6.22}$$

$$p(b_n; \Delta r, s_n, \sigma_w^2) = \frac{1}{\pi \sigma_w^2} \exp\left(-\frac{1}{\sigma_w^2} \left|b_n - s_n e^{-jk_n \Delta r}\right|^2\right) \tag{6.23}$$

Then the likelihood function for frequency k_n is

$$p(a_n, b_n; \Delta r, s_n, \sigma_w^2) = \frac{1}{(\pi \sigma_w^2)^2} \exp\left(-\frac{1}{\sigma_w^2} \left[|a_n - s_n|^2 + \left|b_n - s_n e^{-jk_n \Delta r}\right|^2\right]\right) \tag{6.24}$$

and the likelihood function for all N frequencies is

$$p(\boldsymbol{x}; \boldsymbol{\theta}) = \prod_{n=0}^{N-1} p(a_n, b_n; \boldsymbol{\theta})$$

$$= \frac{1}{(\pi \sigma_w^2)^{2N}} \exp\left(-\frac{1}{\sigma_w^2} \sum_{n=0}^{N-1} |a_n - s_n|^2 + \left|b_n - s_n e^{-jk_n \Delta r}\right|^2\right) \tag{6.25}$$

Since $\ln x$ increases monotonically as x increases, the likelihood function is usually written as the log-likelihood function to remove the exponential

$$\ln p(\boldsymbol{x}; \boldsymbol{\theta}) = -2N \ln\left(\pi \sigma_w^2\right) - \frac{1}{\sigma_w^2} \sum_{n=0}^{N-1} |a_n - s_n|^2 + \left|b_n - s_n e^{-jk_n \Delta r}\right|^2 \tag{6.26}$$

The maximum likelihood estimator $\widehat{\boldsymbol{\theta}}_{ml}$ is the value of $\boldsymbol{\theta}$ which maximizes $\ln p(\boldsymbol{x}; \boldsymbol{\theta})$. This is equivalent to solving the log-likelihood equation

$$\left.\frac{\partial \ln p(\boldsymbol{x}; \boldsymbol{\theta})}{\partial \boldsymbol{\theta}}\right|_{\boldsymbol{\theta} = \widehat{\boldsymbol{\theta}}_{ml}} = 0 \tag{6.27}$$

provided that $\ln p(\boldsymbol{x}|\boldsymbol{\theta})$ has its only local extremum at the global maximum. If there is more than one local extremum, some other information must be available to choose the solution of (6.26) which maximizes $\ln p(\boldsymbol{x}; \boldsymbol{\theta})$.

6.3.2   Finding $\widehat{s}_{n,ml}$

The partial derivative of $\ln p(\boldsymbol{x};\boldsymbol{\theta})$ with respect to s_n, the target's reflectivity at frequency k_n, is

$$\frac{\partial \ln p(\boldsymbol{x};\boldsymbol{\theta})}{\partial s_n} = -\frac{1}{\sigma_w^2}\frac{\partial}{\partial s_n}\sum_{n'=0}^{N-1}\left|a_{n'}-s_{n'}\right|^2+\left|b_{n'}-s_{n'}e^{-jk_{n'}\Delta r}\right|^2 \qquad (6.28)$$

Using the definition of the derivative of a real function of a complex argument in (2.34),

$$\begin{aligned}
\frac{\partial \ln p(\boldsymbol{x};\boldsymbol{\theta})}{\partial s_n} &= -\frac{1}{\sigma_w^2}\frac{\partial}{\partial s_n}\left(\left|a_n-s_n\right|^2+\left|b_n-s_ne^{-jk_n\Delta r}\right|^2\right)\\
&= -\frac{1}{\sigma_w^2}\frac{\partial}{\partial s_n}\left(\left|s_n-a_n\right|^2+\left|s_n-b_ne^{jk_n\Delta r}\right|^2\right)\\
&= -\frac{1}{\sigma_w^2}\left[\left(\overline{s_n}-\overline{a_n}\right)+\left(\overline{s_n}-\overline{b_n}e^{-jk_n\Delta r}\right)\right]\\
&= -\frac{1}{\sigma_w^2}\overline{\left(2s_n-(a_n+b_ne^{jk_n\Delta r})\right)} \qquad (6.29)
\end{aligned}$$

Replacing s_n and Δr with their maximum likelihood estimators $\widehat{s}_{n,ml}$ and $\widehat{r}_{ml}$, then equating to zero shows that

$$\widehat{s}_{n,ml} = \frac{1}{2}\left(a_n+b_ne^{jk_n\widehat{r}_{ml}}\right) \qquad (6.30)$$

Therefore the maximum likelihood estimate of the target's response at frequency k_n is the average of the noisy measurements at $t=0$ and $t=T$ after b_n has had its phase adjusted to compensate for the target's radial motion during the interval $[0,T]$.

6.3.3   Finding $\widehat{r}_{ml}$

The partial derivative of $\ln p(\boldsymbol{x};\boldsymbol{\theta})$ with respect to Δr, the radial distance the target has moved, is

$$\begin{aligned}
\frac{\partial \ln p(\boldsymbol{x};\boldsymbol{\theta})}{\partial \Delta r} &= -\frac{1}{\sigma_w^2}\frac{\partial}{\partial \Delta r}\sum_{n=0}^{N-1}\left|a_n-s_n\right|^2+\left|b_n-s_ne^{-jk_n\Delta r}\right|^2\\
&= -\frac{1}{\sigma_w^2}\sum_{n=0}^{N-1}\frac{\partial}{\partial \Delta r}\left|b_n-s_ne^{-jk_n\Delta r}\right|^2 \qquad (6.31)
\end{aligned}$$

Since Δr is real, this is the derivative of a real function of a real variable. So

$$\frac{\partial \ln p(\boldsymbol{x};\boldsymbol{\theta})}{\partial \Delta r} = -\frac{1}{\sigma_w^2}\sum_{n=0}^{N-1}\frac{\partial}{\partial \Delta r}\left|b_n-s_ne^{-jk_n\Delta r}\right|^2$$

$$= \frac{1}{\sigma_w^2} \sum_{n=0}^{N-1} jk_n \left(b_n \overline{s_n} e^{jk_n \Delta r} + \overline{b_n} s_n e^{-jk_n \Delta r} \right)$$

$$= -\frac{2}{\sigma_w^2} \Im \left\{ \sum_{n=0}^{N-1} k_n b_n \overline{s_n} e^{jk_n \Delta r} \right\} \tag{6.32}$$

Replacing Δr with its maximum likelihood estimator $\widehat{r}_{ml}$ and s_n with the expression for $\widehat{s}_{n,ml}$ from (6.30), then equating to zero gives the solution of the likelihood equation as

$$0 = \Im \left\{ \sum_{n=0}^{N} k_n \widehat{s}_{n,ml} \overline{b_n} e^{-jk_n \widehat{r}_{ml}} \right\}$$

$$= \frac{1}{2} \Im \left\{ \sum_{n=0}^{N} k_n \left(a_n + b_n e^{jk_n \widehat{r}_{ml}} \right) \overline{b_n} e^{-jk_n \widehat{r}_{ml}} \right\}$$

$$= \frac{1}{2} \Im \left\{ \sum_{n=0}^{N} k_n a_n \overline{b_n} e^{-jk_n \widehat{r}_{ml}} \right\} \tag{6.33}$$

because the imaginary part of $b_n \overline{b_n}$ is zero.

Therefore the maximum likelihood estimator $\widehat{r}_{ml}$ is one of the solutions of

$$\Im \left\{ \sum_{n=0}^{N} k_n a_n \overline{b_n} e^{-jk_n \widehat{r}_{ml}} \right\} = 0 \tag{6.34}$$

This has many solutions, not all of which maximize $\ln p(\boldsymbol{x}; \boldsymbol{\theta})$.

To find which of these solutions maximizes $\ln p(\boldsymbol{x}; \boldsymbol{\theta})$, use the maximum likelihood estimator of s_n in (6.30) to eliminate the s_n from (6.25). Then

$$\left| a_n - \widehat{s}_{n,ml} \right|^2 = \left| a_n - \frac{1}{2} \left(a_n + b_n e^{jk_n \widehat{r}_{ml}} \right) \right|^2$$

$$= \frac{1}{4} \left| a_n - b_n e^{jk_n \widehat{r}_{ml}} \right|^2 \tag{6.35}$$

and

$$\left| b_n - \widehat{s}_{n,ml} e^{-jk_n \widehat{r}_{ml}} \right|^2 = \left| b_n - \frac{1}{2} \left(a_n + b_n e^{jk_n \widehat{r}_{ml}} \right) e^{-jk_n \widehat{r}_{ml}} \right|^2$$

$$= \frac{1}{4} \left| b_n - a_n e^{-jk_n \widehat{r}_{ml}} \right|^2$$

$$= \frac{1}{4} \left| a_n - b_n e^{jk_n \widehat{r}_{ml}} \right|^2 \tag{6.36}$$

Therefore the maximum value of $p(\boldsymbol{x}; \boldsymbol{\theta})$ is

$$p(\boldsymbol{x}; \boldsymbol{\theta}) = \frac{1}{(\pi \sigma_w^2)^{2N}} \exp \left(-\frac{1}{\sigma_w^2} \sum_{n=0}^{N-1} \left| a_n - \widehat{s}_{n,ml} \right|^2 + \left| b_n - \widehat{s}_{n,ml} e^{-jk_n \Delta r} \right|^2 \right)$$

$$= \frac{1}{(\pi \sigma_w^2)^{2N}} \exp \left(-\frac{1}{2\sigma_w^2} \sum_{n=0}^{N-1} \left| a_n - b_n e^{jk_n \widehat{r}_{ml}} \right|^2 \right) \tag{6.37}$$

Thus the maximum likelihood estimator $\widehat{r}_{ml}$ is found by minimizing

$$\sum_{n=0}^{N-1} \left| a_n - b_n e^{jk_n r} \right|^2 \tag{6.38}$$

which is the same cost function as $J(r)$ in equation (6.17) derived using the scalar maximum likelihood estimator. Therefore

$$\widehat{r}_{ml} = \arg \min_r J(r) \tag{6.39}$$

where the cost function is

$$J(r) = \sum_{n=0}^{N-1} \left| a_n - b_n e^{jk_n r} \right|^2 \tag{6.40}$$

6.3.4   Finding $\widehat{\sigma}^2_{w,ml}$

The final parameter to be estimated is the noise variance σ^2_w. The partial derivative of $\ln p(\boldsymbol{x}; \boldsymbol{\theta})$ with respect to σ^2_w is

$$\frac{\partial \ln p(\boldsymbol{x}; \boldsymbol{\theta})}{\partial \sigma^2_w} = -\frac{2N}{\sigma^2_w} + \frac{1}{(\sigma^2_w)^2} \sum_{n=0}^{N-1} \left| a_n - s_n \right|^2 + \left| b_n - s_n e^{-jk_n \Delta r} \right|^2 \tag{6.41}$$

Equating to zero and substituting in $\widehat{\sigma}^2_{w,ml}$, $\widehat{s}_{n,ml}$ and $\widehat{r}_{ml}$ shows that

$$\widehat{\sigma}^2_{w,ml} = \frac{1}{2N} \sum_{n=0}^{N-1} \left| a_n - \widehat{s}_{n,ml} \right|^2 + \left| b_n - \widehat{s}_{n,ml} e^{-jk_n \widehat{r}_{ml}} \right|^2 \tag{6.42}$$

Using the expression for $\widehat{s}_{n,ml}$ in (6.30) gives the noise variance as $1/4N$ times the minimum of $J(r)$

$$\widehat{\sigma}^2_{w,ml} = \frac{1}{4N} \sum_{n=0}^{N-1} \left| a_n - b_n e^{jk_n \widehat{r}_{ml}} \right|^2$$

$$= \frac{1}{4N} J(\widehat{r}_{ml}) \tag{6.43}$$

6.4   Properties of the Cost Function $J(r)$

In this section, the cost function $J(r)$ is examined in detail to discover why it is useful for ISAR motion estimation, and to see whether the assumption of a unique global minimum necessary for the existence of the maximum likelihood estimator is justified.

   The exact behaviour of $J(r)$ depends on the target's frequency response, which in turn depends on the target's geometry and orientation. However,

Figure 6.1: The cost function $J(r)$ for a variety of simulated and experimental radar data as a function of estimated radial motion, r.

These used a stepped-frequency radar with an initial frequency of $f_0 = 9.16$ GHz and 128 frequency steps with a 2 MHz spacing. In (a) and (b), the target has no radial motion, while in (c) and (d), the target moved -0.58 m between the two frequency responses.

(a) $J(r)$ for a simple simulated target with a frequency response of $s(f) \equiv 1$.

(b) A magnified view of the global minimum of (a), showing how the high frequency modulation locates the minimum very accurately.

(c) $J(r)$ for a simulation of a 737 aircraft composed of 165 point scatterers. This shows a similar shape to that of (a).

(d) $J(r)$ for a real 737 aircraft whose frequency responses were measured while landing at Adelaide Airport.

the general features of $J(r)$ are common to all targets, and these will be illustrated by considering a very simple target geometry. For this simple geometry, it will be shown that $J(r)$ has a unique global minimum when the frequency response is known for a continuum of frequencies. For arbitrary targets imaged using stepped-frequency ISAR, it will be shown that $J(r)$ is periodic but this does not invalidate the maximum likelihood estimate because the period is exactly the length of the ISAR range ambiguity window. Therefore, it can be safely assumed that for real targets, $J(r)$ has a unique global minimum whose location is the maximum likelihood estimate of Δr.

6.4.1   General Features of $J(r)$

To illustrate the general behaviour of the cost function $J(r)$, consider a simple target whose frequency responses are measured in the absence of noise at times $t = 0$ and $t = T$ respectively to give

$$
\begin{aligned}
a(f) &= 1 \\
b(f) &= e^{-j\frac{4\pi}{c}f\Delta r}
\end{aligned}
\tag{6.44}
$$

This represents a target, with a physically unrealistic constant radar cross-section, which moves a distance Δr between $t = 0$ and $t = T$. For analytical simplicity, assume that the frequency responses are measured over a continuous frequency band from f_0 to $f_1 = f_0 + \Delta f$. Then equation (6.17) for $J(r)$ becomes an integral rather than a summation

$$
J(r) = \frac{1}{\Delta f} \int_{f_0}^{f_1} \left| a(f) - b(f)e^{j\frac{4\pi}{c}fr} \right|^2 \, df
\tag{6.45}
$$

Solving this for the frequency responses in (6.44) gives

$$
J(r) = 2\left[1 - m(r)e(r)\right]
\tag{6.46}
$$

where $e(r)$ is the low frequency envelope

$$
e(r) = \text{sinc}\left(\frac{2}{c}\Delta f(\Delta r - r)\right)
\tag{6.47}
$$

which has zero crossings every $c/2\Delta f$, and $m(r)$ is the high frequency modulation

$$
m(r) = \cos\left(\frac{4\pi}{c}\overline{f}(\Delta r - r)\right)
\tag{6.48}
$$

which has a period of $c/2\overline{f}$ where $\overline{f} = (f_0 + f_1)/2$.

From (6.46), $J(r)$ is only ever zero when both $e(r)$ and $m(r)$ are unity. The envelope $e(r)$ is only unity when $r = \Delta r$ and the cosine modulation $m(r)$ has one of its local maxima at $r = \Delta r$.

Therefore the global minimum of $J(r)$ occurs when r is equal to the radial distance Δr the target moved, and so

$$\widehat{r}_{ml} = \Delta r \tag{6.49}$$

This combination of low frequency envelope and high frequency modulation enables the global minimum of $J(r)$ to be estimated very accurately. The envelope alone would give only a rough estimate of Δr because the envelope is so flat in the neighbourhood of $r = \Delta r$. The cosinusoidal modulation alone is not suitable for estimating Δr because there is no way of knowing which of the closely spaced local extrema locates Δr. But by multiplying the envelope and the modulation together, the modulation's high frequency ensures that the global minimum can be located accurately, and the envelope ensures that there is no ambiguity in choosing which of the local minima is the global minimum.

$J(r)$ is plotted for a number of simulations and real targets in figure 6.1. Figure 6.1(a) is $J(r)$ for the simple target in equation (6.46). The nearly solid mass of black inside the envelope indicates that the local minima of $J(r)$ are very closely spaced. The region surrounding the global minimum is enlarged in 6.1(b), clearly showing how closely spaced the local extrema of $J(r)$ are. $J(r)$ for a simulated aircraft and a real aircraft are presented in figures 6.1(c) and (d).

The consistency of the overall shape of the three different cost function curves in figure 6.1 shows how the general form of $J(r)$ is maintained, even in the presence of noise for the real aircraft in 6.1(d). Note that in 6.1(d), the maximum likelihood estimate of the signal-to-noise ratio is given by the amplitude of $J(r)$ at the global minimum.

6.4.2   Uniqueness of $J(r)$'s Global Minimum

The existence of the maximum likelihood estimator $\widehat{r}_{ml}$ requires that the cost function $J(r)$ has a unique global minimum. This is because if $J(r)$ has a number of equally deep local minima but no unique global minimum, there is no way of telling which of the local minima should be chosen as $\widehat{r}_{ml}$.

By considering stepped-frequency ISAR with uniformly spaced frequency steps, it will be shown that $J(r)$ is periodic, which would seem to deny the existence of the maximum likelihood estimator. However, the period of $J(r)$ is equal to the size of the ISAR range ambiguity window so the periodicity of $J(r)$ may be neglected and the global minimum is considered unique.

If the frequency responses are sampled at discrete evenly-spaced frequencies[3], $J(r)$ is periodic. To find the period explicitly, consider a target with

---

[3]A uniformly spaced stepped-frequency waveform is only required for this periodicity proof and for some of the efficient ways of evaluating the maximum likelihood estimator in chapter 7.

frequency response s_n at frequency f_n moving a radial distance Δr between $t = 0$ and $t = T$ in the absence of noise. Then

$$a_n = s_n$$
$$b_n = s_n e^{-j\frac{4\pi}{c} f_n \Delta r} \tag{6.50}$$

From this noiseless model, $J(r)$ is

$$J(r) = 2 \left(\sum_{n=0}^{N-1} |s_n|^2 \right) - 2\Re \left\{ e^{-j\frac{4\pi}{c} f_0(\Delta r - r)} \sum_{n=0}^{N-1} |s_n|^2 \, e^{-j\frac{4\pi}{c} (f_n - f_0)(\Delta r - r)} \right\} \tag{6.51}$$

Because $f_n - f_0 = n\Delta f$ for stepped-frequency ISAR,

$$J(r) = 2 \left(\sum_{n=0}^{N-1} |s_n|^2 \right) - 2\Re \left\{ m(r)\overline{e(r)} \right\} \tag{6.52}$$

where the high frequency complex modulation is

$$m(r) = e^{-j\frac{4\pi}{c} f_0(\Delta r - r)} \tag{6.53}$$

and the low frequency complex envelope is

$$e(r) = \sum_{n=0}^{N-1} |s_n|^2 \, e^{j\frac{4\pi}{c} n\Delta f(\Delta r - r)} \tag{6.54}$$

So $J(r)$ is minimized when the magnitude of $e(r)$ is greatest and $e(r)$ and $m(r)$ have the same phase modulo 2π.

For $e(r)$ to attain its greatest magnitude, each term in the summation of (6.54) must have the same phase modulo 2π

$$\frac{4\pi}{c} n\Delta f(\Delta r - r) = 2u_n\pi + \phi \tag{6.55}$$

where each of the u_n is integral. Since this has to hold for every n from 0 to $N - 1$, $u_n = un$ for some integer u. Putting $n = 0$ shows that $\phi = 0$. Therefore $e(r)$'s magnitude is greatest if

$$\Delta r - r = \frac{uc}{2\Delta f} \tag{6.56}$$

Whenever this is satisfied, $m(r)$'s phase must also be an integral multiple of 2π. Therefore

$$uf_0(\Delta r - r) = 2v\pi \tag{6.57}$$

where v is integral. Putting (6.56) and (6.57) together gives the condition

$$uf_0 = v\Delta f \tag{6.58}$$

on u and v. The first solution, $u = v = 0$, occurs when $\Delta r = r$. At worst, the next solution is $u = \pm 1$ when Δf is a factor of f_0. Therefore the period of $J(r)$ is a multiple of

$$\frac{c}{2\Delta f}$$

This is exactly the size of the range ambiguity window in stepped-frequency ISAR. Since radial movements of exact multiples of the range ambiguity window do not affect the final ISAR image, this shows that the periodic nature of $J(r)$ can be ignored for motion estimation for ISAR imaging.

Therefore $\widehat{r}_{ml}$ found by minimizing $J(r)$ is indeed the maximum likelihood estimate of Δr.

6.5 Summary of Maximum Likelihood Motion Estimation

To summarize the results of this chapter, applying maximum likelihood estimation to the problem of estimating the unknown parameters of a target moving during an interval $[0, T]$ shows that

- The maximum likelihood estimator of the radial distance the target has moved during the time interval is

$$\widehat{r}_{ml} = \arg \min_{r} J(r)$$

  where the cost function is

$$J(r) = \sum_{n=0}^{N-1} \left| a_n - b_n e^{jk_n r} \right|^2$$

- The maximum likelihood estimator of the noise variance is $1/4N$ times the value of $J(\widehat{r}_{ml})$

$$\widehat{\sigma}_{w,ml}^2 = \frac{1}{4N} \min_{r} J(r)$$

- The maximum likelihood estimator of the target's frequency response is the average of the noisy measurements at times $t = 0$ and $t = T$ once the measurements at $t = T$ have been phase-shifted to move the target back a radial distance of $\widehat{r}_{ml}$

$$\widehat{s}_{n,ml} = \frac{1}{2} \left(a_n + b_n e^{jk_n \widehat{r}_{ml}} \right)$$

Chapter 7

Evaluating the Maximum Likelihood Motion Estimator

One problem with maximum likelihood estimation is that the estimator is found by maximizing the likelihood function. In some cases, this maximization problem gives the estimator as an explicit function of the measurements

$$\widehat{\boldsymbol{\theta}}_{ml} = f(\boldsymbol{x}) \tag{7.1}$$

Unfortunately, estimating a target's radial motion Δr is not such a case. The maximum likelihood estimator $\widehat{r}_{ml}$ is found by minimizing the cost function

$$J(r) = \sum_{n=0}^{N-1} \left| a_n - b_n e^{jk_n r} \right|^2 \tag{7.2}$$

but the machinery of maximum likelihood estimation does not reveal how to minimize $J(r)$, or even say whether $\widehat{r}_{ml}$ can be found with sufficient accuracy for ISAR motion estimation at an acceptably low cost in both time and computational resources.

The straightforward approach of maximizing a function using Newton-Raphson iteration or gradient descent is not practical because $J(r)$ has many closely-spaced local minima. An order-of-magnitude calculation shows that the motion estimation for a 128×128 pixel ISAR image taken at X-band would require about one billion floating point arithmetic operations if one of these methods were used.

Clearly, an exhaustive search is not suitable for finding the global minimum of $J(r)$. This chapter examines the problem of minimizing $J(r)$ and proposes a number of efficient methods. Each method uses a global minimization scheme to find the approximate location of $\widehat{r}_{ml}$ followed by a local minimization scheme which converges to $\widehat{r}_{ml}$.

7.1   Global Minimization of $J(r)$

Two algorithms for the approximate global minimization of $J(r)$ are presented here. The first algorithm is based on a discrete Fourier transform (DFT) and gives an approximation $\widehat{r}$ to the global minimum of $J(r)$ that is at most $c/2N\Delta f$, or one ISAR range bin, away from $\widehat{r}_{ml}$.

The second algorithm uses a chirp-Z transform (CZT) [66, 67] to interpolate part of the Fourier spectrum of the first method, and so determine $\widehat{r}_{ml}$ with an accuracy much better than one ISAR range bin. The parameters of the chirp-Z transform can be adjusted to select the resolution and the portion of the Fourier spectrum zoomed into.

These algorithms are efficient because they look only at the envelope of $J(r)$, ignoring the high frequency carrier. They can be implemented efficiently using the fast Fourier transform if the frequencies in the stepped-frequency waveform are uniformly spaced, as in (6.3)

$$k_n = k_0 + n\Delta k \qquad \text{for } n = 0, 1, \ldots, N - 1 \tag{7.3}$$

Note that these global minimizations of $J(r)$ are not using the discrete Fourier transform as a spectral estimator. Rather one form of the expression for $J(r)$ is as the real part of a continuous-range[1] Fourier series. The maximum likelihood estimate of Δr is found by locating the maximum of the Fourier spectrum. Since this is really implementing a correlation, it is misguided to try modern spectral estimators with the hope of achieving a higher resolution estimate of Δr.

7.1.1   Global Minimization Using a DFT

The following algorithm describes an efficient way to find the approximate location $\widehat{r}$ of the global minimum of $J(r)$, which occurs when $r = \widehat{r}_{ml}$. The estimate $\widehat{r}$ is guaranteed to be within $c/2N\Delta f$ of the true global minimum at $\widehat{r}_{ml}$.

Algorithm 7.1 (Global Minimization of $J(r)$ using a DFT)
  To obtain a rough estimate $\widehat{r}$ of the location of the global minimum of $J(r)$:

  1. From the set of measurements $\boldsymbol{x}$ in (6.9), form

$$c_n = a_n\overline{b_n} \qquad \forall n = 0, 1, \ldots, N - 1 \tag{7.4}$$

---

[1]The continuous-time Fourier series gives a continuous-time representation of a function with a discrete frequency spectrum. Here, the two domains are range and frequency, not time and frequency. Hence $J(r)$ is a continuous-range Fourier series.

2. *Take the discrete Fourier transform (in the form of an FFT) of the $\{c_n\}$ to give the vector $\{C_m\}$*

$$C_m = \mathcal{F}\{c_n\} \tag{7.5}$$

3. *Find the index of the absolute maximum of the $\{C_m\}$*

$$k = \arg \max_m |C_m| \tag{7.6}$$

4. *A rough estimate $\widehat{r}$ of the location of the global minimum of $J(r)$ is*

$$\widehat{r} = k \frac{c}{2N\Delta f} \tag{7.7}$$

The next theorem is a formal statement of the accuracy of $\widehat{r}$. Note that it is a theorem concerning the maximum distance between $\widehat{r}$ and $\widehat{r}_{ml}$, not the distance between $\widehat{r}$ and Δr. That depends on the bias and variance of $\widehat{r}_{ml}$, and is discussed in chapter 8.

Theorem 7.2 (Global Minimization of $J(r)$ using a DFT)
Let $\widehat{r}_{ml} = \arg \min_r J(r)$ where $J(r)$ is the cost function given by (7.2) and the stepped-frequency waveform is given by (7.3). Then $\widehat{r}$, the rough estimate of $\widehat{r}_{ml}$ calculated using algorithm 7.1, is less than one ISAR range bin from $\widehat{r}_{ml}$

$$|\widehat{r} - \widehat{r}_{ml}| < \frac{c}{2N\Delta f} \tag{7.8}$$

Proof: See appendix 7A. ■

7.1.2 Global Minimization Using a CZT

The procedure in algorithm 7.1 determines $\widehat{r}_{ml}$ to within one ISAR range bin, which is typically orders of magnitude larger than the small fraction of a wavelength required for ISAR motion estimation. The procedure is also inefficient because the minimum of $J(r)$ is sought over the whole ISAR range ambiguity window. Most targets, even those moving as swiftly as aircraft, can move only a few range bins in the time between measuring consecutive frequency responses. It would make sense to examine only part of the range ambiguity window, and do so with a higher resolution than algorithm 7.1.

The resolution of the DFT can be increased by appending zeros to the end of the data sequence before transforming. This interpolates the discrete frequency spectrum, giving a a discrete spectrum which more closely approximates the data's continuous Fourier transform. Note that the discrete spectrum has more samples, so the spectral peaks may be found more

accurately, but the fundamental frequency resolution of the transform is unchanged because this depends on the interval between the measurements, which stays the same. (This is illustrated convincingly in figure 4 of [52].)

While zero padding can be used to interpolate the Fourier spectrum and so achieve more accurate estimates of $\widehat{r}_{ml}$, the increase in resolution comes at the cost of longer vectors to be transformed. Another disadvantage of zero-padding is that the Fourier spectrum is still calculated over the whole of the range ambiguity window.

Both of these difficulties with the DFT may be overcome by using a chirp-Z transform to compute the Fourier spectrum over an arbitrary portion of the range ambiguity window with an arbitrary resolution.

The chirp-Z transform, described by Rabiner, Schafer and Rader in [66] and [67], is an efficient way of evaluating the Z transform[2]

$$X_k = \sum_{n=0}^{N-1} x_n z_k^{-n} \tag{7.9}$$

along a spiral contour in the Z plane where

$$z_k = AW^{-k} \qquad \text{for } k = 0, 1, \ldots, M-1 \tag{7.10}$$

A is the start of the contour, $\arg W$ is the angular spacing between samples and $|W|$ determines how quickly the contour moves towards or away from the origin. The number of samples, M, in the contour is independent of the number of data points, N.

When $M = N$, $A = 1$, and $W = e^{j\frac{2\pi}{N}}$, the spiral contour is the set of points spaced uniformly around the unit circle and the chirp-Z transform becomes a discrete Fourier transform.

Well-chosen values of M, A and W can achieve a higher resolution over a small part of the spectrum, and this is used in the following algorithm to obtain a much better approximation to $\widehat{r}_{ml}$ than algorithm 7.1.

Algorithm 7.3 (Global Minimization of $J(r)$ using a CZT)
   To obtain a rough estimate $\widehat{r}$ of the location of the global minimum $\widehat{r}_{ml}$ of $J(r)$ when it is known that $\widehat{r}_{ml}$ lies within the range $[r_l, r_u]$:

1. *Choose the desired accuracy of the estimate $\widehat{r}$ of $\widehat{r}_{ml}$. This accuracy ϵ_r should be smaller than an ISAR range bin but larger than half the radar wavelength*

$$\frac{c}{2f_0} < \epsilon_r < \frac{c}{2N\Delta f} \tag{7.11}$$

---

[2]Incidentally, the chirp-Z transform implemented in `MATLAB` version 4.1 does not follow Rabiner's, Schafer's and Rader's papers. A revised version of `czt.m` is included in appendix 7D.

2. *Choose an integer M (not necessarily a power of 2) such that the resolution of the CZT is better than the desired accuracy ϵ_r*

$$\frac{r_u - r_l}{M - 1} < \epsilon_r \tag{7.12}$$

3. *From the set of measurements $\boldsymbol{x}$ in (6.9), form*

$$c_n = a_n \overline{b_n} \qquad \forall n = 0, 1, \ldots, N - 1 \tag{7.13}$$

4. *Given M, r_l and r_u, define A and W by*

$$A = e^{j \frac{4\pi}{c} \Delta f r_l} \tag{7.14}$$

and

$$W = e^{j \frac{4\pi}{c} \Delta f \frac{r_u - r_l}{M - 1}} \tag{7.15}$$

5. *Take the CZT of the $\{c_n\}$ using the values of M, A and W just calculated to give the sequence $\{C_m\}$ for $m = 0, 1, \ldots, M - 1$.*

6. *Find the index of the absolute maximum of the $\{C_m\}$*

$$k = \arg \max_m |C_m| \tag{7.16}$$

7. *The estimate $\widehat{r}$ of $\widehat{r}_{ml}$ accurate to ϵ_r is*

$$\widehat{r} = r_l + k \frac{r_u - r_l}{M - 1} \tag{7.17}$$

The correctness of the algorithm is stated formally in the following theorem:

Theorem 7.4 (Global Minimization of $J(r)$ using a CZT)
    Let $\widehat{r}_{ml} = \arg \min_r J(r)$ where $J(r)$ is the cost function given by (7.2) and the stepped-frequency waveform is given by (7.3). Then $\widehat{r}$, the estimate of $\widehat{r}_{ml}$ calculated using algorithm 7.3, attains the desired accuracy, ϵ_r providing

$$\epsilon_r > \frac{c}{2 f_0} \tag{7.18}$$

Proof: This is an outline of the proof of theorem 7.4. Most of the additional steps needed to fill in the gaps and make it rigorous are given in the proof of theorem 7.2 in appendix 7A.
    Minimizing $J(r)$ is equivalent to maximizing the bandpass signal

$$g(r) = \Re \left\{ e^{-jk_0 r} \sum_{n=0}^{N-1} c_n e^{-jn\Delta kr} \right\} \tag{7.19}$$

so that

$$\widehat{r}_{ml} = \arg\max_r g(r) \tag{7.20}$$

The complex envelope of $g(r)$ is

$$g_+(r) = e^{-jk_0 r} \sum_{n=0}^{N-1} c_n e^{-jn\Delta k r} \tag{7.21}$$

Because $g(r)$ is a bandpass signal, the location of the global maximum of $g(r)$ differs from the location of the global maximum of $|g_+(r)|$ by at most half the period of the modulation of $g(r)$. Therefore

$$\left| \widehat{r}_{ml} - \arg\max_r |g_+(r)| \right| \le \frac{c}{4f_0} \tag{7.22}$$

Similarly, the peak in the CZT spectrum is at most half the resolution of the CZT away from the global maximum of $|g_+(r)|$

$$\left| \widehat{r} - \arg\max_r |g_+(r)| \right| \le \frac{1}{2}\epsilon_r \tag{7.23}$$

Therefore using the triangle inequality

$$|\widehat{r} - \widehat{r}_{ml}| \le \frac{c}{4f_0} + \frac{1}{2}\epsilon_r < \epsilon_r \tag{7.24}$$

and the accuracy in the estimate of $\widehat{r}_{ml}$ is better than ϵ_r.   ■

7.1.3   Justifying the Incorporation of Prior Knowledge

Algorithm 7.3 has suggested that one way to speed up the search for the global minimum of $J(r)$ is to restrict the scope of the search by including some *a priori* information. The theoretical justification for this is discussed in the context of the maximum likelihood estimator.

Maximizing the likelihood function in maximum likelihood estimation is justified on the basis that no *a priori* information about the unknown parameter is available. But when *a priori* information about the unknown parameter is available, it should be used along with the likelihood function. In this situation, the appropriate estimator of θ is not the maximum likelihood estimator $\widehat{\theta}_{ml}$ but the maximum *a posteriori* estimator $\widehat{\theta}_{map}$ which maximizes the *a posteriori* probability density function $p(\theta|\boldsymbol{x})$.

The discussion of diffuse priors in section 2.4.1 shows that when the *a priori* information takes the form of a closed interval on which the unknown parameter has uniform prior probability, the maximum *a posteriori* estimator has the same form as the maximum likelihood estimator restricted to that closed interval.

This justifies using *a priori* information to restrict the search for the global minimum of $J(r)$ to a particular portion of the ISAR range ambiguity window in algorithm 7.3. The estimate of Δr is no longer the maximum likelihood estimate but the maximum *a posteriori* estimate. Since the difference is one of name rather than form, the estimate of Δr will continue to be called the maximum likelihood estimate, even though this is strictly speaking incorrect.

As an example, if a ship's maximum velocity is v, and two frequency responses are measured separated by a time interval of length T, Δr must lie in the interval $[-vT, vT]$. If the prior distribution of Δr is uniform over this interval and the maximum likelihood estimator $\widehat{r}_{ml}$ lies within the interval, the maximum likelihood and the maximum *a posteriori* estimates are identical.

7.2 Exact Local Minimization

Once one of the two approximate global minimization algorithms 7.1 or 7.3 have been used to obtain a rough estimate of $\widehat{r}_{ml}$, another step is needed to find the global minimum of $J(r)$ in the neighbourhood of the rough estimate $\widehat{r}$.

The two exact local minimization algorithms presented here find the position of r_0, the local minimum of $J(r)$ closest to any r. Once one local minimum r_0 has been located and $J(r_0)$ found, this process can be repeated for all the local minima of $J(r)$ near $\widehat{r}$. Then the local minimum at which $J(r_0)$ is smallest gives the location of the global minimum of $J(r)$, which is $\widehat{r}_{ml}$.

The number of local minima which have to be examined depends on the accuracy of the rough estimate $\widehat{r}$. For the global minimization algorithm using the DFT, this may mean 50 or more local minima (depending on the radar's parameters). For the global minimization algorithm using the CZT, this may mean only a few local minima. Since the number of arithmetic operations required to find one local minimum is about the same as the number required to implement either of the approximate global minimization algorithms, the maximum likelihood estimator can be found most efficiently by using algorithm 7.3 with an accuracy that is at most a couple of wavelengths at frequency f_0.

The first local minimization algorithm assumes that because $J(r)$ is bandpass, the phase of a sinusoidal signal fitted to $J(r)$ can be used to locate r_0. The second method uses the likelihood equation for Δr to derive an iterative procedure that converges to r_0. This is shown to be a contraction mapping and the rate of contraction is analysed to find how many iterations are necessary to achieve any desired accuracy in r_0.

7.2.1 Minimization by Sinusoidal Parameter Estimation

Given an initial value of r, the approximate position r_0 of the local minimum of $J(r)$ closest to r may be found using the following algorithm.

In practice, algorithm 7.6 on page 106 should be used as it is guaranteed to converge to the exact location of the closest local minimum. The statement and derivation of algorithm 7.5 are included here because the statements of the two algorithms are similar, and the derivation of this algorithm conveys a degree of geometrical insight which is absent in the purely analytical derivation of algorithm 7.6.

Algorithm 7.5 (Approximate Local Minimization of $J(r)$)
Suppose that r_0 is the position of the local minimum of $J(r)$ closest to r. Then an approximation to r_0 may be obtained by solving

$$\tan\left(\overline{k}(r_0 - r)\right) = \frac{\Im\left\{\sum\limits_{n=0}^{N-1} a_n \overline{b_n} e^{-jk_n r}\right\}}{\Re\left\{\sum\limits_{n=0}^{N-1} a_n \overline{b_n} e^{-jk_n r}\right\}} \tag{7.25}$$

where $\overline{k}$ is $4\pi/c$ times the centre frequency of the stepped-frequency waveform.

If the denominator of this equation is negative, a local maximum has been found instead of a local minimum. Let

$$r' = r_0 + \frac{\pi}{\overline{k}}\mathrm{sgn}\left(r - r_0\right) \tag{7.26}$$

and repeat the algorithm with $r = r'$ to find the closest local minimum.

An informal derivation of this algorithm will now be presented. No attempt is made to formalize how accurate the approximation to r_0 may be; this will be left for the next algorithm, which converges to the exact value of r_0.

Given a value of r, the local extremum of $J(r)$ closest to r may be found by assuming that the envelope of $J(r)$ is constant in the neighbourhood of r. This assumption is valid because the envelope varies very slowly in comparison to the modulation since the stepped-frequency waveform has a small relative bandwidth. Therefore $J(r)$ may be written

$$J(r) = A - B\cos\left(\overline{k}(r_0 - r)\right) \tag{7.27}$$

where r_0 is the location of the local extremum closest to r and $\lambda = 2\pi/\overline{k}$ is the instantaneous period of $J(r)$. A and B are constants. A is always

positive and B is positive if the local extremum is a minimum, or negative if it is a maximum.

Now

$$2B \sin\left(\overline{k}(r_0 - r)\right) = J\left(r - \frac{\lambda}{4}\right) - J\left(r + \frac{\lambda}{4}\right) \tag{7.28}$$

and

$$2B \cos\left(\overline{k}(r_0 - r)\right) = \frac{1}{2}\left[J\left(r + \frac{\lambda}{2}\right) + J\left(r - \frac{\lambda}{2}\right)\right] - J(r) \tag{7.29}$$

Cancelling out the unknown amplitude B in these two equations shows that

$$\tan\left(\overline{k}(r_0 - r)\right) = \frac{J\left(r - \frac{\lambda}{4}\right) - J\left(r + \frac{\lambda}{4}\right)}{\frac{1}{2}\left[J\left(r + \frac{\lambda}{2}\right) + J\left(r - \frac{\lambda}{2}\right)\right] - J(r)} \tag{7.30}$$

Substitute in $J(r)$ using (7.2) and expand each of the $|\cdot|^2$. After a small algebraic struggle,

$$\tan\left(\overline{k}(r_0 - r)\right) = \frac{\Im\left\{\sum_{n=0}^{N-1} \sin\left(\frac{\pi k_n}{2\overline{k}}\right) a_n \overline{b_n} e^{-jk_n r}\right\}}{\Re\left\{\sum_{n=0}^{N-1} \sin^2\left(\frac{\pi k_n}{2\overline{k}}\right) a_n \overline{b_n} e^{-jk_n r}\right\}} \tag{7.31}$$

Since the stepped-frequency waveform is assumed to have a narrow relative bandwidth, $k_n/\overline{k} \approx 1$ so each of the $\sin\left(\pi k_n/2\overline{k}\right)$ terms is

$$\sin\left(\frac{\pi k_n}{2\overline{k}}\right) \approx \sin\left(\frac{\pi}{2}\right) = 1 \tag{7.32}$$

Neglecting these in (7.31) gives

$$\tan\left(\overline{k}(r_0 - r)\right) = \frac{\Im\left\{\sum_{n=0}^{N-1} a_n \overline{b_n} e^{-jk_n r}\right\}}{\Re\left\{\sum_{n=0}^{N-1} a_n \overline{b_n} e^{-jk_n r}\right\}} \tag{7.33}$$

as required.

This method of calculating r_0 is independent of the sign of B, so r_0 is the extremum that is closest to r, not necessarily the local minimum that is closest. The extremum is a local minimum if the denominator of (7.33) is positive. If the denominator is negative, increment the calculated value of r_0 by $\lambda/4$ and use it as r once again to find the local minimum.

The approximations inherent in equations (7.27) and (7.32) are dependent on the ISAR's relative bandwidth. In the limit as

$$\frac{N\Delta k}{k_0} \to 0 \qquad (7.34)$$

the approximations become exact, and the algorithm determines the positions of the local minima of $J(r)$ exactly.

7.2.2   Minimization by Contraction Mapping

Given an initial value of r, the position r_0 of the local minimum of $J(r)$ closest to r may be found to any desired accuracy using the following iterative algorithm, whose derivation is given in appendix 7B.

Algorithm 7.6 (Iterative Local Minimization of $J(r)$)
Suppose that r_0 is the position of the local extremum of $J(r)$ closest to r. Let $r_1 = r$ and use the iterative equation

$$\tan\left(\overline{k}(r_{k+1} - r_k)\right) = \frac{\Im\left\{\sum_{n=0}^{N-1} k_n a_n \overline{b_n} e^{-jk_n r_k}\right\}}{\Re\left\{\sum_{n=0}^{N-1} k_n a_n \overline{b_n} e^{-jk_n r_k}\right\}} \qquad (7.35)$$

to generate a sequence $\{r_k\}$. Here $\overline{k}$ is $4\pi/c$ times the centre frequency of the stepped-frequency waveform. Then

$$\lim_{k\to\infty} r_k = r_0 \qquad (7.36)$$

If the denominator of the iterative equation is negative, a local maximum has been found instead of a local minimum. Let

$$r_1 = r_0 + \frac{\pi}{\overline{k}}\mathrm{sgn}\left(r - r_0\right) \qquad (7.37)$$

and start iterating again to find the closest local minimum.
If the denominator of the iterative equation is zero, r is exactly mid-way between a local maximum and a local minimum. Increase or decrease r by $\pi/2\overline{k}$ if the numerator is respectively positive or negative.

The following theorem shows that the algorithm converges to the closest local extremum to the initial estimate r, and that the rate of convergence is dependent on the ISAR's relative bandwidth.

Theorem 7.7 (Iterative Local Extremum of $J(r)$)

Suppose that r_0 is the position of the local extremum of $J(r)$ closest to r, where $J(r)$ is the cost function in (7.2). Let $r_1 = r$ and use the iterative equation

$$\tan\left(\bar{k}(r_{k+1} - r_k)\right) = \frac{\Im\left\{\sum_{n=0}^{N-1} k_n a_n \overline{b_n} e^{-jk_n r_k}\right\}}{\Re\left\{\sum_{n=0}^{N-1} k_n a_n \overline{b_n} e^{-jk_n r_k}\right\}} \tag{7.38}$$

with $k_0 \leq \bar{k} \leq k_{N-1}$ to generate a sequence $\{r_k\}$. Then $r_k \to r_0$ as $k \to \infty$ for all r whose closest extremum of $J(r)$ is at r_0.

This is a contraction mapping whose fixed point is r_0

$$|r_{k+1} - r_0| < \alpha^k \, |r - r_0| \tag{7.39}$$

α, the speed of convergence to r_0 is given by

$$\alpha = \frac{\Delta_k}{\bar{k}} \tag{7.40}$$

where

$$\Delta_k = \max_n \left|k_n - \bar{k}\right| \tag{7.41}$$

Proof: See appendix 7C. ∎

This proof shows that the algorithm is guaranteed to converge to r_0 if $\Delta_k < \bar{k}$. This is equivalent to

$$k_0 \leq \bar{k} \leq k_{N-1} \tag{7.42}$$

For a given stepped-frequency waveform and arbitrary target, the guaranteed rate of convergence α is maximized if

$$\bar{k} = \arg\min_{k_0 \leq k \leq k_{N-1}} \max_n \left|\frac{k_n}{k} - 1\right| \tag{7.43}$$

which implies, not unsurprisingly, that the best choice of $\bar{k}$ is

$$\bar{k} = \frac{1}{2}\left(k_0 + k_{N-1}\right) \tag{7.44}$$

For a target with a given geometry, orientation and radar scattering characteristics, the optimal choice of $\bar{k}$ is much harder to calculate.

In the limit as the stepped-frequency waveform's relative bandwidth tends to zero, $\alpha \to 0$, the algorithm converges in a single step, and the approximate algorithm 7.5 becomes equivalent to the iterative algorithm 7.6.

To illustrate calculating the number of iterations required for a typical X-band ISAR image with parameters of $f_0 = 9.16$ GHz, $\Delta f = 2$ MHz and $N = 128$,

$$\alpha = \frac{k_{N-1} - k_0}{k_{N-1} + k_0} = \frac{f_{N-1} - f_0}{f_{N-1} + f_0} = 0.014 \tag{7.45}$$

Since the wavelength at X-band is about 30 mm, any initial guess r_1 is at most 7.5 mm from a local extremum of $J(r)$. One iteration determines r_0 to an accuracy of ± 0.1 mm and two iterations gives an accuracy of ± 1.5 μm, which is more than good enough for ISAR motion compensation.

Once one local minimum has been located, the uncertainty in the position of the next one is much less than 7.5 mm so only one iteration is all that is required when hopping along adjacent local minima.

7.3 Summary of the Procedure to Obtain $\widehat{r}_{ml}$

In summary, the maximum likelihood estimator $\widehat{r}_{ml}$ of the radial distance Δr a target moves in the interval between two measurements of the target's frequency response, using a stepped-frequency radar operating at N uniformly spaced frequencies, is found as follows:

1. Use any prior knowledge to restrict Δr to some subinterval $[r_l, r_u]$ on which Δr is uniformly probable.

2. Given the subinterval $[r_l, r_u]$ and the radar's initial frequency, f_0, use algorithm 7.3 to determine a rough estimate $\widehat{r}$ of $\widehat{r}_{ml}$ with an accuracy of $c/2f_0$.

3. Use algorithm 7.6 to determine the positions of the local minima of $J(r)$ within a distance given by the accuracy in the previous step to $\widehat{r}$. The number of iterations of the contraction mapping required for each local minimum may be calculated using theorem 7.7.

4. Find which of the local minima has the smallest $J(r_0)$. This is now $\widehat{r}_{ml}$, the global minimum of $J(r)$ and the maximum likelihood estimate of Δr

7A Proof of Theorem 7.2

The proof of theorem 7.2 given here shows that the rough estimates $\widehat{r}$ of the location of the global minimum of $J(r)$ satisfy

$$|\widehat{r} - \widehat{r}_{ml}| < \frac{c}{2N\Delta f} \tag{7.46}$$

which means that $\hat{r}$ is less than one ISAR range bin away from the global minimum of $J(r)$.

Proof: $J(r)$ can be rewritten as

$$J(r) = \sum_{n=0}^{N-1} \left| a_n - b_n e^{jk_n r} \right|^2$$

$$= \sum_{n=0}^{N-1} \left(|a_n|^2 + |b_n|^2 \right) - 2 \sum_{n=0}^{N-1} \Re \left\{ a_n \overline{b_n} e^{-jk_n r} \right\} \tag{7.47}$$

so an equivalent definition of $\hat{r}_{ml}$ is

$$\hat{r}_{ml} = \arg \max_r g(r) \tag{7.48}$$

where $g(r)$ is

$$g(r) = \sum_{n=0}^{N-1} \Re \left\{ a_n \overline{b_n} e^{-jk_n r} \right\}$$

$$= \Re \left\{ e^{-jk_0 r} \sum_{n=0}^{N-1} c_n e^{-jn\Delta k r} \right\} \tag{7.49}$$

where $c_n = a_n \overline{b_n}$ and each k_n has been split into

$$k_n = k_0 + n\Delta k \tag{7.50}$$

From this, $g(r)$ is a bandpass signal whose centre frequency is $f_c = \frac{1}{2} f_0$ and bandwidth is $W = \frac{1}{2} N \Delta f$.[3] The envelope of $g(r)$ is given by $|g_+(r)|$, where $g_+(r)$ is the pre-envelope of $g(r)$

$$g_+(r) = e^{-jk_0 r} \sum_{n=0}^{N-1} c_n e^{-jn\Delta k r} \tag{7.51}$$

Formally, the pre-envelope is defined as the complex bandpass signal with $g(r)$ as its real part and the Hilbert transform of $g(r)$ as its imaginary part

$$g_+(r) = g(r) + j\breve{g}(r) \tag{7.52}$$

Because $g(r)$ is bandpass, the distance between the global maxima of $g(r)$ and its envelope is at most half a carrier wavelength

$$\left| \hat{r}_{ml} - \arg \max_r |g_+(r)| \right| \leq \frac{c}{4f_0} \tag{7.53}$$

---

[3]Strictly speaking, this is not the best choice for f_c and W because f_0 is the base frequency of the stepped-frequency waveform, not the centre frequency. The difference is not important providing $N\Delta f > f_0$, but the theorem remains true even if this condition is not satisfied. Incidentally, f_c and W are half what may be expected because of the factor of 2 included in k_n to account for all ranges being measured as round-trip distances from radar to target and back again.

Now

$$\arg\max_r |g_+(r)| = \arg\max_r \left| e^{-jk_0 r} \sum_{n=0}^{N-1} c_n e^{-jn\Delta kr} \right|$$

$$= \arg\max_r \left| \sum_{n=0}^{N-1} c_n e^{-jn\Delta kr} \right|$$

$$= \arg\max_r \left| \sum_{n=0}^{N-1} c_n e^{-j\frac{2\pi}{N}\frac{2N\Delta f}{c} r n} \right|$$

$$= \arg\max_r |N\mathcal{F}\{c_n\}| \tag{7.54}$$

From this, the global maximum of the envelope of $g(r)$ is found by the peak in the magnitude of the Fourier transform of the c_n. This transform is implemented using a DFT, so the peak in the discrete Fourier spectrum occurs at the discrete frequency that is closest to the actual peak in the continuous spectrum. The resolution is $c/2N\Delta f$, therefore the error is at most half this, or

$$\left| \hat{r} - \arg\max_r |g_+(r)| \right| \leq \frac{c}{4N\Delta f} \tag{7.55}$$

Finally, using the triangle inequality shows that

$$\left| \hat{r} - \arg\max_r |g_+(r)| \right| = \left| (\hat{r} - \hat{r}_{ml}) + \left(\hat{r}_{ml} - \arg\max_r |g_+(r)| \right) \right|$$

$$\leq |\hat{r} - \hat{r}_{ml}| + \left| \hat{r}_{ml} - \arg\max_r |g_+(r)| \right|$$

$$\leq \frac{c}{4N\Delta f} + \frac{c}{4f_0}$$

$$< \frac{c}{2N\Delta f} \tag{7.56}$$

as required.   ∎

7B   Derivation of Algorithm 7.6

The derivation of algorithm 7.6 starts with the condition for a local extremum of $J(r)$ at $r = r_0$

$$\left. \frac{\partial J(r)}{\partial r} \right|_{r=r_0} = 0 \tag{7.57}$$

Writing $J(r)$ in (7.2 as

$$J(r) = \sum_{n=0}^{N-1} |a_n|^2 + \sum_{n=0}^{N-1} |b_n|^2 - 2\Re\left\{ \sum_{n=0}^{N-1} a_n \overline{b_n} e^{-jk_n r} \right\} \tag{7.58}$$

the existence of a local extremum at $r = r_0$ means that

$$\Im\left\{\sum_{n=0}^{N-1} k_n a_n \overline{b_n} e^{-jk_n r_0}\right\} = 0 \tag{7.59}$$

Using the relationship

$$k_n r_0 = \overline{k}(r_0 - r) + k_n r + (k_n - \overline{k})(r_0 - r) \tag{7.60}$$

equation (7.59) can be written as

$$\Im\left\{e^{-j\overline{k}(r_0-r)} \sum_{n=0}^{N-1} k_n a_n \overline{b_n}\, e^{-jk_n r}\, e^{-j(k_n-\overline{k})(r_0-r)}\right\} = 0 \tag{7.61}$$

Expanding the imaginary component of (7.61) explicitly gives

$$\tan\left(\overline{k}(r_0 - r)\right) = \frac{\Im\left\{\sum_{n=0}^{N-1} k_n a_n \overline{b_n} e^{-jk_n r} e^{-j(k_n-\overline{k})(r_0-r)}\right\}}{\Re\left\{\sum_{n=0}^{N-1} k_n a_n \overline{b_n} e^{-jk_n r} e^{-j(k_n-\overline{k})(r_0-r)}\right\}} \tag{7.62}$$

This cannot be solved for r_0 directly because r_0 appears on both the left and the right hand sides. However, because r_0 is the closest extremum to r,

$$\overline{k}\,|r_0 - r| < \pi \tag{7.63}$$

Furthermore, the stepped-frequency waveform has a narrow relative bandwidth so that

$$\left|k_n - \overline{k}\right| \ll \overline{k} \tag{7.64}$$

Combining (7.63) and (7.64) shows that

$$\left|(k_n - \overline{k})(r_0 - r)\right| \ll \overline{k}\,|r_0 - r| < \pi \tag{7.65}$$

Therefore each $e^{-j(k_n-\overline{k})(r_0-r)}$ in (7.62) is very close to unity and (7.62) may be written as the close approximation

$$\tan\left(\overline{k}(r_0 - r)\right) \approx \frac{\Im\left\{\sum_{n=0}^{N-1} k_n a_n \overline{b_n} e^{-jk_n r}\right\}}{\Re\left\{\sum_{n=0}^{N-1} k_n a_n \overline{b_n} e^{-jk_n r}\right\}} \tag{7.66}$$

which can be solved directly to give an approximate value for r_0.

This is only an approximation, but it is an approximation which gets progressively better as $r \to r_0$. So rewriting the approximation as the iterative equation

$$\tan\left(\overline{k}(r_{k+1} - r_k)\right) = \frac{\Im\left\{\displaystyle\sum_{n=0}^{N-1} k_n a_n \overline{b_n} e^{-jk_n r_k}\right\}}{\Re\left\{\displaystyle\sum_{n=0}^{N-1} k_n a_n \overline{b_n} e^{-jk_n r_k}\right\}} \tag{7.67}$$

where r_1 is an initial estimate of r_0 and r_k is used to find r_{k+1}, gives a sequence $\{r_k\}$ which it is hoped converges to r_0

$$\lim_{k \to \infty} r_k = r_0 \tag{7.68}$$

7C   Proof of Theorem 7.7

Banach's Fixed Point Theorem will be used to show that the iterative equation (7.38) is a contraction mapping whose iterates $\{r_k\}$ converge to the closest local extremum of $J(r)$ at $r = r_0$. This requires that when (7.38) is written as the mapping T

$$r_{k+1} = T\left(r_k\right) \tag{7.69}$$

whose domain R is the set of points that are less than an eighth of a wavelength from r_0

$$R = \left\{ r \text{ such that } |r - r_0| < \frac{\pi}{2\overline{k}} \right\} \tag{7.70}$$

the following two conditions be satisfied:

(i) r_0 is a fixed point of T

$$T\left(r_0\right) = r_0 \tag{7.71}$$

and that

(ii) T is a contraction for all $r \in R$. This means that there exists some constant $0 \leq \alpha < 1$ such that

$$|T\left(r\right) - r_0| \leq \alpha\, |r - r_0| \tag{7.72}$$

for all $r \in R$.

The first condition is satisfied because if $r_k = r_0$, (7.59) shows that

$$\Im\left\{\sum_{n=0}^{N-1} k_n a_n \overline{b_n} e^{-jk_n r_k}\right\} = 0 \tag{7.73}$$

But $r_{k+1} = T(r_k)$, which is

$$\Im\left\{e^{-j\bar{k}(r_{k+1}-r_k)}\sum_{n=0}^{N-1}k_n a_n \bar{b}_n e^{-jk_n r_k}\right\} = 0 \qquad (7.74)$$

Therefore $e^{-j\bar{k}(r_{k+1}-r_k)} = \pm 1$ and

$$r_{k+1} = r_k + l\frac{\pi}{\bar{k}} \qquad (7.75)$$

for some integer l. The only solution with $r_{k+1} \in R$ occurs when $l = 0$. Thus

$$r_{k+1} = r_k \qquad (7.76)$$

and r_0 is a fixed point of T.

To show that T is a contraction for all $r \in R$, define a new mapping $r'_{k+1} = T'(r'_k)$ from T by changing variables

$$r'_k = r_k - r_0 \qquad (7.77)$$

Then T' is given implicitly by

$$\Im\left\{e^{-j\bar{k}(r'_{k+1}-r'_k)}\sum_{n=0}^{N-1}c_n e^{-jk_n r'_k}\right\} = 0 \qquad (7.78)$$

where $c_n = k_n a_n \bar{b}_n e^{-jk_n r_0}$ and the domain of T' is

$$R' = \left\{r' \text{ such that } |r'| < \frac{\pi}{2\bar{k}}\right\} \qquad (7.79)$$

Also define Δ_k as

$$\Delta_k = \max_n \left|k_n - \bar{k}\right| \qquad (7.80)$$

Since r_0 is a fixed point of T, $r'_0 = r_0 - r_0 = 0$ is a fixed point of T'. One consequence of this is

$$\Im\left\{\sum_{n=0}^{N-1}c_n\right\} = 0 \qquad (7.81)$$

Now consider the image r'_{k+1} of some $r'_k \in R'$ under T'.

Multiplying the complex constant c_n by $e^{-jk_n r'_k}$ rotates c_n by an angle $\theta_n = -k_n r'_k$ which satisfies

$$|\theta_n| = k_n |r'_k| \leq \left(\bar{k} + \Delta_k\right)|r'_k| \qquad (7.82)$$

and

$$\left|\theta_n + \bar{k}r'_k\right| = \left|(k_n - \bar{k})r'_k\right| \leq \Delta_k |r'_k| \qquad (7.83)$$

Let θ be the angle that $\sum_{n=0}^{N-1} c_n$ is rotated to give $\sum_{n=0}^{N-1} c_n e^{-jk_n r'_k}$. Then

$$\min_n \theta_n \leq \theta \leq \max_n \theta_n \tag{7.84}$$

In particular,

$$|\theta| \leq \left(\overline{k} + \Delta_k \right) |r'_k| \tag{7.85}$$

and

$$\left| \theta + \overline{k} r'_k \right| \leq \Delta_k |r'_k| \tag{7.86}$$

From (7.78) and the definition of θ,

$$e^{-j\overline{k}(r'_{k+1} - r'_k)} = \pm e^{j\theta} \tag{7.87}$$

Therefore

$$\overline{k}(r'_{k+1} - r'_k) = \theta + l\pi \tag{7.88}$$

for some integer l which is set appropriately to ensure that r'_{k+1} is in R'. Thus

$$
\begin{aligned}
|l|\,\pi &= \left| \overline{k}(r'_{k+1} - r'_k) - \theta \right| \\
&\leq \overline{k}\left| r'_{k+1} \right| + \left| \theta + \overline{k} r'_k \right| \\
&< \frac{\pi}{2} \left(1 + \frac{\Delta_k}{\overline{k}} \right)
\end{aligned}
\tag{7.89}
$$

This has the unique solution $l = 0$ if $\Delta_k < \overline{k}$. Therefore

$$\overline{k}(r'_{k+1} - r'_k) = \theta \tag{7.90}$$

which can be rearranged into

$$\left| r'_{k+1} \right| = \frac{1}{\overline{k}} \left| \theta + \overline{k} r'_k \right| \leq \frac{\Delta_k}{\overline{k}} |r'_k| \tag{7.91}$$

So setting $\alpha' = \Delta_k / \overline{k}$ shows that

$$\left| r'_{k+1} \right| \leq \alpha' |r'_k| \tag{7.92}$$

and T' is a contraction mapping.

Expressing this in terms of T and r_k, T is a contraction mapping with fixed point r_0

$$|r_{k+1} - r_0| \leq \alpha |r_k - r_0| \tag{7.93}$$

providing

$$\alpha = \frac{\Delta_k}{\overline{k}} < 1 \tag{7.94}$$

Finally, applying the contraction mapping k times in succession shows that

$$|r_{k+1} - r_0| < \alpha^k |r - r_0| \tag{7.95}$$

to complete the proof.

7D   Corrected `MATLAB` Code to Implement the CZT

The chirp-Z transform routine that comes with `MATLAB` version 4.1 does not follow the notation used by Rabiner in [66] and [67]. This is a version of the MathWorks' `czt.m` routine that has been rewritten to follow Rabiner's notation. It also works for a chirp-Z transform giving fewer elements that the input vector.

```
function g = czt(x, m, w, a)
%CZT    Chirp-z transform.
%       G = CZT(X, M, W, A) returns:
%       G   the M-element chirp-z transform of data X,
%       X   the input matrix of signal columns
%       M   the length of the chirp z-transform
%       W   is the ratio W between points along the
%           complex-plane spiral contour of interest
%       A   the complex starting point on that contour

% Reference:
%  L.R. Rabiner, R.W. Schafer and C. M. Rader, The Chirp-Z
%  Transform and Its Application, Bell System Technical Journal,
%  May-June 1969, pp. 1249-1292.

% The original MATLAB algorithm, dated 15-Aug-90, did not work
% for M<N, and the circular convolution was specified
% differently from Rabiner et al.'s original paper.
% Rewritten by Stephen Simmons (simmons@ee.mu.oz.au), 16-Feb-94,
% to correct these problems and to follow Rabiner's notation.

[n, k] = size(x); oldn = n;
if n == 1, x = x(:); [n, k] = size(x); end

if nargin < 2, m = length(x); end
if nargin < 3, w = exp(-sqrt(-1) .* 2 .* pi ./ m); end
if nargin < 4, a = 1; end

%------- Length for power-of-two fft.
l = 1;
while l < (m + n - 1), l = 2 .* l; end

%------- Premultiply data.
aa=a.^([0:-1:-(n-1)].');
wn=w.^((([0:1:n-1].').^2)/2);
wm=w.^(-(([0:1:m-1].').^2)/2);
```

```
y=[x .* [(aa.*wn)*ones(1,k)]; zeros(l-n,k) ];

v=zeros(l,1);
v(1:m,1)=wm;
v(l-n+2:l,1)=1./wn([n-1:-1:1]);

%------- Fast convolution via FFT.
fy = fft(y);
fv = fft(v);
fy = fy .* ( fv * ones(1,k) );
g  = ifft( fy );

%------- Final multiply.
g = g(1:m,:) .* [ wm * ones(1,k) ];
if oldn == 1, g = g.'; end
```

Chapter 8

Statistical Properties of the Maximum Likelihood Motion Estimator

Broadly speaking, estimators may be divided into two classes, *simple* and *complex*. If simple estimators are defined as those which can be expressed as an explicit function of the measurements, $\widehat{\theta} = f(\boldsymbol{x})$, then complex estimators may be defined as the remainder that are not simple. Typically, complex estimators can only be expressed as implicit functions $f(\widetilde{\theta}, \boldsymbol{x}) = 0$ which require numerical, rather than analytical, solutions.

When analysing the performance of simple estimators, the mean and variance may be calculated exactly from the explicit functions giving the estimator in terms of the measurements. Complex estimators, by their very nature, usually do not allow such exact performance analyses. In such cases, approximate or asymptotic results for large samples are often calculated.

Since the definition of a maximum likelihood estimator takes the form of the location of the maximum of the likelihood function, many maximum likelihood estimators fall into the class of complex estimators. This makes exact analyses of their performance quite difficult. Nevertheless, because maximum likelihood estimators are asymptotically efficient under fairly general regularity conditions, asymptotic results like the Cramér-Rao bound are very commonly used.

For many maximum likelihood estimators, the asymptotic behaviour is almost trivial to derive while the corresponding non-asymptotic results are almost impossibly complicated. As a result, the asymptotic results are often applied to estimators using small data sets without checking how rapidly the estimator's behaviour becomes asymptotic.

This chapter is a detailed examination of the statistical properties of the

maximum likelihood motion estimator $\widehat{r}_{ml}$ derived in chapter 6. The regularity conditions for the estimator's asymptotic normality are established. The Fisher information matrix is used to calculate the Cramér-Rao lower bound on the variance of any unbiased estimator $\widehat{r}$ of Δr. The maximum likelihood estimator $\widehat{r}_{ml}$ is shown to be unbiased, hence the Cramér-Rao bound on any $\widehat{r}$ applies to $\widehat{r}_{ml}$. The analysis of $\widehat{r}_{ml}$ concludes with some tentative steps towards non-asymptotic statistical properties, and a discussion of why the estimator's variance is not the most important criterion for radar imaging.

The chapter concludes with analyses of the statistical properties of the maximum likelihood estimators of the noise variance σ_w^2 and the target's frequency response $\widehat{s}_{n,ml}$.

8.1   Conditions for Asymptotic Normality

The asymptotic normality of the maximum likelihood estimator of Δr will be established using the sufficient but not necessary regularity conditions of theorem 2.1. This requires that the log-likelihood function $\ln p(\boldsymbol{x};\boldsymbol{\theta})$ has well-defined first and second partial derivatives, and the expectations of the first partial derivatives be zero.

The first and second partial derivatives of $\ln p(\boldsymbol{x};\boldsymbol{\theta})$ are given in appendix 8A while deriving the Fisher information matrix. The expectation of the first partial derivative of $\ln p(\boldsymbol{x};\boldsymbol{\theta})$ with respect to Δr is also zero because

$$
\begin{aligned}
\mathrm{E}\left\{\frac{\partial \ln p(\boldsymbol{x};\boldsymbol{\theta})}{\partial \Delta r}\right\} &= \mathrm{E}\left\{j\frac{1}{\sigma_w^2}\sum_{n=0}^{N-1} k_n\left(b_n\overline{s_n}e^{jk_n\Delta r} - \overline{b_n}s_n e^{-jk_n\Delta r}\right)\right\} \\
&= j\frac{1}{\sigma_w^2}\sum_{n=0}^{N-1} k_n\left(|s_n|^2 - |s_n|^2\right) \\
&= 0
\end{aligned}
\tag{8.1}
$$

Since the regularity conditions are satisfied, the maximum likelihood estimator $\widehat{r}_{ml}$ of Δr is asymptotically normal.[1] That is, as the number of frequencies sampled in each frequency response tends to infinity, the expected

---

[1]Strictly speaking, this conclusion is not valid because it has applied Kay's theorem about the asymptotic normality of the scalar maximum likelihood estimator to a vector estimator.

Rigorous results concerning the asymptotic normality of the maximum likelihood estimator are hard to find in the literature. Kay states a theorem regarding asymptotic normality [51, thm 7.3] but this begins "If ...$p(\boldsymbol{x};\boldsymbol{\theta})$ ...satisfies some 'regularity' conditions ...", never stating what these conditions might be. Rao [69, section 5f] considers only the assumptions required for asymptotic normality of a scalar maximum likelihood estimator. Even Stuart and Ord in *Kendall's Advanced Theory of Statistics* [93] do not state these regularity conditions; instead the reader is referred to a 1943 paper by Wald.

Having said this, there is nothing about $p(\boldsymbol{x};\boldsymbol{\theta})$ to suggest that $\widehat{r}_{ml}$ is not asymptotically normal. On the other hand, the $\widehat{s}_{n,ml}$ are not asymptotically normal, and the reason for this is discussed at the end of the chapter.

value of $\widehat{r}_{ml}$ is Δr

$$\mathrm{E}\left\{\widehat{r}_{ml}\right\} \to \Delta r \qquad \text{as } N \to \infty \tag{8.2}$$

and the variance of $\widehat{r}_{ml}$ tends to the Cramér-Rao bound

$$\mathrm{Var}\left\{\widehat{r}_{ml}\right\} \to \left(\boldsymbol{I}^{-1}(\boldsymbol{\theta})\right)_{22} \qquad \text{as } N \to \infty \tag{8.3}$$

The Cramér-Rao bound for $\widehat{r}_{ml}$ is $(\boldsymbol{I}^{-1}(\boldsymbol{\theta}))_{22}$, the second element on the diagonal of $\boldsymbol{I}^{-1}(\boldsymbol{\theta})$, because Δr is the second element of $\boldsymbol{\theta}$.

8.2   Cramér-Rao Bounds for Unbiased Estimators of Δr

In this section, a lower bound on the variance of any unbiased estimator of the radial motion $\widehat{r}$ of a radar target is obtained using the Cramér-Rao bound. This derivation is done twice, once for the case when Δr is the only unknown parameter, and once for the more realistic case when Δr is estimated along with the noise variance σ_w^2 and the target's frequency response s_n. A comparison of the resulting Cramér-Rao bound illustrates why assuming that Δr is the only unknown gives different statistical properties for the two estimators.

8.2.1   The Cramér-Rao Bound for Estimating Δr Only

The likelihood function for estimating Δr only when the noise variance σ_w^2 and the target's reflectivities s_n are known exactly, is given by equation (6.16)

$$p(\boldsymbol{x}; \Delta r) = \frac{2^N}{(\pi\sigma_w^2)^N} \; \exp\left(-\frac{1}{2\sigma_w^2} \sum_{n=0}^{N-1} \left|a_n - b_n e^{jk_n\Delta r}\right|^2\right) \tag{8.4}$$

Since only a single parameter Δr is unknown, the Fisher information matrix is scalar, and its inverse is its reciprocal. The information is

$$
\begin{aligned}
I(\Delta r) &= -\mathrm{E}\left\{\frac{\partial^2 \ln p(\boldsymbol{x}; \Delta r)}{\partial \Delta r^2}\right\} \\
&= \frac{1}{\sigma_w^2} \sum_{n=0}^{N-1} \Re\left\{k_n^2 \mathrm{E}\left\{a_n\overline{b_n}\right\} e^{-jk_n\Delta r}\right\} \\
&= \frac{1}{\sigma_w^2} \sum_{n=0}^{N-1} k_n^2 \left|s_n\right|^2
\end{aligned}
\tag{8.5}
$$

so the Cramér-Rao bound on the variance of any unbiased estimator $\widehat{r}$ of Δr is

$$\mathrm{Var}\left\{\widehat{r}\right\} \geq \frac{1}{I(\Delta r)} = \frac{\sigma_w^2}{\displaystyle\sum_{n=0}^{N-1} k_n^2 \left|s_n\right|^2} \tag{8.6}$$

8.2.2   The Cramér-Rao Bound for Estimating Δr With Other Parameters

Chapter 6 showed that the proper approach to estimating Δr was to include the noise variance and the target reflectivities along with Δr in a vector of unknown parameters

$$\boldsymbol{\theta} = \left[\sigma_w^2, \Delta r, s_0, s_1, \ldots, s_{N-1}\right]^T \tag{8.7}$$

As it happens, the expression for $\hat{r}_{ml}$ in (6.39) is independent of σ_w^2 and the s_n, and is the same estimator as (6.18) where Δr was the only unknown parameter.

Although the estimators of Δr for the two cases are identical, this does not mean that their statistical performances are identical. An estimator's performance depends on both the function giving the estimator in terms of the measurements and the model from which the estimator is derived. The model involving the multiple unknowns is different from the model involving Δr as the only unknown, so the statistical performances of the two $\hat{r}_{ml}$ estimators may well be different.

The Cramér-Rao bound on the covariance matrix $\boldsymbol{C}(\hat{\boldsymbol{\theta}})$ of any unbiased estimator $\hat{\boldsymbol{\theta}}$ of $\boldsymbol{\theta}$ requires the Fisher information matrix $\boldsymbol{I}(\boldsymbol{\theta})$. The elements of $\boldsymbol{I}(\boldsymbol{\theta})$ are calculated in appendix 8A using the rules for complex differentiation summarized in section 2.5. When the elements of $\boldsymbol{\theta}$ are ordered as in (8.7), the information matrix is the $(N+2) \times (N+2)$ matrix

$$\boldsymbol{I}(\boldsymbol{\theta}) = \frac{2}{\sigma_w^2} \begin{bmatrix} N/\sigma_w^2 & 0 & 0 & 0 & \cdots & 0 \\ 0 & \sum_{n=0}^{N-1} k_n^2 |s_n|^2 & -j\frac{1}{2}k_0\overline{s_0} & -j\frac{1}{2}k_1\overline{s_1} & \cdots & -j\frac{1}{2}k_{N-1}\overline{s_{N-1}} \\ 0 & j\frac{1}{2}k_0 s_0 & 1 & 0 & \cdots & 0 \\ 0 & j\frac{1}{2}k_1 s_1 & 0 & 1 & \cdots & 0 \\ \vdots & \vdots & \vdots & \vdots & \ddots & \vdots \\ 0 & j\frac{1}{2}k_{N-1}s_{N-1} & 0 & 0 & \cdots & 1 \end{bmatrix} \tag{8.8}$$

This has the block structure

$$\boldsymbol{I}(\boldsymbol{\theta}) = \frac{2}{\sigma_w^2} \left[\begin{array}{c|c} N/\sigma_w^2 & \boldsymbol{0} \\ \hline \boldsymbol{0} & \boldsymbol{M} \end{array} \right] \tag{8.9}$$

where $\boldsymbol{M}$ is

$$\boldsymbol{M} = \begin{bmatrix} 4\sum_{n=0}^{N-1}|z_n|^2 & \overline{z_0} & \overline{z_1} & \cdots & \overline{z_{N-1}} \\ z_0 & 1 & 0 & \cdots & 0 \\ z_1 & 0 & 1 & \cdots & 0 \\ \vdots & \vdots & \vdots & \ddots & \vdots \\ z_{N-1} & 0 & 0 & \cdots & 1 \end{bmatrix} \qquad (8.10)$$

with $z_n = j\frac{1}{2}k_n s_n$.

The inverse of $\boldsymbol{I}(\boldsymbol{\theta})$ has the form

$$\boldsymbol{I}^{-1}(\boldsymbol{\theta}) = \frac{\sigma_w^2}{2}\left[\begin{array}{c|c} \sigma_w^2/N & \mathbf{0} \\ \hline \mathbf{0} & \boldsymbol{M}^{-1} \end{array}\right] \qquad (8.11)$$

It can be shown (in appendix 8B) that the inverse of $\boldsymbol{M}$ is

$$\boldsymbol{M}^{-1} = \frac{1}{3\sum_{n=0}^{N-1}|z_n|^2}\begin{bmatrix} 1 \\ -z_0 \\ -z_1 \\ \vdots \\ -z_{N-1} \end{bmatrix}\begin{bmatrix} 1 \\ -z_0 \\ -z_1 \\ \vdots \\ -z_{N-1} \end{bmatrix}^H + \mathrm{diag}\,[0,1,1,\ldots,1] \qquad (8.12)$$

In particular, the diagonal elements of $\boldsymbol{I}^{-1}(\boldsymbol{\theta})$ are

$$\left[\frac{\sigma_w^4}{2N}, \frac{2\sigma_w^2}{s}, \frac{\sigma_w^2}{2}\left(1 + \frac{k_0^2\,|s_0|^2}{s}\right),\ldots,\frac{\sigma_w^2}{2}\left(1 + \frac{k_{N-1}^2\,|s_{N-1}|^2}{s}\right)\right] \qquad (8.13)$$

where

$$s = 3\sum_{n=0}^{N-1}k_n^2\,|s_n|^2 \qquad (8.14)$$

The second element on the diagonal of $\boldsymbol{I}^{-1}(\boldsymbol{\theta})$ is the Cramér-Rao lower bound on the variance of any unbiased estimator of Δr. Hence

$$\mathrm{Var}\,\{\widehat{r}\} \geq \frac{2\sigma_w^2}{3\sum_{n=0}^{N-1}k_n^2\,|s_n|^2} \qquad (8.15)$$

8.2.3   Comparison of the Cramér-Rao Bounds

Section 8.2.1 gave the Cramér-Rao bound on any unbiased estimator of Δr as

$$\mathrm{Var}\,\{\widehat{r}\} \geq \frac{1}{I(\Delta r)} = \frac{\sigma_w^2}{\sum_{n=0}^{N-1}k_n^2\,|s_n|^2} \qquad (8.16)$$

which applies if Δr is the only unknown parameter. Section 8.2.2 gave a different Cramér-Rao bound

$$\text{Var}\left\{\widehat{r}\right\} \geq (\boldsymbol{I}^{-1}(\boldsymbol{\theta}))_{22} = \frac{2\sigma_w^2}{3\sum\limits_{n=0}^{N-1} k_n^2 \left|s_n\right|^2} \tag{8.17}$$

which applies if Δr is part of the vector $\boldsymbol{\theta}$ of unknowns in (8.7).

Ordinarily, the Cramér-Rao bound for estimating Δr would be smaller when Δr is the only unknown than when Δr is merely one of a whole vector of unknowns. There is a simple reason why this is not the case, and that is that the two Cramér-Rao bounds are for different models. Eliminating the s_n from (6.7) to give (6.10) changes the model because if the s_n were genuinely known *a priori*, there would be no need use two measurements to eliminate them. Using two measurements means twice the noise, hence a doubling of the Cramér-Rao bound.

If Δr really were the only unknown parameter, the Cramér-Rao bound for estimating Δr alone could be found using by using the likelihood function from the standard model in (6.7) and assuming that every parameter but Δr was known perfectly. The Cramér-Rao bound is given by the reciprocal of $(\boldsymbol{I}(\boldsymbol{\theta}))_{22}$

$$\text{Var}\left\{\widehat{r}\right\} \geq \frac{1}{(\boldsymbol{I}(\boldsymbol{\theta}))_{22}} = \frac{\sigma_w^2}{2\sum\limits_{n=0}^{N-1} k_n^2 \left|s_n\right|^2} \tag{8.18}$$

Now, as expected, this bound is less than the bound in (8.17) where Δr was only one of many unknowns, and exactly half the bound in (8.16) where twice as many noisy measurements as necessary were used to estimate Δr.

This comparison of the Cramér-Rao bounds has indicated that the scalar $\widehat{r}_{ml}$ is estimating Δr based on (6.10) rather than the proper model in (6.7). Therefore, from this point on, any reference to $\widehat{r}_{ml}$ is assumed to refer to $\widehat{r}_{ml}$ found using vector maximum likelihood estimation, and the appropriate Cramér-Rao bound is that in (8.17).

8.3   Performance of $\widehat{r}_{ml}$

This section presents a performance analysis of $\widehat{r}_{ml}$. The estimator is shown to be unbiased independently of the number of measurements, so the Cramér-Rao bound calculated in (8.17) gives a lower bound on the variance of $\widehat{r}_{ml}$. This is followed by a brief outline of some non-asymptotic results.

8.3.1 Asymptotic Normality of $\widehat{r}_{ml}$

In section 8.1, the regularity conditions for asymptotic normality of $\widehat{r}_{ml}$ were established before the Cramér-Rao bound had been calculated. Now that the Cramér-Rao bound has been found in (8.17), the asymptotic distribution of $\widehat{r}_{ml}$ is normal with mean Δr and variance equal to the Cramér-Rao bound

$$\widehat{r}_{ml} \overset{d}{\sim} \mathcal{N}\left(\Delta r, \frac{2\sigma_w^2}{3\sum_{n=0}^{N-1} k_n^2 |s_n|^2}\right) \tag{8.19}$$

as $N \to \infty$.

8.3.2 Bias of $\widehat{r}_{ml}$

$\widehat{r}_{ml}$ is found by locating the maximum of $J(r)$. Since $J(r)$ is a function whose period is equal to the ISAR range ambiguity window

$$J(r) = J\left(r + k\frac{c}{2\Delta f}\right) \qquad \text{for any integer } k \tag{8.20}$$

the support of r must be restricted to some subinterval of the real line centred at r_0 of length $c/2\Delta f$.

The following theorem shows that $\widehat{r}_{ml}$ is an unbiased estimator of Δr. The proof assumes that the support of $J(r)$ has been located so that the centre of the ISAR range ambiguity window r_0 is at $r = \Delta r$.

Theorem 8.1 *The maximum likelihood estimator $\widehat{r}_{ml}$ of the target's radial motion found using (6.17) and (6.18)*

$$\widehat{r}_{ml} = \arg\min_r J(r) \tag{8.21}$$

where

$$J(r) = \sum_{n=0}^{N-1} \left|a_n - b_n e^{jk_n r}\right|^2 \tag{8.22}$$

is an unbiased estimator of Δr when the support of $J(r)$ is centred at $r_0 = \Delta r$ and has length $c/2\Delta f$.

Proof: This proof shows that the probability density function of $J(r)$ is symmetric about $r = \Delta r$, so that the probability density function of $\widehat{r}_{ml}$ is also symmetric about $r = \Delta r$. From this, the expectation of $\widehat{r}_{ml}$ is shown to be Δr.

Using (6.7) to write $J(r)$ in terms of

$$a_n = s_n + w_{1,n}$$
$$b_n = s_n e^{-jk_n \Delta r} + w_{2,n} \tag{8.23}$$

where $w_{1,n}$ and $w_{2,n}$ are zero mean additive white Gaussian noise, shows that

$$J(r) = \sum_{n=0}^{N-1} \left| s_n \left(1 - e^{-jk_n(\Delta r - r)} \right) + \left(w_{1,n} - w_{2,n} e^{jk_n r} \right) \right|^2 \tag{8.24}$$

When r is written as $\Delta r + r$ to make the symmetry about $r = \Delta r$ more apparent,

$$J(\Delta r + r) = \sum_{n=0}^{N-1} \left| s_n \left(1 - e^{jk_n r} \right) + \left(w_{1,n} - w_{2,n} e^{jk_n(\Delta r + r)} \right) \right|^2 \tag{8.25}$$

At the point r from Δr in the opposite direction,

$$J(\Delta r - r) = \sum_{n=0}^{N-1} \left| s_n \left(1 - e^{-jk_n r} \right) + \left(w_{1,n} - w_{2,n} e^{jk_n(\Delta r - r)} \right) \right|^2$$

$$= \sum_{n=0}^{N-1} \left| s_n \left(1 - e^{jk_n r} \right) - e^{jk_n r} \left(w_{1,n} - w_{2,n} e^{jk_n(\Delta r - r)} \right) \right|^2$$

$$= \sum_{n=0}^{N-1} \left| s_n \left(1 - e^{jk_n r} \right) + \left(w_{2,n} e^{jk_n \Delta r} - w_{1,n} e^{jk_n r} \right) \right|^2$$

$$= \sum_{n=0}^{N-1} \left| s_n \left(1 - e^{jk_n r} \right) + \left(w_{1,n}' - w_{2,n}' e^{jk_n(\Delta r + r)} \right) \right|^2 \tag{8.26}$$

where

$$w_{1,n}' = w_{2,n} e^{jk_n \Delta r} \tag{8.27}$$

and

$$w_{2,n}' = w_{1,n} e^{-jk_n \Delta r} \tag{8.28}$$

Multiplying $w_{1,n}$ by the constant phase shift $e^{-jk_n \Delta r}$ does not change the statistical properties of $w_{1,n}$ because its probability density function is independent of phase angle. Therefore $w_{2,n}'$ is equivalent, statistically, to $w_{1,n}$. Similarly, $w_{1,n}'$ is equivalent to $w_{2,n}$. Since $w_{1,n}$ and $w_{2,n}$ have identical statistical properties, so do $w_{1,n}'$ and $w_{2,n}'$.

Comparing equations (8.25) and (8.26) shows that they have identical statistical properties. Therefore the probability density function of $J(\Delta r + r)$ is equal to the probability density function of $J(\Delta r - r)$.

Because $\hat{r}_{ml}$ is the location of the maximum of $J(r)$ and the probability density function of $J(r)$ is symmetric about $r = \Delta r$, the probability density function of $\hat{r}_{ml}$ is also symmetric about $r = \Delta r$. Writing $p_r(r)$ for the probability density function of $\hat{r}_{ml}$, this means that

$$p_r(\Delta r + r) = p_r(\Delta r - r) \tag{8.29}$$

Now the support of $p_r(r)$ is not the whole real line $(-\infty, \infty)$, but the ISAR range ambiguity window $\left(\Delta r - \frac{c}{4\Delta f}, \Delta r + \frac{c}{4\Delta f}\right)$. Therefore the expectation of $\widehat{r}_{ml}$ is

$$
\begin{aligned}
\mathrm{E}\left\{\widehat{r}_{ml}\right\} &= \int_{\Delta r - \frac{c}{4\Delta f}}^{\Delta r + \frac{c}{4\Delta f}} r\, p_r(r)\, dr \\
&= \int_{\Delta r - \frac{c}{4\Delta f}}^{\Delta r + \frac{c}{4\Delta f}} \Delta r\, p_r(r)\, dr + \int_{\Delta r - \frac{c}{4\Delta f}}^{\Delta r + \frac{c}{4\Delta f}} (r - \Delta r)\, p_r(r)\, dr \\
&= \Delta r \int_{\Delta r - \frac{c}{4\Delta f}}^{\Delta r + \frac{c}{4\Delta f}} p_r(r)\, dr + \int_{-\frac{c}{4\Delta f}}^{\frac{c}{4\Delta f}} r\, p_r(\Delta r + r)\, dr \\
&= \Delta r \cdot 1 + 0 \\
&= \Delta r
\end{aligned}
\tag{8.30}
$$

Here the integral of $r\, p_r(\Delta r + r)$ is zero because the integrand is odd, being the product of an even function $p_r(\Delta r + r)$ and an odd function r. ∎

This proof shows that $\widehat{r}_{ml}$ is an unbiased estimator of Δr when the ISAR range ambiguity window is centred on Δr. If the window were moved so that Δr was no longer at the centre, $\widehat{r}_{ml}$ would appear biased. However this bias is the result of artificially constraining the support of $J(r)$ when taking the expectation of $\widehat{r}_{ml}$. The correct approach is to join the ends of the range ambiguity window together to form a cylinder. Then with the expectation modified to make it suitable for periodic functions, $\widehat{r}_{ml}$ is always unbiased.

Finally, because $\widehat{r}_{ml}$ is an unbiased estimator of Δr, the variance of $\widehat{r}_{ml}$ is greater than the Cramér-Rao bound in (8.17)

$$
\mathrm{Var}\left\{\widehat{r}_{ml}\right\} \geq \frac{2\sigma_w^2}{3\sum_{n=0}^{N-1} k_n^2 |s_n|^2}
\tag{8.31}
$$

8.3.3 Non-Asymptotic Results

Non-asymptotic results for the statistical performance of $\widehat{r}_{ml}$ are much harder to obtain than the asymptotic results. The basic result needed is the probability density function of $\widehat{r}_{ml}$ because the variance and other properties can be derived from it.

If $J(r)$ is expressed in complex form as in appendix 7A, it may be possible to derive one expression for the probability density function of the location of the maximum of the magnitude of $J(r)$, and another for the probability density function of the locations of the points where the phase is a multiple of 2π. Then by combining the two separate probability density functions, it may be possible to obtain at least an approximate probability density function for $\widehat{r}_{ml}$.

Expressions for the probability density function of the location of the maximum likelihood frequency estimator based on a fast Fourier transform have been obtained by Ritcey [77]. This gives a discrete form of the probability density function of $\widehat{r}_{ml}$ at intervals of an ISAR range bin, although it is not in a form that can be used conveniently.[2]

The other end of the scale is the probability density function of estimates of the location of each local minimum of the cost function $J(r)$. This can be used to see how clustered the estimates of Δr are around multiples of half a wavelength. An approximate solution of this is derived in appendix 8C.

These results are not sufficiently complete to discuss further, except to say that the variance of $\widehat{r}_{ml}$ is not a good guide to the performance of the radial motion estimator for radar imaging. The variance of $\widehat{r}_{ml}$ measures the total spread of estimates of Δr, ignoring the clustering of the errors at intervals of half a wavelength. But as long as the total spread is not too wide, the clustering is more important for focusing ISAR images than the total spread.[3] Therefore some better measure than variance is needed for comparing different motion estimators.

8.4   Performance of $\widehat{\sigma}^2_{w,ml}$

The maximum likelihood estimator of the noise variance is given in (6.43) as $1/4N$ times the minimum of $J(r)$, or

$$\widehat{\sigma}^2_{w,ml} = \frac{1}{4N} \sum_{n=0}^{N-1} \left| a_n - b_n e^{jk_n \widehat{r}_{ml}} \right|^2 \tag{8.32}$$

If $\widehat{r}_{ml}$ were known exactly, then substituting in the expressions for a_n and b_n in terms of the target's noisy frequency responses would show that

$$\mathrm{E}\left\{\widehat{\sigma}^2_{w,ml}\right\} = \sigma^2_w \tag{8.33}$$

However, $\widehat{r}_{ml}$ has to be estimated, so the actual expectation of $\widehat{\sigma}^2_{w,ml}$ turns out to be

$$\mathrm{E}\left\{\widehat{\sigma}^2_{w,ml}\right\} = \frac{\sigma^2_w}{2} \tag{8.34}$$

This is a consequence of $\widehat{r}_{ml}$ being estimated from two sets of frequency responses. If $\widehat{r}_{ml}$ were estimated from M frequency responses, the expectation would be

$$\mathrm{E}\left\{\widehat{\sigma}^2_{w,ml}\right\} = \sigma^2_w \frac{M-1}{M} \tag{8.35}$$

---

[2]This suggests the general problem of finding the probability density function of the location of the maximum of a known bandlimited function in bandlimited noise. See 11.1 on page 187 for a longer discussion of this.

[3]This is analyses in section 10.5.

which is similar to the bias of the standard deviation of a sample. If $M \to \infty$, then $\widehat{\sigma}^2_{w,ml}$ would become unbiased. However, the averaging does not work like this as M is fixed at 2 and the expectation of $\widehat{\sigma}^2_{w,ml}$ is always half the true noise variance.

Since the bias is a constant factor, an unbiased estimator of the noise variance is given by

$$\widehat{\sigma^2_w} = 2\widehat{\sigma}^2_{w,ml} \tag{8.36}$$

8.5 Performance of $\widehat{s}_{n,ml}$

The maximum likelihood estimators $\widehat{s}_{n,ml}$ of the target's frequency response s_n at each of the N frequencies are biased. Their expectation is

$$\begin{aligned}
\mathrm{E}\left\{\widehat{s}_{n,ml}\right\} &= \mathrm{E}\left\{\frac{1}{2}\left(a_n + b_n e^{jk_n\widehat{r}_{ml}}\right)\right\} \\
&= \mathrm{E}\left\{\frac{1}{2}\left(s_n + s_n e^{-jk_n\Delta r}e^{jk_n\widehat{r}_{ml}}\right)\right\} \\
&= s_n \cdot \frac{1}{2}\left(1 + \mathrm{E}\left\{e^{-jk_n(\Delta r - \widehat{r}_{ml})}\right\}\right)
\end{aligned} \tag{8.37}$$

If the motion estimator $\widehat{r}_{ml}$ were exact, $\widehat{s}_{n,ml}$ would be unbiased

$$\mathrm{E}\left\{\widehat{s}_{n,ml}\right\} = s_n \tag{8.38}$$

Working out the exact bias requires

$$\mathrm{E}\left\{e^{-jk_n(\Delta r - \widehat{r}_{ml})}\right\} = \int e^{-jk_n(\Delta r - r)}\,p_r(r)\,dr \tag{8.39}$$

to be evaluated, where $p_r(r)$ is the probability density function of $\widehat{r}_{ml}$.

At this stage, the probability density function of $\widehat{r}_{ml}$ is unknown. But if it is assumed that $\widehat{r}_{ml}$ is Gaussian (since it is asymptotically Gaussian) with variance $\sigma^2_{r_{ml}}$, the identity [1, 7.4.6–7]

$$\int_{-\infty}^{\infty} e^{-at^2}\,e^{j2xt}\,dt = \frac{1}{2}\sqrt{\frac{\pi}{a}}e^{-x^2/a^2} \tag{8.40}$$

shows that

$$\mathrm{E}\left\{\widehat{s}_{n,ml}\right\} = s_n \frac{1 + e^{-k_n^2\sigma^2_{r_{ml}}/2}}{2} \tag{8.41}$$

So when there is little noise, $\sigma^2_{r_{ml}}$ is close to zero and $\widehat{s}_{n,ml}$ is nearly unbiased. As the noise level increases, $\widehat{s}_{n,ml}$ gets more and more biased, until at extremely high noise levels, the expected value of $\widehat{s}_{n,ml}$ is half the true value s_n.

In practice, the bias of $\widehat{s}_{n,ml}$ does not matter because estimating $\widehat{r}_{ml}$ does not require estimates of the s_n.

8A Elements of the Fisher Information Matrix

The Fisher information matrix $\boldsymbol{I}(\boldsymbol{\theta}) = (I_{ij})$ has elements

$$I_{ij} = -\mathrm{E}\left\{\frac{\partial^2 \ln p(\boldsymbol{x};\boldsymbol{\theta})}{\partial \overline{\theta}_i \partial \theta_j}\right\} \tag{8.42}$$

where the vector of parameters being estimated, $\boldsymbol{\theta}$, is given in (8.7) and the likelihood function is

$$p(\boldsymbol{x};\boldsymbol{\theta}) = \frac{1}{(\pi\sigma_w^2)^{2N}} \exp\left(-\frac{1}{\sigma_w^2}\sum_{n=0}^{N-1} |a_n - s_n|^2 + |b_n - s_n e^{-jk_n\Delta r}|^2\right) \tag{8.43}$$

The first partial derivatives of the likelihood function are

$$\frac{\partial \ln p(\boldsymbol{x};\boldsymbol{\theta})}{\partial \sigma_w^2} = -\frac{2N}{\sigma_w^2} + \frac{1}{\sigma_w^4}\sum_{n=0}^{N-1} |a_n - s_n|^2 + |b_n - s_n e^{-jk_n\Delta r}|^2 \tag{8.44}$$

$$\frac{\partial \ln p(\boldsymbol{x};\boldsymbol{\theta})}{\partial \Delta r} = -j\frac{1}{\sigma_w^2}\sum_{n=0}^{N-1} k_n\left(b_n\overline{s_n}e^{jk_n\Delta r} - \overline{b_n}s_n e^{-jk_n\Delta r}\right) \tag{8.45}$$

$$\frac{\partial \ln p(\boldsymbol{x};\boldsymbol{\theta})}{\partial s_n} = -\frac{1}{\sigma_w^2}\left[(\overline{s_n} - \overline{a_n}) + \left(\overline{s_n} - \overline{b_n}e^{-jk_n\Delta r}\right)\right] \tag{8.46}$$

$$\frac{\partial \ln p(\boldsymbol{x};\boldsymbol{\theta})}{\partial \overline{s_n}} = -\frac{1}{\sigma_w^2}\left[(s_n - a_n) + \left(s_n - b_n e^{jk_n\Delta r}\right)\right] \tag{8.47}$$

The elements on the diagonal of $\boldsymbol{I}(\boldsymbol{\theta})$ are

$$-\mathrm{E}\left\{\frac{\partial^2 \ln p(\boldsymbol{x};\boldsymbol{\theta})}{\partial \overline{\sigma_w^2} \partial \sigma_w^2}\right\} = -\mathrm{E}\left\{\frac{2N}{\sigma_w^4} - \frac{2}{\sigma_w^6}\sum_{n=0}^{N-1} |a_n - s_n|^2 + |b_n - s_n e^{-jk_n\Delta r}|^2\right\}$$

$$= -\frac{2N}{\sigma_w^4} + \frac{2}{\sigma_w^6}\sum_{n=0}^{N-1}\mathrm{E}\left\{|w_{1,n}|^2 + |w_{2,n}|^2\right\}$$

$$= -\frac{2N}{\sigma_w^4} + \frac{4N}{\sigma_w^4}$$

$$= \frac{2N}{\sigma_w^4} \tag{8.48}$$

$$-\mathrm{E}\left\{\frac{\partial^2 \ln p(\boldsymbol{x};\boldsymbol{\theta})}{\partial \overline{\Delta r} \partial \Delta r}\right\} = \mathrm{E}\left\{\frac{2}{\sigma_w^2}\Re\left\{\sum_{n=0}^{N-1} k_n b_n \overline{s_n} e^{jk_n\Delta r}\right\}\right\}$$

$$= \frac{2}{\sigma_w^2}\Re\left\{\sum_{n=0}^{N-1} k_n^2 \mathrm{E}\left\{b_n\right\}\overline{s_n}e^{jk_n\Delta r}\right\}$$

$$= \frac{2}{\sigma_w^2}\sum_{n=0}^{N-1} k_n^2 |s_n|^2 \tag{8.49}$$

$$-\mathrm{E}\left\{\frac{\partial^2 \ln p(\boldsymbol{x};\boldsymbol{\theta})}{\partial \overline{s_n}\partial s_n}\right\} = \mathrm{E}\left\{\frac{2}{\sigma_w^2}\right\}$$

$$= \frac{2}{\sigma_w^2} \tag{8.50}$$

The elements of $\boldsymbol{I}(\boldsymbol{\theta})$ whose partial derivatives involve σ_w^2 are zero, as the following shows:

$$-\mathrm{E}\left\{\frac{\partial^2 \ln p(\boldsymbol{x};\boldsymbol{\theta})}{\partial \overline{\sigma_w^2}\partial \Delta r}\right\} = \mathrm{E}\left\{\frac{2N}{\sigma_w^4}\Im\left\{\sum_{n=0}^{N-1} k_n b_n \overline{s_n} e^{jk_n\Delta r}\right\}\right\}$$

$$= \frac{2N}{\sigma_w^4}\Im\left\{\sum_{n=0}^{N-1} k_n \left|s_n\right|^2\right\}$$

$$= 0 \tag{8.51}$$

$$-\mathrm{E}\left\{\frac{\partial^2 \ln p(\boldsymbol{x};\boldsymbol{\theta})}{\partial \overline{\sigma_w^2}\partial s_n}\right\} = -\mathrm{E}\left\{\frac{1}{\sigma_w^4}\left[\left(\overline{s_n} - \overline{a_n}\right) + \left(\overline{s_n} - \overline{b_n}e^{-jk_n\Delta r}\right)\right]\right\}$$

$$= -\frac{1}{\sigma_w^4}\left[\mathrm{E}\left\{\overline{w_{1,n}}\right\} + \mathrm{E}\left\{\overline{w_{2,n}}\right\}e^{-jk_n\Delta r}\right]$$

$$= 0 \tag{8.52}$$

The elements of $\boldsymbol{I}(\boldsymbol{\theta})$ whose partial derivatives involve Δr and s_n are

$$-\mathrm{E}\left\{\frac{\partial^2 \ln p(\boldsymbol{x};\boldsymbol{\theta})}{\partial \overline{\Delta r}\partial s_n}\right\} = \mathrm{E}\left\{-j\frac{1}{\sigma_w^2}k_n \overline{b_n} e^{-jk_n\Delta r}\right\}$$

$$= -j\frac{k_n\overline{s_n}}{\sigma_w^2}$$

$$\tag{8.53}$$

$$-\mathrm{E}\left\{\frac{\partial^2 \ln p(\boldsymbol{x};\boldsymbol{\theta})}{\partial \overline{\Delta r}\partial s_n}\right\} = \overline{-\mathrm{E}\left\{\frac{\partial^2 \ln p(\boldsymbol{x};\boldsymbol{\theta})}{\partial \overline{s_n}\partial \Delta r}\right\}}$$

$$= j\frac{k_n s_n}{\sigma_w^2} \tag{8.54}$$

This leaves the elements whose partial derivatives involve s_m and s_n where $m \neq n$. All $N^2 - N$ of these are zero.

$$-\mathrm{E}\left\{\frac{\partial^2 \ln p(\boldsymbol{x};\boldsymbol{\theta})}{\partial \overline{s_m}\partial s_n}\right\} = 0 \tag{8.55}$$

8B   Inverse of Fisher's Information Matrix

Taking the inverse of $\boldsymbol{I}(\boldsymbol{\theta})$ involves inverting the submatrix which is left when $\boldsymbol{I}(\boldsymbol{\theta})$ has its first row and column removed. The general inverse for matrices of this form is the subject of the following theorem.

Theorem 8.2 *The inverse of the matrix*

$$
\boldsymbol{M} =
\begin{bmatrix}
c & \overline{z_0} & \overline{z_1} & \cdots & \overline{z_{N-1}} \\
z_0 & 1 & 0 & \cdots & 0 \\
z_1 & 0 & 1 & \cdots & 0 \\
\vdots & \vdots & \vdots & \ddots & \vdots \\
z_{N-1} & 0 & 0 & \cdots & 1
\end{bmatrix}
\tag{8.56}
$$

where

$$
c = 4 \sum_{n=0}^{N-1} |z_n|^2
\tag{8.57}
$$

is

$$
\boldsymbol{M}^{-1} = \frac{1}{3 \sum\limits_{n=0}^{N-1} |z_n|^2} \boldsymbol{v}\,\boldsymbol{v}^H + \boldsymbol{D}
\tag{8.58}
$$

where $\boldsymbol{v}$ is

$$
\boldsymbol{v} =
\begin{bmatrix}
1 \\
-z_0 \\
-z_1 \\
\vdots \\
-z_{N-1}
\end{bmatrix}
\tag{8.59}
$$

and $\boldsymbol{D}$ is the diagonal matrix

$$
\boldsymbol{D} = \operatorname{diag}\left[0, 1, 1, \ldots, 1\right]
\tag{8.60}
$$

Proof: Note that

$$
\boldsymbol{M}\boldsymbol{v}\boldsymbol{v}^H = \left(c - \sum_{n=0}^{N-1} |z_n|^2 \right)
\begin{bmatrix}
1 & -\overline{z_0} & -\overline{z_1} & \cdots & -\overline{z_{N-1}} \\
0 & 0 & 0 & \cdots & 0 \\
0 & 0 & 0 & \cdots & 0 \\
\vdots & \vdots & \vdots & \ddots & \vdots \\
0 & 0 & 0 & \cdots & 0
\end{bmatrix}
\tag{8.61}
$$

and that

$$
\boldsymbol{M}\boldsymbol{D} =
\begin{bmatrix}
0 & \overline{z_0} & \overline{z_1} & \cdots & \overline{z_{N-1}} \\
0 & 1 & 0 & \cdots & 0 \\
0 & 0 & 1 & \cdots & 0 \\
\vdots & \vdots & \vdots & \ddots & \vdots \\
0 & 0 & 0 & \cdots & 1
\end{bmatrix}
\tag{8.62}
$$

Therefore

$$
\boldsymbol{M}\left(\frac{1}{3 \sum\limits_{n=0}^{N-1} |z_n|^2} \boldsymbol{v}\boldsymbol{v}^H + \boldsymbol{D} \right) = \boldsymbol{I}
\tag{8.63}
$$

This shows that $MM^{-1} = I$.

To show that $M^{-1}M = I$ — the other condition needed for M^{-1} to be the inverse of M — note that both M and M^{-1} are Hermitian. Then

$$
\begin{aligned}
M^{-1}M &= \left[\left(M^{-1}M\right)^H\right]^H \\
&= \left[M^H\left(M^{-1}\right)^H\right]^H \\
&= \left[M\,M^{-1}\right]^H \\
&= I^H \\
&= I
\end{aligned}
\tag{8.64}
$$

Therefore M^{-1} in (8.58) is the inverse of M. ∎

This result can also be obtained by applying the Sherman-Morrison formula [36]

$$
(A + uv^H)^{-1} = A^{-1} - \frac{A^{-1}uv^H A^{-1}}{1 + v^H A^{-1}u}
\tag{8.65}
$$

two times in succession to

$$
M = I + uv^H + vu^H
\tag{8.66}
$$

where

$$
u = \left[\frac{c-1}{2}, z_0, z_1, \ldots, z_{N-1}\right]^H
\tag{8.67}
$$

and

$$
v = [1, 0, 0, \ldots, 0]^H
\tag{8.68}
$$

8C Probability Density Function of Each Local Minimum of $J(r)$

This appendix derives an approximate expression for the probability density function of estimates of the location of each local minimum of the cost function $J(r)$. The variance and other properties of the estimates of Δr given by algorithm 7.6 can be calculated numerically from this probability density function.

8C.1 Conditions for a Local Minimum of $J(r)$

Suppose that $r = r_0$ is the location of a local minimum of $J(r)$ when noise is not present. When noise is added to the frequency responses, the location

of the local minimum of $J(r)$ closest to r_0 is now $r_0 + \epsilon_r$ where ϵ_r is the error caused by the presence of noise. Then

$$\left. \frac{\partial J(r)}{\partial r} \right|_{r=r_0+\epsilon_r} = 0 \tag{8.69}$$

Differentiating the cost function $J(r)$ in (6.39) gives the equation

$$\Im \left\{ \sum_{n=0}^{N-1} k_n a_n \overline{b_n} e^{-jk_n(r_0+\epsilon_r)} \right\} = 0 \tag{8.70}$$

Substituting the noisy frequency responses in (6.7) into this gives

$$\Im \left\{ \sum_{n=0}^{N-1} k_n (s_n + w_{1,n})(\overline{s_n} e^{jk_n\Delta r} + \overline{w_{2,n}}) e^{-jk_n(r_0+\epsilon_r)} \right\} = 0 \tag{8.71}$$

which can be expressed as

$$\Im \left\{ \sum_{n=0}^{N-1} k_n (s_n + w_{1,n})(\overline{s_n} + \overline{w_{2,n}} e^{-jk_n\Delta r}) e^{-jk_n(r_0+\epsilon_r-\Delta r)} \right\} = 0 \tag{8.72}$$

This can be simplified by noting that each of the $w_{2,n}$ noise terms is the realization of a complex Gaussian random process, so the probability density function of their phases is uniform over $[0, 2\pi)$. Therefore shifting the phase of each $w_{2,n}$ by $-k_n\Delta r$ gives random variables with identical probability density functions to the original random variables. So each $w_{2,n} e^{jk_n\Delta r}$ can be replaced by $w_{2,n}$ for notational convenience without altering the statistical properties of $J(r)$. Hence

$$\Im \left\{ \sum_{n=0}^{N-1} k_n (s_n + w_{1,n})(\overline{s_n} + \overline{w_{2,n}}) e^{-jk_n(r_0+\epsilon_r-\Delta r)} \right\} = 0 \tag{8.73}$$

Separating the initial frequency k_0 from the frequency steps gives

$$\Im \left\{ e^{-jk_0(r_0+\epsilon_r-\Delta r)} \sum_{n=0}^{N-1} k_n (s_n + w_{1,n})(\overline{s_n} + \overline{w_{2,n}}) e^{-jn\Delta k(r_0+\epsilon_r-\Delta r)} \right\} = 0 \quad (8.74)$$

Since this can only be solved unambiguously for ϵ_r over an interval containing r_0 whose extent is half the carrier wavelength, the magnitude of ϵ_r is limited by

$$|\epsilon_r| < \frac{c}{8f_0} \tag{8.75}$$

Over this interval, the phase of $e^{-jn\Delta k\epsilon_r}$ varies negligibly in comparison to the phase of $e^{-jk_0\epsilon_r}$ for all values of n because of the narrow relative bandwidth.

Therefore the ϵ_r term can be omitted from the second complex exponential in (8.74) to give the very good approximation

$$\Im\left\{e^{-jk_0(r_0+\epsilon_r-\Delta r)}\sum_{n=0}^{N-1}k_n(s_n+w_{1,n})(\overline{s_n}+\overline{w_{2,n}})e^{-jn\Delta k(r_0-\Delta r)}\right\}=0 \quad (8.76)$$

This can be written

$$\Im\left\{d\,e^{-jk_0\epsilon_r}\right\}=0 \quad (8.77)$$

where d is the random variable

$$d=\sum_{n=0}^{N-1}k_n(s_n+w_{1,n})(\overline{s_n}+\overline{w_{2,n}})e^{-jk_n(r_0-\Delta r)} \quad (8.78)$$

From this, if the phase of d varies by $\delta\phi$, the phase of $e^{-jk_0\epsilon_r}$ must vary by $-\delta\phi$ to keep the imaginary part of (8.77) zero. So the probability density function of the angle of d completely determines the probability density function of ϵ_r.

8C.2 Statistical Characteristics of d

Since the noise processes $w_{1,n}$ and $w_{2,n}$ are independent zero-mean complex Gaussians with variance σ_w^2, their expectations, variances and covariances are given by

$$\mathrm{E}\left\{w_{1,n}\right\}=\mathrm{E}\left\{w_{2,n}\right\}=0$$
$$\mathrm{E}\left\{w_{1,m}\overline{w_{1,n}}\right\}=\mathrm{E}\left\{w_{2,m}\overline{w_{2,n}}\right\}=\sigma_w^2\delta_{m,n}$$
$$\mathrm{E}\left\{w_{1,m}w_{1,n}\right\}=\mathrm{E}\left\{w_{2,m}w_{2,n}\right\}=0$$
$$\mathrm{E}\left\{w_{1,m}w_{2,n}\right\}=\mathrm{E}\left\{w_{1,m}\overline{w_{2,n}}\right\}=\mathrm{E}\left\{\overline{w_{1,m}}w_{1,n}\right\}=\mathrm{E}\left\{\overline{w_{2,m}}w_{2,n}\right\}=0 \quad (8.79)$$

Using these, the expected value of the random variable d given by (8.78) is

$$\mu_d=\mathrm{E}\left\{d\right\}=\sum_{n=0}^{N-1}k_n\left|s_n\right|^2 e^{-jk_n(r_0-\Delta r)} \quad (8.80)$$

and the variance is

$$\sigma_d^2=\mathrm{E}\left\{\left|d-\mathrm{E}\left\{d\right\}\right|^2\right\}=\sum_{n=0}^{N-1}k_n^2\sigma_w^2\left[2\left|s_n\right|^2+\sigma_w^2\right] \quad (8.81)$$

d can be broken into two parts d_g and d_c, which respectively are the Gaussian components of d

$$d_g=\sum_{n=0}^{N-1}k_n(\left|s_n\right|^2+\overline{s_n}w_{1,n}+s_n\overline{w_{2,n}})e^{-jk_n(r_0-\Delta r)} \quad (8.82)$$

and the non-Gaussian components

$$d_c = \sum_{n=0}^{N-1} k_n w_{1,n} \overline{w_{2,n}} e^{-jk_n(r_0 - \Delta r)} \tag{8.83}$$

It is shown in appendix 8D that $w_{1,n} \overline{w_{2,n}} e^{-jk_n(r_0 - \Delta r)}$ has the probability density function $p_w(z)$ where

$$p_w(z) = \frac{2}{\pi \sigma_w^4} K_0 \left(\frac{2|z|}{\sigma_w^2} \right) \tag{8.84}$$

Here $K_0(x)$ is the modified Bessel function defined in (8.116).

Now, the N terms of d_c are independent and approximately identically distributed, so by the central limit theorem, d_c/N tends to a Gaussian random variable as $N \to \infty$. For stepped-frequency waveforms, N does not tend to infinity. However, for adequate range resolution for radar imaging, N has to be sufficiently large that the Gaussian random variable approximation is very good.

Since d_g is Gaussian and d_c is approximately Gaussian, d is approximately a Gaussian random variable with mean and variance

$$\mu_d = \sum_{n=0}^{N-1} k_n |s_n|^2 e^{-jk_n(r_0 - \Delta r)} \tag{8.85}$$

and

$$\sigma_d^2 = \sum_{n=0}^{N-1} k_n^2 \sigma_w^2 \left[2 |s_n|^2 + \sigma_w^2 \right] \tag{8.86}$$

respectively.

8C.3 The Probability Density Function of ϵ_r

The probability density function of d, $p_d(z)$, is approximately that of a complex Gaussian process with mean μ_d and variance σ_d^2

$$p_d(z) = \frac{1}{\pi \sigma_d^2} e^{-|z - \mu_d|^2 / \sigma_d^2} \tag{8.87}$$

This can be converted to the probability density function of θ, the angle of d, by changing variables to polar coordinates and integrating over magnitudes from 0 to ∞

$$p_\Theta(\theta) = \int_0^\infty p_d(re^{j\theta}) \, r \, dr$$

$$= \frac{1}{\pi \sigma_d^2} \int_0^\infty e^{-\left| re^{j\theta} - \mu_d \right|^2 / \sigma_d^2} r \, dr \tag{8.88}$$

The exponent $\left|re^{j\theta} - \mu_d\right|^2$ can be written in a more tractable form using

$$\left|re^{j\theta} - \mu_d\right|^2 = \left|r - \mu_d e^{-j\theta}\right|^2$$
$$= (r - a(\theta))^2 + b^2(\theta) \tag{8.89}$$

where $a(\theta)$ and $b(\theta)$ are

$$a(\theta) = \Re\left\{\mu_d e^{-j\theta}\right\} \tag{8.90}$$
$$b(\theta) = \Im\left\{\mu_d e^{-j\theta}\right\} \tag{8.91}$$

Then

$$p_\Theta(\theta) = \frac{1}{\pi\sigma_d^2} e^{-b^2(\theta)/\sigma_d^2} \int_0^\infty r e^{-(r-a(\theta))^2/\sigma_d^2}\,dr \tag{8.92}$$

Now

$$\int_0^\infty r e^{-(r-a(\theta))^2/\sigma_d^2}\,dr$$
$$= \int_0^\infty (r - a(\theta))\, e^{-(r-a(\theta))^2/\sigma_d^2}\,dr + a(\theta) \int_0^\infty e^{-(r-a(\theta))^2/\sigma_d^2}\,dr$$
$$= \sigma_d^2 e^{-a^2(\theta)/\sigma_d^2} + \frac{\sqrt{\pi}\,\sigma_d a(\theta)}{2} \operatorname{erfc}\left(-\frac{a(\theta)}{\sigma_d}\right) \tag{8.93}$$

Putting these back into (8.92) gives the probability density function of θ as

$$p_\Theta(\theta) = \frac{1}{\pi} e^{-b^2(\theta)/\sigma_d^2} \left[e^{-a^2(\theta)/\sigma_d^2} + \frac{\sqrt{\pi}\,\sigma_d a(\theta)}{2} \operatorname{erfc}\left(-\frac{a(\theta)}{\sqrt{2}\sigma_d}\right) \right] \tag{8.94}$$

for $\theta \in (-\pi, \pi]$.

Finally, from (8.77),

$$p_{\epsilon_r}(\epsilon_r) = \frac{1}{k_0} p_\Theta\left(-\frac{\epsilon_r}{k_0}\right) \tag{8.95}$$

which gives the probability density function of the error in finding the local minimum due to the noise.

8C.4 Conditions for ϵ_r Being Unbiased

In general, ϵ_r is a biased estimator. But in the special case of $r_0 = \Delta r$, ϵ_r is unbiased. To see this, note that a sufficient condition for ϵ_r being unbiased is that

$$p_{\epsilon_r}(x) = p_{\epsilon_r}(-x) \tag{8.96}$$

When $r_0 = \epsilon_r$, μ_d is real and

$$a(\theta) = \mu_d \cos\theta \tag{8.97}$$
$$b(\theta) = -\mu_d \sin\theta \tag{8.98}$$

$p_\Theta(\theta)$ can be written as a function of functions of θ in the form

$$p_\Theta(\theta) = F\left(\cos\theta, \sin^2\theta, \mu_d, \sigma_d\right) \tag{8.99}$$

Both $\cos\theta$ and $\sin^2\theta$ are even functions of θ so $p_\Theta(\theta)$ is an even function of θ, and $p_{\epsilon_r}(\epsilon_r)$ is an even function of ϵ_r. Therefore ϵ_r is an unbiased estimator when $r_0 = \Delta r$.

8D Probability Density Function of the Product of Two Independent and Identically Distributed Zero Mean Complex Gaussian Random Variables

It is well known that the sum of independent Gaussian random variables is a Gaussian random variable whose mean is the sum of the individual means and whose variance is the sum of the individual variances. This follows from the probability density function of the sum of two independent random variables being the convolution of their respective probability density functions.

In this appendix, the probability density function of the product of two independent and identically distributed zero-mean complex Gaussian random variables is derived. The mean and variance of the product is obtained, along with expressions for the higher order moments.[4]

8D.1 Problem Definition

Let w_1 and w_2 be independent and identically distributed complex Gaussian random variables with zero mean and variance σ^2. Define the random variable w as the product of w_1 and w_2

$$w = w_1 w_2 \tag{8.100}$$

The probability density functions of w_1 and w_2 are

$$p_{w_1}(z) = p_{w_2}(z) = \frac{1}{\pi\sigma^2} e^{-|z|^2/\sigma^2} \tag{8.101}$$

which can be written in polar coordinates as

$$p_{w_1}(r_1, \theta_1) = p_r(r_1)p_\theta(\theta_1) \tag{8.102}$$

$$p_{w_2}(r_2, \theta_2) = p_r(r_2)p_\theta(\theta_2) \tag{8.103}$$

---

[4]This is such a straightforward result in the theory of noise processes that it must have been obtained before by someone such as Rice or Middleton. Nevertheless, no references to this result in the signal processing literature could be found.

where the magnitudes have a Rayleigh distribution on $[0, \infty)$

$$p_r(r) = \frac{2r}{\sigma^2} e^{-r^2/\sigma^2} \tag{8.104}$$

and the phases have a uniform distribution on $[0, 2\pi)$

$$p_\theta(\theta) = \frac{1}{2\pi} \tag{8.105}$$

By writing $w = w_1 w_2$ in polar form as $w = se^{j\phi}$,

$$\phi = \theta_1 + \theta_2 \bmod 2\pi \tag{8.106}$$
$$s = r_1 r_2 \tag{8.107}$$

The polar random variables s and ϕ are independent because r_1 and r_2 are independent of θ_1 and θ_2. The polar probability density function of w can be written in the form

$$p_w(s, \phi) = p_s(s) p_\phi(\phi) \tag{8.108}$$

When expressed in Cartesian coordinates, this becomes

$$p_w(z) = \frac{1}{|z|} p_s(|z|) \, p_\phi(\arg z) \tag{8.109}$$

where the scale factor $1/|z|$ is the Jacobian for changing variables from polar to Cartesian coordinates.

8D.2 Probability Density Function of the Phase of the $w_1 w_2$

The probability density function of $\phi = \arg(w_1 w_2) = \theta_1 + \theta_2 \bmod 2\pi$ will be derived here in two ways. The first is a simple application of the principle of insufficient reason, while the second uses mathematics to do it properly.

Intuitive Proof

w_1 and w_2 are random phasors which may be pointing in any direction in the complex plane with uniform probability. So choose a reference phasor α pointing in an arbitrary direction and express all angles with respect to this phasor. Since the probability density functions of θ_1 and θ_2 are uniform when the angles are expressed relative to α, the probability density function of ϕ with respect to α must be independent of α. This is only possible if the probability density function of ϕ is constant. So that the total probability sums to unity, this constant must be $1/2\pi$. Therefore

$$p_\phi(\phi) = \frac{1}{2\pi} \tag{8.110}$$

Rigorous Proof

A proper proof of this uses the fact that the probability density function of the sum of two random variables is the convolution of the two random variables' respective probability density functions [23, p. 37]. In this case, $p_\phi(\phi)$ is the convolution of two functions that are constant on $[0, 2\pi)$ and zero elsewhere. Write $p_\theta(\theta)$ as

$$p_\theta(\theta) = \frac{1}{2\pi} \chi_{[0,2\pi)}(\theta) \tag{8.111}$$

where the characteristic function $\chi_A(x)$ of a set A is

$$\chi_A(x) = \begin{cases} 1 & \text{if } x \in A \\ 0 & \text{if } x \notin A \end{cases} \tag{8.112}$$

Then $p_\phi(\phi)$ is the convolution

$$\begin{aligned} p_\phi(\phi) &= p_\theta(\theta_1) \star p_\theta(\theta_2) \\ &= \int_0^{2\pi} p_\theta(\theta) p_\theta(\phi - \theta) \, d\theta \\ &= \int_0^{2\pi} \frac{1}{4\pi^2} \chi_{[0,2\pi)}(\theta) \chi_{[0,2\pi)}(\phi - \theta) \, d\theta \\ &= \begin{cases} \frac{1}{4\pi^2} \left(2\pi - |2\pi - \phi|\right) & \text{if } \phi \in [0, 4\pi) \\ 0 & \text{otherwise} \end{cases} \end{aligned} \tag{8.113}$$

This result is slightly incorrect because $p_\phi(\phi)$ is non-zero for some ϕ outside $[0, 2\pi)$. The correct answer is found by adding the probabilities for $\phi \in [2\pi, 4\pi)$ to the probabilities for $\phi \in [0, 2\pi)$ and then restricting ϕ to the interval $[0, 2\pi)$. Essentially, this makes the convolution a circular convolution on $[0, 2\pi)$. Therefore

$$\begin{aligned} p_\phi(\phi) &= \frac{1}{4\pi^2} \left(2\pi - |2\pi - \phi| + 2\pi - |2\pi - (\phi + 2\pi)|\right) \\ &= \frac{1}{4\pi^2} \left(\phi + 2\pi - \phi\right) \\ &= \frac{1}{2\pi} \end{aligned} \tag{8.114}$$

for $\phi \in [0, 2\pi)$.

This is the same answer as that obtained via the intuitive proof, but with the added respectability provided by a veneer of mathematics.

8D.3   Probability Density Function of the Magnitude of $w_1 w_2$

The probability density function of $s = |w_1 w_2| = r_1 r_2$ will be obtained here in two different ways which fortunately give the same answer, which is

$$p_s(s) = \frac{4s}{\sigma^4} \mathrm{K}_0 \left(\frac{2s}{\sigma^2} \right) \tag{8.115}$$

where $\mathrm{K}_0(x)$ is a modified Bessel function [1, eq. 9.6.24]. This has an integral representation

$$\mathrm{K}_0(x) = \int_0^\infty e^{-x \cosh u} \, du \tag{8.116}$$

First Proof using Jacobians

If a second random variable $t = t(r_1, r_2)$ is defined so that the pairs (r_1, r_2) and (s, t) uniquely determine one another, the joint probability density functions $p(s, t)$ and $p(r_1, r_2)$ are related by

$$p(s, t) = |J| \, p\left(r_1(s, t), r_2(s, t)\right) \tag{8.117}$$

where the Jacobian J is

$$J = \frac{\partial(r_1, r_2)}{\partial(s, t)} = \left[\frac{\partial(s, t)}{\partial(r_1, r_2)} \right]^{-1} \tag{8.118}$$

Then the probability density function of s is

$$\begin{aligned}
p_s(s) &= \int_T p(s, t) \, dt \\
&= \int_T |J| \, p\left(r_1(s, t), r_2(s, t)\right) \, dt \tag{8.119}
\end{aligned}$$

where the set T is the support of t.

   This integration may be easy or difficult depending on the choice of $t(r_1, r_2)$. Also $t(r_1, r_2)$ must be chosen so that the Jacobian does not change sign over the domain of integration. Note that the inverse of the Jacobian

$$\begin{aligned}
J^{-1} &= \frac{\partial(s, t)}{\partial(r_1, r_2)} \\
&= \begin{vmatrix} \dfrac{\partial s}{\partial r_1} & \dfrac{\partial s}{\partial r_2} \\ \dfrac{\partial t}{\partial r_1} & \dfrac{\partial t}{\partial r_2} \end{vmatrix} \\
&= r_2 \frac{\partial t}{\partial r_1} - r_1 \frac{\partial t}{\partial r_2} \tag{8.120}
\end{aligned}$$

is always non-negative when

$$\frac{\partial t}{\partial r_1} = 1 \tag{8.121}$$

and

$$\frac{\partial t}{\partial r_2} = -1 \tag{8.122}$$

These conditions are satisfied when t is

$$t(r_1, r_2) = r_1 - r_2 \tag{8.123}$$

Since r_1 and r_2 are defined on $[0, \infty)$, the support of t is $T = (-\infty, \infty)$. When r_1 and r_2 are written in terms of s and t, they become

$$r_1(s, t) = \frac{1}{2}\left[t + \sqrt{t^2 + 4s}\right] \tag{8.124}$$

$$r_2(s, t) = \frac{1}{2}\left[-t + \sqrt{t^2 + 4s}\right] \tag{8.125}$$

from which the Jacobian is

$$J = \frac{1}{r_1 + r_2} = \frac{1}{\sqrt{t^2 + 4s}} \tag{8.126}$$

and $r_1^2 + r_2^2$ is

$$r_1^2 + r_2^2 = (r_1 - r_2)^2 + 2r_1 r_2 = t^2 + 2s \tag{8.127}$$

Before the integral in (8.119) is evaluated, note that because r_1 and r_2 are independent,

$$
\begin{aligned}
p(r_1, r_2) &= p_r(r_1) p_r(r_2) \\
&= \frac{4}{\sigma^4} r_1 r_2 e^{-(r_1^2 + r_2^2)/\sigma^2} \\
&= \frac{4}{\sigma^4} s e^{-(t^2 + 2s)/\sigma^2}
\end{aligned}
\tag{8.128}
$$

Therefore

$$
\begin{aligned}
p_s(s) &= \int_{-\infty}^{\infty} |J|\, p(r_1(s, t), r_2(s, t))\, dt \\
&= \frac{4s}{\sigma^4} \int_{-\infty}^{\infty} \frac{1}{\sqrt{t^2 + 4s}} e^{-(t^2 + 2s)/\sigma^2}\, dt \\
&= \frac{8s}{\sigma^4} \int_{0}^{\infty} \frac{1}{\sqrt{t^2 + 4s}} e^{-(t^2 + 2s)/\sigma^2}\, dt
\end{aligned}
\tag{8.129}
$$

Now make the substitution $2s \cosh u = t^2 + 2s$. From this,

$$\sqrt{t^2 + 4s} = 2\sqrt{s} \cosh \frac{u}{2} = 2\frac{dt}{du} \tag{8.130}$$

so $p_s(s)$ becomes

$$p_s(s) = \frac{4s}{\sigma^4} \int_0^\infty e^{-(2s/\sigma^2)\cosh u} \, du \tag{8.131}$$

which in terms of the modified Bessel function is

$$p_s(s) = \frac{4s}{\sigma^4} K_0 \left(\frac{2s}{\sigma^2} \right) \tag{8.132}$$

Second Proof using Convolutions

The probability density function of s can be obtained more directly by noting that

$$\ln s = \ln r_1 + \ln r_2 \tag{8.133}$$

When $a = \ln s$, $b_1 = \ln r_1$ and $b_2 = \ln r_2$, $a = b_1 + b_2$ so the probability density function of a is the convolution of the probability density functions of b_1 and b_2. Then with $b = \ln r$,

$$
\begin{aligned}
p_b(b) &= p_r(r(b)) \frac{dr}{db} \\
&= e^b p_r \left(e^b \right)
\end{aligned}
\tag{8.134}
$$

Therefore

$$
\begin{aligned}
p_a(a) &= p_b(b) \star p_b(b) \\
&= \int_{-\infty}^\infty p_b(b) p_b(a-b) \, db \\
&= \int_{-\infty}^\infty \frac{4}{\sigma^4} e^{2b} e^{-e^{2b}/\sigma^2} e^{2(a-b)} e^{-e^{2(a-b)}/\sigma^2} \, db \\
&= \frac{4}{\sigma^4} e^{2a} \int_{-\infty}^\infty e^{-\left(e^{2b} + e^{2(a-b)} \right)/\sigma^2} \, db
\end{aligned}
\tag{8.135}
$$

Convert $p_a(a)$ back to a probability density function with respect to s, giving

$$
\begin{aligned}
p_s(s) &= p_a(a(s)) \frac{da}{ds} \\
&= \frac{1}{s} p_a(a(s)) \\
&= \frac{4s}{\sigma^4} \int_{-\infty}^\infty e^{-\left(e^{2b} + s^2 e^{-2b} \right)/\sigma^2} \, db
\end{aligned}
\tag{8.136}
$$

Now make the substitution

$$u = 2b - \ln s \tag{8.137}$$

so that $e^{2b} + s^2 e^{-2b}$ becomes $2s \cosh u$ and $du = 2db$. Therefore

$$
\begin{aligned}
p_s(s) &= \frac{2s}{\sigma^4} \int_{-\infty}^{\infty} e^{-(2s/\sigma^2)\cosh u} \, du \\
&= \frac{4s}{\sigma^4} \int_0^{\infty} e^{-(2s/\sigma^2)\cosh u} \, du \\
&= \frac{4s}{\sigma^4} \mathrm{K}_0 \left(\frac{2s}{\sigma^2} \right)
\end{aligned}
\tag{8.138}
$$

which agrees with (8.131).

8D.4 Probability Density Function of $w_1 w_2$

Putting equations (8.114) and (8.138) together gives the result

$$
p_w(z) = \frac{1}{|z|} \cdot \frac{4|z|}{\sigma^4} \mathrm{K}_0 \left(\frac{2|z|}{\sigma^2} \right) \cdot \frac{1}{2\pi}
\tag{8.139}
$$

from which it is concluded that

$$
p_w(z) = \frac{2}{\pi \sigma^4} \mathrm{K}_0 \left(\frac{2|z|}{\sigma^2} \right)
\tag{8.140}
$$

8D.5 Mean, Variance and Higher-Order Moments

The mean μ_w and variance σ_w^2 of $w = w_1 w_2$ are given by

$$
\mu_w = \mathrm{E}\{w\} = \int z p_w(z) \, dz
\tag{8.141}
$$

and

$$
\sigma_w^2 = \mathrm{E}\left\{|w - \mu_w|^2\right\} = \int |z - \mu_w|^2 p_w(z) \, dz
\tag{8.142}
$$

These are particular cases of the nth moment. With real random variables, the nth moment is $\mathrm{E}\{x^n\}$. Here the random variables are complex and it is not clear which of $\mathrm{E}\{w^n \overline{w}^m\}$ should be chosen as the $(n+m)$th moment. So define all of the $\mathrm{E}\{w^n \overline{w}^m\}$ as the $(n+m)$th moments, and work out a general expression applicable for any n and m that are positive integers or zero. In fact, the domain of allowable n and m can be broadened by insisting only that $n + m$ be a positive integer or zero and that $n - m$ be integral. This obtains $\mathrm{E}\left\{|w|^k\right\}$ at the same time for odd k (put $n = m = k/2$). So

$$
\begin{aligned}
\mathrm{E}\{w^n \overline{w}^m\} &= \int z^n \overline{z}^m \, p_w(z) \, dz \\
&= \int \frac{2}{\pi \sigma^4} z^n \overline{z}^m \mathrm{K}_0 \left(\frac{2|z|}{\sigma^2} \right) dz \\
&= \int_0^{\infty} \int_0^{2\pi} \frac{2}{\pi \sigma^4} s^{n+m+1} e^{j(n-m)\phi} \mathrm{K}_0 \left(\frac{2s}{\sigma^2} \right) d\phi ds \\
&= \left(\frac{1}{2\pi} \int_0^{2\pi} e^{j(n-m)\phi} \, d\phi \right) \left(\frac{4}{\sigma^4} \int_0^{\infty} s^{n+m+1} \mathrm{K}_0 \left(\frac{2s}{\sigma^2} \right) ds \right)
\end{aligned}
\tag{8.143}
$$

Because of the condition that $n - m$ be integral, the integral with respect to ϕ is unity if $n = m$, otherwise zero. Therefore

$$\mathrm{E}\left\{w^n \overline{w}^m\right\} = 0 \quad \forall\, n \neq m \tag{8.144}$$

Note that this means that $\mu_w = 0$ so each of the moments is a central moment.

If the moment has any chance of being non-zero, n must equal m, so put $k = n + m$ and consider $\mathrm{E}\left\{|w|^k\right\}$.

$$
\begin{aligned}
\mathrm{E}\left\{|w|^k\right\} &= \frac{4}{\sigma^4} \int_0^\infty r^{k+1} \mathrm{K}_0\left(\frac{2r}{\sigma^2}\right) dr \\
&= \frac{\sigma^{2k}}{2^k} \int_0^\infty u^{k+1} \mathrm{K}_0\left(u\right) du \\
&= \sigma^{2k} \Gamma^2\left(1 + \frac{k}{2}\right)
\end{aligned}
\tag{8.145}
$$

This last step uses the identity [1, eq. 11.4.22]

$$\int_0^\infty u^{k+1} \mathrm{K}_0\left(u\right) du = 2^k \Gamma^2\left(1 + \frac{k}{2}\right) \tag{8.146}$$

Using (8.145), $\mathrm{E}\{1\} = \Gamma^2(1) = 1$ as expected, and the variance of w is

$$
\begin{aligned}
\mathrm{Var}\left\{w_1 w_2\right\} &= \mathrm{E}\left\{|w|^2\right\} \\
&= \sigma^4 \Gamma^2(2) \\
&= \sigma^4
\end{aligned}
\tag{8.147}
$$

This is not unexpected because for any two independent random variables z_1 and z_2 with zero mean and identical variances σ^2

$$
\begin{aligned}
\mathrm{Var}\left\{z_1 z_2\right\} &= \iint |z_1 z_2|^2 p_{z_1, z_2}(z_1, z_2)\, dz_1 dz_2 \\
&= \iint |z_1|^2 |z_2|^2 p_{z_1}(z_1)\, p_{z_2}(z_2)\, dz_1 dz_2 \\
&= \left(\int |z_1|^2 p_{z_1}(z_1)\, dz_1\right)\left(\int |z_2|^2 p_{z_2}(z_2)\, dz_2\right) \\
&= \mathrm{Var}\left\{z_1\right\} \mathrm{Var}\left\{z_2\right\} \\
&= \sigma^4
\end{aligned}
\tag{8.148}
$$

8D.6 Summary

Let w_1 and w_2 be independent and identically distributed complex Gaussian random variables with zero mean and variance σ^2. Then $w_1 w_2$ has probability density function

$$p_w(z) = \frac{2}{\pi \sigma^4} \mathrm{K}_0\left(\frac{2|z|}{\sigma^2}\right) \tag{8.149}$$

The mean of $w_1 w_2$ is zero and the variance is σ^4.

Chapter 9

Conventional Motion Estimators and the Maximum Likelihood Solution

Chapter 8 completed the analysis of the maximum likelihood ISAR radial motion estimator which was derived in chapter 6 and implemented efficiently in chapter 7. Therefore, this chapter is an appropriate place to compare the maximum likelihood solution with some of the conventional radial motion estimators discussed in detail in chapter 5.

The three motion estimators from chapter 5 reexamined here are the cross-correlation methods of range profile alignment from section 5.4.2, and the adaptive beamforming and phase gradient autofocus algorithms of phase compensation from sections 5.4.4 and 5.4.5 respectively. The image-quality methods from section 5.4.3 are not considered here because they are not related closely enough to the maximum likelihood solution for the comparison to be worthwhile.

Reinterpreting conventional radial motion estimators in the light of the maximum likelihood solution is a valuable exercise. If there is a strong connection between the estimator and the maximum likelihood solution, this helps to provide a formal justification for what would otherwise be an *ad hoc* or "intuitively obvious" approach. If there is not a strong connection between the estimator and the maximum likelihood solution, this prompts the questions of whether there is some additional information that the estimator uses, and whether this information could possibly be incorporated into the radial motion estimation model to give a better maximum likelihood estimator.

9.1   The Maximum Likelihood Estimator as a Cross-Correlation

The maximum likelihood estimator $\hat{r}_{ml}$ from (6.39) can be written in terms of the cross-correlation of the range profiles formed from the two frequency responses.

From (6.39), the maximum likelihood estimator is

$$\hat{r}_{ml} = \arg \min_r \sum_{n=0}^{N-1} \left| a_n - b_n e^{jk_n r} \right|^2 \tag{9.1}$$

Following appendix 7A, this can be written in the equivalent form

$$\hat{r}_{ml} = \arg \max_r \Re \left\{ \sum_{n=0}^{N-1} a_n \overline{b_n} e^{-jk_n r} \right\} \tag{9.2}$$

The target's range profiles are the continuous-range Fourier series of the discrete frequency responses.[1] Therefore by defining the target's range profiles at the two times as

$$s_1(r) = \sum_{n=0}^{N-1} a_n\, e^{jk_n r} \tag{9.3}$$

and

$$s_2(r) = \sum_{n=0}^{N-1} b_n\, e^{jk_n r} \tag{9.4}$$

the discrete frequency responses may be written in terms of the range profiles using the formula for the discrete Fourier transform

$$a_n = \frac{1}{N} \sum_{n'=0}^{N-1} \left[s_1(r_{n'})\, e^{-jk_0 r_{n'}} \right] e^{-j\frac{2\pi}{N} nn'} \tag{9.5}$$

$$b_n = \frac{1}{N} \sum_{n'=0}^{N-1} \left[s_2(r_{n'})\, e^{-jk_0 r_{n'}} \right] e^{-j\frac{2\pi}{N} nn'} \tag{9.6}$$

Now define the cross-correlation of the two range profiles $s_1(t)$ and $s_2(t)$ as

$$R_{12}(r) = \int_{-\frac{c}{4\Delta f}}^{\frac{c}{4\Delta f}} s_1(r')\overline{s_2(r' + r)}\, dr' \tag{9.7}$$

where the limits of integration have been set to cover a total width of $c/2\Delta f$, equal to the extent W_r of the ISAR image's range ambiguity window. The cross-correlation is periodic because the range profiles themselves are periodic, so any upper and lower limits differing by W_r could have been used in this integral.

---

[1]See the footnote on page 98.

Writing the range profiles in (9.7) in terms of the discrete frequency responses shows that

$$R_{12}(r) = \int_{-\frac{c}{4\Delta f}}^{\frac{c}{4\Delta f}} \sum_{n=0}^{N-1} a_n\, e^{jk_n r'} \sum_{n'=0}^{N-1} \overline{b_{n'}}\, e^{-jk_{n'}(r'+r)}\, dr'$$

$$= \sum_{n=0}^{N-1} \sum_{n'=0}^{N-1} a_n \overline{b_{n'}}\, e^{-jk_{n'}r} \int_{-\frac{c}{4\Delta f}}^{\frac{c}{4\Delta f}} e^{-j\Delta k r'(n'-n)}\, dr' \qquad (9.8)$$

where, as usual, each k_n is $k_0 + n\Delta k$. Now the integral can be evaluated to give a Kronecker delta

$$\int_{-\frac{c}{4\Delta f}}^{\frac{c}{4\Delta f}} e^{-j\Delta k r'(n'-n)}\, dr' = \frac{c}{2\Delta f} \operatorname{sinc}(n'-n)$$

$$= \frac{c}{2\Delta f}\, \delta_{n'n} \qquad (9.9)$$

because n and n' are always integral. Then the cross-correlation is equal to

$$R_{12}(r) = \frac{c}{2\Delta f} \sum_{n=0}^{N-1} \sum_{n'=0}^{N-1} a_n \overline{b_{n'}}\, e^{-jk_{n'}r}\, \delta_{n'n}$$

$$= \frac{c}{2\Delta f} \sum_{n=0}^{N-1} a_n \overline{b_n}\, e^{-jk_n r} \qquad (9.10)$$

This shows that the maximum likelihood estimator $\widehat{r}_{ml}$ of Δr can be written in terms of the cross-correlation of the range profiles in (9.7) as

$$\widehat{r}_{ml} = \arg \max_r \Re\left\{R_{12}(r)\right\} \qquad (9.11)$$

9.2 Range Profile Alignment

The cross-correlation method of range profile alignment presented in section 5.4.2 is similar to algorithms 7.1 and 7.3 in chapter 7. These algorithms accomplished the approximate global minimization of the cost function $J(r)$ used to find the maximum likelihood estimate $\widehat{r}_{ml}$ of Δr, the radial distance moved by the target.

In this section, it is shown that $\widehat{r}_{ml}$ may be expressed as the maximum of a cross-correlation. This cross-correlation is slightly different from the cross-correlation used by Chen and Andrews for range profile alignment [19]. The reasons for this difference are discussed, and it is demonstrated that the cross-correlation used by Chen and Andrews sacrifices accuracy for robustness to changes in the target's aspect angle.

Equation (9.11) is the form of the maximum likelihood estimator of Δr capable of estimating the target's radial movement unambiguously to a fraction of a wavelength. An accuracy this good is not needed for range profile

alignment. Following the proof of algorithm 7.3, taking the absolute value of $R_{12}(r)$ rather than the real part gives an estimate that is within a wavelength of $\widehat{r}_{ml}$. Therefore

$$\widehat{r}_{ml} \approx \arg \max_r |R_{12}(r)| \tag{9.12}$$

The actual form of the cross-correlation used by Chen and Andrews for range profile alignment is

$$R'_{12}(r) = \int_{-\frac{c}{4\Delta f}}^{\frac{c}{4\Delta f}} |s_1(r')|\ |s_2(r' + r)|\ dr' \tag{9.13}$$

which is different from the $|R_{12}(r)|$ derived from the maximum likelihood estimator. The implications of this are discussed next.

9.2.1   Cross-Correlation and Rotating Targets

At first glance, there would seem to be no reason not to use the complex form of the cross-correlation,[2] except perhaps if it were not known to be related to the maximum likelihood estimator. However, there is a simple explanation of why Chen and Andrews used the particular form of cross-correlation that they did, and it is related to the target's rotation and the low resolution of their fast correlation.

When the target's frequency response is measured at two different times, as long as the target's rotation is negligible, the responses differ by a frequency-dependent phase shift that is directly proportional to the radial distance moved by the target. If the target is moving and rotating at approximately constant radial and angular velocities, this suggests two possible strategies for measuring the target's radial position. The first is to measure the distance the target moves between successive range profiles. The second is to choose the target's range profile at the middle of the ISAR imaging period as a reference, and then for any other range profile, to measure the radial distance the target has moved relative to the reference profile.

The first strategy ensures that the target's rotation is negligible because the time between consecutive range profiles is very short, but the estimates of each radial movement must be made very accurately because the target only moves a very short distance in the time between successive profiles, and these differences must be summed to give the overall change in the target's position. The second strategy measures radial movements that are up to $M/2$ times greater than the radial movements using the first strategy, so estimates of the radial movement need not be so accurate. The disadvantage is that the target rotates through an angle up to $M/2$ times larger so its rotation can no longer be considered negligible.

---

[2]Indeed Xu *et al.* did use the complex form of the cross-correlation in [101] and [103]. In [102], they switched back to cross-correlating the magnitudes of the range profiles.

Before discussing which is the optimum strategy to use, the effect of the target's rotation must be considered. When the target does not rotate, the effect is simple: the range profile is offset by the distance moved and the phase changes by an amount proportional to the distance moved. Both effects are measured by cross-correlating the complex range profiles.

When the target moves radially and rotates, the radial motion produces the effects described above but the rotation affects the profile slightly differently. Different scatterers move different radial distances depending on their position relative to the target's centre of rotation. These radial distances are small relative to the size of a range bin but large relative to the wavelength. Therefore the phase of each scatterer in a range bin changes by a different amount from the phases of other scatterers in that range bin. If the range bin contains many scatterers, the sum of the scatterer's reflections produces a significant change in the range bin's amplitude as well as its phase. If, however, the range bin contains only a single scatterer, or one scatterer with a much greater amplitude than the rest, the amplitude of that range bin will be largely unaffected but its phase may be changed significantly. The overall effect of the target's rotation is to change the phases of different range bins in different ways but it leaves their magnitudes largely untouched. Since man-made targets tend to have a high dynamic range with a small number of strong point scatterers, this suggests that the effect of the target's rotation can be mitigated by cross-correlating the magnitudes of the range profiles.

The disadvantage of cross-correlating the magnitudes of the profiles is that the phase carries much of the information about the target's radial movement. Once the phase information has been destroyed by taking the magnitude, the estimates of the cross-correlation are less accurate. The loss of accuracy from neglecting the radial movement's phase changes has to be balanced against the increase of accuracy from removing some of the deleterious effects of the target's rotation.

The choice of which of the two strategies mentioned above to use depends on how the cross-correlation is implemented. Chen and Andrews used cross-correlation implemented as a fast correlation based on the fast Fourier transform. The resolution of the fast correlation is equal to the resolution of the discrete range profiles, which in turn is equal to the width of a range bin or $\Delta r_r = c/2N\Delta f$.

As an example, consider a target moving through a third of a range bin between each range profile. Cross-correlating adjacent range profiles with an accuracy of one range bin would conclude that the target has no radial motion thoughout the ISAR imaging period. However, using the centre range profile as a reference, cross-correlating each range profile with the reference would conclude that the target moves through one range bin for every three range profiles across from the reference.

Therefore, if the FFT-based fast correlation were used, the only viable

Figure 9.1: In this figure, the two range profiles are from consecutive frequency responses so the target's rotation is negligible. The cross-correlation of the complex range profiles is shown in grey and the cross-correlation of their magnitudes is in black.
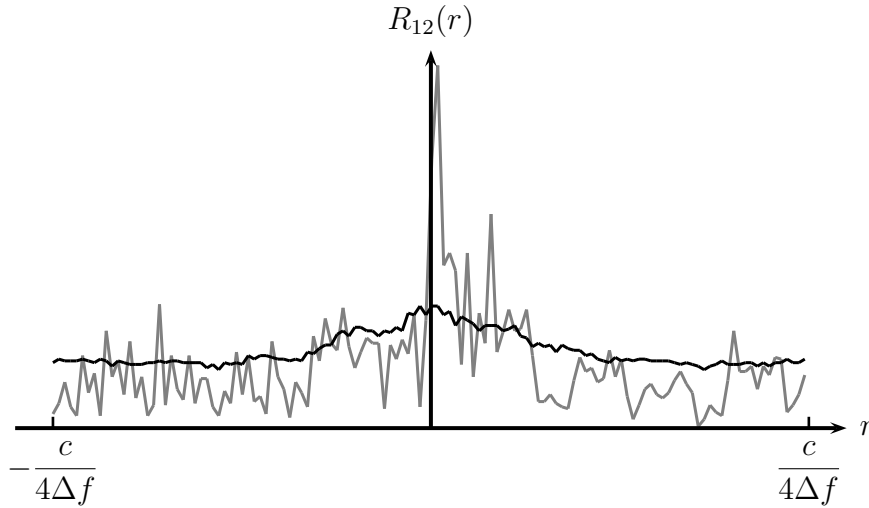
option would be to measure the radial motion relative to one reference range profile. As the target's rotation is not negligible, cross-correlation of the magnitudes of the range profiles must be used.

If, however, the chirp-Z transform were used as in algorithm 7.3, the radial movement could be estimated down to about a wavelength. Now the target's rotation may be considered negligible and the model under which the maximum likelihood estimator derived is valid. These are suitable conditions for the complex cross-correlation of adjacent range profiles.

9.2.2 Example of Large and Small Rotations

The difference between the complex and magnitude forms of the cross-correlation can be seen in figures 9.1 and 9.2. These are calculated from frequency responses of the same 737 aircraft used in figure 6.1. In figure 9.1, the two range profiles are from consecutive frequency responses so the target's rotation is negligible. The peak in the cross-correlation is much sharper for the cross-correlation of the complex profiles than for the cross-correlation of their magnitudes.

In figure 9.2, the two range profiles are separated by half the ISAR imaging period, so the target's rotation is now significant. The cross-correlation of the complex profiles still shows a sharp peak, but new sharp peaks with amplitudes that are close to that of the maximum have appeared. These new peaks are widely separated so if any of their amplitudes were slightly

Figure 9.2: In this figure, the two range profiles are separated by half the ISAR imaging period so the target's rotation is not negligible. The cross-correlation of the complex range profiles is shown in grey and the cross-correlation of their magnitudes is in black.
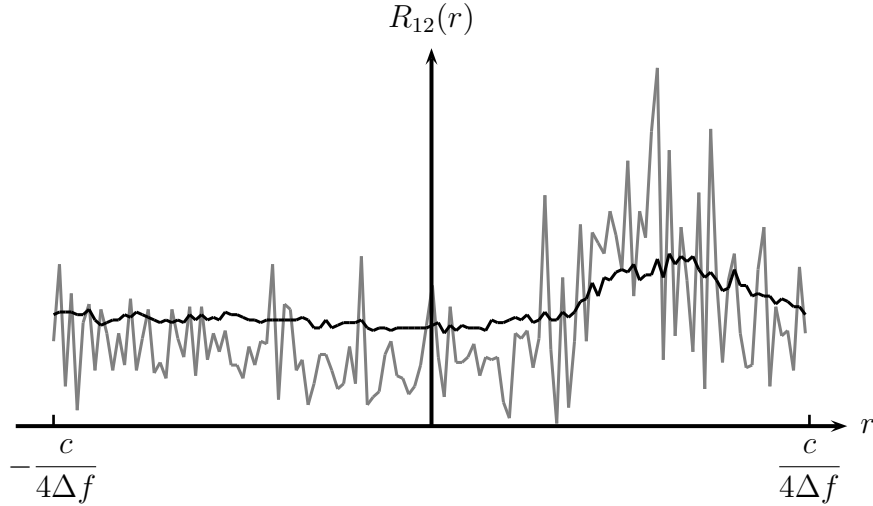
higher, the estimate of Δr would be very inaccurate. In comparison, the cross-correlation of the magnitudes of the range profiles is almost unchanged in shape from that in figure 9.1, indicating how cross-correlating the magnitudes of the profiles has reduced the effect of the target's rotation.

The question of how much the target can rotate before its rotation is no longer negligible for the purposes of motion estimation is considered in section 10.4.

9.3   Phase Compensation

Just as range profile alignment using cross-correlation is related to the approximate global minimization algorithms of section 7.1, phase compensation using adaptive beamforming and the phase gradient autofocus are related to the exact local minimization algorithms of section 7.2.

As shown in equation (9.11), finding the maximum likelihood estimator of Δr is equivalent to maximizing the cross-correlation

$$\widehat{r}_{ml} = \arg \max_r \Re \left\{ R_{12}(r) \right\} \tag{9.14}$$

Because this correlation has a very high frequency modulation, the maximization can be carried out in two parts. First the magnitude is maximized, as in section 9.2. Then the value of r that maximizes $|R_{12}(r)|$ is adjusted over a range of half a wavelength. The optimum value of r rotates the phase so

that $R_{12}(r)$ has no imaginary component and the real component is positive. This second part, to adjust the phase of the cross-correlation, is equivalent to the operation of phase compensation algorithms.

However, dividing the maximization into two parts like this pretends that the magnitude of the cross-correlation does not change as r varies over half a wavelength. The magnitude does change, not by much if r is close to $\widehat{r}_{ml}$, but by significantly more if r is larger than a small fraction of a range bin away from $\widehat{r}_{ml}$. From the derivation of algorithm 7.6 in appendix 7B, the value of r should be adjusted so that

$$\Im\left\{\sum_{n=0}^{N-1} k_n a_n \overline{b_n} e^{-jk_n r}\right\} = 0 \tag{9.15}$$

Ignoring the changing magnitude for small variations in r is equivalent to solving the slightly different condition

$$\Im\left\{\sum_{n=0}^{N-1} a_n \overline{b_n} e^{-jk_n r}\right\} = 0 \tag{9.16}$$

These give similar estimates of $\widehat{r}_{ml}$, particularly if the initial estimate from maximizing the magnitude is close to $\widehat{r}_{ml}$. This is because the radar has a narrow relative bandwidth so $k_n \approx \overline{k}$ for all frequencies in the stepped-frequency waveform.

From (9.11), equation (9.16) is equivalent to adjusting r so that

$$\Im\left\{\int_{-\frac{c}{4\Delta f}}^{\frac{c}{4\Delta f}} s_1(r')\overline{s_2(r'+r)}\, dr'\right\} = 0 \tag{9.17}$$

Now suppose that range profile alignment has been performed so that most of the radial motion Δr has been corrected, except for a small amount δr less than a range bin. Then the value of δr modulo half a wavelength is found by solving the above equation for values of r between $-\lambda/4$ and $\lambda/4$. Over such a small variation in r,

$$s_2(r'+r) \approx e^{-j\overline{k}r}\, s_2(r') \tag{9.18}$$

so that δr is found by solving

$$\Im\left\{e^{-j\overline{k}r} \int_{-\frac{c}{4\Delta f}}^{\frac{c}{4\Delta f}} s_1(r')\overline{s_2(r')}\, dr'\right\} = 0 \tag{9.19}$$

which is equivalent to

$$\overline{k}r = -\arg\left\{\int_{-\frac{c}{4\Delta f}}^{\frac{c}{4\Delta f}} s_1(r')\overline{s_2(r')}\, dr'\right\} \tag{9.20}$$

This is very similar to the maximum likelihood estimator of δr on which the phase gradient autofocus and adaptive beamforming methods of phase compensation are based.

To see how phase gradient autofocus is related to (9.20), the phase gradient operator in (5.47) is just one of many phase gradient or phase difference operators that can be used with phase gradient autofocus giving images of similar quality. Another phase difference operator suggested by Wahl *et al.* is [96, eq. (5)]

$$\Delta\phi = \arg\left\{\int_{-\frac{c}{4\Delta f}}^{\frac{c}{4\Delta f}} s_1(r')\overline{s_2(r')}\,dr'\right\} \tag{9.21}$$

which is the same as (9.20).

Therefore, the phase gradient autofocus can use an estimator of the phase difference between profiles that is very closely related to the maximum likelihood estimator, thus justifying its use.

This is only a small part of the complete phase gradient autofocus algorithm, with the shifting and windowing parts not yet discussed. When expressed in ISAR language instead of the phase gradient autofocus's native SAR language, these operations help to reduce the phase noise associated with the target's rotation. It seems likely that the shifting and windowing parts of the phase gradient autofocus could be used with the maximum likelihood phase estimator to produce estimates of Δr that are more robust to the target's rotation.

Adaptive beamforming is a more difficult phase estimator to relate to the maximum likelihood solution because the dominant scatterer does no averaging at all to determine the reference phases in each range profile. The effects of noise are reduced somewhat in Haywood's modification [42] of the dominant scatterer algorithm by ensuring that the average amplitude in the reference range bin is above a threshold, but this is still not an optimum solution.

To try and balance the reduction of rotation-related phase noise obtained by selecting a reference range bin containing only a single scatterer, it is possible that the dominant scatterer algorithm could be improved by selecting several range bins to use as references and averaging the phase adjustments across these ranges. These range bins could be chosen as the range bins with the least variance and greatest amplitude, or similar such criteria. This is only a tentative idea, and more development is needed to determine whether it is worthwhile.

Chapter 10

Resolution and Motion Constraints

A number of approximations have been made throughout this thesis to justify various simplifying assumptions that may be needed for ISAR inversion algorithms. In this chapter, three approximations will be analysed in detail. These are:

Range-Doppler Processing With range-Doppler ISAR, it is assumed that $r_{xy}(t)$, the range of a scatterer at (x, y) on the target at time t, can be written as a linear function of x and y.

Polar Reformatting Polar reformatting can be avoided if the polar grid on which the radar measurements give $G(k_x, k_y)$ is approximately rectangular.

Motion Estimation For accurate motion estimation, the target's radar reflections, $s(k, 0)$ and $s(k, \tau)$, at two times $t = 0$ and $t = \tau$, are assumed to differ only by a phase shift of $e^{-jk\Delta r}$, where Δr is the radial distance the target moves between the two times. This is justified if the target has neglible rotation during $[0, \tau]$.

The chapter also contains an analysis of the residual motion errors remaining after motion estimation and motion compensation. Conceptually, this analysis of motion estimation errors belongs in chapter 5. However, because it uses the same techniques that have been developed here for analysing the three assumptions mentioned above, it has been included in section 10.5.

For each of the three assumptions to be valid, constraints must be imposed on the size and motion of the target and the resolution of the ISAR image. These constraints can be checked when imaging a target to see whether the

range-Doppler approximation is justified, and if so, whether polar reformatting can be left out without seriously compromising the image's quality.

The classical[1] view of ISAR as imaging by velocity-induced Doppler shifts also imposes restrictions on the size of the target and the image's resolution. Breaking the target into range cells and cross-range cells, and insisting that no scatterer moves through a resolution cell in the range or cross-range directions, leads to constraints such as [3]

$$\Delta r_c^2 > \frac{\lambda D_r}{4} \tag{10.1}$$

$$\Delta r_r \Delta r_c > \frac{\lambda D_c}{4} \tag{10.2}$$

Here D_r and D_c are the dimensions of the target in range and cross-range, and λ is the wavelength at the radar's centre frequency. Similar expressions have been obtained by Brown [16], Walker [97] and Wehner [98, eq. (7.31)], and they are also derived in section 4B.2 on page 61.

However, constraining the target's motion so that no point moves through more than one range cell or one cross-range cell is an artifact of the Doppler-shift view of ISAR. This is dubious reasoning because these are not fundamental limits of ISAR or even of range-Doppler ISAR. Rather they are constraints on the need for polar reformatting, a fact that is obscured in the Doppler-shift description of ISAR.[2]

This chapter contains a proper analysis of both the constraints due to range-Doppler processing and the constraints due to avoiding polar reformatting. These are followed by a derivation of the constraints due to the need for motion estimation and motion compensation in ISAR imaging.

10.1   Describing the Target's Size

Since this chapter is concerned with finding some straightforward limits on the resolution of an ISAR image and the size of a target, the target will be described in a very simple way.

The target is characterized by its reflectivity function $g(x, y)$, so the support of $g(x, y)$ will be taken to be the extent of the target. For simplicity, assume that the target's x axis is parallel to the radar's boresight axis and

---

[1]i.e. Incorrect.

[2]To be fair to Wehner, he does mention that the existence of the blur radius is due to the lack of polar reformatting, although he does not analyse the equivalent constraints when polar reformatting is used. However, these conditions on polar reformatting are obtained from the Doppler-shift view of ISAR, a model of ISAR in which polar reformatting does not exist! The coincidence that the blur radius constraint is the same as that for polar reformatting perpetuates the myth that the blur radius is important.

its y axis is perpendicular to the boresight axis. This corresponds to the orientation of the rotating target at time $t = 0$ in figure 4.1 on page 42. Then the target's range extent D_r and cross-range extent D_c are chosen so that

$$|x| \leq \frac{D_r}{2} \tag{10.3}$$

$$|y| \leq \frac{D_c}{2} \tag{10.4}$$

for all points (x, y) on the target.

This is not a complete description of the target's size in other directions, but the simple model of the target's size as a rectangle $D_r \times D_c$ is sufficient. A degree of flexibility can be used in establishing the constraints derived here because the approximations to which they apply gradually become invalid. This leads to gentle degradations in the ISAR image that affect scatterers at the target's extremities more severely than those at target's centre.

As an example, the sets of constraints obtained in this chapter are derived by assuming a maximum phase variation of $\pi/2$. This could just as easily have been specified as maximum phase variation of $\pi/4$ or π or any other sensible amount. Similarly, there is no reason why the RMS phase variation could not have been used (except that the mathematics is considerably more difficult). As a consequence of this flexibility, the limits on range and cross-range resolution throughout this chapter should be interpreted as "soft" limits rather than exact limits.

So when a constraint is written in the form

$$\alpha > \beta \tag{10.5}$$

it does not mean that the ISAR image is prefectly focussed if $\alpha > \beta$ and completely blurred if $\alpha \leq \beta$. Rather, it means that the particular approximation is valid if $\alpha \gg \beta$, and that as α approaches β, the image's quality starts to degrade.

10.2 Range-Doppler ISAR

ISAR using range-Doppler processing, as described in section 4.2, expresses the range of a scatterer at (x, y) on the target at time t as a time-varying linear function of x and y. The error in this linear approximation can be used to derive limits on the maximum size of a target for a given range and cross-range resolution.

The analysis in this section applies to stationary targets rotating at constant angular velocity. Similar results have been obtained in different ways by Munson and Soumekh. Munson analysed the curvature in the wavefront for spotlight-mode SAR [60, eq. (22)–(24)] and Soumekh considerd phase

errors due to the plane wave approximation, also for spotlight-mode SAR [83, eq. (A16)]. The approach taken in this section is slightly different from these. Here, the variation in the phase error across the (k_x, k_y) plane is used to obtain the constraints on the target and the ISAR image. The difference between this and Soumekh's approach is more conceptual than mathematical; its advantage is that the same framework can be used to analyse any approximations in $r_{xy}(t)$, including polar reformatting and motion estimation (which are the subjects of sections 10.3 and 10.4).

10.2.1 Defining the Phase Variation $\Delta\psi_{xy}$

From equation (4.10), the distance between a scatterer at (x, y) in the target's local coordinate system and the radar is

$$r_{xy}(t) = \sqrt{(r_0 + x\cos\omega t - y\sin\omega t)^2 + (x\sin\omega t + y\cos\omega t)^2} \qquad (10.6)$$

at time t. The range-Doppler approximation assumes that $r_{xy}(t)$ can be written as a linear function of x and y, as in equation (4.12). The error inherent in this approximation is found by taking the first order Taylor series of r_{xy} while including the remainder. This gives

$$r_{xy}(t) = r_0 + x\cos\omega t - y\sin\omega t + \epsilon_{xy}(t) \qquad (10.7)$$

where $\epsilon_{xy}(t)$ is the Taylor series' remainder.

From the model (4.4) of the radar measurements at frequency k and time t,

$$s(k, t) = \iint g(x, y)\, e^{-jkr_{xy}(t)}\, dx\, dy \qquad (10.8)$$

the range-Doppler approximation is equivalent to using a modified model

$$s(k, t) = e^{-jkr_0} \iint g'(x, y, k, t)\, e^{-jk(x\cos\omega t - y\sin\omega t)}\, dx\, dy \qquad (10.9)$$

where the target's reflectivity $g(x, y)$ has been replaced by an apparent reflectivity $g'(x, y, k, t)$. This includes the frequency-varying and time-varying phase errors due to the linear approximation of $r_{xy}(t)$

$$g'(x, y, k, t) = g(x, y)\, e^{-jk\epsilon_{xy}(t)} = g(x, y)\, e^{-j\psi_{xy}(k,t)} \qquad (10.10)$$

where the phase error in $g(x, y)$ at time t and frequency k has been written $\psi_{xy}(k, t)$.

Most ISAR inversion algorithms assume that $g(x, y)$ is independent of time and frequency,[3] so any change in $\psi_{xy}(k, t)$ for the N values of k from

---

[3]One that does not is described by Synder *et al.*, who consider target reflectivity functions to be random processes [80]. Their approach is too demanding for the current state of the art in computer technology.

k_0 to k_{N-1} or for the M values of t from $t_0 = -T/2$ to $t_{M-1} = T/2$ causes blurring in the final ISAR image. Note that for any particular point on the target, (x, y), the average value of $\psi_{xy}(k, t)$ is unimportant because this can be absorbed into the phase of $g(x, y)$. What matters is the variation over all k_n and t_m of $\psi_{xy}(k, t)$ for the single point (x, y) on the target. Define the total variation in $\psi_{xy}(k, t)$ for the scatterer at (x, y) as $\Delta\psi_{xy}$ where

$$\Delta\psi_{xy} = \max_{k,t,k',t'} |\psi_{xy}(k, t) - \psi_{xy}(k', t')| \tag{10.11}$$

Then $\Delta\psi_{xy}$ can be directly related to the blurring in the ISAR image in the neighbourhood of (x, y) due to the linear range-Doppler approximation. Setting an upper limit on the variation in phase error across the target imposes restrictions on the size of the target and the resolution of the ISAR image.

Define $\Delta\psi$ as the maximum phase variation over the whole of the target,

$$\Delta\psi = \sup_{(x,y)} \Delta\psi_{xy} \tag{10.12}$$

where the supremum is taken for (x, y) ranging over the whole of the target.[4] The upper limit used in [3] is a quarter of a wavelength, which corresponds to a maximum phase variation of $\pi/2$. Munson used $\pi/4$ [60]. Using a maximum of $\pi/2$ here, the maximum phase variation must satisfy

$$\Delta\psi < \frac{\pi}{2} \tag{10.13}$$

10.2.2 Evaluating the Phase Variation

The range error $\epsilon_{xy}(t)$ is given by the remainder for a first order Taylor series in two variables

$$\epsilon_{xy}(t) = \frac{1}{2}\left(x\frac{\partial}{\partial x'} + y\frac{\partial}{\partial y'}\right)^2 r_{x'y'}(t) \tag{10.14}$$

for some x' between 0 and x and some y' between 0 and y. x' and y' depend on (x, y), the point at which the Taylor series is evaluated, and on t because the Taylor series has time-varying coefficients. They can be written

$$x' = \alpha(t)\, x \tag{10.15}$$
$$y' = \alpha(t)\, y \tag{10.16}$$

for some $\alpha(t)$ satisfying $0 < \alpha(t) < 1$. Strictly speaking, $\alpha(t)$ should be written $\alpha(t, x, y)$, but the extra parameters will be omitted because at the

---

[4]$\Delta\psi$ is a *supremum* over x and y because x and y are continuous variables. $\Delta\psi_{xy}$ is a *maximum* of k, t, k' and t' because these are discrete variables, taking on one of the M time steps or one of the N frequency steps.

moment, the variation in $\epsilon_{xy}(t)$ with time is being analysed for one particular point on the target.

Evaluating the second order partial derivatives in the Taylor series' remainder shows that

$$\epsilon_{xy}(t) = \frac{x^2 + y^2}{2r_{x'y'}(t)} - \frac{1}{2r_{x'y'}^3(t)} \left[x(x' + r_0 \cos \omega t) + y(y' + r_0 \sin \omega t)\right]^2 \quad (10.17)$$

Under the standard ISAR assumption that the size of the target is small in comparison to its range (an assumption that is consistent with the constraints at the conclusion of this analysis), $r_{x'y'}(t)$ may be replaced by r_0 to give a simpler expression for the range error

$$\epsilon_{xy}(t) = \frac{r_0}{2} \left[\frac{x^2}{r_0^2} + \frac{y^2}{r_0^2} - \left(\frac{x}{r_0}\left(\frac{x'}{r_0} + \cos \omega t\right) + \frac{y}{r_0}\left(\frac{y'}{r_0} + \sin \omega t\right)\right)^2\right] \quad (10.18)$$

Write (x, y) in polar coordinates

$$x = d \cos \phi \quad (10.19)$$
$$y = d \sin \phi \quad (10.20)$$

so that $(x', y') = (\alpha(t) d \cos \phi, \alpha(t) d \sin \phi)$. Using this in (10.18) shows that the range error is

$$\epsilon_{xy}(t) = \frac{d^2}{2r_0} \left[1 - \left(\frac{\alpha(t) d}{r_0} + \cos(\phi - \omega t)\right)^2\right] \quad (10.21)$$

so that

$$\psi_{xy}(k, t) = k \frac{d^2}{2r_0} \left[1 - \left(\frac{\alpha(t) d}{r_0} + \cos(\phi - \omega t)\right)^2\right] \quad (10.22)$$

Therefore from the definition of the phase variation in (10.11),

$$\Delta \psi_{xy} = \max_{k,t,k',t'} |\psi_{xy}(k, t) - \psi_{xy}(k', t')|$$

$$= \max_{k,t,k',t'} \frac{d^2}{2r_0} \left| (k - k') - k \left(\frac{\alpha(t) d}{r_0} + \cos(\phi - \omega t)\right)^2 \right.$$

$$\left. + k' \left(\frac{\alpha(t) d}{r_0} + \cos(\phi - \omega t')\right)^2 \right| \quad (10.23)$$

The $\alpha(t) d/r_0$ inside the modulus may be neglected, giving a simpler approximate form of the phase variation. With the approximation written as equality, this is

$$\Delta \psi_{xy} = \max_{k,t,k',t'} \frac{d^2}{2r_0} \left| k \sin^2(\phi - \omega t) - k' \sin^2(\phi - \omega t') \right| \quad (10.24)$$

From lemma 10.1 in appendix 10A, the maximum is attained when k and k' are the upper and lower limits of the stepped-frequency waveform

$$k = k_{N-1} \tag{10.25}$$

$$k' = k_0 \tag{10.26}$$

and t and t' are respectively the maximum and minimum values of $\sin^2(\phi - \omega\tau)$ for $\tau \in [-T/2, T/2]$

$$t = \max_\tau \sin^2(\phi - \omega\tau) \tag{10.27}$$

$$t' = \min_\tau \sin^2(\phi - \omega\tau) \tag{10.28}$$

Therefore

$$\Delta\psi_{xy} = \frac{d^2}{2r_0} \left[k_{N-1} \max_\tau \sin^2(\phi - \omega\tau) - k_0 \min_\tau \sin^2(\phi - \omega\tau) \right] \tag{10.29}$$

Because of this dependence on ϕ, the angle of the point (x, y) from the x axis, $\Delta\psi$ in (10.12) is best expressed as the supremum over d and ϕ rather than the supremum over x and y

$$\Delta\psi = \sup_{d,\phi} \frac{d^2}{2r_0} \left[k_{N-1} \max_\tau \sin^2(\phi - \omega\tau) - k_0 \min_\tau \sin^2(\phi - \omega\tau) \right] \tag{10.30}$$

The maximum and minimum over $\tau \in [-T/2, T/2]$ in the square brackets can be written as one of the following six algebraic expressions depending on the value of ϕ at which the supremum is attained:

Interval 1: If $\phi \in [0, \frac{\omega T}{2}] \cup [\pi, \pi + \frac{\omega T}{2}]$,

$$\Delta\psi = \sup_{d,\phi} \frac{d^2}{2r_0} k_{N-1} \sin^2\left(\phi + \frac{\omega T}{2}\right) \tag{10.31}$$

Interval 2: If $\phi \in [\frac{\omega T}{2}, \frac{\pi}{2} - \frac{\omega T}{2}] \cup [\pi + \frac{\omega T}{2}, \frac{3\pi}{2} - \frac{\omega T}{2}]$,

$$\Delta\psi = \sup_{d,\phi} \frac{d^2}{2r_0} \left[k_{N-1} \sin^2\left(\phi + \frac{\omega T}{2}\right) - k_0 \sin^2\left(\phi - \frac{\omega T}{2}\right) \right] \tag{10.32}$$

Interval 3: If $\phi \in [\frac{\pi}{2} - \frac{\omega T}{2}, \frac{\pi}{2}] \cup [\frac{3\pi}{2} - \frac{\omega T}{2}, \frac{3\pi}{2}]$,

$$\Delta\psi = \sup_{d,\phi} \frac{d^2}{2r_0} \left[k_{N-1} - k_0 \sin^2\left(\phi - \frac{\omega T}{2}\right) \right] \tag{10.33}$$

Interval 4: If $\phi \in [\frac{\pi}{2}, \frac{\pi}{2} + \frac{\omega T}{2}] \cup [\frac{3\pi}{2}, \frac{3\pi}{2} + \frac{\omega T}{2}]$,

$$\Delta\psi = \sup_{d,\phi} \frac{d^2}{2r_0} \left[k_{N-1} - k_0 \sin^2\left(\phi + \frac{\omega T}{2}\right) \right] \tag{10.34}$$

Interval 5: If $\phi \in [\frac{\pi}{2} + \frac{\omega T}{2}, \pi - \frac{\omega T}{2}] \cup [\frac{3\pi}{2} + \frac{\omega T}{2}, 2\pi - \frac{\omega T}{2}]$,

$$\Delta\psi = \sup_{d,\phi} \frac{d^2}{2r_0} \left[k_{N-1} \sin^2\left(\phi - \frac{\omega T}{2}\right) - k_0 \sin^2\left(\phi + \frac{\omega T}{2}\right) \right] \qquad (10.35)$$

Interval 6: Finally, if $\phi \in [\pi - \frac{\omega T}{2}, \pi] \cup [2\pi - \frac{\omega T}{2}, 2\pi]$,

$$\Delta\psi = \sup_{d,\phi} \frac{d^2}{2r_0} k_{N-1} \sin^2\left(\phi - \frac{\omega T}{2}\right) \qquad (10.36)$$

The suprema are greatest in intervals 2 and 5 because they are where the maxima and minima of $\sin^2(\phi - \omega\tau)$ have the greatest separation (the remaining four intervals are special cases where the gradient of $\sin^2(\phi - \omega\tau)$ starts to change sign). These two intervals constitute a proportion of $1 - 4\omega T/2\pi$ of the whole target, which is almost the whole target because $\omega T \ll 1$. Therefore unless the target's extent suddenly increases in intervals 1, 3, 4 or 6, the supremum of $\Delta\psi$ almost certainly occurs in intervals 2 or 5. The target's extent does not suddenly increase because it is modelled as approximately rectangular, so the supremum of $\Delta\psi$ may be found by considering the form of the supremum in intervals 2 and 5 only.

In interval 2, a little algebra shows that

$$\Delta\psi_{xy} \le \frac{d^2}{2r_0} \Big[(k_{N-1} + k_0)\, |\sin\phi\cos\phi|\sin\omega T$$
$$+ (k_{N-1} - k_0)\left(\sin^2\phi + \sin^2\frac{\omega T}{2}\right) \Big] \qquad (10.37)$$

Exactly the same expression is obtained for $\Delta\psi_{xy}$ in interval 5.

Therefore $\Delta\psi$ may be written

$$\Delta\psi \le \sup_{d,\phi} \frac{d^2}{2r_0} \Big[(k_{N-1} + k_0)\, |\sin\phi\cos\phi|\sin\omega T$$
$$+ (k_{N-1} - k_0)\left(\sin^2\phi + \sin^2\frac{\omega T}{2}\right) \Big] \qquad (10.38)$$

If ϕ is not close to 0 or π, the $\sin^2\phi$ term is much greater than the $\sin^2(\omega T/2)$ term, which may then be neglected. Writing $d\cos\phi = x$ and $d\sin\phi = y$ gives an upper bound on $\Delta\psi$ in terms of each point's x and y coordinates

$$\Delta\psi \le \sup_{(x,y)} \frac{1}{2r_0} \left[(k_{N-1} + k_0)\, |xy|\sin\omega T + (k_{N-1} - k_0)y^2 \right] \qquad (10.39)$$

The supremum is attained when $|y| = D_c/2$ and $|x| = D_r/2$. Since the maximum phase variation has been set at $\pi/2$ in (10.13), this means that the target's extent and the ISAR image's resolution must satisfy

$$\frac{1}{8r_0} \left[(k_{N-1} + k_0) D_r D_c \sin\omega T + (k_{N-1} - k_0) D_c^2 \right] < \frac{\pi}{2} \qquad (10.40)$$

10.2.3 Constraints Due to Range-Doppler Processing

Equation (10.40) is the basic constraint due to the range-Doppler plane-wave approximation. It is more useful, however, if it is expressed in terms of the target and the image's resolution, not the radar waveform's parameters.

From equations (4.35) and (4.37), the ISAR image's resolution in the range and cross-range directions are approximately

$$\Delta r_r = \frac{2\pi}{k_{N-1} - k_0} \tag{10.41}$$

$$\Delta r_c = \frac{4\pi}{(k_0 + k_{N-1}) \sin \omega T} \tag{10.42}$$

Substituting these for k_0 and k_{N-1} in (10.40) gives the condition

$$\frac{1}{8r_0} \left[\frac{4\pi}{\Delta r_c} D_r D_c + \frac{2\pi}{\Delta r_r} D_c^2 \right] < \frac{\pi}{2} \tag{10.43}$$

which is

$$\frac{D_r D_c}{r_0 \Delta r_c} + \frac{D_c^2}{2r_0 \Delta r_r} < 1 \tag{10.44}$$

This is certainly satisfied if

$$\frac{D_r D_c}{r_0 \Delta r_c} < \frac{1}{2} \tag{10.45}$$

$$\frac{D_c^2}{2r_0 \Delta r_r} < \frac{1}{2} \tag{10.46}$$

Rearranging these gives limits on the best resolution that can be used with range-Dopler processing for a target of a given size and range.

$$\Delta r_c > \frac{2D_r D_c}{r_0} \tag{10.47}$$

$$\Delta r_r > \frac{D_c^2}{r_0} \tag{10.48}$$

When designing a range-Doppler ISAR system, the first step should be using equations (10.47) and (10.48) to determine the highest resolution that the imaging geometry allows. Then the parameters of the stepped-frequency waveform can be selected to give the desired resolution providing this is consistent with these limits.

These limits are consistent with the example used throughout chapter 3, which had a resolution of 1 m by 1 m for a target 30 m across at a range of 10 km. The minimum cross-range resolution is 18 cm and the minimum

range resolution is 9 cm.[5] Both of these are substantially better than the required resolution of 1 m by 1 m.

One final comment about range-Doppler imaging is that the target does not have to be in the far-field for the Taylor series to be valid. The target is in the far-field when

$$r_0 > \frac{D^2}{\lambda} \tag{10.49}$$

where D is the target's extent. For the parameters above, at X-band where λ=3 cm, the far-field starts at a range of 30 km, whereas the $\pi/2$ phase condition says that the target may be as close as $r_0 = 2 \cdot 30^2/1 = 1.8$ km.

10.3   Polar Reformatting

The classical but incorrect view of ISAR imaging as a temporal Doppler process restricted by the motion of scatterers through resolution cells leads to the bounds on Δr_r and Δr_c given in equations (10.1) and (10.2).

In this section, errors arising from omitting polar reformatting are analysed to derive simple conditions under which acceptable ISAR images may be formed without the complexity of polar reformatting. These conditions are similar to those in equations (10.1) and (10.2) derived by considering the target's motion through resolution cells. However, the more exact analysis presented here also includes an extra factor of D_c in (10.1) that has not been included in any other analyses of polar reformatting.

The results presented here are explicitly for ISAR imaging a uniformly rotating target using range-Doppler processing. However, the same method can also be used for targets moving in a straight line or for ISAR imaging using $\omega - k$ processing.

10.3.1   Defining the Phase Variation $\Delta\psi_{xy}$

As for the analysis of phase errors due to the range-Doppler approximation, the distance between the radar and a scatterer at (x, y) is, at time t,

$$r_{xy}(t) = r_0 + x \cos \omega t - y \sin \omega t + \epsilon_{xy}(t) \tag{10.50}$$

where $\epsilon_{xy}(t)$ is the Taylor series' remainder, which is the error due to the range-Doppler linear approximation.

Not performing polar reformatting is equivalent to assuming that the polar grid in (k_x, k_y)-space is rectangular. Therefore the point $(k_x(k, t), k_y(k, t))$

---

[5]Note that the analysis in this section does not mean that it is possible to obtain resolutions of 18 cm by 9 cm. Other constraints, principly that of a narrow relative bandwidth, have to be violated for the limits in (10.47) and (10.48) to be approached.

Figure 10.1: The polar grid is assumed to be rectangular when the ISAR inversion does not use polar reformatting.
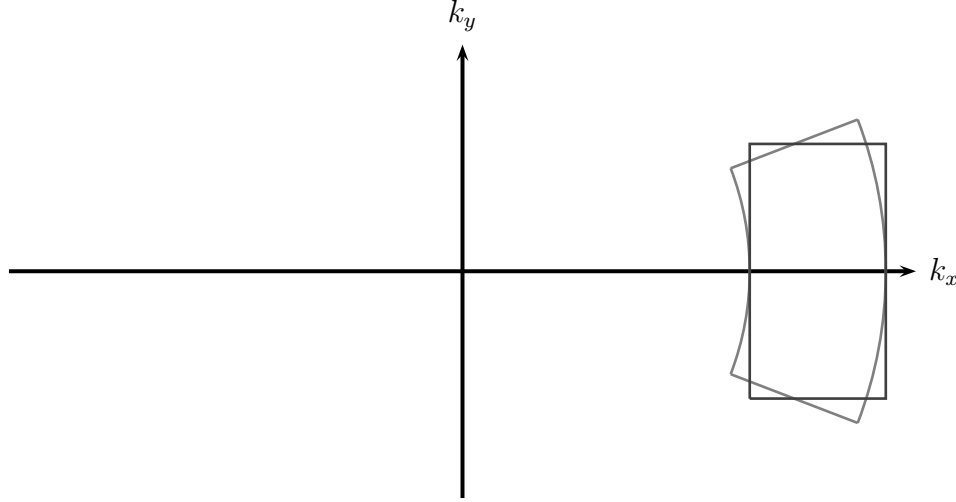
in (k_x, k_y)-space is assumed to lie at the point given by (k, t) under a linear scaling, translation and a rotation. In matrix notation,

$$\begin{bmatrix} k_x(k,t) \\ k_y(k,t) \end{bmatrix} \approx \begin{bmatrix} \cos\zeta & \sin\zeta \\ -\sin\zeta & \cos\zeta \end{bmatrix} \begin{bmatrix} \alpha & 0 \\ 0 & \beta \end{bmatrix} \left(\begin{bmatrix} k \\ t \end{bmatrix} - \begin{bmatrix} k_c \\ t_c \end{bmatrix} \right) \qquad (10.51)$$

where (k_c, t_c) is the translation, (α, β) the scale factors and ζ the angle the rectangular grid is rotated.

For the case considered here of a uniformly rotating target, the polar grid is

$$k_x(k,t) = k\cos\omega t \qquad (10.52)$$
$$k_y(k,t) = k\sin\omega t \qquad (10.53)$$

which is centred about the k_x axis because t varies from $-T/2$ to $T/2$. The polar grid's symmetry indicates that the optimum rectangular grid has its axes parallel with the k_x and k_y axes, thus $\zeta = 0$. The perimeters of the polar grid for a uniformly rotating target and the assumed rectangular grid are shown in figure 10.1.

Under this assumption of a rectangular grid, the phase $kr_{xy}(t)$ in $e^{-jkr_{xy}(t)}$ can be written as

$$kr_{xy}(t) = kr_0 + (k - k_c)\alpha x + (t - t_c)\beta y + \psi_{xy}(k,t) + k\epsilon_{xy}(t) \qquad (10.54)$$

Here $\psi_{xy}(k,t)$ is the phase error associated with ignoring polar reformatting and $k\epsilon_{xy}(t)$ is the phase error associated with the range-Doppler plane-wave approximation.

The optimum rectangular grid depends on the choice of α and β and ζ; the choice of translation (k_c, t_c) does not matter because this can be absorbed into the phase of $g(x, y)$.

As for the analysis of the range-Doppler approximation, define the total variation in the phase error at a point (x, y) over all k and t as

$$\Delta\psi_{xy}(\alpha, \beta, \zeta) = \max_{k,t,k',t'} |\psi_{xy}(k, t) - \psi_{xy}(k', t')| \tag{10.55}$$

This is a function of the rectangular grid, hence $\Delta\psi_{xy}(\alpha, \beta, \zeta)$ depends on α, β and ζ. Since the aim of the selecting the rectangular grid is to minimize the maximum phase variation over the whole of the target, define the maximum phase variation for a particular rectangular grid as

$$\begin{aligned}
\Delta\psi(\alpha, \beta, \zeta) &= \sup_{(x,y)} \Delta\psi_{xy}(\alpha, \beta, \zeta) \\
&= \sup_{(x,y)} \max_{k,t,k',t'} |\psi_{xy}(k, t) - \psi_{xy}(k', t')|
\end{aligned} \tag{10.56}$$

Finally, as the rectangular grid should be selected so that $\Delta\psi(\alpha, \beta, \zeta)$ is minimized, define the optimum maximum phase variation, $\Delta\psi$, as

$$\begin{aligned}
\Delta\psi &= \inf_{\alpha,\beta,\zeta} \Delta\psi(\alpha, \beta, \zeta) \\
&= \inf_{\alpha,\beta,\zeta} \sup_{(x,y)} \max_{k,t,k',t'} |\psi_{xy}(k, t) - \psi_{xy}(k', t')|
\end{aligned} \tag{10.57}$$

Now, once an upper limit on $\Delta\psi$ has been selected, such as

$$\Delta\psi < \frac{\pi}{2} \tag{10.58}$$

substitute (10.57) and solve for the infinum, supremum and maximum to obtain some constraints on the target's motion and the ISAR image's resolution.

10.3.2   Evaluating the Phase Variation

For the uniformly rotating target and range-Doppler processing, the phase error $\psi_{xy}(k, t)$ if polar reformatting is omitted is

$$\psi_{xy}(k, t) = x\,(\alpha k - k\cos\omega t) - y\,(\beta t - k\sin\omega t) \tag{10.59}$$

As mentioned earlier, symmetry dictates that $\zeta = 0$ so that the total phase variation $\Delta\psi_{xy}(\alpha, \beta, 0)$ is less than

$$\begin{aligned}
\Delta\psi_{xy}(\alpha, \beta, 0) &\leq \max_{k,t,k',t'} |x|\,|(\alpha k - k\cos\omega t) - (\alpha k' - k'\cos\omega t')| \\
&\quad + |y|\,|(\beta t - k\sin\omega t) - (\beta t' - k'\sin\omega t')| \\
&\leq \max_{k,t,k',t'} \frac{D_r}{2}\,|(\alpha k - k\cos\omega t) - (\alpha k' - k'\cos\omega t')| \\
&\quad + \frac{D_c}{2}\,|(\beta t - k\sin\omega t) - (\beta t' - k'\sin\omega t')|
\end{aligned} \tag{10.60}$$

because $|x| < D_r/2$ and $|y| < D_c/2$ for all points on the target. Since this last expression is independent of x and y, the supremum over (x, y) has been evaluated, leaving

$$\Delta\psi \leq \inf_{\alpha,\beta} \max_{k,t,k',t'} \frac{D_r}{2} |(\alpha k - k\cos\omega t) - (\alpha k' - k'\cos\omega t')|$$
$$+ \frac{D_c}{2} |(\beta t - k\sin\omega t) - (\beta t' - k'\sin\omega t')| \qquad (10.61)$$

which is bounded above by an expression where the two moduli are maximized separately

$$\Delta\psi \leq \inf_{\alpha} \max_{k,t,k',t'} \frac{D_r}{2} |(\alpha k - k\cos\omega t) - (\alpha k' - k'\cos\omega t')|$$
$$+ \inf_{\beta} \max_{k,t,k',t'} \frac{D_c}{2} |(\beta t - k\sin\omega t) - (\beta t' - k'\sin\omega t')| \qquad (10.62)$$

Split this upper bound on $\Delta\psi$ into two halves, L_r and L_c so that

$$\Delta\psi \leq \frac{D_r}{2} L_r + \frac{D_c}{2} L_c \qquad (10.63)$$

where

$$L_r = \inf_{\alpha} \max_{k,t,k',t'} |(\alpha k - k\cos\omega t) - (\alpha k' - k'\cos\omega t')| \qquad (10.64)$$

and

$$L_c = \inf_{\beta} \max_{k,t,k',t'} |(\beta t - k\sin\omega t) - (\beta t' - k'\sin\omega t')| \qquad (10.65)$$

Starting with L_r, note that L_r can be written

$$L_r = \inf_{\alpha} \max_{k,b,k',b'} |kb - k'b'| \qquad (10.66)$$

where the maximum includes values of k and k' in $[k_0, k_{N-1}]$ and values of b and b' in B which is the interval

$$B = \left[\cos\left(\frac{\omega T}{2}\right) - \alpha, 1 - \alpha\right] \qquad (10.67)$$

Apply theorem 10.2 in appendix 10A with $a = k$, $a' = k'$ and $A = [k_0, k_{N-1}]$ to show that

$$L_r = k_{N-1}\left(1 - \cos\left(\frac{\omega T}{2}\right)\right) \approx k_{N-1}\frac{(\omega T)^2}{8} \qquad (10.68)$$

where α may take any value between $\cos(\omega T/2)$ and 1.

The exact value of L_c is much more difficult to obtain, so a slightly loose upper bound on L_c will be found instead of the exact value. First, use the triangle inequality twice to show that

$$
\begin{aligned}
L_c = \inf_{\beta} \max_{k,t,k',t'} & |(\beta t - k \sin \omega t) - (\beta t' - k' \sin \omega t')| \\
\le\ & 2 \inf_{\beta} \max_{k,t} |\beta t - k \sin \omega t| \\
\le\ & 2 \left(\max_{k,t} |k(\sin \omega t - \omega t)| + \max_{k,t} \left|(\overline{k} - k)\omega t\right| \right)
\end{aligned}
\tag{10.69}
$$

where one particular $\beta = \omega \overline{k}$ has been chosen so that the infinum over β can be removed. Here $\overline{k} = (k_0 + k_{N-1})/2$. The optimum choice of β satisfies

$$
k_0 \frac{2}{T} \sin \frac{\omega T}{2} \le \beta \le k_{N-1} \omega
\tag{10.70}
$$

but finding it is quite difficult. With $\beta = \omega \overline{k}$, the maximum occurs when $t = T/2$ and $k = k_{N-1}$ so that

$$
\begin{aligned}
L_c &\le 2 \left(k_{N-1} \left(\frac{\omega T}{2} - \sin \frac{\omega T}{2} \right) + \frac{N \Delta k}{2} \frac{\omega T}{2} \right) \\
&\approx k_{N-1} \frac{(\omega T)^3}{24} + \frac{N \Delta k \, \omega T}{2}
\end{aligned}
\tag{10.71}
$$

Combining these bounds on L_r and L_c shows that

$$
\Delta \psi \le \frac{D_r}{2} k_{N-1} \frac{(\omega T)^2}{8} + \frac{D_c}{2} \left(k_{N-1} \frac{(\omega T)^3}{24} + \frac{N \Delta k \, \omega T}{2} \right)
\tag{10.72}
$$

Neglecting the $(\omega T)^3$ term,

$$
\Delta \psi \le D_r \, k_{N-1} \frac{(\omega T)^2}{16} + D_c \frac{N \Delta k \, \omega T}{16}
\tag{10.73}
$$

Since the maximum value of $\Delta \psi$ has been set to $\pi/2$, this means that the target's extent and the ISAR image's resolution must satisfy

$$
D_r \, k_{N-1} \frac{(\omega T)^2}{16} + D_c \frac{N \Delta k \, \omega T}{16} < \frac{\pi}{2}
\tag{10.74}
$$

if polar reformatting is not required.

10.3.3 Constraints Due to Neglecting Reformatting

Equation (10.74) is the basic constraint due to neglecting polar reformatting. As for the equivalent constraint for the range-Doppler approximation

in (10.40), it is more usefully expressed in terms of the target and the image's resolution, rather than the radar waveform's parameters. The radar's average wavelength is the only waveform parameter that cannot be eliminated, giving

$$\frac{\lambda D_r}{8\Delta r_c^2} + \frac{\lambda D_c}{8\Delta r_r \Delta r_c} < 1 \tag{10.75}$$

This is satisfied if both terms on the left-hand side are less than a half, which gives the following two constraints for neglecting polar reformatting

$$\Delta r_c^2 > \frac{\lambda D_r}{4} \tag{10.76}$$

$$\Delta r_r \Delta r_c > \frac{\lambda D_c}{4} \tag{10.77}$$

which are exactly the same as the classical constraints due to motion through resolution cells quoted at the beginning of the chapter in equations (10.1) and (10.2), which is rather a surprising result.

10.4   Motion Estimation for Rotating Targets

Because ISAR is designed to image moving targets, motion estimation and motion compensation are essential parts of producing a well-focussed image. The primary assumption of motion estimation is that the target rotates sufficiently slowly that over a short period of time, $t \in [0, \tau]$ for some $0 \leq \tau \leq T$, measurements of the target's frequency response show a phase change due to its radial displacement so that

$$s(k, \tau) = e^{-jk\Delta r} \, s(k, 0) \tag{10.78}$$

where Δr is the radial distance the target moves between $t = 0$ and $t = \tau$.

In this section, this basic assumption of a target rotating sufficiently slowly for motion estimation is analysed to find a constraint on a target's maximum allowable rotation rate. It is shown that if the target is rotating fast enough that it fills most of the ISAR image's cross-range window, it is rotating too quickly for accurate motion estimation. This leads to a constraint that the cross-range extent of the target should be at most one-quarter of the size of the image's cross-range window.

This result, one that has not appeared in the ISAR literature before, is slightly surprising because it suggests a fundamental limitation on accurate motion estimation for ISAR that is much stricter than the resolution constraints due to range-Doppler processing or ignoring polar reformatting. Since many ISAR images have a target that fills more than a quarter of the cross-range window, this constraint is often violated. When this happens,

reflections from scatterers that are far from the centre of the target appear as random phase shifts while reflections from those closer to the centre have phase shifts that are more tightly concentrated about $-k\Delta r$. This leads to a type of rotation-induced noise which increases in variance as the target fills more and more of the cross-range window.

The target motion considered in this section is that of a uniformly-rotating target a fixed distance from the radar. This particular motion has been chosen because it is the same as that in the other two analyses in this chapter. The same method can be used with any other target motion, and it is a simple matter to rewrite the results in terms of a target moving in a straight line at constant speed. Using a target that is uniformly rotating with no radial motion emphasizes that this effect is due to the target's rotation, not to the radial motion itself.

10.4.1 Defining the Total Phase Variation $\Delta\psi$

From equation (4.10), the distance between a scatterer at (x, y) in the target's local coordinate system and the radar is

$$r_{xy}(t) = \sqrt{(r_0 + x\cos\omega t - y\sin\omega t)^2 + (x\sin\omega t + y\cos\omega t)^2} \qquad (10.79)$$

at time t. This can be written slightly differently as

$$r_{xy}(t) = \sqrt{(r_0 + x)^2 + y^2 - 2r_0(x(1 - \cos\omega t) + y\sin\omega t)} \qquad (10.80)$$

The radar measurement of the target at frequency k and time $t = 0$ is

$$s(k, 0) = \iint g(x, y)\, e^{-jkr_{xy}(0)}\, dx\, dy \qquad (10.81)$$

If the target is rotates negligibly between $t = 0$ and $t = \tau$, then

$$s(k, \tau) = e^{-jk\Delta r}\, s(k, 0) \qquad (10.82)$$

which suggests that

$$s(k, \tau) = e^{-jk\Delta r} \iint g(x, y)\, e^{-jkr_{xy}(0)}\, dx\, dy \qquad (10.83)$$

However, the target is rotating slowly, so the correct expression for $s(k, \tau)$ is

$$s(k, \tau) = e^{-jk\Delta r} \iint g'(x, y, k, \tau)\, e^{-jkr_{xy}(0)}\, dx\, dy \qquad (10.84)$$

where the target's reflectivity function has been modified to give

$$g'(x, y, k, \tau) = g(x, y)\, e^{-jk\epsilon_{xy}(\tau)} \qquad (10.85)$$

with $\epsilon_{xy}(\tau)$ being the error in the range of a scatterer at $(0,0)$ due to the assumption that the target is not rotating. Thus

$$r_{xy}(\tau) = r_{xy}(0) + \Delta r + \epsilon_{xy}(\tau) \tag{10.86}$$

The variation in $\epsilon_{xy}(\tau)$ at different points (x, y) on the target means that the phase difference between $(s(k, 0)$ and $s(k, \tau)$ is not exactly $-k\Delta r$. This is the cause of rotation-induced noise.

Define the total phase variation as

$$\Delta\psi = \sup_{xy,x'y'} |k\epsilon_{xy}(\tau) - k\epsilon_{x'y'}(\tau)| \tag{10.87}$$

To limit the rotation-induced noise to an acceptable level, place an upper limit on the total phase variation over all points on the target, so that

$$\Delta\psi < \frac{\pi}{2} \tag{10.88}$$

10.4.2 Evaluating the Total Phase Variation

For the uniformly-rotating target, $\epsilon_{xy}(\tau)$ is

$$\begin{aligned}
\epsilon_{xy}(\tau) &= \sqrt{(r_0 + x)^2 + y^2 - 2r_0(x(1 - \cos\omega\tau) + y\sin\omega\tau} - \sqrt{(r_0 + x)^2 + y^2} \\
&\approx x(1 - \cos\omega\tau) + y\sin\omega\tau
\end{aligned} \tag{10.89}$$

so that

$$\Delta\psi = \sup_{xy,x'y'} k \left| (x - x')(1 - \cos\omega\tau) + (y - y')\sin\omega\tau \right| \tag{10.90}$$

This supremum is attained for (x, y) and (x', y') at opposite ends of the target. The maximum value of $|x - x'|$ is D_r, the target's range extent, and the maximum value of $|y - y'|$ is D_c, the target's cross-range extent. Therefore

$$\Delta\psi = kD_r(1 - \cos\omega\tau) + kD_c\sin\omega\tau \tag{10.91}$$

The time $t = \tau$, at which the measurement of $s(k, \tau)$ was made, is between 0 and T, the period over which the data for the ISAR image is acquired. Therefore $|\omega\tau| \leq |\omega T| \ll 1$ and $\Delta\psi$ can be written

$$\Delta\psi = \frac{k}{2}D_r(\omega\tau)^2 + kD_c\omega\tau \tag{10.92}$$

Since τ is some fraction of the total imaging period, write

$$\tau = \eta T \qquad \text{for some } \eta \in [0, 1] \tag{10.93}$$

Then using $\Delta\psi < \pi/2$, the constraint becomes

$$\frac{k\eta^2}{2}D_r(\omega T)^2 + k\eta D_c\omega T < \frac{\pi}{2} \tag{10.94}$$

10.4.3   Constraints Due to Motion Estimation

Equation (10.94), the basic constraint due to the target's rotation during motion estimation, can be written

$$\pi \eta^2 \frac{\lambda D_r}{\Delta r_c^2} + 2\pi \eta \frac{D_c}{\Delta r_c} < \frac{\pi}{2} \qquad (10.95)$$

The first term is negligible in comparison with the second as $\Delta r_c \gg \lambda$. Therefore the single constraint due to the need for reliable motion estimation is

$$\Delta r_c > 4\eta D_c \qquad (10.96)$$

From this, a small value of η is needed for a high cross-range resolution. The smallest η can be is $1/M$, where M is the number of time steps at which the target's frequency response is sampled. The width W_c of the ISAR image's cross-range ambiguity window is

$$W_c = M \Delta r_c \qquad (10.97)$$

so the constraint on the target's size is

$$D_c < \frac{W_c}{4} \qquad (10.98)$$

which indicates that the target can occupy no more than a quarter of the cross-range ambiguity window.

10.4.4   Rotation-Induced Noise

When a target is rotating slowly, all scatterers move approximately the same radial distance as the target moves. The phase shifts due to each scatterer's radial motion add coherently so they can easily be detected for motion compensation.

As the target rotates faster, differences in the radial movement of scatterers at the outside of the target become greater than a wavelength. The phase shifts due to these scatterers' radial motion add incoherently, causing motion-induced noise. Near the centre of the target, differences in the scatterers' ranges are still small enough for their phase shifts to add coherently. As the target rotates more quickly, a smaller component of the radar reflection contains information that is useful for motion estimation. Therefore, the apparent signal-to-noise ratio for motion compensation decreases as the target's angular velocity increases.

This motion-induced noise can be observed in ISAR simulations of a rotating target with no background noise. Using the maximum likelihood estimator of the signal-to-noise ratio in (6.43), the apparent signal-to-noise ratio

Figure 10.2: Rotation-induced noise as a function of a simulated target's angular velocity. The shaded horizontal line indicates the expected variance of the rotation-induced noise when the target is rotating very quickly and motion estimation becomes random. The shaded vertical line shows the rotation rate when the simulated target completely fills the ISAR cross-range window.

is
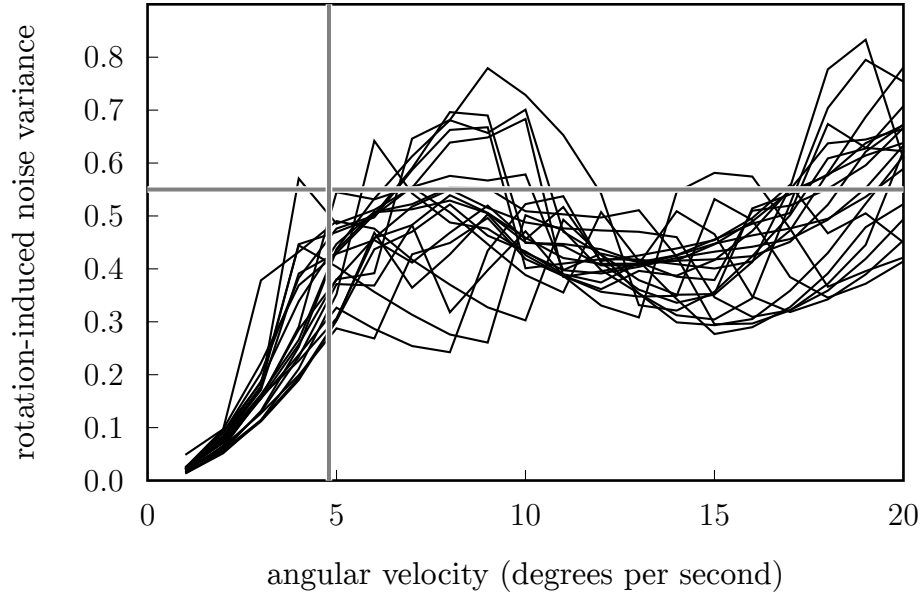
$$\widehat{\sigma}^2_{w,ml} = \frac{1}{4N} \sum_{n=0}^{N-1} \left| s(k_n, 0) - s(k_n, \tau)e^{jk_n\widehat{r}_{ml}} \right|^2 \tag{10.99}$$

where $\widehat{r}_{ml}$ is the maximum likelihood estimate of the radial distance the target has moved between $t = 0$ and $t = \tau$. Since the simulation has no background noise, a non-zero $\widehat{\sigma}^2_{w,ml}$ indicates noise caused by the target's rotation.

The rotation-induced noise's variance increases as the target rotates faster. The upper limit of the noise variance's expectation is

$$\frac{1}{4N} \sum_{n=0}^{N-1} |s(k_n, 0)|^2 + |s(k_n, \tau)|^2 \tag{10.100}$$

when the phase changes from all scatterers add incoherently and motion estimation becomes random.

This is illustrated in figure 10.2 for twenty estimates of the rotation-induced noise for target angular velocities ranging from 1° per second to 20° per second. The horizontal line at a noise variance of about 0.55 indicates the noise variance for which motion compensation gives totally random results. This shows that motion compensation is not possible when this simulated target is rotating faster than about 5° per second.

Since the target, a simulated 737 aircraft, is 30 metres by 26 metres, and the stepped-frequency radar had a centre frequency of 9.19 GHz, the target fills the ISAR cross-range window when $\omega = 4.8^o$ per second. At this rate, the rotation-induced noise is very high and motion estimation will perform poorly.

For motion estimation to work well for this particular simulation, the target's rotation rate should be kept below about 1.2^o per second, when the ISAR image fills about a quarter of the cross-range window. This may require sampling the target's frequency response more frequently so that the motion estimation is accurate, but using only a subset of the data for forming the ISAR image.

10.5 Accuracy of Motion Estimation

Many discussions of motion estimation for radar imaging and of focussing phased-array radars quote a benchmark of $\lambda/10$ as the conventional tolerance required. This figure is mentioned by Steinberg [94] and by Xu *et al.* [101, 102, 103].

In this section, a similar analysis to that used throughout this chapter is employed to show that for a maximum phase error of $\pi/2$, the magnitude of the residual phase errors after motion compensation must be less than $\lambda/8$.

This simple result is then extended to show that the residual range errors can be substantially larger than $\lambda/8$ without having a maximum phase error greater than $\pi/2$ providing they are clustered around multiples of $\lambda/2$. Since the radial motion estimates produced by the maximum likelihood motion estimator are clustered around multiples of $\lambda/2$, this justifies using the maximum likelihood motion estimator for ISAR motion compensation, and it also indicates that simple measures of motion estimation errors such as variance are inadequate for ISAR.

10.5.1 Simple Analysis of Residual Errors

Suppose that motion estimation and motion compensation have been applied to the radar measurements $s(k,t)$. If the motion compensation were perfect, the measurements would be

$$s(k,t) = \iint g(x,y)\, e^{-jkr_{xy}(t)}\, dx\, dy \qquad (10.101)$$

where $r_{xy}(t)$ is the range of point (x,y) on the target at time t expected by the ISAR inversion algorithm. However, no motion compensation is perfect so the actual measurements are different from the ideal

$$s(k,t) = \iint g(x,y)\, e^{-jkr_e(t)}\, e^{-jkr_{xy}(t)}\, dx\, dy \qquad (10.102)$$

where $r_e(t)$ is the residual motion error at time t.

This is equivalent to applying the ISAR inversion to a target reflectivity function $g'(x, y, k, t)$ that varies with time and frequency according to the severity of the motion estimation error at that time

$$g'(x, y, k, t) = g(x, y) \, e^{-jkr_e(t)} \tag{10.103}$$

Define the maximum phase variation in $g(x, y)$ as

$$\Delta\psi = \max_{k,t,k't,} |kr_e(t) - k'r_e(t')| \tag{10.104}$$

Then by setting an upper limit on the maximum phase variation, such as

$$\Delta\psi < \frac{\pi}{2} \tag{10.105}$$

bounds on $r_e(t)$ can be established.

In general, $r_e(t)$ is just as likely to be positive as negative. Using theorem 10.2 in appendix 10A,

$$\Delta\psi < 2k_{N-1} \max_{\tau} |r_e(\tau)| \tag{10.106}$$

Since $k_{N-1} \approx 8\pi/\lambda$ where λ is the average wavelength of the frequencies in the stepped-frequency waveform, this shows that the residual motion errors must satisfy

$$|r_e(t)| < \frac{\lambda}{16} \qquad \forall t \in [-T/2, T/2] \tag{10.107}$$

which is equivalent to

$$|r_e(t) - r_e(t')| < \frac{\lambda}{8} \qquad \forall t, t' \in [-T/2, T/2] \tag{10.108}$$

These limits are similar to the benchmark accuracy of $\lambda/10$ quoted above.

10.5.2 Better Analysis of Residual Errors

The analysis of residual motion estimation errors in (10.108) is inadequate because only the residual error modulo 2π is important.[6] One example of motion estimation where omitting the modulo 2π condition does matter is the maximum likelihood motion estimator in chapter 6, where the residual motion errors are tightly clustered around small multiples of $\lambda/2$.

---

[6]The modulo 2π is not important in the other three assumptions analysed in this chapter because for all three, $\Delta\psi$ is a supremum over all points (x, y) on the target. Since x and y are continuous variables, taking the phase variation modulo 2π would give $\Delta\psi = 2\pi$ if any phase variations greater than 2π were present.

When modulo 2π phase errors are included, the definition of $\Delta\psi$ is modified to read

$$\Delta\psi = \min_n \max_{k,t,k't,} |kr_e(t) - k'r_e(t') + 2n\pi| \tag{10.109}$$

where the minimum is taken over all integers n.

Now suppose that the range errors $r_e(t)$ are clustered around multiples of $\lambda/2$, so that $r_e(t) \in R$ where the set R is the union of intervals of width $2\delta_i$ centred about $r_i = i\lambda/2$, where i is any integer

$$R = \bigcup_{i=-\infty}^{\infty} \left[i\frac{\lambda}{2} - \delta_i, i\frac{\lambda}{2} + \delta_i \right] \tag{10.110}$$

Since the phase error $\psi_e(k,t)$ corresponding to a motion error of $r_e(t)$ at frequency k is

$$\psi_e(k,t) = kr_e(t) \tag{10.111}$$

the set of phase errors resulting from motion errors in R and frequencies in $[k_0, k_{N-1}]$ can be found using similar considerations to lemma 10.1 and theorem 10.2 in appendix 10A. This set of phase errors Ψ is

$$\Psi = \left(\bigcup_{i=-\infty}^{-1} \left[k_{N-1} \left(i\frac{\lambda}{2} - \delta_i \right), k_0 \left(i\frac{\lambda}{2} + \delta_i \right) \right] \right) \cup [-k_{N-1}\delta_0, k_{N-1}\delta_0]$$
$$\cup \left(\bigcup_{i=1}^{\infty} \left[k_0 \left(i\frac{\lambda}{2} - \delta_i \right), k_{N-1} \left(i\frac{\lambda}{2} + \delta_i \right) \right] \right) \tag{10.112}$$

Then the maximum modulo 2π phase variation will always be less than $\pi/2$ if Ψ is a subset of Ψ_0 where

$$\Psi_0 = \bigcup_{i=-\infty}^{\infty} \left[2i\pi - \frac{\pi}{4}, 2i\pi + \frac{\pi}{4} \right] \tag{10.113}$$

This leads to three sets of conditions on δ_i, depending on whether $i < 0$, $i = 0$ or $i > 0$.

Case (i): If $i < 0$, δ_i must be chosen so that

$$\left[k_{N-1} \left(i\frac{\lambda}{2} - \delta_i \right), k_0 \left(i\frac{\lambda}{2} + \delta_i \right) \right] \subset \left[2i\pi - \frac{\pi}{4}, 2i\pi + \frac{\pi}{4} \right] \tag{10.114}$$

This imposes the following two conditions on the interval's endpoints

$$k_{N-1} \left(i\frac{\lambda}{2} - \delta_i \right) \geq 2i\pi - \frac{\pi}{4} \tag{10.115}$$

$$k_0 \left(i\frac{\lambda}{2} + \delta_i \right) \leq 2i\pi + \frac{\pi}{4} \tag{10.116}$$

Subtracting them shows that each δ_i must satisfy

$$\delta_i \leq \frac{\frac{\pi}{2} + i(k_{N-1} - k_0)\frac{\lambda}{2}}{k_{N-1} + k_0} \tag{10.117}$$

Case (ii): If $i = 0$, δ_0 must be chosen so that

$$[-k_{N-1}\delta_0, k_{N-1}\delta_0] \subset \left[-\frac{\pi}{4}, \frac{\pi}{4}\right] \tag{10.118}$$

which shows that δ_0 must satisfy

$$\delta_0 \leq \frac{\pi}{4k_{N-1}} \tag{10.119}$$

Case (iii): If $i > 0$, δ_i must be chosen so that

$$\left[k_0\left(i\frac{\lambda}{2} - \delta_i\right), k_{N-1}\left(i\frac{\lambda}{2} + \delta_i\right)\right] \subset \left[2i\pi - \frac{\pi}{4}, 2i\pi + \frac{\pi}{4}\right] \tag{10.120}$$

This imposes the following two conditions on the interval's endpoints

$$k_0\left(i\frac{\lambda}{2} - \delta_i\right) \geq 2i\pi - \frac{\pi}{4} \tag{10.121}$$

$$k_{N-1}\left(i\frac{\lambda}{2} + \delta_i\right) \leq 2i\pi + \frac{\pi}{4} \tag{10.122}$$

Subtracting them shows that each δ_i must satisfy

$$\delta_i \leq \frac{\frac{\pi}{2} - i(k_{N-1} - k_0)\frac{\lambda}{2}}{k_{N-1} + k_0} \tag{10.123}$$

Now that all three cases have been considered, putting their separate conditions together shows that

$$\delta_i \leq \begin{cases} \dfrac{\pi}{4k_{N-1}} & \text{if } i = 0 \\ \dfrac{\frac{\pi}{2} - |i|\,(k_{N-1} - k_0)\frac{\lambda}{2}}{k_{N-1} + k_0} & \text{otherwise} \end{cases} \tag{10.124}$$
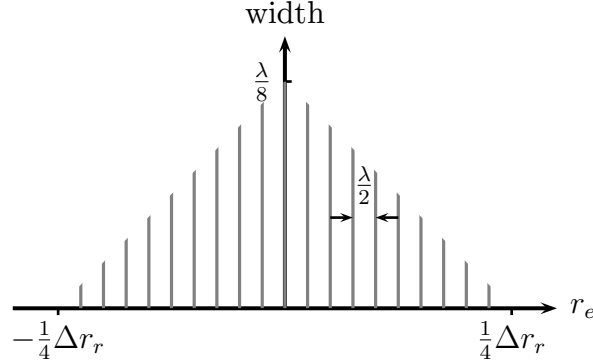
Now

$$k_{N-1} - k_0 \approx \frac{4\pi N \Delta f}{c} = 4\pi \frac{N \Delta f}{\lambda \bar{f}} \tag{10.125}$$

and

$$2k_{N-1} \approx k_{N-1} + k_0 = \frac{8\pi}{\lambda} \tag{10.126}$$

Figure 10.3: The allowable values of the residual motion estimation errors r_e lie in small intervals centred at multiples of $\lambda/2$. The width of each interval (twice δ_i) is shown plotted against the position of its centre.

so that each δ_i must satisfy

$$\delta_i \leq \frac{\lambda}{16}\left(1 - 4\frac{N\Delta f}{\overline{f}}|i|\right) \tag{10.127}$$

Since each δ_i must be positive, this sets an upper limit on $|i|$

$$|i| \leq \frac{\overline{f}}{4N\Delta f} \tag{10.128}$$

From this, the greatest allowable range error $r_e(t)$ can be calculated. Using the formula for the ISAR image's range resolution Δr_r from (4.35), the residual error at the maximum values of i has absolute value $\Delta r_r/4$, so the range errors may vary between

$$-\Delta r_r/4 \leq r_e(t) \leq \Delta r_r/4 \tag{10.129}$$

providing the $r_e(t)$ become increasingly tightly clustered about multiples of $\lambda/2$ the further from $r_e = 0$ they are. This is shown in figure 10.3, where the length of each interval has been plotted against its centre.

Note that when using the maximum likelihood motion estimator $\widehat{r}_{ml}$, the spread of residual motion estimation errors may be as wide as half the ISAR image's range resolution, which is a quarter the width of the central lobe of the envelope of $J(r)$ (which can be seen in figure 6.1(a)).

10.6 Summary of the Constraints

To summarize the results of this chapter, sets of constraints have been obtained for the three assumptions commonly made for ISAR imaging. These

constraints involve the radar's average wavelength λ, the target's extent in the range and cross-range directions, D_r and D_c, the ISAR image's resolutions in the range and cross-range directions, Δr_r and Δr_c, and the width W_c of the ISAR image's cross-range window.

Range-Doppler Processing The approximation of a spherical wave as a plane-wave in range-Doppler ISAR is valid providing

$$\Delta r_c > \frac{2 D_r D_c}{r_0}$$

and

$$\Delta r_r > \frac{D_c^2}{r_0}$$

Polar Reformatting The polar reformatting step of the ISAR inversion algorithm can be omitted if

$$\Delta r_c^2 > \frac{\lambda D_r}{4}$$

and

$$\Delta r_r \Delta r_c > \frac{\lambda D_c}{4}$$

which are identical to the classical constraints obtained by limiting the motion of all scatterers to a single resolution cell.

Motion Estimation Accurate motion estimation necessary for ISAR imaging requires that

$$D_c < \frac{W_c}{4}$$

Finally, the analysis of the motion estimation accuracy required for well-focussed ISAR images shows that residual motion errors after motion compensation may be significantly greater than the conventional limit of $\lambda/10$ providing the errors are nearly integral multiples of $\lambda/2$.

10A Theorems Concerning Maxima

Lemma 10.1 *Let $A = [A_0, A_1]$ be an interval of the real line where*

$$A_1 \geq A_0 \geq 0 \tag{10.130}$$

Similarly, let $B = [B_0, B_1]$ be an interval of the real line where

$$B_1 \geq B_0 \geq 0 \tag{10.131}$$

Then

$$\sup_{\substack{a,a' \in A \\ b,b' \in B}} |ab - a'b'| = A_1 B_1 - A_0 B_0 \tag{10.132}$$

Proof: For any $a \in A$ and any $b \in B$,[7]

$$A_1 \geq a \geq A_0 \geq 0 \tag{10.133}$$
$$B_1 \geq b \geq B_0 \geq 0 \tag{10.134}$$

Therefore
$$A_1 B_1 \geq a B_1 \geq ab \geq A_0 b \geq A_0 B_0 \geq 0 \tag{10.135}$$

for all $a \in A$ and $b \in B$. Therefore, for any $a, a' \in A$ and any $b, b' \in B$,

$$A_1 B_1 \geq ab \qquad \text{and} \qquad a'b' \geq A_0 B_0 \geq 0 \tag{10.136}$$

Subtracting $a'b'$ from ab shows that

$$A_1 B_1 - A_0 B_0 \geq ab - a'b' \geq A_0 B_0 - A_1 B_1 \tag{10.137}$$

so that
$$A_1 B_1 - A_0 B_0 \geq |ab - a'b'| \tag{10.138}$$

Therefore
$$A_1 B_1 - A_0 B_0 \geq \sup_{\substack{a,a' \in A \\ b,b' \in B}} |ab - a'b'| \tag{10.139}$$

To show that this upper bound is attained, let $a = A_1$, $b = B_1$, $a' = A_0$ and $b' = B_0$. Therefore

$$A_1 B_1 - A_0 B_0 = \sup_{\substack{a,a' \in A \\ b,b' \in B}} |ab - a'b'| \tag{10.140}$$

and the lemma is proved. ∎

Theorem 10.2 *Let $A = [A_0, A_1]$ be an interval of the real line where*

$$A_1 \geq A_0 \geq 0 \tag{10.141}$$

Similarly, let $B = [B_0, B_1]$ be an interval of the real line where

$$B_1 \geq B_0 \tag{10.142}$$

where now B_0 and B_1 may be negative. Then for s real

$$\inf_s \sup_{\substack{a,a' \in A \\ b,b' \in B}} |a(b - s) - a'(b' - s)| = A_1(B_1 - B_0) \tag{10.143}$$

and this is attained for any value of s in B.

---

[7]This is a very laborious proof for a lemma which seems intuitively obvious. This is because there are two classes of obvious results; those that are obvious and true, and those that are obvious and false. Sometimes, to be sure which class a result belongs to, it is necessary to follow through every single step.

Proof: First note that the intervals A and B are finite and bounded, hence the space $A^2 \times B^2$ from which each (a, a', b, b') comes is compact. Therefore for all finite s, the supremum of $|a(b - s) - a'(b' - s)|$ is attained for some (a, a', b, b') in $A^2 \times B^2$. Now suppose $s \in S$ for some sufficiently large closed set S. Then the infimum of $\sup |a(b - s) - a'(b' - s)|$ is also attained for some $s \in S$.[8]

Initially, consider

$$\sup_{\substack{a,a' \in A \\ b,b' \in B}} |a(b - s) - a'(b' - s)| \tag{10.144}$$

for a fixed real s. There are three cases to consider depending on the value of s for which the infimum is attained; $s \leq B_0$, $s \geq B_1$ and $B_0 \leq s \leq B_1$.

Case (i): $s \leq B_0$

For every $b, b' \in B$, $b - s$ and $b' - s$ are positive. Using the lemma 10.1 shows that

$$\sup_{\substack{a,a' \in A \\ b,b' \in B}} |a(b - s) - a'(b' - s)| = A_1(B_1 - s) - A_0(B_0 - s)$$

$$= (A_1 B_1 - A_0 B_0) - (A_1 - A_0)s$$
$$\geq (A_1 B_1 - A_0 B_0) - (A_1 - A_0)B_0$$
$$= A_1(B_1 - B_0) \tag{10.145}$$

Case (ii): $s \geq B_1$

For every $b, b' \in B$, $s - b$ and $s - b'$ are positive. Using the lemma 10.1 again shows that

$$\sup_{\substack{a,a' \in A \\ b,b' \in B}} |a(b - s) - a'(b' - s)| = A_1(s - B_0) - A_0(s - B_1)$$

$$= (A_0 B_1 - A_1 B_0) + (A_1 - A_0)s$$
$$\geq (A_0 B_1 - A_1 B_0) + (A_1 - A_0)B_1$$
$$= A_1(B_1 - B_0) \tag{10.146}$$

Case (iii): $B_0 \leq s \leq B_1$

If the supremum is attained with $s \leq b, b' \leq B_1$, apply case (i) with B_0

---

[8]This artificial compact set S is needed to ensure that the infimum is attained, not just approached as $s \to \pm\infty$. The conclusion of the theorem that the infimum is attained for every $s \in B$ is an *a posteriori* justification for choosing any closed finite set S such that $B \subset S$.

replaced by s to show that

$$\sup_{\substack{a,a'\in A \\ b,b'\in B}} |a(b-s) - a'(b'-s)| = A_1(B_1 - s) - A_0(s-s)$$

$$= A_1(B_1 - s)$$
$$\leq A_1(B_1 - B_0) \qquad (10.147)$$

If the supremum is attained with $B_0 \leq b, b' \leq s$, apply case (ii) with B_1 replaced by s to show that

$$\sup_{\substack{a,a'\in A \\ b,b'\in B}} |a(b-s) - a'(b'-s)| = A_1(s - B_0) - A_0(s-s)$$

$$= A_1(s - B_0)$$
$$\leq A_1(B_1 - B_0) \qquad (10.148)$$

The third possibility is that the supremum is attained with $B_0 \leq b \leq s \leq b' \leq B_1$. For all b and b' between these limits

$$|a(b-s) - a'(b'-s)| = a(s-b) + a'(b'-s)$$
$$\leq A_1(s - B_0) + A_1(B_1 - s)$$
$$= A_1(B_1 - B_0) \qquad (10.149)$$

This upper bound on the supremum is attained when $a = a' = A_1$, $b = B_0$ and $b' = B_1$. Therefore, if $B_0 \leq b \leq s \leq b' \leq B_1$

$$\sup_{\substack{a,a'\in A \\ b,b'\in B}} |a(b-s) - a'(b'-s)| = A_1(B_1 - B_0) \qquad (10.150)$$

Since all three cases have an identical upper bound, the supremum must be less than or equal to this common upper bound

$$\sup_{\substack{a,a'\in A \\ b,b'\in B}} |a(b-s) - a'(b'-s)| \leq A_1(B_1 - B_0) \qquad (10.151)$$

so that

$$\inf_s \sup_{\substack{a,a'\in A \\ b,b'\in B}} |a(b-s) - a'(b'-s)| \leq A_1(B_1 - B_0) \qquad (10.152)$$

Setting $a = a' = A_1$, $b = B_0$ and $b' = B_1$ for any $s \in B$ shows that this bound is reached with equality. Therefore

$$\inf_s \sup_{\substack{a,a'\in A \\ b,b'\in B}} |a(b-s) - a'(b'-s)| = A_1(B_1 - B_0) \qquad (10.153)$$

as required.   ■

Chapter 11

Conclusions

This thesis has applied the formal methodology of estimation theory to the problem of radial motion estimation for stepped-frequency ISAR imaging. The maximum likelihood estimator of the target's radial motion was derived, efficient algorithms were developed for evaluating the maximum likelihood estimator and its statistical properties were examined in detail. The maximum likelihood estimator has been compared with other methods of ISAR motion estimation, and the differences and similarities discussed. Finally, a number of assumptions made in ISAR imaging have been analysed, leading to several new constraints on the target's motion and the resolution of the ISAR image.

After discussing the conclusions in more detail, some possible topics for further research are suggested.

11.1 Conclusions

This thesis has investigated the use of estimation theory to find optimal estimators of a target's radial motion during stepped-frequency ISAR imaging and to analyse their statistical performance. The aim of this was two-fold: to apply a rigorously mathematical approach to a problem that has traditionally been solved using more intuitive methods, and to develop a unifying framework in whose terms the intuitive methods could be reinterpreted and reappraised.

The first step of applying estimation theory involved specifying a model relating the target's radial motion to measurements of its frequency response at two different times. This model assumed that as the target moved, its rotation was negligible.

The maximum likelihood estimator $\widehat{r}_{ml}$ of the radial distance Δr moved by the target was obtained in two different ways. The first was the scalar

maximum likelihood estimator, which assumed that Δr was the only un-
known parameter. The second, the vector maximum likelihood estimator,
estimated Δr along with the measurement noise variance σ_w^2 and the target's
frequency response. Both estimators of Δr took the same form, that of a
cost function, $J(r)$, whose global minimum is located at $\widehat{r}_{ml}$.

The cost function $J(r)$ has a slowly varying envelope modulated by a
high frequency carrier at twice the stepped-frequency waveform's average
frequency. Conventional methods of minimizing a function could not be
applied because of the closely spaced local extrema of $J(r)$, so algorithms for
the approximate global minimization of $J(r)$ and the exact local minimization
of $J(r)$ were developed. The global algorithms were based on the fast Fourier
transform and the chirp-Z transform and provided efficient ways of finding
the approximate value of $\widehat{r}_{ml}$. The local algorithm was iterative, and by
proving that it was a contraction mapping which converged at a rate equal
to the radar's relative bandwidth, it was shown that two iterations are usually
sufficient to estimate $\widehat{r}_{ml}$ for X-band ISAR.

The statistical properties of $\widehat{r}_{ml}$ were examined next. It was shown that
$\widehat{r}_{ml}$ is an unbiased estimator of Δr, and the Cramér-Rao bound was used to
establish a lower bound on the estimator's variance. Some progress was also
made towards finding the probability density function of $\widehat{r}_{ml}$.

Before comparing the maximum likelihood estimator to conventional meth-
ods of range profile alignment and phase compensation, it was shown that $\widehat{r}_{ml}$
could be rewritten as the location of the maximum of the cross-correlation of
the complex range profiles formed by Fourier-transforming the two frequency
responses. The cross-correlation methods of range profile alignment usually
cross-correlate the magnitudes of the target's range profiles. It was shown
that taking the magnitudes of the range profiles makes the cross-correlation
less sensitive to the target's rotation at the expense of a reduced accuracy.
This led to two strategies for range profile alignment.

The first strategy cross-correlated consecutive pairs of complex range pro-
files. This would be used if the cross-correlation has a high resolution (imple-
mented, for example, using the chirp-Z transform). This is justified because
the target's rotation is negligible in the period between the consecutive pro-
files.

The alternative strategy cross-correlated the magnitude of each range
profile with the magnitude of a reference profile. This was appropriate when
a cross-correlation with a low resolution was used (implemented, for example,
using a fast Fourier transform) because only radial movements greater than
about a range bin could be measured. Correlating the complex profiles is
not possible because the interval between profiles could be much larger than
under the first strategy so the target's rotation could no longer be considered
negligible.

Phase alignment techniques of the phase gradient autofocus and adaptive

beamforming were also compared to the maximum likelihood estimator. It was shown that the phase gradient part of phase gradient autofocus could be implemented using slightly sub-optimal versions of the algorithm for the exact local minimization of the cost function $J(r)$. This suggested that the performance of the maximum likelihood motion estimator might be improved by applying the same shift and windowing stages as the phase gradient autofocus, although this is yet to be verified.

Finally, four assumptions commonly made during ISAR imaging were analysed. Constraints under which the assumptions are valid were derived by considering the magnitude of the phase errors they cause to samples of the target's reflectivity in the (k_x, k_y)-plane immediately before the ISAR inversion. The first assumption involved the conditions under which the plane wave approximation of range-Doppler ISAR is valid. The second assumption was that polar reformatting could be omitted from the ISAR inversion algorithm. The constraints resulting from this assumption were found to be identical to the constraints obtained by restricting the movement of scatterers on the target through range and cross-range resolution cells.

The third assumption questioned whether the target's rotation during ISAR imaging could be considered negligible for the purposes of motion estimation. It was found that the target's rotation caused acceptably small phase errors between consecutive frequency responses provided the target filled no more than one-quarter of the ISAR cross-range ambiguity window. The term rotation-induced noise was used to describe the phase errors during motion estimation caused by the target's motion and it was verified experimentally how sensitive rotation-induced noise is to the target's rotation rate.

The fourth assumption questioned whether the ISAR image would be degraded if the small radial motion errors were only corrected using phase alignment. It was found that if phase alignment completely corrected for the fractional number of half-wavelengths moved by the target, the residual radial motion error could be up to one-quarter of an ISAR range bin.

To conclude, this work has illustrated how a mathematical approach using estimation theory can be used to obtain useful ISAR motion estimators and provide valuable insights into other motion estimators whose derivations otherwise could not be justified so easily.

11.2 Future Research

As is often the case, this research has prompted just as many questions as it has resolved. Here is a brief description of some unresolved issues and some suggestions for related future research. They are loosely divided into those concerned with radar imaging and those concerned with estimation theory.

11.2.1   Radar Imaging

- Test the maximum likelihood motion estimators of chapter 6 and the efficient algorithms of chapter 7 on real radar data and ISAR simulations to determine their effectiveness under a wide range of conditions.

- Perform proper theoretical analyses of the methods of range profile alignment and phase compensation described in chapter 5. Some theoretical results concerning their performance in noise and their robustness to the target's rotation are long overdue.

- As discussed in chapter 9, modify Steinberg's dominant scatterer algorithm to use more than one reference range bin for phase compensation without losing the ability to correct phase errors of rotating targets.

- Restate the motion estimation model for chirp waveforms and derive the equivalent maximum likelihood motion estimator in the range domain.

- Extend the model used to derive the maximum likelihood motion estimator to include the effects of the target's rotation implicitly. From this, derive new maximum likelihood motion estimators that are better able to deal with the target's rotation.

- Define a measure of a motion estimator's performance that is better than variance at describing the quality of the resulting ISAR image. Section 10.5 shows how motion estimation errors may extend for a significant fraction of a range bin if they are clustered enough around multiples of half a wavelength. Therefore any performance measure must take into account the total range of errors and how tightly they are clustered.

- Consider applying the maximum likelihood motion estimators to SAR imaging. This would have to use many of the elements of the phase gradient autofocus method as SAR images have strong scatterers over a much broader cross-range extent than does ISAR. The end result would probably be much like the phase gradient autofocus, but able to detect errors between range profiles of more than half a wavelength without ambiguities.

- Perform proper statistical analyses of the phase gradient autofocus, and in particular, prove that it converges to a focussed SAR image. Figure 4 of [96] suggests that the phase gradient autofocus converges even for SAR scenes with very low dynamic ranges and few strong point-like scatterers. If this is the case, the way it converges must be much more complicated that the simple explanation given in [25], [26] and [50].

- Look at the problem of angular motion estimation.

- Consider adaptive ISAR waveforms which achieve an optimal balance between the needs of accurate motion estimation and collecting enough data for a high resolution image. Because ISAR motion estimation requires lower rotation rates than ISAR imaging, perhaps some form of interleaved stepped-frequency waveforms could be used. One stepped-frequency waveform would be used for imaging and the other for motion estimation. Depending on the target's rotation rate, the signal-to-noise ratio and the desired resolution of the ISAR image, the parameters of the two stepped-frequency waveforms could be adjusted to match the accuracy of the motion estimation with that needed for the particular ISAR image.

11.2.2   Estimation Theory

- Work out more of the non-asymptotic properties of the maximum likelihood motion estimator, especially the probability density function.

- Generalizing the previous topic suggests the following problem, related to the probability density function of a maximum likelihood estimator:

Problem 11.1 (Maximum of a Bandlimited Function I)

Given a bandlimited function $f(t)$ whose values are known on an interval $[0, T]$ and a bandlimited Gaussian noise process $w(t)$, determine the probability density function $p(t, \sigma_w^2)$ of the location of the maximum of $f(t) + w(t)$ on $[0, T]$ as a function of the noise's variance σ_w^2.

This problem is very simply stated, but the solution is probably not at all simple. When the noise process's variance is zero, $p(t, 0) = \delta(t - t_0)$ where t_0 is the location of the global maximum of $f(t)$ on $[0, T]$. As $\sigma_w^2 \to \infty$, $p(t, \sigma_w^2) \to 1/T$. For some values of σ_w^2 between these two extremes, $p(t, \sigma_w^2)$ will have a shape that is similar to $f(t)$ itself, in that the peaks of the probability density function will occur at the location of the peaks of $f(t)$, and similarly for the troughs.

- Problem 11.1 leads to a more abstract problem:

Problem 11.2 (Maximum of a Bandlimited Function II)

Define $f(t)$ and $p(t, \sigma_w^2)$ as in problem 11.1. Determine the set B which contains all bandlimited functions $f(t)$ such that

$$p(t, \sigma_w^2) = f(t) \tag{11.1}$$

for all $t \in [0, T]$ and for some σ_w^2 dependent on f.

Clearly $f(t) = 1/T$ is a member of B. Are there any non-trivial members?

- Or yet another:

Problem 11.3 (Maximum of a Bandlimited Function III)

Define $f(t)$ and $p(t, \sigma_w^2)$ as in problem 11.1. Is $p(t, \sigma_w^2)$ bandlimited?

These problems are similar to the questions considered by the branch of statistics called extreme value theory. However, extreme value theory has many results about expected numbers of local extrema, expected frequencies of level crossings, and other asymptotic properties of local phenomena, but few about non-asymptotic properties of global phenomena.

Some of the early work of Rice [70, 71, 72, 73] and of Middleton [57] concerned extreme values of random waveforms, but they considered nothing quite like these three problems. Surveys of extreme value theory such as [11] and [99] do not indicate any comparable results either.

Bibliography

[1] ABRAMOWITZ, M., AND STEGUN, I. A. *Handbook of Mathematical Functions.* Dover, New York, 1965.

[2] ATTIA, E. H., AND STEINBERG, B. D. Self-cohering large antenna arrays using the spatial correlation properties of radar clutter. *IEEE Transactions on Antennas and Propagation 37*, 1 (Jan. 1989), 30–38.

[3] AUSHERMAN, D., KOZMA, A., WALKER, J., JONES, H., AND POGGIO, E. Developments in radar imaging. *IEEE Transactions on Aerospace and Electronic Systems 20*, 4 (July 1984), 363–400.

[4] BAMLER, R. A comparison of range-Doppler and wavenumber domain SAR focusing algorithms. *IEEE Transactions on Geoscience and Remote Sensing 30*, 4 (July 1992), 706–713.

[5] BAR-SHALOM, Y., AND FORTMANN, T. E. *Tracking and Data Association.* Academic Press, Orlando, Florida, 1988.

[6] BARANKIN, E. W. Locally best unbiased estimates. *Annals of Mathematical Statistics 20* (1949), 477–501.

[7] BERNFELD, M. Chirp doppler radar. *Proceedings of the IEEE 72*, 4 (Apr. 1984), 540–541.

[8] BHATTACHARYYA, A. On some analogues of the amount of information and their use in statistical estimation, part I. *Sankhyā: The Indian Journal of Statistics 8*, 1 (1946), 1–14.

[9] BHATTACHARYYA, A. On some analogues of the amount of information and their use in statistical estimation, part II. *Sankhyā: The Indian Journal of Statistics 8*, 3 (1947), 201–218.

[10] BHATTACHARYYA, A. On some analogues of the amount of information and their use in statistical estimation, part III. *Sankhyā: The Indian Journal of Statistics 8*, 4 (1948), 315–328.

[11] BLAKE, I. F., AND LINDSAY, W. C. Level-crossing problems for random processes. *IEEE Transactions on Information Theory 19*, 3 (May 1973), 295–315.

[12] BLAKE, L. V. *Radar Range Performance Analysis.* Artech House, Norwood, MA, 1986.

[13] BLUESTEIN, L. I. A linear filtering approach to the computation of discrete Fourier transform. *IEEE Transactions on Audio and Electroacoustics 18*, 4 (Dec. 1970), 451–455.

[14] BOCKER, R. P., HENDERSON, T. B., JONES, S. A., AND FRIEDEN, B. R. A new inverse synthetic aperture radar algorithm for translational motion compensation. In *Proceedings of the SPIE – Stochastic and Neural Methods in Signal Processing, Image Processing and Computer Vision* (July 1991), vol. 1569, pp. 298–310.

[15] BRACEWELL, R. N. *The Fourier Transform and its Application*, second ed. McGraw-Hill, New York, 1986.

[16] BROWN, W. M., AND FREDRICKS, R. J. Range-Doppler imaging with motion through resolution cells. *IEEE Transactions on Aerospace and Electronic Systems 5*, 1 (Jan. 1969), 98–102.

[17] CAFFORIO, C., PRATI, C., AND ROCCA, E. SAR data focusing using seismic migration techniques. *IEEE Transactions on Aerospace and Electronic Systems 27*, 2 (Mar. 1991), 194–207.

[18] CHEN, C.-C., AND ANDREWS, H. C. Multifrequency imaging of radar turntable data. *IEEE Transactions on Aerospace and Electronic Systems 16*, 1 (Jan. 1980), 15–22.

[19] CHEN, C.-C., AND ANDREWS, H. C. Target-motion-induced radar imaging. *IEEE Transactions on Aerospace and Electronic Systems 16*, 1 (Jan. 1980), 2–14.

[20] CHUANG, W., AND HUANG, T. S. Estimating rotation speed from projections in SAR. In ICASSP92 [48], pp. 21–24.

[21] COHEN, M. H. Introduction to Very-Long-Baseline interferometry. *Proceedings of the IEEE 61*, 9 (Sept. 1973), 1192–1197.

[22] CRAMÉR, H. *Mathematical Methods of Statistics.* Princeton University Press, 1946.

[23] DAVENPORT, JR., W. B., AND ROOT, W. L. *An Introduction to the Theory of Random Signals and Noise.* McGraw-Hill, New York, 1958. (reprinted by IEEE Press, 1987).

[24] DELISLE, G. Y., AND WU, H. Moving target imaging and trajectory computation using ISAR. *IEEE Transactions on Aerospace and Electronic Systems 30*, 3 (July 1994), 887–899.

[25] EICHEL, P. H., GHIGLIA, D. C., AND JAKOWATZ, JR., C. V. Speckle processing method for synthetic aperture radar phase correction. *Optics Letters 14*, 1 (Jan. 1989), 1–3.

[26] EICHEL, P. H., AND JAKOWATZ, JR., C. V. Phase-gradient algorithm as an optimal estimator of the phase derivative. *Optics Letters 14*, 20 (15 Oct. 1989), 1101–1103.

[27] FARINA, A., PRODI, F., AND VINELLI, F. Application of superresolution techniques to radar imaging. *Chinese Journal of Systems Engineering and Electronics 5*, 1 (Jan. 1994), 1–14.

[28] FISHER, R. A. Theory of statistical estimation. *Proceedings of the Cambridge Philosophical Society 22* (1925), 700–725. reprinted in Volume II of *Collected Papers of R. A. Fisher*, edited by J. H. Bennett, University of Adelaide, 1973.

[29] FISHER, R. A. Inverse probability. *Proceedings of the Cambridge Philosophical Society 26* (1930), 528–535. reprinted in Volume II of *Collected Papers of R. A. Fisher*, edited by J. H. Bennett, University of Adelaide, 1973.

[30] FISHER, R. A. Probability likelihood and quantity of information in the logic of uncertain inference. *Proceedings of Royal Society of London, A 146* (1934), 1–8. reprinted in Volume III of *Collected Papers of R. A. Fisher*, edited by J. H. Bennett, University of Adelaide, 1973.

[31] FISHER, R. A. Two new properties of mathematical likelihood. *Proceedings of Royal Society of London, A 144* (1934), 285–307. reprinted in Volume III of *Collected Papers of R. A. Fisher*, edited by J. H. Bennett, University of Adelaide, 1973.

[32] FLORES, B. C. *Robust Methods for the Motion Compensation of Inverse Synthetic Aperture Radar Imagery.* PhD thesis, Arizona State University, Aug. 1990.

[33] FLYNN, T. J. Wavenumber-domain SAR focusing from a nonuniform synthetic aperture. In ICASSP92 [48], pp. 1–4.

[34] FOMALONT, E. B. Earth-rotation aperture synthesis. *Proceedings of the IEEE 61*, 9 (Sept. 1973), 1211–1218.

[35] GERLACH, D. A method for wide-rotation-angle radar cross section (RCS) measurement using a tomographic inverse synthetic aperture radar (ISAR) algorithm. Tech. rep., Naval Ocean Systems Centre, Radar Branch, Code 755, San Diego, CA, Aug. 1989.

[36] GOLUB, G. H., AND VAN LOAN, C. F. *Matrix Computations*. Johns Hopkins University Press, 1983.

[37] GOODALL, J. C. *America's Stealth Fighters and Bombers*. Motorbooks International, Osceola, WI, 1992.

[38] GOODMAN, J. W. *Introduction to Fourier Optics*. McGraw-Hill, New York, 1968.

[39] GUPTA, I. J. High-resolution radar imaging using 2-D linear prediction. *IEEE Transactions on Antennas and Propagation 42*, 1 (Jan. 1994), 31–37.

[40] HARRIS, F. Overview of radar imaging (SAR and ISAR). In *Radarcon 90* (Adelaide, Australia, 18–20 Apr. 1990), vol. 1, pp. 155–163.

[41] HAYKIN, S., Ed. *Array Signal Processing*. Prentice-Hall, Englewood Cliffs, NJ, 1985.

[42] HAYWOOD, B. *Contributions to Inverse Synthetic Aperture Radar Imaging*. PhD thesis, The University of Newcastle, Feb. 1992.

[43] HAYWOOD, B., AND EVANS, R. J. Motion compensation for ISAR imaging. In *Proceedings of the Australian Symposium on Signal Processing and Applications* (Adelaide, Australia, 17–19 Apr. 1989), R. F. Barrett, Ed., pp. 112–117.

[44] HAYWOOD, B., AND EVANS, R. J. Discrete 2-D system identification for imaging rotating radar targets. *Signal Processing 29*, 2 (1992), 191–211.

[45] HAYWOOD, B., AND EVANS, R. J. Discrete 2-D system identification for ISAR imaging. In Radar92 [68], pp. 411–414.

[46] HUA, Y. High resolution imaging of continuously moving object using stepped frequency radar. *Signal Processing 35*, 1 (Jan. 1994), 33–40.

[47] HUA, Y., BAQAI, F., ZHU, Y., AND HEILBRONN, D. Imaging of point scatterers from step-frequency ISAR data. *IEEE Transactions on Aerospace and Electronic Systems 29*, 1 (Jan. 1993), 195–205.

[48] *Proceedings of ICASSP '92* (San Francisco, 23–26 Mar. 1992), IEEE Press.

[49] JACKSON, P. L. Radar superresolution? Perhaps! *IEEE Transactions on Aerospace and Electronic Systems 17*, 5 (Sept. 1981), 734–735.

[50] JAKOWATZ, JR., C. V., EICHEL, P. H., AND GHIGLIA, D. C. Autofocus of SAR imagery degraded by ionospheric-induced phase errors. In *Proceedings of the SPIE - Millimeter Wave and Synthetic Aperture Radar* (1989), vol. 1101, pp. 46–52.

[51] KAY, S. M. *Fundamentals of Statistical Signal Processing: Estimation Theory.* Prentice-Hall, Englewood Cliffs, NJ, 1993.

[52] KAY, S. M., AND MARPLE, JR., S. L. Spectrum analysis - a modern perspective. *Proceedings of the IEEE 69*, 11 (Nov. 1981), 1380–1419.

[53] KLAUDER, J. R., PRICE, A. C., DARLINGTON, S., AND ALBERSHEIM, W. J. The theory and design of chirp radars. *Bell System Technical Journal 39*, 4 (July 1960), 745–808.

[54] LAWTON, W. New polar Fourier transform for computer-aided tomography and spotlight synthetic aperture radar. *IEEE Transactions on Acoustics, Speech and Signal Processing 36*, 6 (June 1988), 931–934.

[55] MENSA, D. L. *High Resolution Radar Cross-Section Imaging.* Artech House, Norwood, MA, 1991.

[56] MENSA, D. L., HALEVY, S., AND WADE, G. Coherent Doppler tomography for microwave imaging. *Proceedings of the IEEE 71*, 2 (Feb. 1983), 254–261.

[57] MIDDLETON, D. Some general results in the theory of noise through non-linear devices. *Quarterly of Applied Mathematics 5*, 4 (Jan. 1948), 445–498.

[58] MORSE, P. M., AND FESHBACH, H. *Methods of Theoretical Physics, Part I.* McGraw-Hill, New York, 1953.

[59] MORSE, P. M., AND FESHBACH, H. *Methods of Theoretical Physics, Part II.* McGraw-Hill, New York, 1953.

[60] MUNSON, JR., D. C., O'BRIEN, J. D., AND JENKINS, W. K. A tomographic formulation of spotlight-mode synthetic aperture radar. *Proceedings of the IEEE 71*, 8 (Aug. 1983), 917–925.

[61] MUNSON, JR., D. C., AND VISENTIN, R. L. A signal processing view of strip-mapping synthetic aperture radar. *IEEE Transactions on Acoustics, Speech and Signal Processing 37*, 12 (Dec. 1989), 2131–2147.

[62] NGUYEN, H. T., AND ROGERS, G. S. *Fundamentals of Mathematical Statistics. Volume II: Statistical Inference.* Springer Texts in Statistics. Springer-Verlag, New York, 1989.

[63] NUTHALAPATI, R. M. High resolution reconstruction of ISAR images. *IEEE Transactions on Aerospace and Electronic Systems 28*, 2 (Apr. 1992), 462–472.

[64] ODENTAAL, J. W., BARNARD, E., AND PISTORIUS, C. W. I. Two-dimensional superresolution radar imaging using the MUSIC algorithm. *IEEE Transactions on Antennas and Propagation 42*, 10 (Oct. 1994), 1386–1391.

[65] POLYA, G. *How to Solve It*, second ed. Princeton University Press, Princeton, NJ, 1957.

[66] RABINER, L. R., SCHAFER, R. W., AND RADER, C. M. The chirp Z-transform algorithm. *IEEE Transactions on Audio and Electroacoustics 17*, 2 (June 1969), 86–92.

[67] RABINER, L. R., SCHAFER, R. W., AND RADER, C. M. The chirp Z-transform algorithm and its application. *Bell System Technical Journal 48*, 3 (May–June 1969), 1249–1292.

[68] *Proceedings of Radar 92* (Brighton, U. K., 12–13 Oct. 1992), IEE Conference Publication No. 365.

[69] RAO, C. R. *Linear Statistical Inference and Its Applications*, first ed. John Wiley & Sons, New York, 1965.

[70] RICE, S. O. The distribution of the maxima of a random curve. *American Journal of Mathematics 61* (1939), 409–416.

[71] RICE, S. O. Mathematical analysis of random noise, part I. *Bell System Technical Journal 23*, 3 (July 1944), 282–332.

[72] RICE, S. O. Mathematical analysis of random noise, part II. *Bell System Technical Journal 24*, 1 (Jan. 1945), 46–156.

[73] RICE, S. O. Statistical properties of a sine wave plus random noise. *Bell System Technical Journal 27*, 1 (Jan. 1948), 109–157.

[74] RIHACZEK, A. W. *Principles of High Resolution Radar.* McGraw-Hill, New York, 1969.

[75] RIHACZEK, A. W. Comments on "Radar Superresolution? Perhaps!". *IEEE Transactions on Aerospace and Electronic Systems 17*, 5 (Sept. 1981), 735.

[76] RIHACZEK, A. W. The maximum entropy of radar resolution. *IEEE Transactions on Aerospace and Electronic Systems 17*, 1 (Jan. 1981), 144.

[77] RITCEY, J. A. On the probability density of a maximum likelihood mean frequency estimator. *IEEE Transactions on Acoustics, Speech and Signal Processing 35*, 4 (Apr. 1987), 579–580.

[78] ROBERTSON, B. L., AND MUNSON, JR., D. C. Motion errors in ISAR imaging of approaching targets. In *Proceedings of ICASSP '93* (Minneapolis, 27–30 Apr. 1993), vol. V, IEEE Press, pp. 449–452.

[79] SKOLNIK, M. I., Ed. *Radar Handbook*, second ed. McGraw-Hill, New York, 1990.

[80] SNYDER, D. L., O'SULLIVAN, J. A., AND MILLER, M. I. The use of maximum likelihood estimation for forming images of diffuse radar targets from delay-doppler data. *IEEE Transactions on Information Theory 35*, 3 (May 1989), 536–548.

[81] SNYDER, D. L., WHITEHOUSE, H. J., WOHLSCHLAEGER, J. T., AND LEWIS, R. C. A new approach to radar/sonar imaging. In *Proceedings of the SPIE - Advanced Algorithms and Architectures* (1986), vol. 696, pp. 20–25.

[82] SOUMEKH, M. Bistatic synthetic aperture radar inversion with application in dynamic object imaging. *IEEE Transactions on Signal Processing 39*, 9 (Sept. 1991), 2044–2055.

[83] SOUMEKH, M. A system model for synthetic aperture radar imaging. *IEEE Transactions on Image Processing 1*, 1 (Jan. 1992), 64–76.

[84] SOUMEKH, M. *Fourier Array Imaging.* Prentice-Hall, Englewood Cliffs, NJ, 1994.

[85] SOUMEKH, M., AND CHOI, J.-H. Phase and amplitude restoration in synthetic aperture radar imaging. *IEEE Transactions on Image Processing 1*, 2 (Apr. 1992), 229–242.

[86] STEINBERG, B. D. *Principles of Aperture and Array System Design.* John Wiley & Sons, New York, 1976.

[87] STEINBERG, B. D. Radar imaging from a distorted array: the radio camera algorithm. *IEEE Transactions on Antennas and Propagation 29*, 5 (May 1981), 740–748.

[88] STEINBERG, B. D. *Microwave Imaging with Large Antenna Arrays.* John Wiley & Sons, New York, 1983.

[89] STEINBERG, B. D., WHISTLER, W., AND CARSON, D. Two-dimensional imaging with a radio camera. *Proceedings of the IEEE 71*, 11 (Nov. 1983), 1325–1326.

[90] STIMSON, G. W. *Introduction to Airborne Radar.* Hughes Aircraft Company, El Segundo, CA, 1983.

[91] STOLT, R. H. Migration by Fourier transform. *Geophysics 43*, 1 (Feb. 1978), 23–48.

[92] STUART, A., AND ORD, J. K. *Kendall's Advanced Theory of Statistics: Distribution Theory*, fifth ed., vol. 1. Oxford University Press, New York, 1987.

[93] STUART, A., AND ORD, J. K. *Kendall's Advanced Theory of Statistics: Classical Inference and Relationship*, fifth ed., vol. 2. Oxford University Press, New York, 1991.

[94] TAHERI, S. H., AND STEINBERG, B. D. Tolerances in self-cohering antenna arrays of arbitrary geometry. *IEEE Transactions on Antennas and Propagation 24*, 5 (Sept. 1976), 733–739.

[95] VAN TREES, H. L. *Detection, Estimation and Modulation Theory, Part I.* John Wiley & Sons, New York, 1968.

[96] WAHL, D. E., EICHEL, P. H., GHIGLIA, D. C., AND JAKOWATZ, JR., C. V. Phase gradient autofocus—a robust tool for high resolution SAR phase correction. *IEEE Transactions on Aerospace and Electronic Systems 30*, 3 (July 1994), 827–835.

[97] WALKER, J. L. Range-Doppler imaging of rotating objects. *IEEE Transactions on Aerospace and Electronic Systems 16*, 1 (Jan. 1980), 23–52.

[98] WEHNER, D. R. *High Resolution Radar.* Artech House, Norwood, MA, 1987.

[99] WEINSTEIN, S. B. Theory and application of some classical and generalized asymptotic distributions of extreme values. *IEEE Transactions on Information Theory 19*, 2 (Mar. 1973), 148–154.

[100] WERNESS, S., CARRARA, W., JOYCE, I., AND FRANCZAK, D. Moving target imaging algorithm for SAR data. *IEEE Transactions on Aerospace and Electronic Systems 26*, 1 (Jan. 1990), 57–67.

[101] XU, R., CAO, Z., AND LIU, Y. Method of precise motion compensation for ISAR. *Proceedings of the SPIE – Advanced Algorithms and Architectures for Signal Processing IV 1152* (1989), 288–295.

[102] XU, R., CAO, Z., AND LIU, Y. Motion compensation for ISAR and noise effect. *IEEE Aerospace and Electronic Systems Magazine 5*, 6 (June 1990), 20–22.

[103] XU, R., CAO, Z., AND LIU, Y. A new method of motion compensation for ISAR. In *Proceedings of the 1990 IEEE International Radar Conference* (Arlington, VA, 7–10 May 1990), IEEE, IEEE Press, pp. 234–237.

[104] YANG, H., AND SOUMEKH, M. Blind-velocity SAR/ISAR imaging of a moving target in a stationary background. *IEEE Transactions on Image Processing 2*, 1 (Jan. 1993), 80–95.

[105] ZHAO, Q. ISAR imaging without motion compensation. In Radar92 [68], pp. 473–476.

[106] ZYWECK, A., AND BOGNER, R. E. High-resolution radar imagery of the Mirage III aircraft. *IEEE Transactions on Antennas and Propagation 42*, 9 (Sept. 1994), 1356–1360.